QUANTUM ENGINEERING WITH SUBGAP AND BOUNDARY MODES

Topology, Correlation, and Information in Designer Quantum Systems

DISSERTATION

zur Erlangung des Grades eines
Doktors der Naturwissenschaften

AM FACHBEREICH PHYSIK DER FREIEN UNIVERSITÄT BERLIN

vorgelegt von

JACOB FRIDOLIN STEINER

Berlin, 2023

Erstgutachter: Prof. Felix von Oppen, PhD
Zweitgutachter: Prof. Dr. Piet W. Brouwer
Drittgutachter: Prof. Dr. Christoph Bruder

Tag der Abgabe: 26. Januar 2023
Tag der Disputation: 9. Mai 2023

SELBSTSTÄNDIGKEITSERKLÄRUNG

Name: Steiner
Vornamen: Jacob Fridolin

Ich erkläre gegenüber der Freien Universität Berlin, dass ich die vorliegende Dissertation selbstständig und ohne Benutzung anderer als der angegebenen Quellen und Hilfsmittel angefertigt habe. Die vorliegende Arbeit ist frei von Plagiaten. Alle Ausführungen, die wörtlich oder inhaltlich aus anderen Schriften entnommen sind, habe ich als solche kenntlich gemacht. Diese Dissertation wurde in gleicher oder ähnlicher Form noch in keinem früheren Promotionsverfahren eingereicht.

Mit einer Prüfung meiner Arbeit durch ein Plagiatsprüfungsprogramm erkläre ich mich einverstanden.

Datum: **Unterschrift**:

Kurzfassung

Diese Arbeit befasst sich mit der Nutzung von Subgap- und Randmoden für die Quantenkonstruktion neuartiger Phasen, Bauelemente und Antwortsmerkmale. Sie umfasst vier separate Themen: Quantenmagnetismus in Yu-Shiba-Rusinov-Ketten, einatomige Josephson-Dioden, Majorana-Qubits und photogalvanische Oberflächenantwort in Weyl-Halbmetallen.

Ketten aus magnetischen Adatomen auf Supraleitern wurden als vielversprechende Systeme zur Realisierung von Majorana-Endzuständen diskutiert. Hier zeigen wir, dass Yu-Shiba-Rusinov (YSR)-Ketten auch eine vielseitige Plattform für Quantenmagnetismus und korrelierte Elektronendynamik sind. Mit dem Schwerpunkt auf Subgap-Anregungen leiten wir ein erweitertes $t - J$-Modell für Quanten-YSR-Ketten ab und untersuchen damit das Phasendiagramm und die Tunnelspektren. Wir untersuchen die Implikationen des Quantenmagnetismus für die Bildung einer topologischen supraleitenden Phase und kontrastieren mit bestehenden Modellen, die von klassischen Spinstrukturen ausgehen.

Stromgetriebene Josephson-Kontakte zeigen Hysterese zwischen dissipativem und supraleitendem Zustand. Übergänge treten auf sobald der angelegte Strom den Umschalt- oder Einfangstrom erreicht. Wir betrachten diodenähnliche Effekte in den Umschalt- oder Einfangströmen von schwach gedämpften Josephson-Kontakten. Wir demonstrieren, dass das diodenartige Verhalten der Umschaltströme auf asymmetrischen Strom-Phasen-Relationen beruht, während nicht-reziproke Einfangströme von asymmetrischer Dissipation herrühren. Dies impliziert deutlich unterschiedliche Symmetrieanforderungen. Wir veranschaulichen unsere Ergebnisse anhand eines mikroskopischen Modells für Kontakte mit YSR-Subgap-Zuständen.

Vorraussetzung für topologische Quantencomputer basierend auf lokalisierten Majorana-Zuständen ist die Fähigkeit, Produkte von Majorana-Operatoren projektiv zu messen. Wir modellieren den Messprozess von Majorana-Qubits mithilfe der Technik der Quantentrajektorien. Insbesondere konzentrieren wir uns auf das Auslesen von Majorana-Qubits durch einen tunnelgekoppelten Quantenpunkt welcher wiederum kapazitiv an einen Quantenpunktkontakt gekoppelt ist. Wir zeigen, dass projektive Messungen von Majorana-Produkten durch kontinuierliche Ladungsabtastung unter recht allgemeinen Bedingungen durchgeführt werden können. Wesentliche Voraussetzungen sind, dass eine kombinierte lokale Parität $\hat{\pi}$, die die Quantenpunktladung zusammen mit dem relevanten Majoranaprodukt umfasst, erhalten bleibt und dass die beiden Eigenräume der kombinierten Parität $\hat{\pi}$ unterscheidbare Messsignale erzeugen.

Abschließend untersuchen wir, wie der photogalvanische Effekt in Weyl-Halbmetallen durch die Manipulation von Fermi-Arc-Zuständen an der Materialoberfläche ermöglicht und kontrolliert werden kann. Konkret entwickeln wir eine Theorie des ballistischen photogalvanischen Stroms in einer Weyl-Halbmetall-Platte. Wir zeigen, dass die Oberflächenantwort durch die Konfiguration der Fermi-Arc-Oberflächenzustände festgelegt ist. Dies ermöglicht im Prinzip die Steuerung des photogalvanischen Stroms durch Oberflächenpotentiale.

ABSTRACT

This thesis discusses the use of subgap and boundary modes for quantum engineering of novel phases, devices and response characteristics. It is comprised of four separate topics: quantum magnetism in Yu-Shiba-Rusinov chains, single-atom Josephson diodes, readout of Majorana qubits, and surface photogalvanic response in Weyl semimetals.

Chains of magnetic adatoms on superconductors have been discussed as promising systems for realizing Majorana end states. Here, we show that dilute Yu-Shiba-Rusinov (YSR) chains are also a versatile platform for quantum magnetism and correlated electron dynamics, with widely adjustable spin values and couplings. Focusing on subgap excitations, we derive an extended $t - J$ model for dilute quantum YSR chains and use it to study the phase diagram as well as tunneling spectra. We explore the implications of quantum magnetism for the formation of a topological superconducting phase, contrasting it to existing models assuming classical spin textures.

Current-biased Josephson junctions exhibit hysteretic transitions between dissipative and superconducting states as characterized by switching and retrapping currents. Here, we develop a theory for diode-like effects in the switching and retrapping currents of weakly-damped Josephson junctions. We find that while the diode-like behavior of switching currents is rooted in asymmetric current-phase relations, nonreciprocal retrapping currents originate in asymmetric quasiparticle currents. These different origins also imply distinctly different symmetry requirements. We illustrate our results by a microscopic model for junctions involving YSR subgap states. Our theory provides significant guidance in identifying the microscopic origin of nonreciprocities in Josephson junctions.

Schemes for topological quantum computation with Majorana bound states rely heavily on the ability to measure products of Majorana operators projectively. Here, we employ Markovian quantum measurement theory, including the readout device, to analyze such measurements. Specifically, we focus on the readout of Majorana qubits via continuous charge sensing of a tunnel-coupled quantum dot by a quantum point contact. We show that projective measurements of Majorana products can be implemented by continuous charge sensing under quite general circumstances. Essential requirements are that a combined local parity $\hat{\pi}$, involving the quantum dot charge along with the Majorana product of interest, be conserved, and that the two eigenspaces of the combined parity $\hat{\pi}$ generate distinguishable measurement signals.

The photogalvanic effect requires the intrinsic symmetry of the medium to be sufficiently low, which strongly limits candidate materials for this effect. We explore how in Weyl semimetals the photogalvanic effect can be enabled and controlled by design of Fermi arc states at the material surface. Specifically, we provide a theory of ballistic photogalvanic current in a Weyl semimetal slab. We show that the confinement-induced response is tightly linked to the configuration of Fermi-arc surface states, thus inheriting the same directionality and sensitivity to boundary conditions. In principle this enables the control of the photogalvanic response through manipulation at the surface only.

LIST OF PUBLICATIONS

This thesis is based on seven peer-reviewed and published articles. One further article is in preparation. They are listed here in order-of-appearance:

- Jacob F. Steiner, Christophe Mora, Katharina J. Franke, and Felix von Oppen,
  Quantum magnetism and topological superconductivity in Yu-Shiba-Rusinov chains
  Phys. Rev. Lett. 128, 036801 [I], published 21 January 2022
  `https://doi.org/10.1103/PhysRevLett.128.036801`
  The main results of Chapter 3 are published in this work. Parts of the chapter are based on this work.

- Eva Liebhaber, Lisa M. Rütten, Gaël Reecht, Jacob F. Steiner, Sebastian Rohlf, Kai Rossnagel, Felix von Oppen, and Katharina J. Franke,
  Quantum spins and hybridization in artificially-constructed chains of magnetic adatoms on a superconductor
  Nat. Comm. 13, 2160 [II], published 20 April 2022
  `https://doi.org/10.1038/s41467-022-29879-0`
  Chapter 3 includes part of this work.

- Harald Schmid, Jacob F. Steiner, Katharina J. Franke, and Felix von Oppen,
  Quantum Yu-Shiba-Rusinov dimers
  Phys. Rev. B 105, 235406 [III], published 7 June 2022
  `https://doi.org/10.1103/PhysRevB.105.235406`
  Chapter 3 includes part of this work.

- Jacob F. Steiner, Larissa Melischek, Martina Trahms, Katharina J. Franke, and Felix von Oppen,
  Diode effects in current-biased Josephson junctions
  Phys. Rev. Lett. 130, 177002 [IV], published 27 April 2023
  `https://doi.org/10.1103/PhysRevLett.130.177002`
  The main results of Chapter 4 are published in this work. Parts of the chapter are based on this work.

- Martina Trahms, Larissa Melischek, Jacob F. Steiner, Bharti Mahendru, Idan Tamir, Nils Bogdanoff, Olof Peters, Gael Reecht, Clemens B. Winkelmann, Felix von Oppen, and Katharina J. Franke,
  Diode effect in Josephson junctions with a single magnetic atom
  Nature 615, 628 [V], published 8 March 2023
  `https://doi.org/10.1038/s41586-023-05743-z`
  Chapter 4 includes part of this work.

- Jacob F. Steiner, Larissa Melischek, and Felix von Oppen,
  Keldysh effective action and Langevin dynamics of nonreciprocal Josephson junctions
  in preparation [VI]
  This publication will contain results of Chapter 4.

- Jacob F. Steiner, and Felix von Oppen,
  Readout of Majorana qubits
  Phys. Rev. Research 2, 033255 [VII], published 17 August 2020
  `https://doi.org/10.1103/PhysRevResearch.2.033255`
  Chapter 5 is based on this work.

- Jacob F. Steiner, Anton. V. Andreev, and Maxim Breitkreiz,
  Surface photogalvanic effect in Weyl semimetals
  Phys. Rev. Research 4, 023021 [VIII], published 8 April 2022
  `https://doi.org/10.1103/PhysRevResearch.4.023021`
  Chapter 6 is based on this work.

The author has published one additional article which is not part of this thesis:

- Jacob F. Steiner, Anton V. Andreev, and Dmytro A. Pesin,
  Anomalous Hall effect in type-I Weyl metals
  Phys. Rev. Lett. 119, 036601 [IX], published 18 July 2017
  `https://doi.org/10.1103/PhysRevLett.119.036601`

CONTENTS

1 INTRODUCTION

Inspired by the quantum information revolution [1] as well as the advent of topology as a guiding principle [2–4], the focus of solid-state and many-body research has shifted away from its traditional scientific program of observation and explanation towards a new paradigm of *quantum engineering*: many of the most fascinating and exotic phenomena associated with quantum many-body physics do not arise in naturally occurring materials and ambiance but require the precise and thoughtful design of constituents and environment.

This thesis is concerned with the design and control of quantum matter and quantum devices engineered from spatially localized and energetically isolated *subgap* and *boundary modes*, as well as engineered response characteristics enabled and controlled by subgap and boundary modes. A common feature of these devices and their response is the lack of a classical counterpart.[1]

Assemblies of magnetic adatoms on a superconducting substrate are prime examples of quantum matter designed in a bottom-up fashion. The Hilbert space of the engineered quantum system is spanned by YSR subgap states induced by the low energy spin degree of freedom of magnetic adatoms [5–7]. Due to their overlapping wave-functions and substrate-mediated interactions the YSR states combine into complex quantum systems within and protected by the host superconductor's energy gap [8–10]. The choice of adatom species and substrate superconductor, and most importantly, the precise placement of the adatoms leave a great amount of freedom to engineer the properties of the subgap quantum system [11–14]: atomic scale manipulations in the scanning tunneling microscope (STM) environment enable the design of almost arbitrary adatom structures [15]. This freedom has been widely explored in the case of metallic and semiconducting substrates [16], but for superconducting substrates the field is still in its infancy. While STM experiments which probe the subgap structure of individual adatoms or molecules are well-established [11, 17–20], Yu-Shiba-Rusinov dimers [8, 9, 21–25] and chains [II, 10, 26–29] are subject of very recent experimental studies (the latter should not be confused with densely packed chains, where overlapping d-orbitals directly form bands and pairing is introduced by proximity [30, 31]). The objectives of these YSR assembly designs are multifold. It has recently been proposed that YSR dimers may serve as qubits [32]. Furthermore, YSR spectroscopy provides insight into the nature of the substrate's order parameter and into the substrate's band topology [33–37]. Finally, YSR assemblies are believed to realize novel correlation-driven phases [I, II] and topological superconductivity [38, 39].

---

[1] Note that our understanding of quantum engineering is broad and involves also systems which do not rely on coherence or entanglement as long as their phenomenology relies on quantum effects without classical counterpart, such as the chiral anomaly or superfluidity. This is in contrast to the understanding of, e.g., MacFarlane et al. [1]

One-dimensional topological superconductors have attracted extensive attention in recent years due to their "Majorana" boundary modes [40]. These Majorana boundary modes are distinctly different from regular subgap states in superconductors such as Andreev or YSR states due to their topological nature. First, their excitation energies vanish exponentially in the system size, giving rise to a topological ground state degeneracy. Second, local perturbations leave the quantum information encoded in the ground state manifold unaffected [41]. This is because Majorana zero modes are guaranteed to occur in pairs which reveal their quantum information content only when brought together and fused. Finally, braiding of Majorana bound states provides protected operations acting on their quantum information content [42, 43]. These exotic properties make Majorana zero modes attractive for quantum computing applications [41, 44, 45]. Moreover, the nonlocal nature of spatially separated Majorana bound states enable novel schemes of engineering quantum matter [46–48]. However, one-dimensional topological superconductors require pairing of effectively spinless fermions. In realistic systems, this translates to a combination of spin-orbit coupling, time reversal symmetry breaking through magnetic fields or magnetic order, and superconductivity. These ingredients do not occur together naturally,[2] making this a quantum engineering task [49]. Next to the aforementioned YSR chains, semiconductor nanowires proximitized by an s-wave superconductor and placed into a magnetic field [50, 51] represent the major proposal towards realizing a one-dimensional topological superconductor. So far, evidence for Majorana edge modes is purely spectroscopic [30, 52, 53] and can in principle be mimicked by trivial subgap states. Braiding or coherent manipulation of the ground state manifold has not been demonstrated at the time of writing.

Majorana zero modes are but one example of a boundary signature mandated by a topological bulk [54, 55]. Another example are Fermi arc surface states in topological semimetals, the most well known example being Weyl semimetals [56]. These three-dimensional materials are characterized by touching points of non-degenerate bands at the Fermi energy where Bloch electrons are described by the chiral Weyl equation [57]. The Adler-Bell-Jackiw anomaly demands that these "Weyl points" come in pairs of opposite chirality [58, 59]. This implies that they are topological objects which can only annihilate pairwise [60]. The Adler-Bell-Jackiw anomaly has important ramifications for the bulk electromagnetic response in Weyl semimetals [61, 62]. It gives rise to a semi-quantized intrinsic anomalous Hall conductivity [63] and the chiral magnetic effect [64] manifesting as negative magnetoresistance in Weyl semimetals [65, 66]. The chiral nature of Weyl fermions is further linked to a plethora of optical phenomena related to chiral, i.e. elliptically polarized, light [IX, 67–75]. The Fermi arc surface states may be understood as another consequence of the chiral anomaly: in the presence of a magnetic field chiral fermions at one of the Weyl points move in parallel to the field. This would lead to charge build up at the sample edges which is clearly not physical as constant magnetic fields do not do work. Fermi arc

---

[2] Majorana zero modes also arise in the $\nu = \frac{5}{2}$ fractional quantum Hall state of a two-dimensional electron gas in a large magnetic field. While two-dimensional electron gases are engineering feats on their own, one might argue that these circumstances are somewhat natural. However, this platform for Majorana zero modes has its own challenges and, frankly, the experimental results on competing one-dimensional quantum-engineered platforms are more promising.

states offer a resolution of this quandary by connecting the Weyl points of opposite chirality at the surface, providing a passage for the fermions between the Weyl points and allowing them to move back towards the opposing surface [76]. Such closed orbits may be observed as peculiar quantum oscillations [77]. The Fermi arcs are chiral themselves, having an average velocity perpendicular to the line connecting their end points. Fermi arcs and their chirality again have fascinating consequences for charge transport [78–89]. Indeed, spectroscopic evidence of Fermi arcs is how Weyl semimetals were first discovered in the noncentrosymmetric materials TaAs and NbAs [90–92] and later in magnetic materials such as the Heusler compounds $\mathrm{Co_3Sn_2S_2}$ and GdPtBi [93, 94], and the chiral crystal RhSi [95]. Unfortunately, these materials feature a large number of Weyl points or non-Weyl Fermi pockets which wash out the unique response features associated with Weyl fermions. From a theoretical as well as from an engineering perspective, it is therefore highly desirable to find a platform featuring a single pair of Weyl points. There are proposals to engineer such a system using Josephson junctions [96] or by splitting Dirac nodes using magnetic fields [97]. There are furthermore numerous proposals to engineer the position of the Weyl points and thereby the response properties of the Weyl semimetal [98–102].

Quantum matter engineered from assemblies of YSR states (Chapter 3), quantum devices involving YSR states (Chapter 4) and Majorana zero modes (Chapter 5), and photoresponse due to engineered Fermi arc (Chapter 6) take center stage in this thesis. Each chapter addresses and answers specific open questions within these overlapping but distinct fields of research. These are introduced at the beginning of each chapter. We still summarize the main points below. This is preceded by a chapter on the theoretical foundations of the content chapters to make this thesis more self-contained (Chapter 2).

Quantum Yu-Shiba-Rusinov assemblies Thus far, theoretical modeling of YSR chains has focused on classical adatom spins [38, 39, 103–110]. This presumes that the magnetic anisotropy as well as the Ruderman-Kittel-Kasuya-Yosida (RKKY) interaction give rise to ordered magnetic textures. However, measurements of discrete spin excitations [111–114] as well as the Kondo effect, both on normal metal [115, 116] and on superconducting substrates [10, 11, 14, 117–120], demonstrate that individual adatom spins behave quantum mechanically. There is now also evidence for quantum spin physics in YSR assemblies: in collaboration with the group of Professor Katharina Franke we could show that unscreening transitions observed during adatom-by-adatom construction of a dilute chain of Fe atoms on a $\mathrm{NbSe_2}$ substrate can only be explained if the quantum nature of the adatom spins is taken into account [II]. Motivated by these findings we developed a phenomenological theory of YSR assemblies that treats the adatom spin as a quantum degree of freedom [I, III, 121]. Starting with the simplest adatom assembly, a dimer, we demonstrated that the quantum nature of the adatom spin S has enormous ramifications for the phase diagram and excitation spectrum which are robust against moderate single-ion anisotropy and persist even in the large-S limit [III]. Moreover, in contrast to classical models [32] our approach correctly reproduces the low energy Hilbert space structure of quantum YSR dimers as can be inferred by comparing to Numerical Renormalization Group (NRG) results

[122], while lacking the stringent numerical overhead of NRG calculations. Such correct and cheap insight is necessary for the construction of YSR dimer qubits. Proceeding to chains of magnetic adatoms, and focusing on the quantum-limit $S = \frac{1}{2}$, we showed that quantum YSR chains are described by an effective $t-J$ model [I], implying the intricate coupling of charge and spin degrees of freedom inherent to quantum magnetism. We then studied the phase diagram and tunneling spectra of the effective $t - J$ model through numerical exact-diagonalization and mean field analysis, revealing mechanisms for trivial edge-features at low bias in the tunneling spectrum as well as a drastically suppressed topological phase as compared to classical YSR chains. These results provide new guidance in designing and interpreting experiments aiming to engineer topological superconductivity in chains of magnetic adatoms. Finally, the physics of quantum spin chains and strongly correlated electrons is a rich field in of itself [123, 124], and it would be of great scientific interest to observe associated phenomena such as spin-charge separation on this new platform.

Josephson diode control by Yu-Shiba-Rusinov states Josephson junctions are key elements of quantum engineering [125], as well as technologies ranging from sensing [126] to superconducting quantum computers [127]. In advancing these technologies, nonreciprocity is seen as an essential ingredient [128]. Recently, breakthrough experiments demonstrated for the first time nonreciprocal critical currents in bulk superconductors [129–135] and in Josephson junctions [136–144]. In underdamped Josephson junctions, which are characterized not only by their critical or switching currents, but also by their retrapping current, observed nonreciprocities were dominant in the switching currents [136, 140, 142, 144]. Theoretical attempts to describe these experiments have focused mostly on mechanisms leading to nonreciprocal equilibrium critical current [145–152], establishing that the latter can only arise if time-reversal symmetry is broken in addition to inversion symmetry. In stark contrast to these findings, measurements on atomic Josephson junctions performed by our collaborators in the group of Professor Franke revealed strong nonreciprocity in the retrapping currents while the switching currents were nearly symmetric [V]. Strikingly, the observed nonreciprocity was completely controlled by the species of adatom placed in the junction: while non-magnetic Pb atoms did not lead to any observable nonreciprocity, magnetic adatoms such as Cr and Mn gave rise to oppositely asymmetric retrapping currents. Importantly, this situation is time-reversal symmetric, and thus, this behavior clearly does not fit with the aforementioned theories.[3] Through Monte-Carlo simulations of a generalized RCSJ model we could trace back the observed nonreciprocity in the retrapping currents to nonreciprocity in the quasi-particle current induced by particle-hole symmetry breaking YSR states [V]. Building on the insights gained from this theory-experiment collaboration, we developed a general analytic theory of noise-affected Josephson diodes building on rate equations and the Fokker-Planck equation associated with our generalized RCSJ model [IV]. In particular, we established a general correspondence principle between nonreciproci-

---

[3] Note that Misaki and Nagaosa do not assume broken time-reversal symmetry to find a Josephson diode effect [153]. However, their assumption of asymmetric charging energy is warranted only if the Josephson electrodes consist of different materials. This is not the case in any of the experiments on the Josephson diode effect to date.

ties in the current-phase relation and asymmetric switching currents, as well as nonreciprocities in the dissipative current and asymmetric retrapping currents. Importantly, this implies different symmetry requirements for the Josephson diode effect in the switching versus the retrapping currents, inherited from the symmetry requirements for asymmetric current-phase relations and asymmetric current-voltage characteristics. Finally, in order to substantiate our phenomenological approach we microscopically derived the generalized RCSJ model within a Keldysh-functional-integral approach [VI]. Our results allow identification of the origin of nonreciprocity and hence characterization and categorization of Josephson diodes. This provides important guidance to the current experimental efforts in this subject.

Readout of Majorana qubits A Majorana Box Qubit [154] combines four Majorana zero modes on an electrostatically floating island, forming the simplest example of a topological qubit [44]. Quantum computing based on Majorana Box Qubits relies heavily on quantum-non-demolition measurements to implement Clifford gates [45, 155, 156]. A fast and robust readout protocol is therefore paramount to this quantum computing architecture. We developed a comprehensive theory of readout for Majorana Box Qubits based on the quantum trajectory approach [VII]. The theory explains in detail not only the measurement-induced decoherence but also the readout signal, and thus provides strategies for fast readout. Our theory allowed us to identify the optimal qubit-readout device coupling strength provided that readout relies on time-averaged charge sensing. Interestingly, stronger coupling leads to faster decoherence but may make it harder to detect the measurement outcome. The underlying mechanism of our readout scheme relies on nothing more than a conserved fermion parity and is hence generally applicable. We term this mechanism symmetry-protected readout. In particular, our general analysis implies that decoherence occurs in the eigenbasis of the true zero modes, even if the local Majorana zero modes are coupled to a finite number of environmental fermionic modes [157].

Fermi arc-controlled photoresponse in Weyl semimetals Response to light is one of the most promising aspects of Weyl semimetal response towards technological applications [158]. Of particular interest are nonlinear effects such as second harmonic generation [159] and the photogalvanic effect [160]. The latter represents the dc current response to light and was shown to be strongly enhanced in the infrared range in Weyl semimetals [71, 73, 74, 161–165]. It is noteworthy that under certain circumstances the photogalvanic response to circularly polarized light is believed to be quantized in Weyl semimetals [72], although experiments failed to exhibit quantization as of now [95]. Recently, experiments and first-principles calculations have indicated that the Fermi arc surface states are relevant to the photogalvanic response [166, 167]. To develop a deeper understanding of this contribution, we developed a semiclassical analytical theory of photogalvanic response in Weyl semimetal slabs corroborated by lattice simulations. Focusing on the role of Fermi arc surface states, we showed that the surface contribution to the ballistic photogalvanic current is crucially determined by the Fermi arc orientations. Importantly, this surface contribution remains finite even in bulk-centrosymmetric crystals were the bulk photogalvanic current vanishes by symmetry. In these systems, the photogalvanic response is thus controlled by the Fermi arc orientations, which may be affected through application of external surface potentials [168, 169]. This may make possible the design of the photoresponse of Weyl semimetals, a prospect that is certainly attractive, e.g., for applications in optoelectronics.

2 FOUNDATIONS

In this chapter we will review the theoretical foundations relevant to this thesis. In particular, we will review how subgap and boundary modes arise in superconductors and topological semimetals.

2.1 SUPERCONDUCTIVITY

If metals are cooled to sufficiently low temperatures they may undergo a phase transition to the superconducting state, characterized by the expulsion of magnetic fields and the vanishing of electrical resistance. Microscopically, this instability is due to the formation and condensation of electron pairs at the Fermi surface.

In this thesis we will be concerned only with superconductivity that may be described within the Bardeen-Cooper-Schrieffer (BCS) theory. In these systems, phonons mediate an attractive interaction between electrons sufficiently close to the Fermi energy E_F. The attraction leads to the formation of electron-electron bound states, so called Cooper pairs. The essentials are well-captured by a simple contact interaction [170]

$$\mathcal{V} = -g \int \mathrm{d}^3x \, \psi_\uparrow^\dagger(x)\psi_\downarrow^\dagger(x)\psi_\downarrow(x)\psi_\uparrow(x), \tag{2.1}$$

together with the prescription that only a shell of energies $E_F \pm \omega_D$ contributes. Here, $\psi_\sigma^\dagger(x)$ [$\psi_\sigma(x)$] creates [annihilates] an electron at position x with spin σ, g denotes the strength of the coupling, and $\omega_D \ll E_F$ is the Debye frequency. We also specified to spin-singlet pairing. Below a critical temperature $T_c \sim \omega_D \exp\{-\frac{1}{\nu_0 g}\}$, where ν_0 is the normal state density of states per unit volume at E_F, the attractive interaction leads to an instability of the Fermi surface, marked by the development of a finite expectation value

$$\Delta(x) \exp\{i\theta(x)\} = g\langle\psi_\downarrow(x)\psi_\uparrow(x)\rangle. \tag{2.2}$$

Here, Δ is the superconducting order parameter. Its value is determined by a mean field equation and constant in a homogeneous system.

The order parameter phase θ is intricately tied to the electromagnetic response. In particular, it is related to the density deviation $\delta\varrho$ as well as the current density $\mathbf{j}$ through[1]

$$\delta\varrho = 2e\nu_0\left[\frac{\hbar}{2}\dot{\theta} - e\Phi\right], \quad \mathbf{j} = -\frac{en_s}{m}\left[\frac{\hbar}{2}\nabla\theta + e\mathbf{A}\right], \tag{2.3}$$

in terms of the electric potential Φ, the condensate density n_s, the vector potential $\mathbf{A}$ and the effective mass m. Due to the coupling to the electromagnetic field, the fluctuations of θ have a gapped spectrum, with propagating solutions only at frequencies of the order of the plasma frequency. Similarly, the (gauge invariant) transverse part of the vector potential becomes gapped. This leads to the expulsion of magnetic fields from the superconducting bulk, the Meissner effect.

Thus, one may often ignore fluctuations of the phase and treat it as an externally controlled parameter. This allows for working with a BCS mean field Hamiltonian of the type

$$H_{\mathrm{BCS}} = \int \mathrm{d}^3x \left\{ \sum_\sigma \psi^\dagger_\sigma(x)\xi(-i\nabla)\psi_\sigma(x) + \Delta e^{-i\theta}\psi_\downarrow(x)\psi_\uparrow(x) + \mathrm{h.c.} \right\}, \tag{2.4}$$

giving rise to the single-particle excitation spectrum $E_k = \sqrt{\xi(k)^2 + \Delta^2}$. In consequence, there are no low lying single-particle or collective excitations (with the exception of the lattice phonons, of course).

The term $\propto \Delta$ mixes electron and hole states due to scattering off the superconducting condensate, which absorbs or emits Cooper pairs in order for the total charge to be conserved. Such processes are referred to as Andreev scattering. They are captured by the anomalous (off-diagonal) terms of the (Gorkov) Green function

$$\mathcal{G}_0(x, x'; t, t') = -i\langle \mathrm{T}\Psi(x,t)\Psi^\dagger(x',t')\rangle, \tag{2.5}$$

where T is the time-ordering symbol and we defined the two-component Nambu spinor $\Psi(x) = [\psi_\uparrow(x), \psi^\dagger_\downarrow(x)]^T$. This describes the system in terms of spin up electrons and spin down holes [i.e. $\Psi^\dagger(x)$ creates a spin up excitation] and hence does not involve doubling of the single-particle Hilbert space. The associated retarded Green function can be expressed in terms of the single-particle Bogoliubov-de Gennes Hamiltonian, $\mathcal{G}_0^{\mathrm{r}} = [\omega + i\eta - \mathcal{H}_{\mathrm{BdG}}]^{-1}$. Here, we set $\hbar = 1$, and defined $\eta > 0$ infinitesimal, as well as

$$\mathcal{H}_{\mathrm{BdG}} = \begin{pmatrix} \xi(-i\nabla) & \Delta e^{i\theta} \\ \Delta e^{-i\theta} & -\xi(-i\nabla^T) \end{pmatrix} = \xi(-i\nabla)\tau_z + \Delta(e^{i\theta}\tau_+ + \mathrm{h.c.}). \tag{2.6}$$

---

[1] We define the electron charge as $q = -e$. This gives the minimal coupling prescription $\mathbf{p} \to \mathbf{p} + e\mathbf{A}$.

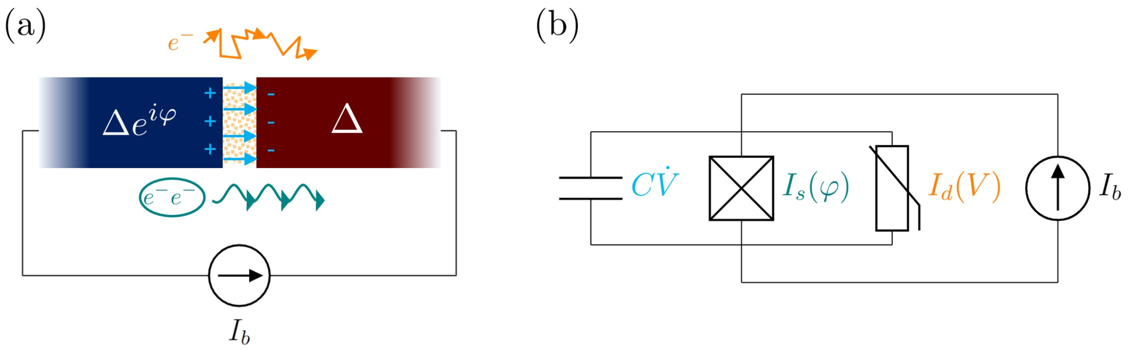

Figure 2.1: Schematic representations of a Josephson junction. (a) Two superconductors (blue and red) are separated by a tunneling barrier. Current across the junction is carried by the coherent transfer of Cooper pairs (green), the dissipative quasiparticle current (orange), and a capacitive current (light blue). (b) Equivalent circuit of the RCSJ model, involving a Josephson component representing the supercurrent shunted by a capacitor and a resistor. Element labels are colored according to equivalent process in (a). In both (a) and (b) the external circuit biases the current across the junction to be I_b.

In the second equality we assumed $\xi(k) = \xi(-k)$ and introduced a set of Pauli matrices τ_i acting in Nambu space. The two component Nambu description can be used as long as the system has a U(1) spin rotation symmetry. If U(1) symmetry is absent (e.g. in the presence of spiralling magnetic moments, see Sec. 2.3.3 below) one instead has to use a four-component Nambu spinor which introduces redundancy into the single-particle spectrum. A convenient choice is $\Psi(x) = [\psi_\uparrow(x), \psi_\downarrow(x), \psi_\downarrow^\dagger(x), -\psi_\uparrow^\dagger(x)]^T$. Finally, note that spinless fermions can be described via two-component Nambu spinor $[\psi(x), \psi^\dagger(x)]$. This again introduces redundancy [c.f. Eq. (2.36) below].

2.2 JOSEPHSON JUNCTIONS AND THE RCSJ MODEL

The workhorse of superconducting devices is the so called Josephson junction. It consists of two superconductors, referred to as left (L) and right (R), which are weakly coupled such that they can exchange electrons. Such a situation is sketched in Fig. 2.1(a). The charge densities $\delta\varrho_{L/R}$ and order parameter phases $\theta_{L/R}$ (and equivalently electric potentials $\Phi_{L/R}$) within the individual superconductors relax at time scales given by the inverse plasma frequency. Conversely, due to the weak coupling between the two superconductors the charge imbalance $Q = Q_L - Q_R$ and phase difference $\varphi = \theta_L - \theta_R$ are slow degrees of freedom. (In fact, they are the only low-lying degrees of freedom.) From Eq. (2.3) we thus have

$$Q = \frac{1}{2}(Q_L - Q_R) = \frac{1}{2}\int \mathrm{d}^3x\,(\delta\varrho_L - \delta\varrho_R) = e\nu_0\left(\frac{\hbar}{2}\dot{\varphi} - eV\right) \times \text{Vol.}, \tag{2.7}$$

where we defined the volume of the bulk superconductors Vol., as well as the voltage drop $V = \Phi_L - \Phi_R$. Because the superconductors are weakly coupled, large charge imbalances Q cannot be expected. On the other hand, the right-hand side of Eq. (2.7) involves the (macroscopic) factor of volume. It follows that the time evolution of the phase difference gets pinned to the voltage drop between the superconductors, i.e.

$$\dot{\varphi} = \frac{2e}{\hbar} V. \tag{2.8}$$

This argument obviously holds even if the two superconductors are completely decoupled. We now include the tunneling of electrons between the superconductors. Due to the single-particle gap, at low energies and temperatures only Cooper pairs can traverse the junction so that both superconductors always hold an even number of electrons. Importantly, the tunneling of Cooper pairs is a coherent process, as the low energy spectra of the individual superconductors are discrete (by virtue of the single-particle gap and the absence of low-lying collective modes). The coherent transfer of charges is linked to a supercurrent $I_s \sim \int \mathrm{d}\mathbf{S} \cdot \mathbf{j}$, which by Eq. (2.3) implies a phase gradient $\nabla\theta \sim \varphi\delta(x)$ across the junction (setting $\mathbf{A} = 0$, i.e. no magnetic fields and fixed gauge). This current should be periodic in $\varphi \to \varphi + 2\pi$ and vanish for $\varphi = 0$.[2] The simplest such current-phase relation is given by

$$I_s(\varphi) = I_c \sin\varphi. \tag{2.9}$$

I_c is the maximum supercurrent that can be supported by the Josephson junction, and referred to as critical current. Eqs. (2.8) and (2.9) are the Josephson relations. If a phase difference is applied to the junction externally, a constant current flows. This is the dc Josephson effect. If a voltage is applied, the current will oscillate with frequency $2eV/\hbar$ due to the time dependence of the phase difference implied by Eq. (2.8). This is the ac Josephson effect.

In the tunneling regime, a microscopic picture of the Josephson current is due to pair tunneling. A single-electron tunneling term of the (schematic) form $\delta H = \psi_L^\dagger \psi_R + \text{h.c.}$ leads to a shift in free energy

$$F \sim \left\langle \psi_L^\dagger \psi_R \frac{1}{-H_{\text{BCS}}} \psi_L^\dagger \psi_R + \text{h.c.} \right\rangle \sim -\cos\varphi. \tag{2.10}$$

A straightforward calculation gives the prefactor as $E_J = \hbar I_c/2e = (G_N/8G_0)\Delta$, where G_N is the normal state conductance and $G_0 = e^2/h$ is the quantum of conductance [171]. E_J is referred to as the Josephson energy. The current across the junction is obtained via[3]

$$I_s(\varphi) = \frac{2e}{\hbar} \frac{\partial F}{\partial \varphi}, \tag{2.11}$$

---

[2] Upon a gauge transformation $\psi_L(x) \to \psi_L(x) \exp\{i\alpha\}$, the phase difference transforms as $\varphi \to \varphi + 2\alpha$. If parity flips can be ruled out, $\alpha = \pi$ suffices to restore the original situation. This implies 2π-periodicity in φ.

[3] This general relationship follows from the minimal coupling term $\delta H_{\text{mc}} = \int \mathrm{d}^3x\, \mathbf{j} \cdot (\frac{\hbar}{2e}\nabla\theta + \mathbf{A}) = \frac{\hbar}{2e} I_s \varphi$, where we again assumed absence of magnetic fields and fixed the gauge such that $\mathbf{A} = 0$.

reproducing Eq. (2.9).

More generally, the Josephson current arises from φ-dependent energies of so called Andreev bound states. These correspond to bound electron-hole orbits in the junction region: For energies below the single-particle gap, an electron (a hole) can only reflect off the superconductors. The Andreev scattering contribution to this process reflects a hole (an electron), which can then again be Andreev reflected as an electron (a hole) off the other superconductor, starting the process anew. By the Bohr-Sommerfeld quantization condition, this gives rise to a bound state if the phases accumulated during this evolution interfere constructively, i.e. for energies E_n which satisfy $2\pi n = \varphi - f(E_n)$. Here, $f(E)$ encompasses the dynamical phases of the electron and hole trajectories as well as the energy dependent part of the Andreev reflection. The phase difference φ enters as the Andreev reflection amplitudes involve a phase shift $\pm\theta_{L/R}$ (sign depending on electron to hole scattering or vice versa). In the simple case of an SNS junction one can evaluate $f(E) = 2(\frac{\hbar L}{v_F}E + \arccos\frac{E}{\Delta})$, where L is the length of the normal region. In the spin-SU(2) symmetric case, the Bogoliubov-de Gennes Hamiltonian is particle hole symmetric, implying corresponding states with energy $-E_n$. As each orbit transfers a Cooper pair between the superconductors, the occupation of negative energy states implies a supercurrent. This can again be obtained from Eq. (2.11) with $F = -2T\sum_n' \ln[2\cosh\left(\frac{E_n}{2T}\right)]$ (with the sum only over positive energies). For $\varphi = 0$, each Andreev bound state is doubly degenerate (Kramers degeneracy) with opposite contributions to the current, hence $I_s(0) = 0$. In a magnetic system, there is no Kramers degeneracy and $I_s(0) \neq 0$ generically. Including explicitly the dependence on the symmetry breaking field, one obtains the general symmetry constraints under inversion (I) and time-reversal (TR),

$$I_s(\varphi, B) =_{\text{IS}} \; - I_s(-\varphi, B), \tag{2.12a}$$

$$I_s(\varphi, B) =_{\text{TRS}} - I_s(-\varphi, -B). \tag{2.12b}$$

We note here that Andreev bound states are another example of subgap states used for quantum engineering purposes [172–174]. They do not however play a major role in this thesis.

So far we have ignored the energy cost associated with the Coulomb repulsion of the extra charges added to the superconductors: a charge mismatch Q causes a voltage drop V. In the simplest case, the superconducting electrodes may be modeled as a capacitor such that the voltage drop is $V = Q/C$ and the associated current is $I_C = C\dot{V}$. Here, C is the junction capacitance. Furthermore, at finite temperatures there will also be a dissipative contribution to the current due to quasiparticle tunneling, which in the simplest case takes an Ohmic form, $I_d(V) = V/R$. By the fluctuation-dissipation thoerem, the dissipative current is associated with Johnson-Nyquist noise δI with $\langle \delta I(t)\delta I(t')\rangle = \frac{2T}{R}\delta(t-t')$. Fig. 2.1(a) shows these contributions together with the supercurrent. Current conservation implies that all these currents sum to the bias current I_b. Putting all these ingredients together gives the so called Resistively Capacitance Shunted Junction (RCSJ) model

$$I_C + I_d + I_s + \delta I = C\dot{V} + \frac{V}{R} + I_c \sin\varphi = I_b. \tag{2.13}$$

The equivalent circuit is shown in Fig. 2.1(b). By virtue of Eq. (2.8), Eq. (2.13) becomes a Langevin equation for the phase difference φ. It describes the stochastic motion of a classical "phase particle" in the tilted washboard potential

$$U(\varphi) = -\frac{\hbar I_b}{2e}\varphi - E_J \cos\varphi. \tag{2.14}$$

It was mentioned already that the charge Q and the phase difference φ are the only low-lying degrees of freedom of the Josephson junction. If the temperature is sufficiently low so that dissipation due to coupling to the quasiparticle continuum is negligible, it is thus sensible to ask under what circumstances their dynamics are governed by quantum mechanics. To this end, we find the Hamiltonian of the phase particle by Legendre transform $H = \Pi\dot{\varphi} - L$ with Lagrangian $L = \frac{1}{2}CV^2 - U(\varphi)$ and canonical momentum $\Pi = (\partial L/\partial\dot{\varphi}) = (\hbar/2e)Q$. Canonical quantization gives

$$\hat{H} = \frac{1}{2C}\hat{Q}^2 + U(\hat{\varphi}), \tag{2.15}$$

with the commutation relation $[\hat{\varphi}, \hat{Q}] = 2ei$. The exponentials $\exp\{\pm i\hat{\varphi}\}$ thus shift the charge imbalance by $\pm 2e$, i.e. they move one Cooper pair across the junction. We can thus interpret the $\cos\hat{\varphi}$ term as low energy remnant of the electron tunneling Hamiltonian. The characteristic frequency at the minima of the washboard potentials is referred to as plasma frequency of the Josephson junction. For small bias $I_b \ll I_c$, the height of the potential barriers is E_J. A classical approximation such as the RCSJ model is permissible if the plasma frequency is much smaller than the barrier height. This translates to $E_J \gg E_C = e^2/C$, where E_C is the charging energy. Note that dissipation improves on the validity of the classical approximation [175].

2.3 Yu-Shiba-Rusinov states

Scalar disorder does not affect the magnitude of the gap in a time-reversal symmetric s-wave superconductor [176]. Conversely, magnetic disorder is detrimental to a superconductor. Microscopically, this is due to the proliferation of subgap states induced by magnetic impurities, which, when sufficiently many of them overlap, lead to a breakdown of the gap. These states are known as Yu-Shiba-Rusinov or YSR states [5–7]. However, from the perspective of quantum engineering YSR states are a blessing in disguise. Under certain circumstances, magnetic adatoms on superconducting substrates behave as pure spin degrees of freedom and as such

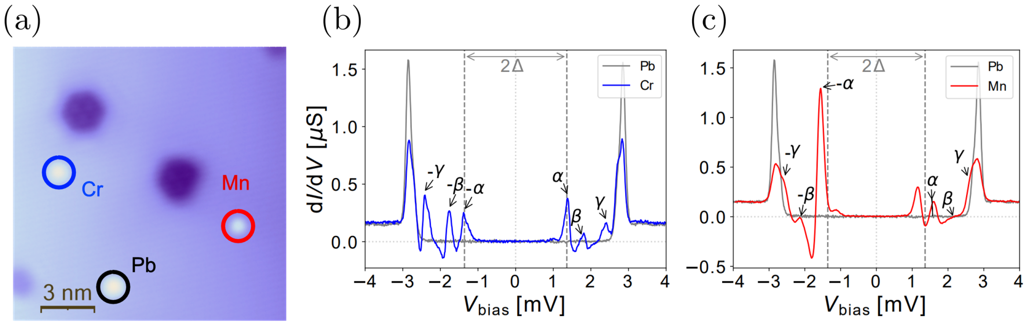

Figure 2.2: Magnetic adatoms on a superconducting Pb surface and their associated YSR states. (a) STM topography showing Cr, Mn and Pb adatoms. (b) and (c) STM $\mathrm{d}I/\mathrm{d}V$ at normal state conductance $G_N = 0.125\mu\mathrm{S}$ above Cr and Mn adatom, respectively. STM $\mathrm{d}I/\mathrm{d}V$ above Pb adatom is shown in grey in both panels. Cr and Mn are magnetic and induce YSR states visible as subgap peaks in the $\mathrm{d}I/\mathrm{d}V$ spectrum. Pb is nonmagnetic and does not exhibit subgap structure. Figure adapted from [V].

induce YSR bound states in the substrate. Fig. 2.2 shows the subgap structure induced by magnetic adatoms in STM data. Atomic scale manipulations of individual magnetic adatoms within the STM setup allow for the design of few-body quantum systems inside the superconducting gap. The coupling of the individual adatoms is provided by the overlap of their YSR states, as well as the RKKY interaction between the adatom spins [177–179].

In this section we will investigate a single magnetic impurity located at the origin, as described by the Hamiltonian

$$H = H_{\mathrm{BCS}} + \int \mathrm{d}^3x \sum_{\sigma\sigma'} \psi^\dagger_\sigma(x) U_{\sigma\sigma'}(x) \psi_{\sigma'}(x), \tag{2.16a}$$

where the impurity potential

$$U_{\sigma\sigma'}(x) = [V\delta_{\sigma\sigma'} + K\mathbf{S}\cdot\mathbf{s}_{\sigma\sigma'}]\delta(x) \tag{2.16b}$$

includes both scalar (V) and antiferromagnetic exchange scattering ($K > 0$). Here, we defined the impurity spin $\mathbf{S}$ as well as the single-particle spin operator $\mathbf{s} = \frac{1}{2}\boldsymbol{\sigma}$, with Pauli matrices σ_i. In real systems, $\mathbf{S}$ is a quantum degree of freedom. We will refer to the bound states induced by a quantum spin as *quantum* YSR states. Their phenomenology will be discussed in the following Sec. 2.3.1, and in Chapter 3. It is sometimes permissible to treat $\mathbf{S}$ as a classical degree of freedom instead and we will refer to the associated bound state as a *classical* YSR state. Classical YSR states are subject of Secs. 2.3.2 and 2.3.3.

2.3.1 The Kondo effect and quantum Yu-Shiba-Rusinov states

Consider first the normal metal case, $\Delta \to 0$, with $S = \frac{1}{2}$ and no potential scattering, $V = 0$. In this case, Eq. (2.16) is simply the Kondo Hamiltonian [180]. The coupling to the impurity

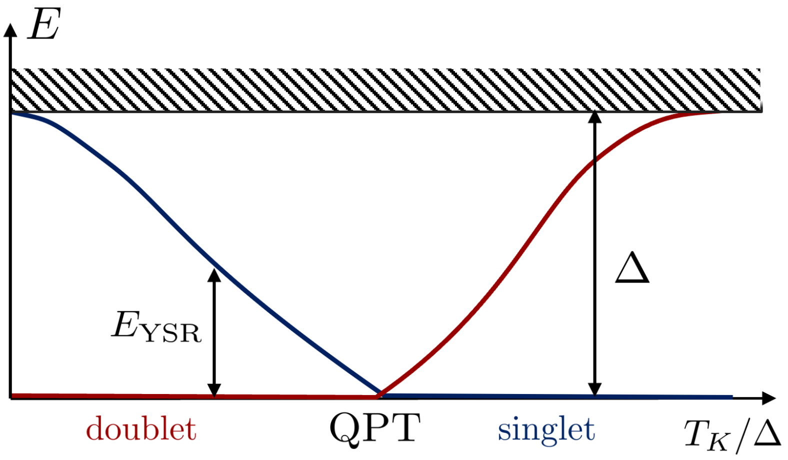

Figure 2.3: Sketch of the many body spectrum of Eq. (2.16). All energies are measured from the ground state energy.

spin $\mathbf{S}$ induces interactions which make a full solution of the problem difficult.[4] In particular, at sufficiently low temperatures, the Kondo problem becomes non-perturbative, no matter the magnitude of the bare coupling K. To see this, we employ the perturbative renormalization group which gives the running exchange coupling as [181]

$$K(E) = \left(\frac{1}{K} - 2\nu_0 \ln \frac{D}{E}\right)^{-1}, \tag{2.17}$$

where D is the bandwidth. This indeed diverges at the Kondo temperature $E = T_K$, where

$$T_K = D \exp\left\{-\frac{1}{2\nu_0 K}\right\}, \tag{2.18}$$

signaling the breakdown of perturbation theory. Wilson developed the numerical renormalization group to demonstrate explicitly that there is a smooth crossover from weak coupling to strong coupling at temperatures well below T_K [182], where the diverging $K_{\text{eff}} = K(E \to 0)$ leads to the formation of a sharp resonance: an infinitely strong exchange impurity locally binds an electron of opposite spin despite the gapless continuum of states in which it is embedded [183].

In a superconductor, due to the presence of the particle-hole excitation gap, the renormalization group flow will be stopped at energies $E \sim \Delta$. For $T_K > \Delta$, the impurity will already be screened when this point is reached, and thus only act as a potential scatterer. Here, the ground state is an odd parity singlet, i.e. $|\text{gs}\rangle \equiv |o\rangle$, with $\mathbf{S}^2_{\text{tot}} = [\mathbf{S} + \int \mathrm{d}^3x\, \psi^\dagger(x)\mathbf{s}\psi(x)]^2 = 0$. Due to the single-particle gap what was the Kondo resonance now is a bound state - the quantum

---

[4] The interacting nature of this Hamiltonian becomes immediately apparent when replacing the Kondo impurity model by the strictly more general Anderson impurity model which includes a manifest quartic term in the impurity fermion operators. Alternatively, elimination of the spin in the large-K limit leads to a local quartic term in the substrate fermion operators.

YSR state. For $\Delta > T_K$ the effective coupling stays finite, albeit renormalized to $K_{\text{eff}} \sim K(\Delta)$. In this case one expects the impurity to remain unscreened even in the ground state. The latter forms an even parity doublet, or explicitly, $|\text{gs}\rangle \equiv |e, S^z\rangle$ and $\mathbf{S}^2_{\text{tot}} = \frac{3}{4}$. A complete picture can be obtained via numerical renormalization group (NRG) considerations [184, 185]: At any (intermediate) ratio $T_K/\Delta > 0$ there are three many body states separated from the quasi-particle continuum. They correspond to the unscreened doublet with even fermion parity and energy E_e (YSR state unoccupied), and the screened singlet with odd fermion parity and energy E_o (YSR state occupied). For $T_K/\Delta \ll 1$ the doublet forms the ground state, while for $T_K/\Delta \gg 1$ the singlet is the ground state. These regimes are separated by a first order quantum phase transition at $T_K/\Delta \sim 0.3$. This is sketched in Fig. 2.3.

In tunneling spectroscopy a transition between these states becomes resonant at energies $|E_{\text{YSR}}| < \Delta$ where we defined the Yu-Shiba-Rusinov excitation energy

$$E_{\text{YSR}} = E_o - E_e. \tag{2.19}$$

In particular, tunneling spectroscopy probes the local spectral function

$$A(E) = \sum_{\lambda,\sigma} \Big\{ |\langle\lambda|\psi^\dagger_\sigma(0)|\text{gs}\rangle|^2 \delta(E - E_\lambda + E_{\text{gs}}) \\ + |\langle\lambda|\psi_\sigma(0)|\text{gs}\rangle|^2 \delta(E + E_\lambda - E_{\text{gs}}) \Big\}. \tag{2.20}$$

This expression assumes vanishing temperature[5] and localized tunneling at the impurity site. The latter assumption is appropriate to describe STM data. For $E_{\text{YSR}} > 0$ the ground state is unscreened, $|\text{gs}\rangle = |e; S^z\rangle$. In this case an electron that is spin-antialigned with the impurity can tunnel into the system and screen the impurity, giving rise to a spectral peak at energy $E = E_{\text{YSR}}$ and with weight $u^2(0) = |\langle o|\psi^\dagger_{\sigma=-S^z}(0)|e; S^z\rangle|^2$. Conversely, an electron that is spin-aligned with the impurity can tunnel out of the system, leaving behind an unpaired spin-antialigned electron which screens the impurity. This gives rise to a spectral peak at energy $E = -E_{\text{YSR}}$ with weight $v^2(0) = |\langle o|\psi_{\sigma=S^z}(0)|e; S^z\rangle|^2$. These subgap features in the tunneling spectrum are the hallmark of YSR states, as visible in Fig. 2.2(b) and (c). If instead $E_{\text{YSR}} < 0$ and the ground state is screened, $|\text{gs}\rangle = |o\rangle$, the weights are reversed. This implies that, as the quantum phase transition is traversed, the electron and hole peaks can be viewed as passing through each other. This can be seen exceptionally well in Fig. 2 of [11].

While the NRG approach yields exact results for a single impurity spin its numerical cost becomes prohibitive once assemblies of impurities or higher spins are considered, with spin-$\frac{1}{2}$ and spin-1 dimers representing the frontier at the time of writing [122, 186]. To make analytical progress one has to make approximations. In the literature [38, 39] most often the impurity spin is approximated as a classical spin or, equivalently, as a local Zeeman field. This approach

---

[5] See App. B.7 for the finite temperature expression and its relationship to the BCS Green function.

will be reviewed in the remainder of this section. While it reproduces the YSR quantum phase transition as well as the YSR tunneling spectrum, the classical impurity spin implies a drastically different Hilbert space structure. In particular, it fails to capture the singlet nature of the screened state. This failure will have strong ramifications when considering assemblies of magnetic adatoms. We will explore this in detail in Chapter 3 using a converse approach: instead of simplifying the impurity spin, we will simplify the superconductor by considering the limit of zero bandwidth [121].

2.3.2 CLASSICAL YU-SHIBA-RUSINOV STATES

We will now treat the impurity spin as a classical degree of freedom and further assume that it is frozen in some direction. This is a good approximation if there is strong easy-axis anisotropy (implying $S > \frac{1}{2}$). The resulting problem is non-interacting and can be treated by standard methods. Without loss of generality, we set $\mathbf{S} = -S\hat{z}$ and define the rescaled exchange coupling $K_0 = KS/2$ such that the impurity potential involves the term $-K_0\sigma_z$. Due to the classical nature of the adatom spin we refer to the subgap states obtained within this model as classical YSR states.

The magnetic impurity breaks the SU(2) spin rotation symmetry of the substrate fermions down to U(1) (assuming absence of spin orbit coupling). We may still employ a two-component Nambu representation, but now the corresponding Bogoliubov-de Gennes theory does not have the usual particle-hole symmetric spectrum. The Bogoliubov-de Gennes Hamiltonian is then $\mathcal{H}'_{\mathrm{BdG}} = \mathcal{H}_{\mathrm{BdG}} + \mathcal{U}(x)$, where $\mathcal{U}(x) = [V\tau_z - K_0]\delta(x)$ and $\mathcal{H}_{\mathrm{BdG}}$ was given in Eq. (2.6). We find the bound state spectrum by identifying the poles of the Green function $\mathcal{G} = [\omega - \mathcal{H}'_{\mathrm{BdG}}]^{-1}$ in the presence of the impurity. In the following, we suppress the retarded label as well as the associated imaginary shift, and set the order parameter phase to zero. The full single-particle Green function of Hamiltonian Eq. (2.16), $\mathcal{G}$, satisfies the Dyson equation

$$\mathcal{G} = \mathcal{G}_0 + \mathcal{G}_0\mathcal{U}\mathcal{G} = \mathcal{G}_0 + \mathcal{G}_0\mathcal{T}\mathcal{G}_0. \tag{2.21}$$

Here, the $\mathcal{T}$-matrix is given by $\mathcal{T} = \mathcal{U}(1-\mathcal{G}_0\mathcal{U})^{-1}$. Due to the δ-scatterer this involves only the bare local Green function

$$\mathcal{G}_0(0;\omega) = \int \mathrm{d}\xi\,\nu(\xi)\frac{\omega + \xi\tau_z + \Delta\tau_x}{\omega^2 - \xi^2 - \Delta^2} \simeq -\frac{\pi\nu_0}{\sqrt{\Delta^2-\omega^2}}(\omega + \Delta\tau_x). \tag{2.22}$$

It may be evaluated straightforwardly as

$$\mathcal{T}(x,x';\omega) = \frac{\delta(x)\delta(x')}{\pi\nu_0}\frac{\sqrt{\Delta^2-\omega^2}(-\alpha+\beta\tau_z) + (\alpha^2-\beta^2)(\omega - \Delta\tau_x)}{2\alpha\omega + (1-\alpha^2+\beta^2)\sqrt{\Delta^2-\omega^2}}. \tag{2.23}$$

Here, we defined the dimensionless potential and exchange scattering strengths,

$$\alpha = \pi\nu_0 K_0, \quad \beta = \pi\nu_0 V. \tag{2.24}$$

As $\mathcal{G}_0$ is regular inside the gap it suffices to look for poles in the $\mathcal{T}$-matrix in order to identify bound states. Indeed, we find a single pole at the Yu-Shiba-Rusinov energy

$$E_{\text{YSR}} = \Delta \frac{1-\alpha^2+\beta^2}{\sqrt{(1-\alpha^2+\beta^2)^2+4\alpha^2}}, \tag{2.25}$$

where the denominator is always positive. For $\alpha = \beta = 0$ the YSR bound state sits at the upper gap edge, $E_{\text{YSR}} = \Delta$. Here, the many-body ground state has $S^z_{\text{tot}} = 0$ and even fermion parity. Upon increasing α E_{YSR} passes through zero. At this point the parity and S^z_{tot} change as the YSR bound state becomes occupied in the ground state. This is the YSR quantum phase transition. In particular, in the two component Nambu framework single-particle excitations carry $S^z = \frac{1}{2}$.[6] Hence, the YSR state is spin-polarized and antialigned with the impurity spin.

It will prove useful to express the YSR quantum phase transition in second quantized form. At small α the (even parity) BCS ground state may be written as $|e\rangle = \gamma_{\text{YSR}} \prod_{a,b} \gamma_a \gamma_b^\dagger |\text{vac}\rangle$. Here, γ_{YSR} empties the YSR bound state, the γ_a empty states with positive Bogoliubov-de Gennes energies $E_a > \Delta$ of $\mathcal{H}_{\text{BdG}}$, and $\gamma_b^\dagger$ fill those with energies $E_b < -\Delta$. For $E_{\text{YSR}} < 0$ the (odd parity) ground state is $|o\rangle = \gamma_{\text{YSR}}^\dagger |e\rangle$. Generalizing to arbitrary $\mathbf{S} = -S\hat{n}$ and impurity location x_0, γ_{YSR} may be expanded as

$$\gamma_{\text{YSR}} = \int \mathrm{d}^3x \Big[u(x-x_0)\psi_{\hat{n}}(x) + v(x-x_0)\psi^\dagger_{-\hat{n}}(x) \Big], \tag{2.26}$$

where $\psi_{\hat{n}}(x)$ annihilates an electron with spin projection $\mathbf{s}\cdot\hat{n} = 1/2$ at position x. The electron and hole wave-functions u, v may be obtained from the residue of the Green function at the YSR energy. At the impurity location they may be obtained in closed form. They are

$$\frac{\mathcal{G}(0,0;\omega)}{\pi\nu_0} = -\frac{\omega + \Delta\tau_x + (\alpha+\beta\tau_z)\sqrt{\Delta^2-\omega^2}}{(1-\alpha^2+\beta^2)\sqrt{\Delta^2-\omega^2} - 2\alpha\omega} \simeq \frac{\phi(0)\otimes\phi^*(0)}{\omega - E_{\text{YSR}}}, \tag{2.27}$$

where $\phi(0) = [u(0), v(0)]^T$ in terms of the electron and hole wave weights

$$u(0), v(0) = 2\Delta \frac{\sqrt{\alpha[1+(\alpha\mp\beta)^2]}}{[(1-\alpha^2+\beta^2)^2+4\alpha^2]^3}. \tag{2.28}$$

---

[6] To see this, note that in the two-component Nambu-Bogoliubov-de Gennes the z-component of the total spin operator takes the form $S^z_{\text{tot}} = \frac{1}{2}[\int \mathrm{d}x\, \Psi^\dagger(x)\Psi(x) - N_0]$, where $N_0 = \text{Vol.} \times \delta(0)$ is the number of fermion levels not accounting for spin. Applied to the BCS ground state, the first term simply counts the number of negative energy states of $\mathcal{H}_{\text{BdG}}$. Thus $\langle S^z_{\text{tot}}\rangle = \frac{1}{2}(N_{\text{BdG}} - N_0)$. For $\alpha = 0$, it is clearly $N_{\text{BdG}} = N_0$ and $\langle S^z_{\text{tot}}\rangle = 0$. For $\alpha > 1+\beta^2$, there is one extra negative energy state and thus $N_{\text{BdG}} = N_0 + 1$ and $\langle S^z_{\text{tot}}\rangle = \frac{1}{2}$.

Importantly, for $\beta \neq 0$, the electron and hole amplitudes differ, resulting in a asymmetric subgap spectral function $A(\omega) \simeq u^2(0)\delta(\omega - E_{\text{YSR}}) + v^2(0)\delta(\omega + E_{\text{YSR}})$.

2.3.3 Yu-Shiba-Rusinov chains

Consider now a chain of magnetic adatoms on the superconducting substrate. If the adatoms are spaced closely their orbitals overlap and form bands, with superconductivity entering by proximity. YSR states do not play a big role in such dense chains [30, 31]. Here, we consider dilute chains,such that the adatoms may still be considered spin degrees of freedom and inter-adatom coupling is mediated by the continuum through their induced YSR states, as well as the RKKY interaction. This is of particular interest in quasi-two-dimensional materials, where the YSR wavefunctions decay only as one over square-root of distance [II].

We will still assume that the impurity spins behave classically. In particular, we assume that they are frozen into a configuration $\mathbf{S}_i = -S\hat{n}_i$, where i labels the adatom. The spin texture is determined through minimization of the RKKY interaction energy. The impurity potential is now a sum over delta scatterers,

$$U(x) = \sum_i [V - K_0\hat{n}_i \cdot \boldsymbol{\sigma}]\delta(x - x_i), \tag{2.29}$$

where x_i is the location of the i-th adatom. For simplicity we assume evenly spaced adatoms, $|x_{i+1} - x_i| = a$. As S^z_{tot} is no longer a good quantum number, we now use the four-component Nambu spinor. The $\mathcal{T}$-matrix reads

$$\mathcal{T}(x, x'; \omega) = \frac{1}{\pi\nu_0} \sum_{ij} \delta(x - x_i)\delta(x' - x_j)(\beta\tau_z - \alpha\hat{n}_j \cdot \boldsymbol{\sigma})(1 - M)^{-1}_{ij}, \tag{2.30}$$

where the matrix M is defined via $\pi\nu_0 M_{ij} = \mathcal{G}_0(x_i - x_j; \omega)[\beta\tau_z - \alpha\hat{n}_j \cdot \boldsymbol{\sigma}]$ in terms of the bare Green function $\mathcal{G}_0^{-1} = [\omega - \xi(-i\nabla)\tau_z + \Delta\tau_x]$.[7] The subgap spectrum can again be obtained from the poles of $\mathcal{T}(\omega)$. In fact, the condition $(1 - M)\phi = 0$ is just the single-particle Bogoliubov-de Gennes equation projected onto the impurity sites,[8]

$$\sum_j (\delta_{ij} - M_{ij})\phi(x_j) = 0. \tag{2.32}$$

---

[7] The Fourier transform of the Green function may be obtained for $x \gg v_F/\omega_D$. It is

$$\mathcal{G}_0(x; \omega) = -\frac{\pi\nu_0}{k_F x} \exp\left\{-\sqrt{\Delta^2 - \omega^2}\frac{x}{v_F}\right\} \left[\frac{\omega + \Delta\tau_x}{\sqrt{\Delta^2 - \omega^2}} \sin(k_F x) + \tau_z \cos(k_F x)\right]. \tag{2.31}$$

[8] The Bogoliubov-de Gennes equation may be written as $\mathcal{G}_0^{-1}|\phi\rangle = U|\phi\rangle$. Multiplying both sides by $\mathcal{G}_0$ (only defined away from the unperturbed energies) and rearranging gives $U^{-1}\mathcal{T}\phi = 0$. Thus, the $\mathcal{T}$-matrix denominator may be seen as an effective Hamiltonian for bound states induced by the perturbation.

Following [39], we consider the limit of deep YSR states, $|E_{\text{YSR}}| \ll \Delta$. Expanding for small E, and projecting Eq. (2.32) onto the wave-functions of the uncoupled YSR states (which have spin anti-parallel to the adatom spin) this gives the tight-binding Hamiltonian

$$H_{\text{subgap}} = \sum_i E_{\text{YSR}} c_i^\dagger c_i - \sum_{i<j} \left[t_{i-j} c_i^\dagger c_j + \Delta_{i-j} c_i^\dagger c_j^\dagger + \text{h.c.} \right]. \tag{2.33}$$

Here, we defined the effective hopping and pairing terms

$$t_\delta = \Delta \cos(k_h a|\delta|) \frac{\sin(k_F a|\delta|)}{k_F a|\delta|} e^{-\frac{\Delta a}{v_F}|\delta|}, \quad \Delta_\delta = \Delta \sin(k_h a|\delta|) \frac{\cos(k_F a|\delta|)}{k_F a|\delta|} e^{-\frac{\Delta a}{v_F}|\delta|}, \tag{2.34}$$

where we specified to a helical adatom spin cofiguration $\mathbf{S}_i = (\cos 2k_h a i, \sin 2k_h a i, 0)$ with pitch π/k_h [39]. Up to a gauge transformation, the operator c_i is simply the YSR annihilation operator defined in Eq. (2.26) corresponding to impurity spin $\mathbf{S}_i = -S\hat{n}_i$ at position x_i. We have renamed them to c_i in order to avoid confusion with the Majorana operators to be introduced below as the latter are customarily called γ. Eq. (2.33) describes a one-dimensional spinless fermion chain inside the host superconducting gap, with $-E_{\text{YSR}}$ acting as the chemical potential and a dispersion $t(k) = \sum_{\delta>0} t_\delta \cos(k\delta)$. If the subgap band overlaps with the Fermi energy (i.e. if there is a solution k_0 to $E_{\text{YSR}} = t(k_0)$) and if the pitch satisfies $0 < k_h < \pi/2a$[9] the effective pairing $\Delta(k) = i \sum_{\delta>0} \Delta_\delta \sin(k\delta)$ will open a p-wave gap of size $\sim 2\Delta(k_0)$ in the subgap dispersion. This puts a constraint on the adatom spacing for any nonzero E_{YSR}.

2.4 The Kitaev model and topological boundary modes

A spinless one-dimensional superconductor hosts topological zero energy states, so called Majorana zero modes, at domain walls or, equivalently, at its ends. To simplify the further discussion, from now on we only keep the on-site and nearest neighbour terms with $|i-j| \leq 1$. We specify to a chain of N adatoms and define $t_{\text{eff}} = t_{\delta=1}$ as well as $\Delta_{\text{eff}} = \Delta_{\delta=1}$. With these simplifications, the model Eq. (2.33) is known as the Kitaev chain [40]. It is instructive to consider the somewhat unphysical case of a band centered at the Fermi energy, $E_{\text{YSR}} = 0$, and matching pairing strength and bandwidth, $\Delta_{\text{eff}} = t_{\text{eff}}$. We decompose the N YSR operators into $2N$ real fermionic (Majorana) operators $\gamma_{j,\pm} = \gamma_{j,\pm}^\dagger$ which satisfy the algebra $\{\gamma_{i,\pm}, \gamma_{j,\pm'}\} = 2\delta_{ij}\delta_{\pm\pm'}$

---

[9] For $k_h = 0$, all YSR states are polarized in the same spin direction. This frustrates the singlet pairing in the host superconductor and hence the effective pairing Δ_δ vanishes. Vice versa, if $k_h = \pi/2a$ neighbouring YSR states have antiparallel spin. This frustrates the kinetic term in the host superconductor (in the absence of spin orbit coupling) and hence the effective hopping t_δ vanishes.

via $c_j = (\gamma_{j,+} + i\gamma_{j,-})/2$ or $\gamma_{j,\pm} = \exp\{i\frac{\pi}{4}(1 \mp 1)\}(c_j^\dagger \pm c_j)$. Expressed in terms of the Majorana operators the Hamiltonian takes the form

$$H_{\text{subgap}} = -it_{\text{eff}} \sum_{j=1}^{N-1} \gamma_{j,-}\gamma_{j+1,+}. \tag{2.35}$$

Importantly, $\gamma_{1,+}$ and $\gamma_{N,-}$ do not feature in H_{subgap}. This implies a nonlocal fermionic zero mode $f = (\gamma_{1,+} + i\gamma_{N,-})/2$ with $[H_{\text{subgap}}, f] = 0$. In other words, there are two degenerate ground states with different occupation of the mode $f^\dagger f$, or equivalently, different fermion parities $p = -i\gamma_{1,+}\gamma_{N,-}$. The next excited states are separated by a gap t_{eff} from the ground state manifold. Thus, the zero mode is again a subgap mode, albeit in the gap of the subgap dispersion. Note that a spatially isolated Majorana bound state is anomalous. It is in some sense half a fermion and as such can arise only at a boundary or a domain wall. This further manifests itself in braiding statistics: the physical exchange of two Majorana fermions results in a nonabelian rotation within the associated ground state manifold. A scheme implementing this exchange requires at minimum of four Majorana bound states. A more detailed discussion can be found in [187].

If one (weakly) relaxes the conditions $E_{\text{YSR}} = 0$ and $\Delta_{\text{eff}} = t_{\text{eff}}$, the support of the Majorana operators $\gamma_{1,+}$ and $\gamma_{N,-}$ extends further into the bulk of the chain. However, as long as the gap stays finite the Majorana mode remains at zero energy (up to corrections which are exponentially suppressed in the system size). To understand this, we now show that the Majorana zero mode is an example of a topological boundary state. Its existence and vanishing energy is guaranteed by the topology of the bulk. To this end, we consider periodic boundary conditions and Fourier transform, giving

$$H_{\text{subgap}} = \frac{1}{2}\sum_k \left[c_k^\dagger, c_{-k}\right] \mathcal{H}_{\text{BdG}}(k) \begin{bmatrix} c_k \\ c_{-k}^\dagger \end{bmatrix} + \text{const.}, \tag{2.36}$$

where $c_k = \sum_j e^{ijk} c_j/\sqrt{N}$ and we defined the subgap Bogoliubov-de Gennes Hamiltonian

$$\mathcal{H}_{\text{BdG}}(k) = [E_{\text{YSR}} - 2t_{\text{eff}}\cos(k)]\tau_z + 2\Delta_{\text{eff}}\sin(k)\tau_y \equiv \mathbf{d}(k) \cdot \boldsymbol{\tau}. \tag{2.37}$$

By construction $\mathcal{H}_{\text{BdG}}(k)$ obeys the particle-hole symmetry $\tau_x \mathcal{H}^*_{\text{BdG}}(-k)\tau_x = -\mathcal{H}_{\text{BdG}}(k)$.[10] This implies that the $\mathbf{d}$-vector has to point along $\hat{z}$ at the invariant momenta $k = 0$ and $k = \pi$. Defining

$$C = \text{sign}[\mathbf{d}(0) \cdot \mathbf{d}(\pi)], \tag{2.38}$$

---

[10] In fact, it also satisfies the spinless time-reversal symmetry $\mathcal{H}^*_{\text{BdG}}(-k) = \mathcal{H}_{\text{BdG}}(k)$ and the chiral symmetry $\tau_x \mathcal{H}_{\text{BdG}}(k)\tau_x = -\mathcal{H}_{\text{BdG}}(k)$. In a more realistic setting, $\mathcal{H}_{\text{BdG}}$ will include a τ_x term and we will hence base our arguments only on the built in particle hole symmetry. In other words, we act as if $\mathcal{H}_{\text{BdG}}$ were in class D rather than class BDI.

there are now two inequivalent situations: either the $\mathbf{d}$-vector is parallel at these points, i.e. $C = 1$, or antiparallel, i.e. $C = -1$. At the special point $E_{\text{YSR}} = 0$ and $\Delta_{\text{eff}} = t$, we have $\mathbf{d} = 2t_{\text{eff}}(0, \sin k, -\cos k)^T$ and thus $C = -1$ (assuming $t_{\text{eff}} > 0$ for simplicity). Small deviations of the parameters from the special point necessarily leave C invariant as its value cannot be changed smoothly. As the special point exhibits Majorana zero modes we refer to the parameter region with $C = -1$ as the topological phase. Conversely, if E_{YSR} is sufficiently large, $d_z(k) \gtrless 0$ for all k and $C = 1$. This is the trivial phase. It clearly does not feature Majorana modes. Transitions between $C = 1$ and $C = -1$ can only occur if either $\mathbf{d}(0)$ or $\mathbf{d}(\pi)$ vanish. This implies that the excitation gap $E_g = \min_k |\mathbf{d}(k)|$ vanishes. Such a transition between is called a topological phase transition.

Consider now a domain wall between the $C = 1$ (e.g. the vacuum) and $C = -1$ phases. Assuming the domain wall to be sufficiently smeared out, the spectrum can be obtained adiabatically as a function of position. At some position the gap has to close such that a transition from $C = 1$ to $C = -1$ can take place, i.e. there is a confined region in space with gapless spectrum. This is the topological boundary. Such a smooth crossover may seem an unnatural description for the end points of a chain of adatoms. However, it is straightforward to show that one also obtains a zero energy bound state in the limit of a hard boundary. Consider the left end point of a chain in the topological phase, with x denoting distance from the end point. Without loss of generality we assume that within the chain (i.e. for $x > 0$) we have $0 < E_{\text{YSR}} < 2t_{\text{eff}}$ while outside the chain (i.e. for $x < 0$) the YSR energy goes up to the host gap edge $E_{\text{YSR}} = \Delta$ which is much larger than all other energies involved. We thus define $m(x) = E_{\text{YSR}} - 2t_{\text{eff}}$ with $m(x < 0) \simeq \Delta$ and $m(x > 0) < 0$. Anticipating that the gap closing occurs at $k = 0$, we expand for small k and let $k \to -ia\partial_x$, giving

$$\mathcal{H}_{\text{BdG}} \simeq m(x)\tau_z - 2\Delta_{\text{eff}} ia\partial_x\tau_y. \tag{2.39}$$

We seek a bound solution $\phi(x) \propto \exp\{-\kappa(x)|x|\}\phi_0$ with $\kappa(x < 0) = \kappa_<$ and $\kappa(x > 0) = \kappa_>$. We find there is a zero energy solution with $\phi_0 = (1, 1)^T$, $\kappa_< = \Delta/(2a\Delta_{\text{eff}}) \gg a^{-1}$ and $\kappa_> = |E_{\text{YSR}} - 2t_{\text{eff}}|/(2a\Delta_{\text{eff}})$. Expressed in terms of the YSR operators c_j the corresponding second quantized operator becomes

$$\gamma \simeq \sum_j \phi^\dagger(x = aj) \cdot \begin{bmatrix} c_j \\ c_j^\dagger \end{bmatrix}. \tag{2.40}$$

As ϕ_0 is an eigenfunction of the particle hole operator, $\tau_x\phi_0^*(x) = \phi_0(x)$, this indeed satisfies $\gamma^\dagger = \gamma$ and thus represents a Majorana bound state. At the special point $E_{\text{YSR}} = 0$ and $t_{\text{eff}} = \Delta_{\text{eff}}$ we can identify it with the left end of the Kitaev chain, i.e. with $\gamma_{1,+}$ (however, note that $\kappa_> = 1/a$ for these parameters while the continuum limit requires $\kappa a \ll 1$). We conclude that a topological bulk implies a gapless boundary mode. Conversely, an anomalous boundary state (i.e. a boundary mode that cannot exist as a standalone system, such as a Majorana zero mode) implies a topological bulk. This is the bulk-boundary correspondence.

To conclude the discussion note that there are other one-dimensional platforms expected to host Majorana zero modes. Most famously, a hybrid system of a semiconductor nanowire with strong spin-orbit coupling proximitized by an s-wave superconductor and placed in a magnetic field realizes the Kitaev model [50, 51]. This platform is more appropriate for quantum information purposes as it should in principle be possible to combine several nanowire-devices onto a single electrostatically floating island [154]. This is necessary for protection against parity flipping processes, see the next section. However, as opposed to the YSR platform, the nanowire devices rely on bulk transport experiments to investigate the edge spectrum which is lacking the spatial resolution of scanning tunneling spectroscopy. This makes distinguishing Majorana zero modes from trivial bound states more difficult.

2.5 Majorana qubits

Majorana zero modes have a number of advantageous properties that make them attractive candidates for quantum information applications. The idea is to use the ground state degeneracy associated with the Majorana zero mode as a quantum memory. Their nonlocal nature provides intrinsic protection against sources of decoherence. Furthermore, braiding provides a number of protected operations on the ground state manifold. This is the essence behind topological quantum computing [41]. Above we have seen that a pair of Majorana bound states γ_1 and γ_2 implies one fermionic zero mode $f_{12} = (\gamma_1 + i\gamma_2)/2$ and a ground state degeneracy of two. We can label the ground states by the occupation of $n_{12} = f_{12}^\dagger f_{12}$, i.e. $|n_{12}\rangle = |0\rangle$ or $|1\rangle$. However, a single pair of Majorana bound states does not suffice to make a qubit due to the principle of fermion parity superselection. In essence, there is simply no way to create a coherent superposition of states that have different fermion parity. We thus add another pair of Majorana bound states γ_3 and γ_4 with associated fermionic mode $f_{34} = (\gamma_3 + i\gamma_4)/2$ and $n_{34} = f_{34}^\dagger f_{34}$ such that the ground state degeneracy is now four, with states $|n_{12}, n_{34}\rangle$. A qubit can then be defined in a subspace of fixed parity

$$p = (-1)^{\sum_{i=1}^{2} n_{2i-1\,2i}} = (-i)^2 \prod_{j=1}^{4} \gamma_j. \tag{2.41}$$

Specifying to the $p = 1$ space $\{|0,0\rangle, |1,1\rangle\}$ we can then define the qubit Pauli operators

$$Z = -i\gamma_1\gamma_2,\; X = -i\gamma_2\gamma_3,\; Y = -i\gamma_3\gamma_1. \tag{2.42}$$

In defining the fermion modes f_{jj+1} we could have chosen a different pairing, e.g. $f_{23} = (\gamma_2 + i\gamma_3)/2$ and $f_{41} = (\gamma_4 + i\gamma_1)/2$. From Eq. (2.42) it is clear that this corresponds to a change in Pauli basis $X \to Z, Y \to X$ and $Z \to Y$. The braiding of the Majorana bound states implements exactly this type of rotation. For instance, the exchange of γ_1 and γ_2 corresponds to the unitary $\exp\{-i\frac{\pi}{4}Z\}$, i.e. a rotation by $\frac{\pi}{2}$ around the z-axis [43]. Similarly, the exchange of γ_2 and γ_3 corresponds to a rotation by $\frac{\pi}{2}$ around the x-axis. Thus, in practice the physical exchange of Majorana bound states is unnecessary as long as it is possible to measure any occupation n_{ij}.

In order to measure the Majorana qubit in any of its Pauli bases one needs to couple the two relevant Majorana bound states, thereby breaking their topological protection. Modeling of the decoherence as well as the measurement signal requires the explicit inclusion of a measurement device into the theory. The coupling Hamiltonian has the general form

$$H_M = -i\lambda\gamma_i\gamma_j \otimes M, \tag{2.43}$$

where M is an operator of the measurement device. Indeed, the possibility of measuring Majorana qubits in all Pauli bases is equivalent to the non-abelian statistics of Majorana zero modes. This is in stark contrast to conventional qubits, and, as a consequence, makes possible a completely new approach to quantum computing based solely on the measurement of non-local products of Pauli operators [45, 156]. Robust quantum non-demolishing readout protocols are paramount to measurement based quantum computing scheme. This is the subject of Chapter 5.

We conclude this section with a discussion of the robustness of Majorana qubits against local noise [188–194]. Electrostatic fluctuations $\Phi(x,t)$ couple to the charge density $\varrho(x) = e\sum_\sigma \psi_\sigma^\dagger(x)\psi_\sigma(x)$ [$= \frac{1}{2}\Psi^\dagger(x)\tau_z\Psi(x) +$ const.] through,

$$\delta H(t) = \int \mathrm{d}^3x\, \Phi(x,t)\varrho(x). \tag{2.44}$$

The latter may be expressed in terms of Majorana operators γ_i and above gap excitations γ_E via

$$\frac{1}{e}\varrho(x) = -i\sum_{i>j} f_{ij}(x)\gamma_i\gamma_j - i\sum_i \gamma_i \int_{E_g}^{\infty} \mathrm{d}E\, \mathcal{N}(E)[f_{iE}(x)\gamma_E + \text{h.c.}] + \text{above gap}, \tag{2.45}$$

where $\mathcal{N}(E)$ is the superconducting density of states at energy E, and we defined the form factor $f_{ab} = i[\phi_a^*\tau_z\phi_b - (\tau_x\phi_b^*)^*\tau_z\phi_a]/2 = i\phi_a^*\tau_z\phi_b = -i\phi_b^*\tau_z\phi_a$ in terms of the Bogoliubov-de Gennes spinors $\phi_a = \phi_a(x)$. Terms in the first sum preserve the qubit parity. Note that diagonal terms in the first sum do not play a role as $\gamma_i^2 = 1$: an isolated Majorana fermion is completely insensitive to parity preserving noise. The off-diagonal terms in the first sum give rise to a perturbation

$$\delta H_{\text{pp}}(t) = \lambda_X(t)X + \lambda_Y(t)Y + \lambda_Z(t)Z, \tag{2.46}$$

where "pp" stands for parity preserving. The coefficients $\lambda \sim f$ involve the overlap of two Majorana bound state wavefunctions and are thus exponentially suppressed in the Majorana bound state separation.[11] Thus, the qubit is indeed exponentially protected against such parity preserving terms. Finally, consider the second term in Eq. (2.45). The corresponding perturbation Hamiltonian δH_{fp} ("fp" as it flips qubit parity) couples the Majorana bound states to the quasiparticle continuum through absorption of a boson from or emission of a boson into the electrostatic environment. A standard derivation (c.f. App. C.3.4) then gives the evolution of the qubit density matrix ρ due to leakage into the quasiparticle continuum,

$$\dot{\rho} = \sum_i k_i(\gamma_i \rho \gamma_i - \rho), \tag{2.48}$$

in terms of the rates

$$k_i = \int_{E_g}^{\infty} \mathrm{d}E\, \mathcal{N}(E) \left[\int \mathrm{d}x\, |f_{iE}(x)|^2 \right] [(1 - n_F(E))S(-E) + n_F(E)S(E)]. \tag{2.49}$$

We defined the noise power spectrum via

$$S(\omega)\delta(x - x') = e^2 \int \mathrm{d}t\, e^{i\omega t} \langle \Phi(x,t)\Phi(x',0) \rangle, \tag{2.50}$$

assuming that the spatial correlations of the electrostatic environment decay fast compared to the distances between the Majorana bound states, and dropped terms $f_{iE}(x) f^*_{jE}(x)$ as they are exponentially suppressed in the Majorana bound state separation. Eq. (2.48) drives the qubit out of the fixed parity subspace and towards the completely mixed state $\rho_\infty = \frac{1}{4}\sum_{n_{12},n_{34}} |n_{12}, n_{34}\rangle\langle n_{12}, n_{34}|$. However, due to the finite energy cost associated with creating an above gap quasiparticle the rates k_i are strongly suppressed: At low temperatures $T \ll E_g$, we can let $n_F \to 0$ in Eq. (2.49). Then, only $S(-E < -E_g)$ enters. The noise power at negative frequencies measures the ability of the electrostatic environment to emit a boson [195]. For a non-interacting bath it is given by $S(\omega < 0) = J(|\omega|)n_B(|\omega|)$ where $J(\omega)$ is the bath spectral density. The Bose function n_B and hence the rates k_i become exponentially small if $E_g/T \gg 1$. To conclude, protection against qubit parity preserving processes is due to the exponentially small overlap of Majorana bound states while qubit parity flipping processes are suppressed only by the gap to the quasiparticle continuum. To further emphasize the different roles of parity conserving and non-conserving noise, consider coupling the Majorana bound states to a gapless fermionic reservoir, e.g. a metallic lead. In fact, the corresponding decay rates can be obtained from Eq. (2.49) by letting $E_g \to 0$ and $\int \mathrm{d}x\, |f_{iE}(x)|^2 S(\pm E) \to 2\pi\nu_0 \mathcal{T}_i^2(E)$, where $\mathcal{T}_i(E)$ is the tunnel matrix element. It is clear that any protection is lost in this case.

---

[11] If the overlap is finite, fluctuations of the form δH represent depolarizing noise with rates

$$k_Z = \lim_{\omega \to 0} S(\omega) \int \mathrm{d}x\, \{\mathrm{Re}[f_{12}(x)]^2 + \mathrm{Re}[f_{34}(x)]^2\}, \tag{2.47}$$

and similar for X, Y. $S(\omega)$ is defined in Eq. (2.50). We dropped terms $\mathrm{Re}[f_{ij}]\,\mathrm{Re}[f_{kl}]$ with $i \neq k, j \neq l$ as such terms are suppressed like $\exp\{-3L/\xi\}$ as opposed to $\exp\{-L/\xi\}$, where L denotes the Majorana bound state separation.

2.6 TOPOLOGICAL SEMIMETALS

In the previous sections we encountered topological boundary modes, i.e. gapless boundary modes guaranteed by bulk topology. Topological semimetals have a gapless bulk but still exhibit a bulk-boundary correspondence. The paradigmatic example is the Weyl semimetal [56], which is characterized by isolated band touching points close to the Fermi energy. In three dimensions such points are generic provided the bands are non-degenerate [196]. This is the case in crystals that break either time-reversal symmetry or inversion symmetry, or both. Consider one such point, $\mathbf{k} \equiv \mathbf{K}$. For crystal momenta close to $\mathbf{K}$, the Bloch Hamiltonian may be expanded as

$$\mathcal{H}(\mathbf{p}) = \sum_{ij} p_i v_{ij} \sigma_j + \mathbf{u} \cdot \mathbf{p} + \mathcal{O}(p^2), \tag{2.51}$$

where we defined $\mathbf{p} = \mathbf{k} - \mathbf{K}$, σ is a set of Pauli matrices corresponding to a spin or pseudospin degree of freedom, the velocity matrix v_{ij} determines the Fermi velocity along the principal axes, and we introduced the tilt velocity $\mathbf{u}$. Eq. (2.51) is just a tilted and anisotropic version of the Weyl Hamiltonian [57]. This gives Weyl semimetals their name. The band touching points are referred to as Weyl points or Weyl nodes. For simplicity we will consider isotropic Weyl points only, i.e. we set $v_{ij} = \chi v \delta_{ij}$ in terms of the Fermi velocity v and the chirality $\chi = \pm 1$, and $\mathbf{u} = 0$. The eigenenergies of the isotropic Weyl point are $E_\pm(\mathbf{p}) = \pm vp$ corresponding to conduction and valence band eigenstates $|\pm, \mathbf{p}\rangle$. Their spinor structure depends on the chirality, and is given by

$$|\chi, \mathbf{p}\rangle = \begin{pmatrix} \cos\frac{\theta}{2} \\ e^{i\phi} \sin\frac{\theta}{2} \end{pmatrix}, \quad |-\chi, \mathbf{p}\rangle = \begin{pmatrix} -\sin\frac{\theta}{2} \\ e^{i\phi} \cos\frac{\theta}{2} \end{pmatrix}, \tag{2.52}$$

where p, θ and ϕ are defined through $\mathbf{p} = p(\sin\theta\cos\phi, \sin\theta\sin\phi, \cos\theta)$. This corresponds to a linear spectrum, plotted in Fig. 2.4.

Weyl points have a number of peculiar properties which determine the characteristics of Weyl semimetals. First, the excitations of the Weyl equation are chiral, $\hat{p} \cdot \boldsymbol{\sigma} |\pm, \mathbf{p}\rangle = \pm\chi$. However, the U(1)-symmetry of chiral fermions is anomalous and does not hold at the quantum level. As a consequence, a combination of parallel electric and magnetic fields can create or annihilate chiral charge,

$$\dot{N}_\chi \propto \chi \mathbf{E} \cdot \mathbf{B}. \tag{2.53}$$

In order for the total charge to be conserved, one therefore needs fermions of opposite chirality, so that $\dot{N} = \dot{N}_+ + \dot{N}_- = 0$. Such anomaly cancellation is a cornerstone of the standard model of particle physics. In the condensed matter realization of chiral fermions, i.e. in Weyl semimetals, this implies that Weyl points come in pairs of opposite chirality which may be located at different points in the Brillouin zone, a statement that is known as Nielsen-Ninomiya theorem [58, 59]. It is straightforward to see that this result is topological in nature as it demands that Weyl

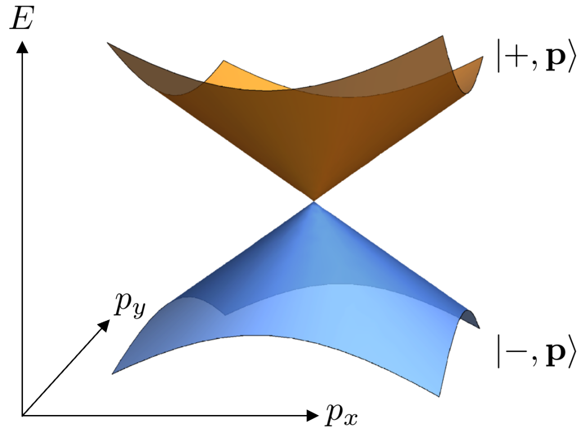

Figure 2.4: Spectrum of an isotropic Weyl point, shown here for $p_z = 0$.

points cannot be removed locally. Indeed, there are several ways to understand the stability of Weyl points. First, consider adding a weak perturbation $V = V_0 + \mathbf{V}\cdot\boldsymbol{\sigma}$ to $\mathcal{H}(\mathbf{p})$. This will simply shift the location of the band touching point to $\mathbf{K}' = \mathbf{K} - \mathbf{V}$ as all Pauli matrices that could open a gap are already in use. A better argument that reveals the connection to topology directly is in terms of the Berry curvature. The latter is defined as

$$\mathcal{B}_i^{\pm}(\mathbf{p}) = i\varepsilon_{ijk}\partial_{p_j}\langle \pm,\mathbf{p}|\partial_{p_k}|\pm,\mathbf{p}\rangle. \tag{2.54}$$

Straightforward evaluation for a Weyl point shows that the latter are monopoles of Berry curvature in momentum space,

$$\boldsymbol{\mathcal{B}}^{\pm} = \pm\chi\frac{\mathbf{p}}{2p^3}. \tag{2.55}$$

Importantly, integration of the Berry curvature over a closed two-dimensional surface gives 2π times an integer, the so called Chern number. Choosing a surface that encloses a Weyl point gives this integer as χ where we focused on the conduction band for concreteness. But since integers cannot be changed smoothly this implies that a Weyl point cannot be removed unless another Weyl point of chirality $-\chi$ enters the region enclosed by the surface we consider. Upon choosing a very small region it becomes clear that Weyl points can only annihilate in pairs.

As usual, the bulk topology manifests itself in anomalous boundary states. Here, this state is a gapless surface mode with sheetlike chiral dispersion. Its Fermi surface is an open arc beginning and ending at the projections of Weyl points onto the surface Brillouin zone. This is the so called Fermi arc. To illustrate this, consider the minimal model $\mathcal{H}(k) = (k_x^2 - K^2)\sigma_x + k_y\sigma_y + k_z\sigma_z$ and a surface with normal $\hat{z}$. The surface states have the spectrum

$$E_{\text{arc}} = vk_y, \ -K < k_x < K. \tag{2.56}$$

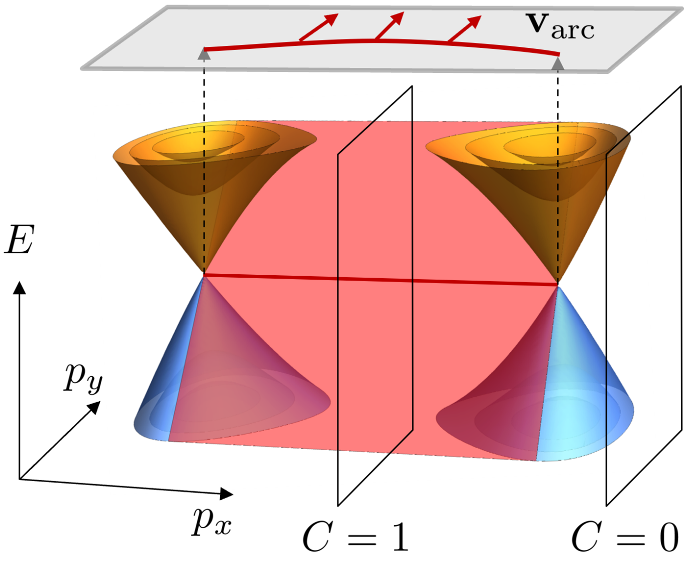

Figure 2.5: Spectrum of semi-infinite Weyl semimetal with minimal number of Weyl points in the surface Brillouin zone. The surface states are localized to the surface in the z-direction but extended states in the directions parallel to the surface. Their energies thus are functions in the surface Brillouin zone. The sheet of surface state energies (red) connects the linear spectra of the two Weyl points. Cuts through the (bulk) Brillouin zone at k_x between the two Weyl points are associated with a Chern number $C = 1$ implying a zero energy surface state at that k_x, while cuts at k_x not between the Weyl points have $C = 0$ and no associated topological zero energy surface state.

and velocity $\mathbf{v}_{\mathrm{arc}} = v\hat{y}$. This situation is depicted in Fig. 2.5. A topological argument for the existence of the Fermi arc is as follows. Consider a cut through the Brillouin zone at $k_x \in [-K, K]$. This is a two-dimensional closed surface and thus has a Chern number associated with it. As the Weyl points are monopoles, that is sources and sinks of Berry flux, the periodicity of the Brillouin zone implies that there needs to be net flux from one Weyl point to the other. This implies that there is flux through the cut and hence a non-zero Chern number. The two-dimensional cut is thus a Chern insulator and associated with a chiral zero energy state. This demands that there is a zero-energy state at some k_y localized at the surface with normal $\hat{z}$. The boundary modes of many such slices form the Fermi arc. Here, we assumed the Chern number to be nonzero for $k_x \in [-K, K]$. There is also the possibility of nonzero Chern number for $k_x \in [-\frac{\pi}{a}, -K]$ and $k_x \in [K, \frac{\pi}{a}]$, where a is the lattice constant. In this case, the Fermi arc crosses the Brillouin zone boundary.

3 QUANTUM YU-SHIBA-RUSINOV CHAINS

The results of this chapter have been published in Refs. [I, II, III].

Dilute chains of magnetic adatoms on superconductors have been proposed as a possible setting for topological superconductivity [38, 39, 49, 124, 197, 198], complementing the frequently studied densely-packed chains [30, 31, 199–202]. While the latter are dominated by direct hybridization of adatom d orbitals [203, 204], the former couple adatoms only indirectly via the substrate provided that the adatoms are spaced close enough that their YSR states [5–7, 18] overlap. Theoretical models assume that the RKKY interaction, possibly aided by magnetic anisotropy, induce ordered magnetic textures, which are then described as chains of classical spins [38, 39, 103–110].

Contrasting with classical spin models, observations of Kondo resonances and discrete spin excitations imply that individual adatom spins behave quantum mechanically, both on normal and on superconducting substrates [11, 111, 115, 116]. Here, we show that the quantum nature of adatom spins makes dilute chains an intriguing experimental platform beyond Majorana physics, displaying rich correlated-electron physics as reflected in qualitatively different phase diagrams and excitation spectra. This is a consequence of quantum phase transitions [121, 205], which change the effective spin due to screening by bound quasiparticles [11, 12, 206], a phenomenon specific to quantum spins and absent for classical spins.

We find that signatures of the quantum spin nature are directly observable in local excitation spectra of adatom chains, as probed for instance by scanning tunneling spectroscopy. Moreover, the topological superconducting phase exhibiting Majorana states can be dramatically reduced in parameter space compared to classical models. The effective spin as well as magnitude and sign of the RKKY coupling between impurity spins can in principle be adjusted. In real materials, magnetic anisotropy, Dzyaloshinskii-Moriya (DM) interactions, and spin-orbit coupled substrate electrons further enrich the physics of these quantum spin chains.

The correlated-electron physics of dilute adatom chains is due to correlated spin-fermion dynamics, which we find to be described by an extension of the $t - J$ model [207], admitting topological superconductivity for ferromagnetic and spin-charge separation for antiferromagnetic RKKY coupling. For a theoretical treatment of quantum chains, we project out the quasiparticle continuum of the superconductor in the limit of a large pairing gap and retain only the subgap YSR excitations induced by the magnetic adatoms. The resulting zero bandwidth model includes a single superconducting site per adatom (and conduction-electron channel), so that Kondo renormalizations must be accounted for separately. Despite its simplicity, the model qualitatively reproduces [121] phase diagrams and excitation spectra of individual higher-spin impurities subject to single-ion anisotropy [186] and spin-$\frac{1}{2}$ dimers [122, 208] obtained from the numerical renormalization group.

This chapter is organized as follows. Section 3.1 gives a sketched derivation of the zero bandwidth model and discusses how YSR states manifest within this model. In particular, it is shown that the zero bandwidth model can capture the low energy physics of quantum YSR states, i.e. those arising from quantum impurity spins. In order to illustrate the difference in screening behavior of quantum and classical spins, a dimer of two magnetic adatoms with spin-$\frac{1}{2}$ is discussed within the zero bandwidth model. In Sec. 3.2 a chain of spin-$\frac{1}{2}$ adatoms is considered and analyzed by means of a low energy projection. The phase diagram is obtained via exact diagonalization, and the phases are analyzed by numerical and analytical techniques. The chapter is concluded in Sec. 3.3. Note that we focus on spin-$\frac{1}{2}$ adatoms throughout as in their case quantum effects are most pronounced.

3.1 Yu-Shiba-Rusinov states in the zero bandwidth model

The starting point of our analysis of *quantum* Yu-Shiba-Rusinov states is again the Hamiltonian [c.f. Eq. (2.16)]

$$H = H_{\text{BCS}} + \sum_{\sigma\sigma'} \psi^\dagger_\sigma(0) \Big[V\delta_{\sigma\sigma'} + \mathbf{S}\cdot\hat{K}\cdot\mathbf{s}_{\sigma\sigma'} \Big] \psi_{\sigma'}(0), \tag{3.1}$$

describing a spinful local scatterer embedded into a superconductor. Here, we generalized to anisotropic exchange interaction $\hat{K} = \text{diag}(K_\perp, K_\perp, K_z)$. We assume antiferromagnetic K_z, $K_\perp > 0$ as ferromagnetic exchange is irrelevant in the renormalization sense. In Sec. 2.3.2 we proceeded by treating the impurity spin as classical. Here, we instead aim to simplify the superconductor by adopting a zero bandwidth approximation. We sketch the derivation of the zero bandwidth model in the following section.

3.1.1 Motivation of the zero bandwidth model

Consider a lattice model of the BCS superconductor described by fermion operators $c_{i,\sigma}$, where i labels lattice sites and σ spin. The impurity spin with $S = \frac{1}{2}$ is coupled only to a single site, say $i = 0$. Then one may formally integrate out all sites except for the site $i = 0$, yielding an effective action

$$\begin{aligned} S = S_{\text{imp}}[\mathbf{S}] + \int_0^\beta d\tau\, \bar{\psi}(\tau) \Big[\partial_\tau + V\tau_z + \Delta\tau_x + \mathbf{S}(\tau)\cdot\hat{K}\cdot\mathbf{s} \Big] \psi(\tau) \\ + \int_0^\beta d\tau \int_0^\beta d\tau'\, \bar{\psi}(\tau)\vartheta^*_{0i}\mathcal{G}_{ij}(\tau-\tau')\vartheta_{j0}\psi(\tau'), \end{aligned} \tag{3.2}$$

where ψ is the four dimensional (Grassmann) Nambu spinor associated with $c_{i=0,\sigma}$, $\mathcal{G}$ is the Nambu Green function of the lattice after removing site $i = 0$, and ϑ_{ji} is the hopping matrix between the site $i = 0$ and other lattice sites $j \neq 0$. The function $\mathbf{S}(\tau)$ takes values on the sphere with radius S, representing the impurity spin within the coherent-state path integral formulation [170]. It satisfies the boundary condition $\mathbf{S}(0) = \mathbf{S}(\beta)$. The classical approximation would amount to dropping the imaginary time dependence of $\mathbf{S}$. In Fourier space, the fermionic part of the action reads

$$-\frac{1}{\beta}\sum_{mn} \bar{\psi}_m \Big\{ [i\omega_m - V\tau_z - \Delta\tau_x - \vartheta^*_{0i}\mathcal{G}_{ij}(i\omega_m)\vartheta_{j0}]\beta\delta_{mn} - \mathbf{S}_{m-n}\cdot\hat{K}\cdot\mathbf{s}\Big\}\psi_n. \tag{3.3}$$

Here, we will be interested in the subgap spectrum with energies $E \ll \Delta$. We can thus neglect the frequency dependence of $\mathcal{G}$ such that we can reconstruct a Hamiltonian (dropping the label $i = 0$)

$$H = \tilde{\Delta}\Big(c^\dagger_\uparrow c^\dagger_\downarrow + \text{h.c.}\Big) + \sum_{\sigma\sigma'} c^\dagger_\sigma \Big(\tilde{V}\delta_{\sigma\sigma'} + \mathbf{S}\cdot\hat{K}\cdot\mathbf{s}_{\sigma\sigma'}\Big)c_{\sigma'} \tag{3.4}$$

in terms of renormalized parameters $\tilde{\Delta}$ and $\tilde{V}$. Upon dropping all frequency dependence of $\mathcal{G}$, we have implicitly neglected the renormalization of the Kondo interaction $\hat{K}$. Thus, $\hat{K}$ should be interpreted as the effective low energy exchange coupling $\hat{K}_{\text{eff}} = \hat{K}(\Delta)$. The relationship between $\tilde{\Delta}$, $\tilde{V}$ and $\hat{K}_{\text{eff}}$ and microscopic parameters is in general complicated. Hence we treat them as phenomenological parameters. To avoid cluttered notation we will drop the tilde and subscript below. The model Eq. (3.4) is simply an impurity spin coupled to a single site superconductor. In the quantum dot community this is known as a zero bandwidth model [209]. The zero bandwidth model works particularly for subgap excitations with energies much below Δ. We will make this more precise at the end of the following section.

3.1.2 SPECTRUM OF THE ZERO BANDWIDTH MODEL

Before we discuss the spectrum of the zero bandwidth model, we want to briefly recap some findings on quantum and classical impurity spins in a superconductor (c.f. Secs. 2.3.1 and 2.3.2). For a quantum impurity spin with $S = \frac{1}{2}$, as the exchange coupling (Kondo temperature) is varied the system undergoes a quantum phase transition accompanied by a change of ground state multiplicity, i.e. a transition between a fully paired even parity doublet and an odd parity singlet. This can be interpreted as a change in occupation of a local bound state, the so called Yu-Shiba-Rusinov state, which if occupied, forms a singlet with the impurity spin. For a classical impurity spin, the system also undergoes a quantum phase transition at which the occupation of the YSR state changes. However, in this case there is no change in ground state multiplicity. The change in ground state multiplicity has important ramifications for the screening properties of the impurity spin as well as the effective theory describing the subgap fermions. We will explore these ramifications by exploiting the simplicity of the zero bandwidth model and the fact that it can treat both quantum and classical spins on even footing.

To this end, we discuss the spectrum of Eq. (3.4) in detail. We make use of the conservation of the fermion parity

$$p = (-1)^{\sum_\sigma c_\sigma^\dagger c_\sigma}. \tag{3.5}$$

as well as conservation of the z-component of the total spin

$$\mathbf{S}_{\text{tot}} = \mathbf{S} + \sum_{\sigma\sigma'} c_\sigma^\dagger \mathbf{s}_{\sigma\sigma'} c_{\sigma'}. \tag{3.6}$$

The lowest-energy states for even fermion parity are given by

$$|\pm\rangle = |\Uparrow / \Downarrow\rangle \otimes |\text{BCS}\rangle. \tag{3.7}$$

They are simply a direct product of a free impurity spin $|\Uparrow / \Downarrow\rangle$ and the paired state

$$|\text{BCS}\rangle = (u + v c_\downarrow^\dagger c_\uparrow^\dagger)|\text{vac}\rangle, \tag{3.8}$$

and have energy

$$E_e = V - \sqrt{\Delta^2 + V^2}, \tag{3.9}$$

which is independent of the exchange coupling $\hat{K}$. Here, $|\text{vac}\rangle$ is the vacuum of the c_σ fermion and we defined the amplitudes

$$u^2 = \frac{1}{2}\left(1 + \frac{V}{\sqrt{\Delta^2 + V^2}}\right), \quad v^2 = \frac{1}{2}\left(1 - \frac{V}{\sqrt{\Delta^2 + V^2}}\right). \tag{3.10}$$

The electron and hole amplitudes are in general different as a result of the potential scattering V by the impurity. The discrete excited states $|\Uparrow / \Downarrow\rangle \otimes |\overline{\text{BCS}}\rangle$ with $|\overline{\text{BCS}}\rangle = (v - u c_\downarrow^\dagger c_\uparrow^\dagger)|\text{vac}\rangle$ and energy $V + \sqrt{\Delta^2 + V^2}$ replace the quasiparticle continuum of a finite bandwidth model and are thus unphysical. Excitations involving these states have to be excluded by choosing the correct hierarchy of energy scales. We will specify this below.

For odd fermion parity, the lowest-energy state binds a quasiparticle and has energy

$$E_o = V - \frac{1}{4}(K_z + 2K_\perp) \tag{3.11}$$

independent of the pairing strength Δ. For purely longitudinal (Ising-like) exchange coupling, the state is a doublet

$$|\Uparrow, \downarrow\rangle = |\Uparrow\rangle \otimes |\downarrow\rangle \quad \text{and} \quad |\Downarrow, \uparrow\rangle = |\Downarrow\rangle \otimes |\uparrow\rangle. \tag{3.12}$$

For nonzero transverse coupling, there is a unique singlet ground state

$$|s\rangle = \frac{1}{\sqrt{2}}(|\Uparrow,\downarrow\rangle - |\Downarrow,\uparrow\rangle) \tag{3.13}$$

corresponding to a screened adatom spin. We also define the even superposition

$$|t\rangle = \frac{1}{\sqrt{2}}(|\Uparrow,\downarrow\rangle + |\Downarrow,\uparrow\rangle), \tag{3.14}$$

which has energy $V - \frac{1}{4}(K_z - 2K_\perp)$ and can not be neglected if $K_\perp$ is small. The singly occupied fermion states

$$|\sigma\rangle = c_\sigma^\dagger|\text{vac}\rangle = \gamma_\sigma^\dagger|\text{BCS}\rangle, \tag{3.15}$$

can be either viewed as excited states with one Bogoliubov quasiparticle or as single-electron states unaffected by pairing. Here, we defined the Bogoliubov quasiparticle operators

$$\gamma_\uparrow^\dagger = uc_\uparrow^\dagger + vc_\downarrow, \quad \gamma_\downarrow^\dagger = uc_\downarrow^\dagger - vc_\uparrow. \tag{3.16}$$

The ferromagnetic states $|\Uparrow,\uparrow\rangle$ and $|\Downarrow,\downarrow\rangle$ have energies $V + \frac{1}{4}K_z$. These will also overlap with the quasiparticle continuum (as we will be interested in exchange couplings of the order of the gap, i.e. $K_z \sim \Delta$) and hence excitations involving these states should be avoided. It will prove useful to express the Hamiltonian of the zero bandwidth model in terms of the Bogoliubov quasiparticle operators γ_σ,

$$H = V + \sqrt{\Delta^2 + V^2}\left(\sum_\sigma \gamma_\sigma^\dagger\gamma_\sigma - 1\right) + \sum_{\sigma\sigma'} \mathbf{S}\cdot\hat{K}\cdot\mathbf{s}_{\sigma\sigma'}\gamma_\sigma^\dagger\gamma_{\sigma'}. \tag{3.17}$$

In this form it is manifestly the quasiparticle operators by which the impurity spin is screened. They are the counterparts to the YSR operator defined in Eq. (2.26) of the classical treatment.

The spectrum of the zero bandwidth model is depicted in Fig. 3.1. The YSR excitation energy is the energy difference between the odd and even parity ground state energies,

$$E_{\text{YSR}} = E_o - E_e = \sqrt{\Delta^2 + V^2} - \frac{1}{4}(K_z + 2K_\perp). \tag{3.18}$$

In order to eliminate transitions to the quasiparticle continuum which are not captured in the zero bandwidth approach, we consider deep YSR states, i.e.

$$E_{\text{YSR}} \ll \Delta \tag{3.19}$$

and focus on energies $E \sim E_{\text{YSR}}$.

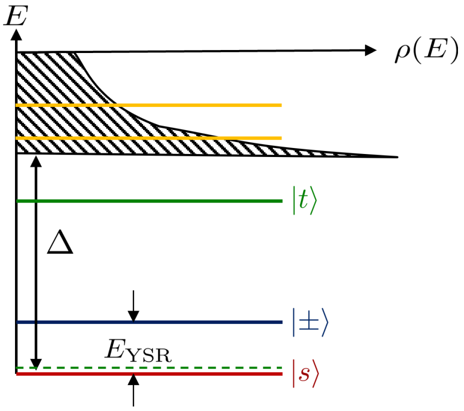

Figure 3.1: Spectrum of the zero bandwidth model given in Eq. (3.4). The zero bandwidth model captures the low energy spectrum of both quantum and classical impurity spins in superconductors: For $K_\perp \sim \Delta \gg E_{\mathrm{YSR}}$, there are only three low energy states as the even superposition $|t\rangle$ lies far from the gap center (green solid line). This situation corresponds to a quantum impurity spin. However, if $K_\perp \ll E_{\mathrm{YSR}}$, this state (green dashed line) is almost degenerate with the singlet $|s\rangle$, corresponding to the classical situation. The zero bandwidth model also has excited states with energies $E \sim \Delta$ (orange lines). These correspond to ferromagnetic spin excitations and an above gap resonance induced by the impurity. In particular these states should couple resonantly to the quasiparticle continuum which is absent in the zero bandwidth model.

For small exchange coupling $K = \max(K_z, K_\perp) \ll \Delta$ the overall ground state is the doublet $|\pm\rangle$, regardless of $K_\perp$. This should be interpreted as an unoccupied Yu-Shiba-Rusinov bound state with unscreened impurity spin. For large $K \gg \Delta$, the overall ground state is, depending on $K_\perp$, either the odd parity doublet $|\Uparrow, \downarrow\rangle$, $|\Downarrow, \uparrow\rangle$, or the singlet $|s\rangle$. This corresponds to an occupied Yu-Shiba-Rusinov bound state. For $K_\perp \sim \Delta$, this bound state screens the impurity spin into a singlet and the low energy structure is the same as in the quantum case, as was described in Sec. 2.3.1. Thus, the $K_\perp \sim \Delta$ case corresponds to the quantum YSR case. If instead $K_\perp$ becomes comparable to the YSR excitation energy E_{YSR} there are two odd parity low energy states instead. For $K_\perp \ll E_{\mathrm{YSR}}$, these states will be almost degenerate, reproducing the main features of the classical spin approximation. Note however, that, in contrast to our calculation in Sec. 2.3, here the classical model encompasses two time reversed copies corresponding to opposite impurity spin configurations. Furthermore, at finite $K_\perp$ spin flip processes between the adatom spin and itinerant electrons lead to a finite lifetime of the impurity spin.

The YSR quantum phase transition occurs at $E_{\mathrm{YSR}} = 0$. Importantly, in the (strictly) classical case $K_\perp = 0$, this transition between the even- and odd-fermion-parity ground states leaves the impurity-spin state unaffected, e.g.

$$|\Uparrow\rangle \otimes |\mathrm{BCS}\rangle \longleftrightarrow |\Uparrow\rangle \otimes |\downarrow\rangle. \tag{3.20}$$

and similarly for impurity spin $|\Downarrow\rangle$. In other words, the ground state multiplicity is unaffected by the quantum phase transition. Consequently, there is no screening of the impurity spin in the strong-coup-ling phase. Conversely, in the quantum case $K_\perp \gg E_{\text{YSR}}$, the impurity spin state changes qualitatively at the quantum phase transition and the ground state multiplicity transits between a doublet and a singlet configuration. In particular, the impurity spin is screened in the strong-coupling phase, where it no longer points in any preferred direction. The difference in screening behavior will become explicit once the RKKY coupling of two impurity spins is taken into account. This will be analyzed in greater detail in the next section for the simple case of an adatom dimer.

The zero-bandwidth approximation fails to account for the quasiparticle continuum and can thus only be expected to describe deep subgap states. We account for this limitation by assuming large Δ, $K = \max(K_z, K_\perp)$, and V in such a way that the YSR energy E_{YSR} (and inter-YSR couplings, see below) remain small by comparison. In particular, this assures that E_{YSR} is well within the gap. We note that these assumptions are consistent with typical experimental situations. In particular, one expects the dimer couplings to decrease rapidly with adatom distance. Thus, our considerations apply as long as the adatoms are not too closely spaced. Moreover, in many cases, a finite value of the gap largely limits the number of excited states, which can still be resolved as subgap excitations. The elimination of high energy operators can be implemented formally by projecting onto the low energy subgap states. In the quantum case $K_\perp = K_z$ the low energy effective theory can then be reformulated in terms of $t - J$- fermions. This will prove useful once chains of adatoms are considered.

3.1.3 Quantum Yu-Shiba-Rusinov dimer

Prior to our discussion of quantum YSR chains, we here consider the shortest chain, the dimer. This serves to illustrate the difference in screening behavior of classical and quantum spins, and the ramifications for the phase diagram.

Within the zero-bandwidth approach, the YSR dimer is given by the following Hamiltonian,

$$H = \sum_{j=1}^{2} \left\{ \Delta(c^\dagger_{j,\uparrow} c^\dagger_{j,\downarrow} + \text{h.c.}) + \sum_{\sigma\sigma'} c^\dagger_{j,\sigma} [V \delta_{\sigma\sigma'} + \mathbf{S}_j \cdot \hat{K} \cdot \mathbf{s}_{\sigma\sigma'}] c_{j,\sigma'} \right\} \\ - t \sum_{\sigma} \left[c^\dagger_{1,\sigma} c_{2,\sigma} + \text{h.c.} \right] + \mathbf{S}_1 \cdot \hat{J} \cdot \mathbf{S}_2. \quad (3.21)$$

Here, the adatom spins $\mathbf{S}_j$ $(j = 1, 2)$ are coupled to separate superconducting sites $(c_{j,\sigma})$. Hybridization of the YSR states due to their orbital overlap is incorporated through intersite hopping of strength t. The effective RKKY interaction $\hat{J} = \text{diag}(J_\perp, J_\perp, J_z)$ is incorporated explicitly as it is mediated by the quasiparticle continuum, which is not accounted for within the zero-bandwidth model. Due to the oscillatory dependence of the RKKY interaction, strength and sign of $\hat{J}$ depend on the distance between the adatoms.

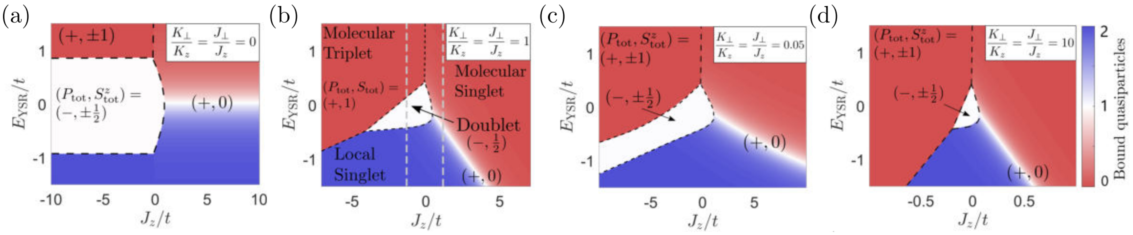

Figure 3.2: Phase diagrams of a spin-$\frac{1}{2}$ YSR dimer as a function of RKKY coupling J_z and YSR energy E_YSR for different anisotropies of the exchange coupling $K_\perp/K_z$. The anisotropy of the RKKY interaction is chosen to match the exchange anistropy, $K_\perp/K_z = J_\perp/J_z$. Phase diagrams are obtained from the zero-bandwidth Hamiltonian in Eq. (3.21). The color scale (see scale bar) indicates the expectation value of the number of bound quasiparticles F as defined in Eq. (3.24). Black dashed lines indicate phase boundaries, at which the spin and/or fermion parity quantum numbers of the ground state change discontinuously. (a) Ising exchange with nonzero K_z and $K_\perp = 0$, corresponding to a classical-spin model of the adatom. Phase boundaries and crossovers essentially depend only on the sign of the RKKY coupling, reflecting the absence of screening of the adatom spin in the classical model. (b) Heisenberg exchange $K = K_\perp = K_z$. Phase boundaries and crossovers depend on the magnitude of the RKKY coupling. This phase diagram qualitatively reproduces the results of NRG simulations in Ref. [122]. (c) Dominant longitudinal and (d) dominant transverse anisotropic couplings as indicated in the panel. The singly-screened phase (white) reduces in extent as $K_\perp/K_z$ increases. Parameters: $(K_z, K_\perp) = 100t(\cos\theta, \sin\theta)$, (a) $\theta = 0$, (b) $\theta = \frac{\pi}{4}$, (c) $\theta = 0.05$, (d) $\theta = \frac{\pi}{2} - 0.1$, $V = 0.9(K_z + 2K_\perp)/4$. Figure from [III].

To characterize the phases of the model in Eq. (3.21), we exploit the symmetries of the system. The superconducting pairing breaks particle-number conservation, but conserves the overall fermion parity

$$p_\text{tot} = (-1)^{\sum_\sigma (c^\dagger_{1\sigma}c_{1\sigma}+c^\dagger_{2\sigma}c_{2\sigma})}. \tag{3.22}$$

Provided that the model retains spin rotation symmetry about the z-axis, the projection S^z_tot of the total spin

$$\mathbf{S}_\text{tot} = \mathbf{S}_1 + \mathbf{S}_2 + \sum_{\sigma\sigma'}\sum_j c^\dagger_{j,\sigma}\mathbf{s}_{\sigma\sigma'}c_{j,\sigma'} \tag{3.23}$$

is also a conserved quantity. For the special case of Heisenberg exchange and RKKY interactions, the model has full spin rotation symmetry and we can further classify phases according to S_tot.

The quantum numbers P_tot and S^z_tot can be used to classify the model's phases. We also find it useful to consider the expectation value of

$$F = \sum_{j=1,2}\left(c^\dagger_{j\uparrow}c_{j\uparrow} - c^\dagger_{j\downarrow}c_{j\downarrow}\right)^2, \tag{3.24}$$

which is a proxy for the number of bound quasiparticles. It should be noted, however, that for nonzero YSR hybridization t, this is not a conserved quantum number due to the presence of pairing correlations in the model. While ground states with different quantum numbers define

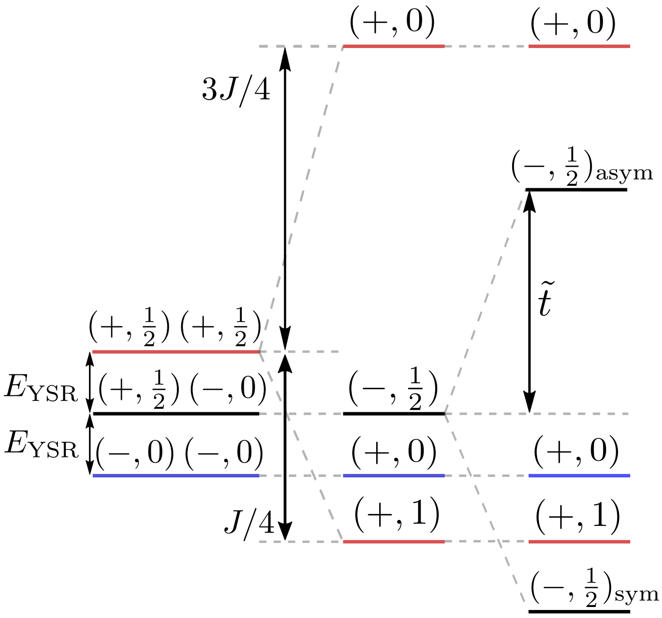

Figure 3.3: Illustrative level scheme of spin-$\frac{1}{2}$ dimers with isotropic exchange and ferromagnetic RKKY coupling $(J < 0)$. The low-energy spectrum of the uncoupled dimer (left) is labeled by the fermion parities P_j and effective spins $S_{\mathrm{eff},j}$ of the monomers as $(P_1, S_{\mathrm{eff},1})(P_2, S_{\mathrm{eff},2})$. For $E_{\mathrm{YSR}} < 0$ the local singlet state ($F \simeq 2$, blue) is the ground state. Nonzero RKKY interaction (center) couples the monomer states into states of total parity and spin $(P_{\mathrm{tot}}, S_{\mathrm{tot}})$. This affects only the unscreened state ($F \simeq 0$, red), which splits into molecular singlet and triplet. For sufficiently large $|J|$, the molecular triplet becomes the ground state. Finally, hybridization of the YSR states splits the odd-fermion-parity states ($F = 1$, black) into symmetric and antisymmetric states. For sufficiently large hybridization $\tilde{t}$ this leads to the singly-screened ground state. Figure from [III].

phases of the quantum YSR dimer, we refer to the unscreened ($F \simeq 0$) or doubly-screened ($F \simeq 2$) parts of the phase diagram as regions.

Figure 3.2 (a) and (b) show dimer phase diagrams as a function of the RKKY interaction J_z and the YSR energy E_{YSR} for Ising coupling (classical spins) and Heisenberg coupling (quantum spins), respectively. The most striking difference is that phase boundaries and crossovers in the classical phase diagram [Fig. 3.2 (a)] essentially depend only on the sign, but not on the magnitude of the RKKY interaction J. In contrast, the magnitude of the RKKY coupling is an important parameter in the quantum phase diagram [Fig. 3.2 (b)].

This difference arises as follows. The phase boundaries correspond to lines in the phase diagram, along which states with different total spin are degenerate. For a classical impurity spin, the quantum phase transition does not affect the impurity-spin state. Consequently, it leaves the RKKY energy of the dimer unchanged, which will then cancel from the energy balance governing phase boundaries and crossovers. In contrast, for quantum spins, the impurity spin is fully screened in the strong-coupling state. Thus, only the unscreened phases benefit from the RKKY interaction, while the RKKY interaction energy vanishes for the phases in which one or both spins are screened. Now, the RKKY interaction enters into the energy balance governing phase boundaries and crossovers.

The phase diagram of a quantum spin-$\frac{1}{2}$ dimer with Heisenberg interactions was also computed in Ref. [122], using the numerical renormalization group (NRG) including the full quasiparticle continuum of the substrate superconductor. Remarkably, the phase diagram of the zero-bandwidth model of Eq. (3.21) in Fig. 3.2 (b) qualitatively reproduces the NRG phase diagram. We now discuss the phase diagram in Fig. 3.2 (b) for isotropic (Heisenberg) exchange and RKKY coupling in more detail. For sufficiently large E_{YSR}, both adatom spins are unscreened ($F \simeq 0$). For ferromagnetic RKKY coupling ($J < 0$), the ground state is a molecular triplet, e.g., $|+\rangle_1 \otimes |+\rangle_2$, with quantum numbers $(P_{\mathrm{tot}}, S_{\mathrm{tot}}) = (+, 1)$. For antiferromagnetic RKKY interactions ($J > 0$), the unscreened impurity spins couple into a molecular singlet $|+\rangle_1 \otimes |-\rangle_2 - |-\rangle_1 \otimes |+\rangle_2$, so that $(P_{\mathrm{tot}}, S_{\mathrm{tot}}) = (+, 0)$. For large and negative E_{YSR}, the adatom spins are individually screened ($F \simeq 2$) and the dimer has a local-singlet ground state, $|s\rangle_1 \otimes |s\rangle_2$. This state also has $(P_{\mathrm{tot}}, S_{\mathrm{tot}}) = (+, 0)$, so that the molecular singlet evolves continuously into the local singlet phase as E_{YSR} is reduced. The absence of a sharp phase transition between these ground states reflects that the pairing term in the model in Eq. (3.21) breaks particle-number conservation. At large and negative RKKY coupling, there is a direct transition between the molecular triplet and the local-singlet phases, with a corresponding change in S_{tot}. For weak RKKY coupling and small $|E_{\mathrm{YSR}}|$, there is an odd-fermion-parity phase with half-integer total spin, $(P_{\mathrm{tot}}, S_{\mathrm{tot}}) = (-, \frac{1}{2})$. The doublet ground state of this phase, $|s\rangle_1 \otimes |\pm\rangle_2 + |\pm\rangle_1 \otimes |s\rangle_2$, emerges when the hybridization splitting of the dimer states with one screened adatom is large enough to offset the cost in YSR energy.

Figure 3.3 shows level diagrams for the RKKY and hybridization splittings, illustrating the mechanisms governing the phase diagram in Fig. 3.2 (b). While the ferromagnetic RKKY coupling favors the molecular triplet, a sufficiently large YSR hybridization t can lower the energy of the doublet with half-integer spin to become the ground state. Note that we use $2\tilde{t}$ to denote the actual energy splitting of the singly-screened states due to the hybridization t.

The phase diagrams in Fig. 3.2 (c) and (d) for, respectively, predominantly longitudinal and transverse exchange and RKKY couplings deviate qualitatively from the isotropic Heisenberg case. Here, we take both the exchange coupling $\hat{K}$ and the RKKY interaction $\hat{J}$ to have the same anisotropy (i.e., $K_\perp/K_z = J_\perp/J_z$). For dominant longitudinal coupling, $K_\perp \ll K_z$, Fig. 3.2 (c), the doublet phase continues to form a stripe as in the Ising case, albeit with boundaries that depend on the RKKY coupling. Beyond a critical value of $K_\perp$, the doublet phase forms an island as in the Heisenberg case. We note that classical behavior with phase boundaries approximately independent of J is recovered only for $K_\perp \ll J, t$. For dominant transverse couplings, $K_\perp \gg K_z$, Fig. 3.2 (d), the doublet phase remains limited to small RKKY couplings as in the isotropic Heisenberg case.

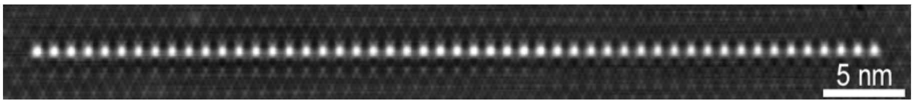

Figure 3.4: Scanning tunneling micrograph of a chain of Fe adatoms on a NbSe$_2$ substrate. Data courtesy of Eva Liebhaber.

3.2 QUANTUM YU-SHIBA-RUSINOV CHAINS IN THE ZERO BANDWIDTH MODEL

We now consider chains of magnetic adatoms. Fig. 3.4 shows a scanning tunneling micrograph of such a system, hosting YSR states at each adatom. In Sec. 2.3.3 we have discussed a chain of classical YSR impurities and found that the overlapping YSR states form a spin polarized one dimensional superconductor inside the host gap. Here, we will focus on the changes that arise if the quantum nature of the adatom spin is taken into account. In the previous section we have seen that already for a dimer, the quantum nature leads to stark differences in the phase diagram. This may be traced back to the change in local ground state multiplicity associated with binding or unbinding a quasiparticle. In particular, this implies that the adatom spin is completely screened to other spins if a quasiparticle is locally present. We will now show that this may be rephrased as an extension to the $t - J$ model.

The extension of the zero bandwidth model Eq. (3.21) to many sites is straightforward. The Hamiltonian is now

$$H = \sum_j \Bigg[\Delta\Big(c^\dagger_{j,\uparrow} c^\dagger_{j,\downarrow} + \text{h.c.}\Big) + \sum_{\sigma\sigma'} c^\dagger_{j,\sigma}\Big(V\delta_{\sigma\sigma'} + \mathbf{S}_j \cdot \hat{K} \cdot \mathbf{s}_{\sigma\sigma'}\Big) c_{j,\sigma'} \\ - t\sum_\sigma \Big(c^\dagger_{j,\sigma} c_{j+1,\sigma} + \text{h.c.}\Big) + \mathbf{S}_{j+1} \cdot \hat{J} \cdot \mathbf{S}_{j+1} \Bigg], \quad (3.25)$$

where $j \in \{1, ..., N\}$ enumerates the adatoms along the chain. We consider both open and closed boundary conditions. In Sec. 2.3.3 we had seen that RKKY coupling and hopping is often long-range. Here, we consider only nearest-neighbor couplings to avoid an excessively large parameter space. We note that the extension of the model as well as the subsequent discussions to long-range couplings is straightforward. Expressing the fermions in terms of the local quasiparticle operators $\gamma_{j,\sigma} = u c_{j,\sigma} + \sigma v c^\dagger_{j,\bar{\sigma}}$, the Hamiltonian instead takes the form

$$H = \sum_j \Bigg[V + \sqrt{\Delta^2 + V^2} \sum_\sigma (\gamma^\dagger_\sigma \gamma_\sigma - 1) + \sum_{\sigma\sigma'} \mathbf{S} \cdot \hat{K} \cdot \mathbf{s}_{\sigma\sigma'} \gamma^\dagger_\sigma \gamma_{\sigma'} + \mathbf{S}_{j+1} \cdot \hat{J} \cdot \mathbf{S}_{j+1} \\ - 2\tilde{t} \sum_\sigma \Big(\gamma^\dagger_{j,\sigma} \gamma_{j+1,\sigma} + \text{h.c.}\Big) + 2\tilde{\Delta}\Big(\gamma^\dagger_{j,\uparrow}\gamma^\dagger_{j+1,\downarrow} - \gamma^\dagger_{j,\downarrow}\gamma^\dagger_{j+1,\uparrow} + \text{h.c.}\Big)\Bigg], \quad (3.26)$$

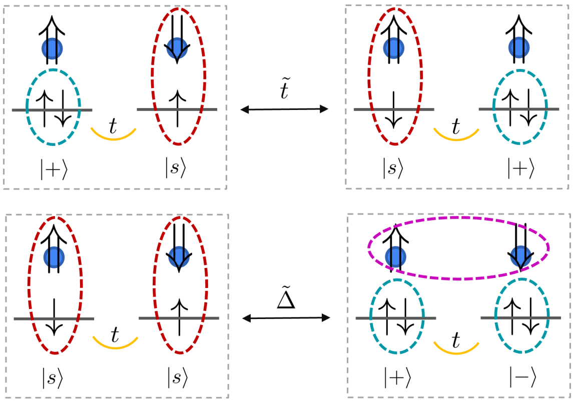

Figure 3.5: Illustration of effective hopping (top row) and pairing processes (bottom row). Impurity spins are indicated by double arrows and sit on adatoms which are represented by blue balls. c-fermion spins are indicated by single arrows. Dashed ellipses correspond to spin singlet configurations with blue corresponding to the fermion-only singlet $|\mathrm{BCS}\rangle$, red corresponding to the impurity-fermion singlet $|s\rangle$ and pink corresponding to the impurity-only singlet $|\Uparrow\rangle_j|\Downarrow\rangle_{j+1}-|\Downarrow\rangle_j|\Uparrow\rangle_{j+1}$. Top row: spin conserving tunneling t may move screening electron between adjacent sites, giving rise to an effective hopping of amplitude $\tilde{t}$ for unscreened sites. Bottom row: similarly, two adjacent screened sites can become unscreened by tunneling an electron between them. Including the opposite-spin process it may be seen that the new configuration is again an overall singlet. Hence, this gives rise to an effective nearest-neighbor singlet pairing of amplitude $\tilde{\Delta}$ for unscreened sites.

where we defined the effective hopping and pairing amplitudes

$$\tilde{t} = \frac{t}{2}(u^2 - v^2) = \frac{tV}{2\sqrt{\Delta^2 + V^2}}, \quad \tilde{\Delta} = tuv = \frac{t\Delta}{2\sqrt{\Delta^2 + V^2}}. \tag{3.27}$$

Thus, the screening quasiparticles $\gamma_{j,\sigma}$ can hop between neighboring sites, or annihilate in pairs. The mechanism for these processes is illustrated in Fig. 3.5.

We will focus here on the quantum case $K_\perp = K_z$. As described in Sec. 3.1.2 the Hamiltonian in Eq. (3.25) has three low-energy states for each site: the BCS-paired doublet

$$|\pm\rangle_j = |\Uparrow / \Downarrow\rangle_j \otimes |\mathrm{BCS}\rangle_j, \tag{3.28}$$

corresponding to an unscreened impurity spin and the singlet

$$|s\rangle_j = \frac{1}{\sqrt{2}}\Big(|\Uparrow\rangle_j \otimes |\downarrow\rangle_j - |\Downarrow\rangle_j \otimes |\uparrow\rangle_j\Big), \tag{3.29}$$

corresponding to a screened impurity spin, separated by an energy $E_{\mathrm{YSR}} = \sqrt{\Delta^2 + V^2} - \frac{3}{4}K$. This resembles the structure of a SU(2) symmetric local fermionic orbital with infinite on-site repulsion - the singlet has no spin and hence corresponds to the empty orbital whereas the doublet carries spin and hence corresponds to the singly occupied orbital. The infinite onsite potential eliminates the doubly occupied orbital as it does not have a counterpart in the local low energy spectrum.

The fermionic operators $d_{j,\sigma}$ for this orbital are introduced as follows. The singlet involves the singly-occupied states $|\sigma\rangle_j = c^\dagger_{j,\sigma}|\mathrm{vac}\rangle_j$, which can also be obtained from the BCS ground state using the Bogoliubov operators γ_σ through $|\sigma\rangle_j = \gamma^\dagger_{j,\sigma}|\mathrm{BCS}\rangle_j$. The free-spin states (involving $|\mathrm{BCS}\rangle$ as the electronic state) are thus obtained from the singlet by annihilating a quasiparticle, and the new fermion creation operators $d^\dagger_{j,\sigma}$ essentially correspond to the quasiparticle annihilation operators $\gamma_{j,\bar{\sigma}}$. Taking into account the detailed singlet state, we find

$$\gamma_{j,\sigma} = u c_{j,\sigma} + \sigma v c^\dagger_{j,\bar{\sigma}} \sim \sigma \frac{(-1)^j}{\sqrt{2}} d^\dagger_{j,\bar{\sigma}}. \tag{3.30}$$

Here, we use $\sim$ rather than an equality since strictly speaking, the two operators are equivalent only when projecting to the low-energy subspace.

Fermions with forbidden double occupation due to infinite onsite repulsion feature in the famous $t-J$ model [210] and we hence refer to them as $t-J$ fermions (they do not satisfy the standard fermionic algebra when the constraint is taken into account). Including the effective hopping and pairing as well as the RKKY interaction, we obtain an effective $t-J$ model describing the subgap structure of the quantum YSR chain. In the following section we will make the mapping to the effective $t-J$ model precise. We will then proceed to present numerical results for the phase diagram and excitation spectra of this model.

3.2.1 LOW ENERGY PROJECTION AND MAPPING TO EFFECTIVE $t-J$ MODEL

In this section, we present details of the mapping from the original model in Eq. (3.25) to the extended $t-J$ model. We will first discuss the mapping for a single impurity and then extend it to a chain of impurities.

To this end consider a single site of the chain and define the projector onto the low-energy subspace through

$$P_j = P_{\mathrm{BCS}_j} + P_{s_j}, \quad \text{with} \quad P_{\mathrm{BCS}_j} = \sum_{\pm} |\pm\rangle_j\langle\pm|_j, \; P_{s_j} = |s\rangle_j\langle s|_j. \tag{3.31}$$

The low-energy projected local Hamiltonian is then

$$P_j H_j P_j = -E_{\mathrm{YSR}} P_{\mathrm{BCS}_j} + \left(V - \frac{3}{4}K\right) P_j. \tag{3.32}$$

We now analyze the action of the projected Bogoliubov operators $P_j\gamma_{j,\sigma}P_j$ and $P_j\gamma^\dagger_{j,\sigma}P_j$ on the low-energy subspace. Up to normalization, $P_j\gamma_{j,\sigma}P_j|s\rangle_j$ creates the state $|\pm = \bar{\sigma}\rangle_j$. Conversely, $P_j\gamma^\dagger_{j,\sigma}P_j|\pm\rangle$ gives back the singlet if $\sigma = \pm$ (the triplet component is projected out)

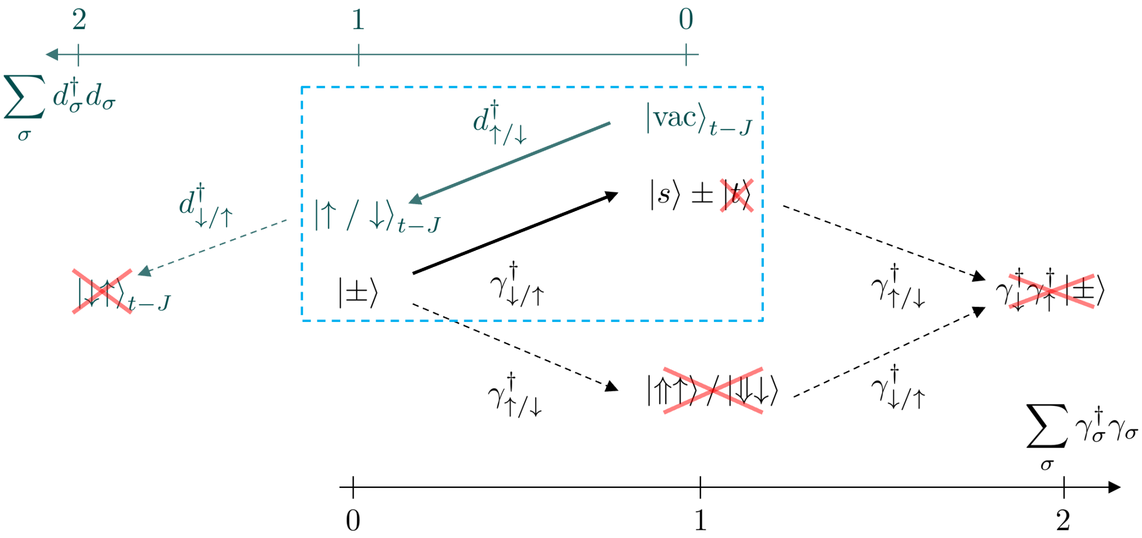

Figure 3.6: Correspondence between the local Hilbert spaces for the original zero bandwidth model (Eq. (3.4), black) and the $t-J$ model (Eq. (3.35), green). There is a direct correspondence between the low-energy states and the fermionic operators acting thereon of both models (indicated by blue dashed box), but no such correspondence between the high-energy states (crossed-out) that are effectively projected out in the limit considered. The correspondence of the low-energy states is guided by matching spin multiplicities. While the relation $\gamma_\sigma \sim d^\dagger_{\bar{\sigma}}$ has aspects of a particle-hole transformation, the fermion parities are different in the two models. The singlet state of the original model (odd fermion parity) corresponds to the vacuum state (even fermion parity) in the $t-J$ representation. Thus, the doubly occupied states of either model have no corresponding states in the other, see the axes with the respective fermion numbers.

and 0 if $\sigma = \mp$. Similarly, acting with $\gamma^\dagger_{j,\sigma}$ on $|\pm\rangle_j$ gives $\left|\overline{\mathrm{BCS}}\right\rangle_j$ which vanishes upon projection. This motivates the definition of new quasifermionic creation operators

$$\Gamma^\dagger_{j,\sigma} = \sigma\sqrt{2}P_j\gamma_{j,\bar{\sigma}}P_j, \tag{3.33}$$

which create the states $|\pm = \sigma\rangle$ from $|s\rangle$. They satisfy

$$\Gamma^\dagger_{j,\sigma}\Gamma^\dagger_{j,\sigma} = 0 = \Gamma_{j,\sigma}\Gamma_{j,\sigma}. \tag{3.34}$$

Due to the forbidden double occupation (i.e. the elimination of the $\left|\overline{\mathrm{BCS}}\right\rangle$ state), these are not proper fermions. In fact, they satisfy the same algebra as the $t-J$ fermions. To see this, consider a local Hamiltonian with forbidden double occupation constraint implemented through infinite onsite potential $U \to \infty$,

$$H_{t-J,j} = V - \frac{3}{4}K - E_{\mathrm{YSR}}\sum_\sigma d^\dagger_{j,\sigma}d_{j,\sigma} + Ud^\dagger_{j,\uparrow}d_{j,\uparrow}d^\dagger_{j,\downarrow}d_{j,\downarrow}. \tag{3.35}$$

Here, the regular fermionic operators $d_{i,\sigma}$ ($d^\dagger_{i,\sigma}$) annihilate (create) a fermion at site i with spin σ. The local low energy spectrum formed by the d-fermions is given by the (spin singlet) vacuum $|\mathrm{vac}\rangle_{t-J,j}$ with energy $V - \frac{3}{4}K = E_o$ and the doublet $|\sigma\rangle_{t-J,j} = d^\dagger_{j,\sigma}|\mathrm{vac}\rangle_{t-J,j}$ with energy $V - \frac{3}{4}K - E_{\mathrm{YSR}} = E_e$. The doubly occupied state $|\downarrow\uparrow\rangle_{t-J,j}$ is eliminated by the projector

$$P_{t-J,j} = |\mathrm{vac}\rangle_{t-J,j}\langle\mathrm{vac}|_{t-J,j} + \sum_\sigma |\sigma\rangle_{t-J,j}\langle\sigma|_{t-J,j}. \tag{3.36}$$

In Fig. 3.6 we illustrate the correspondence of the low energy Hilbert spaces of the single site $t-J$ model and the zero bandwidth model. Note that there is no such correspondence for the high energy states in both models. In App. A.1 we show explicitly that the low energy projected $t-J$ fermions

$$D^\dagger_{j,\sigma} = P_{t-J,j} d^\dagger_{j,\sigma} P_{t-J,j} \tag{3.37}$$

satisfy the same local algebra as the low energy quasifermions of the original model, $\Gamma^\dagger_{j,\sigma}$. Taking into account also the flipped local fermion parity, we arrive at the correspondence given in Eq. (3.30).

So far this discussion may seem abstract and without apparent merit. However, note that the low energy projected impurity spin operators are now also expressed in terms of d-fermions (c.f. App. A.1). In particular, we have the correspondence

$$\mathbf{S}_j \sim \sum_{\sigma\sigma'} \mathbf{s}_{\sigma\sigma'} d^\dagger_{j,\sigma} d_{j,\sigma'}. \tag{3.38}$$

Here, by the symbol $\sim$ we again denote equivalence at the low energy projected level. Thus, the effective $t-J$ model is expressed in terms of (projected) fermions alone, whereas the original model had both spins and fermions.

We now implement the local low energy projection at every site by applying the projection

$$\mathcal{P} = \prod_j P_j, \tag{3.39}$$

where P_j are the local projectors defined by Eq. (3.31). Applying these operators to the Hamiltonian of the chain, $\mathcal{P}H\mathcal{P}$, we obtain

$$\mathcal{P}\sum_j \Bigg[- E_{\mathrm{YSR}} P_{j,\mathrm{BCS}} + \left(V - \frac{3}{4}K\right) P_j - \tilde{t}\sum_\sigma \left(\Gamma_{j,\sigma}\Gamma^\dagger_{j+1,\sigma} + \mathrm{h.c.}\right)$$
$$+ \tilde{\Delta}(-\Gamma_{j,\downarrow}\Gamma_{j+1,\uparrow} + \Gamma_{j,\uparrow}\Gamma_{j+1,\downarrow} + \mathrm{h.c.}) + P_j\mathbf{S}_jP_j \cdot \hat{J} \cdot P_{j+1}\mathbf{S}_{j+1}P_{j+1}\Bigg]\mathcal{P}, \tag{3.40}$$

in terms of the projected operators $\Gamma_{j,\sigma} = \sigma\sqrt{2}P_j\gamma^\dagger_{j,\bar{\sigma}}P_j$. Expressing the single-site projector $P_{j,\text{BCS}}$ in terms of the d operators,

$$P_{j,\text{BCS}} \sim \sum_\sigma d^\dagger_{j,\sigma}d_{j,\sigma} \equiv \sum_\sigma n_{j,\sigma}, \tag{3.41}$$

and introducing the shorthand notation

$$\mathbf{s}_j \equiv \sum_{\sigma\sigma'} \mathbf{s}_{\sigma\sigma'}d^\dagger_{j,\sigma}d_{j,\sigma'}, \tag{3.42}$$

to make obvious the spin-spin nature of interactions, we arrive at the effective model,

$$\begin{aligned} H_{t-J} = \sum_j \Big[&- E_\text{YSR}\sum_\sigma n_{j,\sigma} + Un_{j,\uparrow}n_{j,\downarrow} + \mathbf{s}_j \cdot \hat{J} \cdot \mathbf{s}_{j+1} \\ &- \tilde{t}\sum_\sigma \left(d^\dagger_{j,\sigma}d_{j+1,\sigma} + \text{h.c.}\right) - \tilde{\Delta}\left(d^\dagger_{j,\uparrow}d^\dagger_{j+1,\downarrow} - d^\dagger_{j,\downarrow}d^\dagger_{j+1,\uparrow} + \text{h.c.}\right)\Big], \end{aligned} \tag{3.43}$$

where $U \to \infty$ and we dropped a constant $N\left(V - \frac{3}{4}K\right)$. The equivalence to the original model is expressed as

$$H \sim H_{t-J} \quad \Leftrightarrow \quad \mathcal{P}H\mathcal{P} \equiv \mathcal{P}_{t-J}H_{t-J}\mathcal{P}_{t-J}, \tag{3.44}$$

where $\mathcal{P}_{t-J} = \prod_j P_{t-J,j}$. Eq. (3.43) is similar to the regular $t - J$ model (no double occupation, nearest-neighbor spin interaction), but explicitly includes a pairing term. Furthermore, the spin interaction is not necessarily small and may be ferromagnetic. We hence refer to this model as an effective $t - J$ model. The YSR excitation energy E_YSR now acts as a chemical potential for the d-fermions. We note that periodic boundary conditions in the original model translate to periodic boundary conditions in the effective $t - J$ model for N even, and to antiperiodic boundary conditions for N odd (for both hopping and pairing terms). This is due to the factor of $(-1)^1(-1)^N$ arising from products of γ_N and γ_1 and conjugates and corresponds to a π flux threading the infinite-U Hubbard ring for odd-N chains. Finally note that Eq. (3.43) conserves fermion parity and total spin (for isotropic $\hat{J}$), but not fermion number.

3.2.2 PHASE DIAGRAM

In the language of the effective $t - J$ model screened impurity spins are holes, characterized by the hole density

$$n_\text{holes} = N - \sum_{j,\sigma} n_{j,\sigma}, \tag{3.45}$$

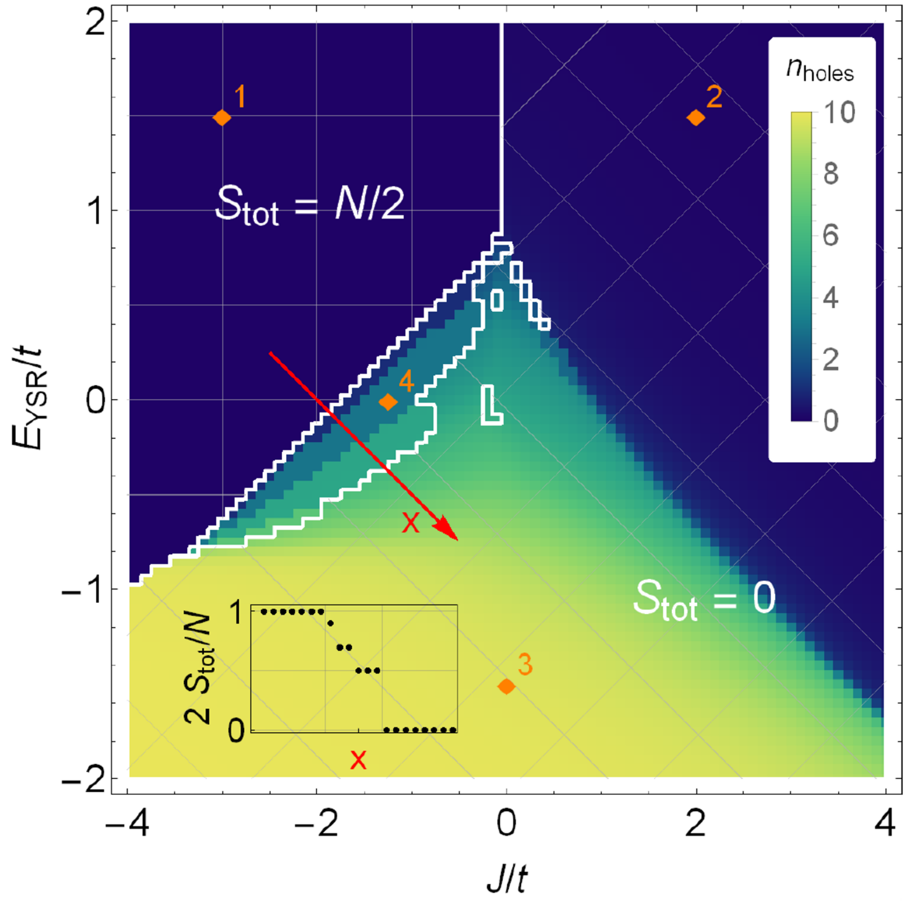

Figure 3.7: Exact-diagonalization results for a chain of $N = 10$ impurity spins ($V = 2\Delta$; $\tilde{t} = 2\tilde{\Delta}$). Phase diagram for a (periodic) chain of quantum spins (with isotropic K) as a function of YSR energy E_{YSR} and isotropic RKKY interaction J, based on the number of holes (screened spins) n_{holes} (color scale) and total spin S_{tot}. White lines delineate borders of maximal/minimal-spin phases, which are indicated by horizontal/tilted mesh. Regions without mesh have intermediate S_{tot}. Figure from [I].

moving in the correlated background of a spin chain described by the RKKY coupling $\hat{J}$. In fact, when coupling individual impurities in the unscreened state (E_{YSR} large and positive, $n_{\text{holes}} = 0$), the system forms a quantum spin-$\frac{1}{2}$ chain subject to RKKY interactions. In contrast, there is only a single low-energy state when coupling impurities in the screened state (E_{YSR} large and negative, $n_{\text{holes}} = N$). For intermediate values of $|E_{\text{YSR}}|$, the impurity spins may neither be all free nor all screened, i.e. $0 < n_{\text{holes}} < N$. Note, however, that the adatom chain gains RKKY energy only when coupling unscreened adatoms, so that RKKY coupling favors the fully unscreened phase. This is the same mechanism that led to the differences in the quantum and classical phase diagrams discussed for the YSR dimer.

In order to substantiate these observations we study the phase diagram of Eq. (3.43) as a function of E_{YSR} and isotropic RKKY interaction $J = J_z = J_\perp$. In this case the Hamiltonian has

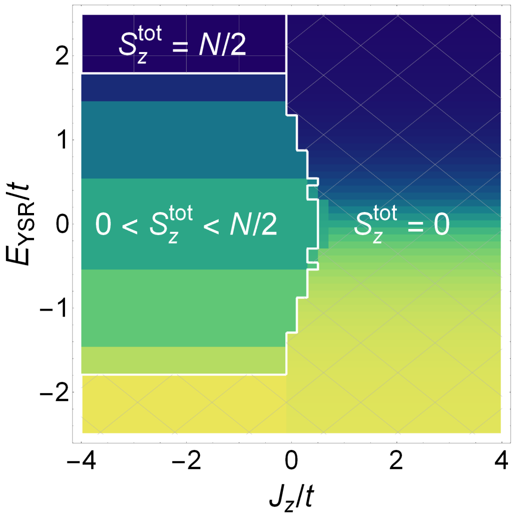

Figure 3.8: Phase diagram for classical (Ising exchange) zero-bandwidth YSR chain, see Sec. 3.2.4 below for details. Figure adapted from [I].

full SU(2) spin rotation symmetry and we may label states by their total spin quantum number S_{tot}, where

$$\mathbf{S}_{\text{tot}} = \sum_j \mathbf{s}_j. \tag{3.46}$$

We will further plot n_{holes} to better understand the nature of the phases. Figure 3.7 shows corresponding exact diagonalization results for a chain of $N = 10$ impurity spins with periodic boundary conditions. For sufficiently large $E_{\text{YSR}} > 0$, the chain has no holes and realizes a spin-$\frac{1}{2}$ Heisenberg chain. As E_{YSR} is reduced, the number of holes increases and eventually becomes equal to N. In this state, all impurity spins are screened and the ground state has $S_{\text{tot}} = 0$.

Figure 3.8 shows a corresponding phase diagram for a chain of classical spins for contrast (see Sec. 3.2.4 below for more details). The classical phase diagram reflects filling of a YSR band. The YSR bands emerging from the positive- and negative-energy YSR states (band energies $\pm E_{\text{YSR}} - \frac{\Lambda}{2} < \epsilon < \pm E_{\text{YSR}} + \frac{\Lambda}{2}$) and overlap when $-\frac{\Lambda}{2} < E_{\text{YSR}} < \frac{\Lambda}{2}$. As E_{YSR} decreases from $\frac{\Lambda}{2}$ to $-\frac{\Lambda}{2}$, the number of holes n_{holes} increases continuously from 0 to N. Here, the bandwidth Λ depends only on the sign, but not on the magnitude of the RKKY coupling.

This contrasts starkly with the strong J-dependence of the phase boundaries for quantum spins. For quantum spins, the RKKY energy contributes only for unscreened spins, so that the Heisenberg phases in which all spins are unscreened are stablized by increasing $|J|$. The physics is reminiscent of the classical picture only near $J = 0$,[1] where n_{holes} varies from 0 to N for $|E_{\text{YSR}}| \lesssim 2\tilde{t}$ [green region in Fig. 3.7].

---

[1] The small isolated regions near $J = 0$ are due to finite-size effects of infinite-U Hubbard physics. They are discussed in Appendix A.2. See also [211].

On the antiferromagnetic side ($J > 0$), the width of the shifted transition region [green in Fig. 3.7] narrows, saturating for larger J. While increasing antiferromagnetic correlations suppress the effect of hopping $\tilde{t}$, the spin-singlet pairing $\tilde{\Delta}$ introduces an uncertainty in n_{holes} which eventually governs the width of the transition region. At the same time, the total spin of the ground state is $S_{\text{tot}} = 0$, regardless of E_{YSR}. As E_{YSR} is reduced, the ground state changes from a total singlet formed by antiferromagnetically coupled impurity spins to a chain of local singlets between impurity spins and conduction electrons.

On the ferromagnetic side ($J < 0$), the transition region rapidly narrows as $|J|$ increases, ultimately giving way to a direct phase boundary between Heisenberg spin chain and fully screened state. This transition is largely insensitive to the spin-singlet pairing $\tilde{\Delta}$ due to the strong spin polarization. Reducing E_{YSR} at smaller $|J|$ eventually introduces holes into the Heisenberg ferromagnet, and the system becomes a metallic ferromagnet. A stepwise increase in the number of holes prompts a corresponding reduction of the total spin S_{tot} from its maximum of $N/2$ [inset in Fig. 3.7]. While this is similar to the classical scenario, S_{tot} jumps discontinuously to zero before the number of holes reaches N. Here, the metallic ferromagnet becomes energetically less favorable than a superconducting phase favored by the spin-singlet pairing $\tilde{\Delta}$. This singlet superconductor has $S_{\text{tot}} = 0$, as do the Heisenberg antiferromagnet and the local-singlet phase at large and negative E_{YSR}. The fine structure of the phase boundaries in Fig. 3.7 reflects finite-size effects related to the infinite-U Hubbard model, see Appendix A.2 and [211].

3.2.3 SPECTRAL FUNCTION

The YSR excitation of one of the adatoms into the screened state, e.g., by tunneling from a scanning tunneling microscope tip, quenches its spin and breaks the adjacent RKKY bonds. The quenched spin is mobile along the chain due to the hybridization of YSR states and propagates in a correlated spin background. This leads to pronounced differences from the classical scenario in the site-resolved single-particle spectral function, c.f. Eq. (2.20). Expressed in terms of the d-fermions, the spin-resolved single-particle spectral function takes the form

$$\begin{aligned} A_{j,\sigma}(E) = \frac{1}{2}\sum_{\lambda}\Bigg\{ \left|\langle\lambda|d^{\dagger}_{j,\sigma}|\text{gs}\rangle\right|^2 \begin{pmatrix} v^2 \\ u^2 \end{pmatrix} + |\langle\lambda|d_{j,\bar{\sigma}}|\text{gs}\rangle|^2 \begin{pmatrix} u^2 \\ v^2 \end{pmatrix} \\ + 2uv\,\text{Re}\left[\langle\lambda|d^{\dagger}_{j,\sigma}|\text{gs}\rangle\langle\text{gs}|d^{\dagger}_{j,\bar{\sigma}}|\lambda\rangle\right] \begin{pmatrix} \sigma \\ -\sigma \end{pmatrix} \Bigg\} \delta(E \mp E_{\lambda} \pm E_{\text{gs}}), \quad (3.47) \end{aligned}$$

where the first row corresponds to $E > 0$ and the second line corresponds to $E < 0$ (with according signs in the delta function). We restrict our discussion to $E > 0$ for concreteness. The first and second terms correspond to the electron and hole spectral functions of the extended $t - J$ model, the last corresponds to the spectral function associated with the anomalous Green function. To obtain the tunneling spectra in Fig. 3.9, we evaluate the matrix elements using

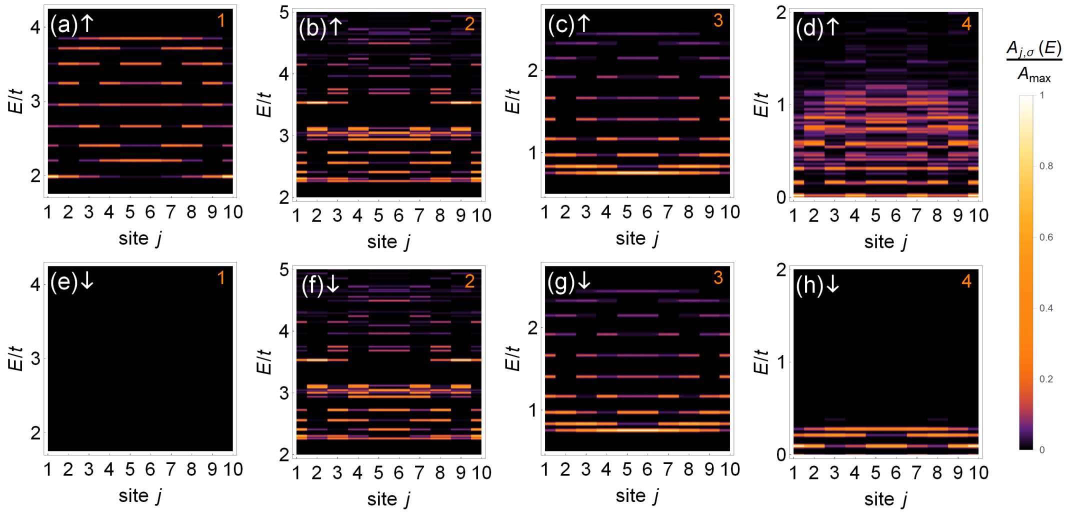

Figure 3.9: Spin-resolved spectral functions $A_{j,\sigma}(E)$ for the parameters indicated by orange markers in Fig. 3.7: numbers in the panels refer to the corresponding labels in the phase diagram in Fig. 3.7. A small magnetic field $B_z = -0.001t$ is included to lift the degeneracy in the ferromagnetically ordered phases, such that the ground state is polarized in the spin-down direction. (a)-(d) show spectral functions for $\sigma =\uparrow$, (e)-(h) for $\sigma =\downarrow$ (see also labels shown in panels). Figure from [I].

the exact-diagonalization wave functions and approximate the δ-function as a Gaussian peak with width $\kappa = 0.01t$ ($\kappa = 0.004t$). The spectra are normalized with respect to their individual maximal values $A_{\text{max}} = \max_{E,j} A_{j,\sigma}(E)$. Thus, the magnitude should not be compared between different plots.

Corresponding exact-diagonalization data for a chain of $N = 10$ impurity spins with open boundary conditions are shown in Fig. 3.9 (a-h). (Corresponding results for classical spins are shown in Fig. 3.11.) First note that the spectra differ between up ($A_\uparrow$) and down spins ($A_\downarrow$) only in the ferromagnetically ordered phases (a) vs. (e) and (d) vs. (h). Note that we include a small magnetic field to break the SU(2) degeneracy towards polarization in the spin-down direction in these cases. In contrast, the spectra are identical in the $S = 0$ phase, see (b) vs. (f), (c) vs. (g).

Probing the Heisenberg spin chain (sufficiently large $E_{\text{YSR}} > 0$), the YSR excitation of one of the impurities screens its spin and induces a mobile hole:

In the ferromagnetic phase [Figs. 3.9 (a) and (e)], such an excitation is only possible if the symmetry broken ground state has opposite spin as the tunneling electron: tunneling into a spin-down background with a spin-down electron has no overlap with the low energy spectrum, see Fig. 3.9 (e). In Fig. 3.9 (a) the excited hole perturbs the spin background only weakly and to a good approximation, its motion is described by a tight-binding chain. Correspondingly, in the lower (upper) half of the hole band, i.e., $2 \lesssim E/t \lesssim 3$ ($3 \lesssim E/t \lesssim 4$), the number of nodes in the spectral function increases (decreases) with energy. Moreover, there is enhanced (reduced) intensity at the ends, since a hole on a boundary site breaks only one rather than two ferromagnetic bonds, inducing a lower site energy. (We note that at finite energy resolution and a small excitation gap, this effect may lead to similar experimental phenomenology as a Majorana zero mode.)

In the antiferromagnetic phase [Figs. 3.9 (b) and (f), identical by symmetry], in contrast, the spectral weight spreads over many more many-body states due to the spin-charge separation in the antiferromagnetic $t - J$ model. This is in stark contrast to the case of classical spins (see Secs. 2.3.3 and 3.2.4, where the spectrum always has single-particle nature).

For a chain of fully screened impurity spins [Fig. 3.9 (c) and (g), identical by symmetry], the YSR excitation unscreens one of the impurity spins. To lowest order, the spectral function can again be understood in terms of a tight-binding band describing the mobile spin, now with uniform site energies throughout the chain. However, unlike in the ferromagnetic phase, the number of spins is no longer a good quantum number due to the effective pairing. The associated redistribution of spectral weight to states with additional spins leads to a reduction in intensity of the single-particle-like spectral peaks with increasing excitation energy.

The metallic ferromagnet has strong similarities with the regime of overlapping YSR bands for classical ferromagnetic textures in the absence of spin-orbit coupling. In particular, it has a gapless excitation spectrum [Fig. 3.9 (d) and (h)]. The spectral function exhibits several nodes even at the lowest energy as holes are already present in the ground state, and becomes dense at higher energies due to the coupling to the particle-hole continuum.

3.2.4 CLASSICAL IMPURITY SPINS

For contrast, this section discusses chains of classical impurity spins in more detail. We have already discussed classical YSR chains in Sec. 2.3.3. Here, we consider classical spins within the zero bandwidth approach to be able to draw more direct comparisons. A chain of classical spin impurities $\mathbf{S}_j$ coupled to a superconducting substrate may be described by the Hamiltonian

$$H = H_{\mathrm{BCS}} + K \sum_j \sum_{\sigma\sigma'} \psi^\dagger_\sigma(x_j) \mathbf{s}_{\sigma\sigma'} \psi_{\sigma'}(x_j) \cdot \mathbf{S}_j + E[\{\mathbf{S}_j\}]. \tag{3.48}$$

Note that unlike in the quantum case, the $\mathbf{S}_j$ are not operators but act on the electrons merely as local Zeeman fields. We assume that the adatom spins couple antiferromagnetically to the substrate electrons, $K > 0$. The configuration of the classical spins minimizes the total energy of the system, and is therefore governed by spin-spin interactions and magnetic anisotropies, which contribute to the energy functional $E[\{\mathbf{S}_j\}]$, as well as the exchange coupling K between adatom spin and substrate electrons.

Figure 3.10 shows representative results for the phase diagram and the spectral functions for classical spins, assuming the Ising-like RKKY interaction

$$E[\{\mathbf{S}_j\}] = J \sum_j S^z_j S^z_{j+1} \tag{3.49}$$

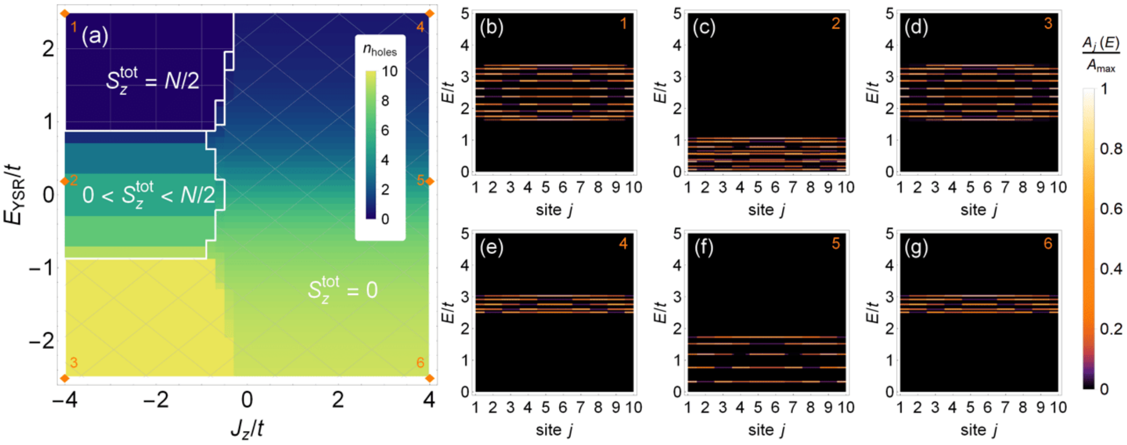

Figure 3.10: Exact diagonalization data for the model in Eq. (3.52) with classical spin and Ising RKKY coupling ($\Delta = 2V$, $N = 10$; Fig. 3.8 shows data for $V = 2\Delta$). (a) Phase diagram analogous to Fig. 3.7. For $\Delta > V$, pairing dominates over kinetic energy, so that the antiferromagnetic phase extends into the $J < 0$ region at small $|E_{\rm YSR}|$. (b - g) Tunneling spectra for $(E_{\rm YSR}, J_z) \in \{(2.5, -4), (0.2, -4), (-2.5, -4), (2.5, 4), (0.2, 4), (-2.5, 4)\}$ [orange diamonds in (a)]. As opposed to the spectral functions for quantum spins, all spectra are single-particle like with $\sim N$ contributing states. Again opposed to quantum spins, the spectral functions are symmetric in energy under $E_{\rm YSR} \to -E_{\rm YSR}$. For ferromagnetic RKKY interaction, (b-d), pairing is ineffective and one observes simple particle-in-a-box states with band-width $4\tilde{t}$. In (c) the band is partially filled and thus the hole and electron spectra overlap. For antiferromagnetic RKKY coupling, (e-g), tunneling is frustrated, but there is still dispersion due to the intersite nature of pairing, with bandwidth $\sim \tilde{\Delta}$. Figure from [I].

for definiteness. The superconductor is treated within the zero-bandwidth approximation, as we do throughout this thesis. Figure 3.10 assumes $\Delta > V$, while Fig. 3.8 includes a corresponding phase diagram with $\Delta < V$.

The phase diagrams and the spectral functions are strikingly different compared to the results for quantum spins shown in Figs. 3.7 and 3.9. In the classical phase diagram, the metallic ferromagnet with S_z intermediate between $N/2$ and 0 extends out to arbitrarily large and negative values of the RKKY coupling J. In contrast, in the case of quantum spins, the metallic ferromagnet appears only up to a maximal J, beyond which there is a direct transition between the ferromagnetic insulator and the fully screened phase. Moreover, while the phase boundaries are independent of J in the classical phase diagram (except at small J), the phase boundaries are strongly dependent on J in the quantum spin case.

These qualitative differences are rooted in two essential differences between the classical and quantum spin models. First, for a given classical spin configuration $\{\mathbf{S}_j\}$, the adatom chain induces a chain of YSR states. The formation of subgap bands can then be discussed within a (single-particle) Bogoliubov-de Gennes approach. There will be partial occupation of the YSR bands as long as they cross the center of the gap. Since the bandwidth is governed by effective hopping terms (energy scale $\tilde{t}$) and the effective pairing terms (energy scale $\tilde{\Delta}$), while being unaffected by J, the partial-filling phases such as the ferromagnetic metal extend out to arbitrarily large values of J in Fig. 3.10 (a), in sharp contrast to the phase diagram for quantum spins in Fig. 3.7.

Second, classical spins are not screened by the electrons in the superconductor. Although classical spins $\mathbf{S}_j$ bind a local quasiparticle when the YSR energy becomes negative, the adatom spin and the bound quasiparticle form a product state,

$$|\psi\rangle = |\{\mathbf{S}_j\}\rangle|\psi_{\mathrm{sc}}(\{\mathbf{S}_j\})\rangle. \tag{3.50}$$

This is in stark contrast to quantum spins, where the screening electrons and the quantum impurity spin form a non-factorizing singlet state. For classical spins, the interaction with other adatom spins will thus remain unaffected when binding or unbinding a quasiparticle. In contrast, spin-$\frac{1}{2}$ quantum spins are effectively screened when binding a quasiparticle. (For higher spins, the adatom spin is reduced by $1/2$ with every channel that binds a quasiparticle.) Screening of the adatom spin is the underlying reason for the dependence of the phase boundary in the quantum spin case. While the energy of the unscreened state is lowered by the RKKY interaction, this is not the case for the screened state.

The single-particle nature of the problem as well as the absence of screening for classical spins also implies that the spectral functions are single-particle-band like, see Fig. 3.10 (b)-(g). This is again in sharp contrast to the result for quantum spins as discussed above. In particular, we find for the case of classical spins that there are no anomalously enhanced or reduced spectral weights at the ends of the chain for ferromagnetic RKKY coupling, and that there is simple band-like behavior for antiferromagnetic RKKY coupling.

For the Ising-like RKKY coupling, we can also make some analytical progress. This energy functional favors spin configurations along the z-axis, so that we can also take the exchange coupling K to be Ising-like. Then, the YSR-energy is

$$E_{\mathrm{YSR}} = \sqrt{\Delta^2 + V^2} - \frac{K_z}{4}. \tag{3.51}$$

Taking the limit $\Delta, V, K \gg J, t$, the full chain is described by the effective Hamiltonian

$$\begin{aligned} H_{\mathrm{eff}} = \mathcal{P} \sum_j \Bigg[& E_{\mathrm{YSR}} \sum_\sigma \gamma^\dagger_{j,\sigma}\gamma_{j,\sigma} - 2\tilde{t} \sum_\sigma \left(\gamma^\dagger_{j,\sigma}\gamma_{j+1,\sigma} + \text{h.c.} \right) \\ & + 2\tilde{\Delta} \left(\gamma^\dagger_{j,\uparrow}\gamma^\dagger_{j+1,\downarrow} - \gamma^\dagger_{j,\downarrow}\gamma^\dagger_{j+1,\uparrow} + \text{h.c.} \right) + E[\{\mathbf{S}_j\}] \Bigg] \mathcal{P}, \end{aligned} \tag{3.52}$$

where $\mathcal{P}$ projects onto the low-energy subspace spanned by the states $|\pm\rangle$, $|\Uparrow, \downarrow\rangle$, and $|\Downarrow, \uparrow\rangle$. Figures 3.8 and 3.10 are obtained by exact diagonalization of this model.

3.2.5 METALLIC FERROMAGNET AND TOPOLOGICAL SUPERCONDUCTIVITY

The metallic ferromagnet can become a topological superconductor for spin-orbit coupled superconductors. Spin-orbit coupling makes the YSR hybridization spin dependent and breaks spin-rotation symmetry. Specifically, we introduce Rashba spin-orbit coupling and anisotropic (Ising-like) RKKY interactions $\hat{J} = \mathrm{diag}(0, 0, J_z)$ polarized perpendicular to the spin-orbit field. Without double-occupation constraint, Ref. [212] studied this model as a paradigm for the interplay of topological superconductivity and interactions.

We assume that the spin chain is aligned along the x-direction with the normal to the surface pointing along the z-direction. This gives the Rashba term

$$H_{\mathrm{SOC}} = -it\alpha \sum_j \left(c_j^\dagger \sigma_y c_{j+1} - \text{h.c.}\right). \tag{3.53}$$

Expressing this in terms of the local Bogoliubov operators given in Eq. (3.16) and performing the replacement Eq. (3.30), we obtain

$$H_{\mathrm{SOC},t-J} = \alpha \sum_j \left[-i\tilde{t}\left(d_j^\dagger \sigma_y d_{j+1} - \text{h.c.}\right) + \tilde{\Delta}\left(d_j^\dagger \sigma_0 d_{j+1}^\dagger + \text{h.c.}\right)\right]. \tag{3.54}$$

Thus, spin-orbit-coupling induces p-wave pairing in the extended $t-J$ model. Note that in the absence of spin order, this does not suffice to open a topological gap. To see this, consider the sum of the hybridization ($H_{t,t-J}$) and spin-orbit terms. This may be written as

$$H_{t,t-J} + H_{\mathrm{SOC},tJ} = \sum_j \left(-d_j^\dagger T_{t-J} d_{j+1} + d_j^\dagger \Delta_{t-J} d_{j+1}^\dagger + \text{h.c.}\right), \tag{3.55}$$

with $T_{t-J} = \tilde{t}(1 + i\alpha\sigma_y)$ and $\Delta_{t-J} = \tilde{\Delta}(1 + i\alpha\sigma_y)(i\sigma_y)$. The tunneling and pairing matrices are phase-locked and no gap opens in the absence of the spin interactions.

We choose Ising RKKY interaction to bypass the Mermin-Wagner theorem, according to which there cannot be spin order for isotropic interactions [212]. Ising RKKY interaction breaks the SU(2) spin rotation symmetry down to a U(1) symmetry corresponding to rotations about the z-axis, so that s_{tot} is no longer conserved but s_{tot}^z still is. Conversely, the spin-orbit coupling, Eq. (3.53), is invariant only under rotations about the y-axis. Thus, for $\alpha > 0$ the model does not have any continuous symmetries anymore which allows broken symmetry at $T = 0$ in principle. We specified to the extreme case of an Ising interaction for simplicity, but the arguments below only require $J_z > J_\perp$. Figure 3.11 (a) shows that the qualitative features of the phase diagram are robust against breaking the spin rotation symmetry. In particular, the ferromagnetic metal phase is maintained. With spin-orbit coupling, see Fig. 3.11 (b), this phase becomes a topological superconductor as we will discuss in more detail below.

We now specify to parameters along the blue cut in Fig. 3.11 (b). Corresponding numerical results are shown in Fig. 3.12 for a chain of $N = 12$ sites with open boundary condi-

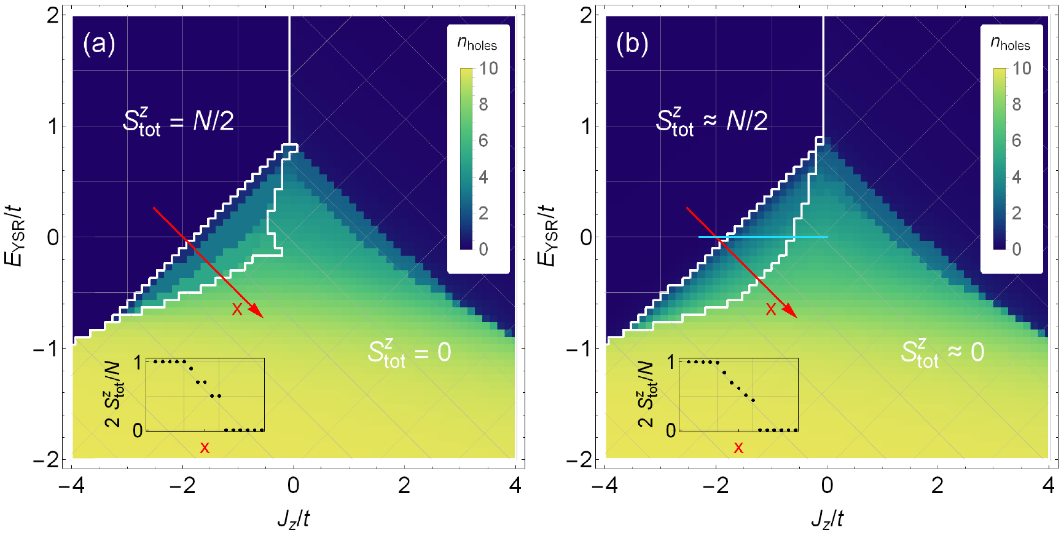

Figure 3.11: Exact-diagonalization results for $N = 10$ chains with Ising RKKY coupling [$J = \mathrm{diag}(0, 0, J_z)$] and periodic boundary conditions, (a) without and (b) with spin-orbit coupling. In (a), the white lines delineate regions of maximum (minimum) s^z_{tot}. In (b), s^z_{tot} is no longer a good quantum number due to spin-orbit coupling. Here, the white lines delineate regions for which s^z_{tot} is within 0.2 of its extremal values 0 and 5. For both (a) and (b), the rough features of the phase diagram are qualitatively similar to the phase diagram for isotropic RKKY interactions shown in Fig. 3.7. On the ferromagnetic side $J_z < 0$, (a) exhibits the metallic ferromagnet (enclosed by the white lines). Across this region, the spin is reduced from its maximal value until the phase boundary to the singlet superconductor is reached (inset). The most striking difference in (b) is the breaking of particle number conservation in the ferromagnetic phases (spin-chain phase and metallic ferromagnet), which reflects the triplet contribution to the pairing. The light blue cut corresponds to the parameter range shown in Figs. 3.12 (a) and (b). Parameters: $V = 2\Delta$, $B_z = -10^{-3}t$, (b) $\alpha = 0.25$. Figure from [I].

tions. Spin-orbit coupling only weakly affects the ferromagnetic insulator at $J_z/t \lesssim -1.8$ or the singlet superconductor at $J_z/t \gtrsim -0.7$, but the spectrum of the metallic ferromagnet ($-1.8 \lesssim J_z/t \lesssim -0.7$) develops a p-wave pairing gap [Fig. 3.12 (a)]. The associated formation of Majorana end states leads to four (up to finite-size corrections) degenerate ground states, a pair of even- and odd- fermion-parity states for each of the two symmetry-broken spin configurations. In line with a topological degeneracy, even- and odd-parity ground states are indistinguishable by the local observables n_{holes} and the total spin projection s^z_{tot} [Fig. 3.12 (b)]. For sufficiently large $|J|$, the p-wave gap [Fig. 3.12 (a)] as well as n_{holes} and s^z_{tot} [Fig. 3.12 (b)] can be well reproduced analytically, using a variational trial state for the metallic ferromagnet and including the spin-orbit coupling into the extended $t-J$ model. The corresponding mean field theory is discussed below. At smaller $|J|$, the analytical description breaks down as it neglects the effects of the singlet pairing $\tilde{\Delta}$. Tunneling spectra clearly reveal the formation of zero-energy Majorana end states protected by a gap [Fig. 3.12 (c)].

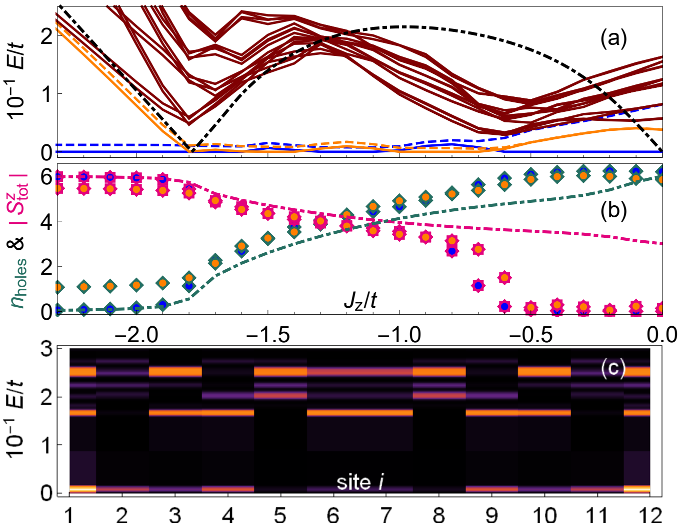

Figure 3.12: Exact-diagonalization results for $N = 12$ chain with Ising RKKY interaction and spin-orbit coupling. (a) Ten lowest-energy eigenstates each vs. RKKY coupling J_z in even- and odd-parity sectors at $E_{\text{YSR}} = 0$, cutting through the metallic ferromagnet. For $-1.8 \lesssim J_z/t \lesssim -0.7$, the four lowest states (even/odd parity: blue/orange) are separated by a topological gap from a continuum of excited states. Black dash-dotted line: Approximate analytical gap, see Eqs. (3.67) and (3.69). (b) Corresponding n_{holes} (green, diamonds) and total magnetization $|S^z_{\text{tot}}|$ (pink, stars). Dash-dotted lines: Analytical results based on trial state. Fillings of symbols color coded as in (a). (c) Tunneling spectra at $J_z = -1.25t$ revealing zero-energy Majorana end states. Parameters: $V = 2\Delta$, spin-orbit coupling $\alpha = 0.25$; a minute Zeeman field $B_z = 10^{-3}t$ singles out spin-polarized states in numerics and induces small intra-parity splittings in ground-state manifold. Figure from [I].

MEAN-FIELD THEORY OF THE METALLIC FERROMAGNET

Topological superconductivity appears in the model of Eq. (3.25) in the parameter region of the metallic ferromagnet. When amending the model by spin-orbit coupling, a p-wave gap can open in this region. Spin-orbit coupling at the level of the model Eq. (3.25) introduces a p-wave-pairing term into the extended $t - J$ model, which does not open a gap in the absence of some form of spin order.

The metallic ferromagnet can be accurately described within a simple Hartree-Fock approach. We specify to ferromagnetic XXZ coupling (with $J_z \geq J_\perp$) and focus on states with maximal spin projection. As double occupation is forbidden, we use a spin-polarized Fermi sea as a variational Hartree-Fock ground state,

$$|\text{FS}, \uparrow\rangle = \prod_{|k|<k_F} d^\dagger_{k,\uparrow}|\text{vac}\rangle, \tag{3.56}$$

in terms of $d_{j,\sigma} = \frac{1}{\sqrt{N}} \sum_k d_{k,\sigma} e^{ikj}$ with $k = \frac{2\pi n}{N} \in [-\pi, \pi]$ and $n \in \mathbb{Z}$ (periodic boundary conditions). The Fermi momentum k_F can be viewed as a variational parameter and the number of holes (screened sites) is given by

$$n_{\text{holes}} = N - \sum_{|k|<k_F} \langle \text{FS}, \uparrow | d^\dagger_{k,\uparrow} d_{k,\uparrow} | \text{FS}, \uparrow \rangle = N\left(1 - \frac{k_F}{\pi}\right). \tag{3.57}$$

Here, the last term on the right hand side takes the thermodynamic limit $N \to \infty$. As the singlet pairing $\tilde{\Delta}$ does not contribute, the Hamiltonian in Eq. (2) implies that this state has energy

$$E_{\text{FS}}(k_F) = \langle \text{FS}, \uparrow | H | \text{FS}, \uparrow \rangle \tag{3.58a}$$

$$= \sum_{|k|<k_F} (-E_{\text{YSR}} - 2\tilde{t} \cos k) + \langle \text{FS}, \uparrow | \sum_j \mathbf{S}_j \cdot J \cdot \mathbf{S}_{j+1} | \text{FS}, \uparrow \rangle. \tag{3.58b}$$

Only the longitudinal exchange coupling J_z contributes to the RKKY interaction and we obtain (for $N \to \infty$)

$$\langle \text{FS}, \uparrow | \sum_j \mathbf{S}_j \cdot J \cdot \mathbf{S}_{j+1} | \text{FS}, \uparrow \rangle = \frac{N J_z}{4\pi^2} (k_F^2 - \sin^2 k_F). \tag{3.59}$$

Altogether, we find the energy

$$\frac{E_{\text{FS}}(k_F)}{N} = -\frac{k_F}{\pi} E_{\text{YSR}} - \frac{2\tilde{t}}{\pi} \sin k_F + \frac{J_z}{4\pi^2}\big(k_F^2 - \sin^2 k_F\big) \tag{3.60a}$$

$$= \int_{-k_F}^{k_F} \frac{\mathrm{d}k}{2\pi}\, \hat{\xi}(k) - \frac{J_z}{4\pi^2}\big(k_F^2 - \sin^2 k_F\big), \tag{3.60b}$$

where we defined the mean-field dispersion

$$\hat{\xi}(k) = -E_{\text{YSR}} - 2\tilde{t} \cos k + J_z \left(\frac{k_F}{2\pi} - \frac{\sin k_F}{2\pi} \cos k \right). \tag{3.61}$$

Minimizing the energy with respect to k_F, we find an implicit expression for k_F and hence the number of holes as a function of the YSR energy E_{YSR} and RKKY interaction J_z,

$$0 = \hat{\xi}(k_F). \tag{3.62}$$

In particular, this expression with $k_F = \pi$ implies that the transition between the Heisenberg spin chain ($n_{\text{holes}} = 0$) and the metallic ferromagnet occurs for

$$E_{\text{YSR}} = 2\tilde{t} + \frac{J_z}{2}. \tag{3.63}$$

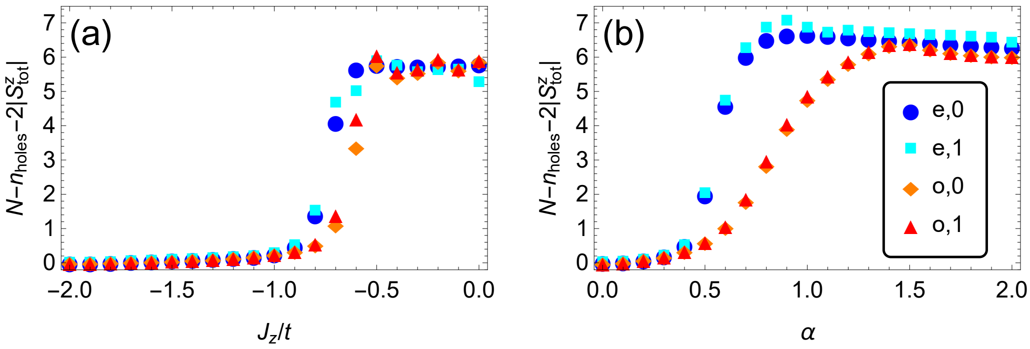

Figure 3.13: Exact-diagonalization data for the deviation from full spin polarization $N - n_\mathrm{holes} - 2|S^z_\mathrm{tot}|$ in a spin-orbit-coupled chain with $N = 12$ sites, with Ising RKKY interactions and open boundary conditions. Blue and cyan markers correspond to two lowest-energy even-parity states (circle, square; labeled by e,0/1), orange and red markers correspond to two lowest-energy odd-parity states (diamond, triangle; labeled by o,0/1). These four states make up the ground-state manifold in Fig. 3.12 (a). The system is approximately spin polarized (deviation from full spin polarization $\simeq 0$) for sufficiently large J_z and sufficiently small α. The latter requirement is due to the tendency of spin-orbit coupling to suppress the spin polarization of the metallic ferromagnet. This delineates the parameter range, for which the spin polarized variational theory developed in this section is adequate. Parameters: $E_\mathrm{YSR} = 0$, (a) $\alpha = 0.25$, (b) $J_z = -1.25t$. As in Fig. 3.12, a small magnetic field $B_z = 10^{-3}t$ along the z-direction was added for numerical reasons. Figure from [I].

This expression can also be understood by noting that the first hole enters at the top of the band at energy $2\tilde{t}$ and breaks two ferromagnetic bonds. Similarly, we find a transition to a fully screened chain ($k_F = 0$) at

$$E_\mathrm{YSR} = -2\tilde{t} \tag{3.64}$$

for negligible pairing $\tilde{\Delta}$. Nonzero pairing preempts the transition from the metallic ferromagnet into the fully screened chain by the formation of a singlet superconducting phase at a finite density of d fermions. This is not captured by the ansatz Eq. (3.56).

Topological phase in mean-field theory

The metallic ferromagnet serves as a parent state for topological superconductivity, which can develop in the presence of spin-orbit coupling. We choose Rashba spin-orbit coupling as defined in Eq. (3.53). To obtain an approximate theory for the topological superconducting phase, we start from the spin-polarized metallic state introduced in the previous section (with k_F determined by $\hat{\xi}(k_F) = 0$) and add p-wave pairing Δ_p. We will discuss the precise form of Δ_p below. This assumes that the ground state remains approximately spin polarized in the presence of weak spin-orbit coupling. This is a good approximation for $J_z \lesssim -t$ and $\alpha \lesssim 0.4t$ as can be inferred from Fig. 3.13. The ground-state energy density is

$$\frac{E_{\mathrm{TSC}}}{N} = \frac{1}{2}\int_{-\pi}^{\pi} \frac{\mathrm{d}k}{2\pi}\left[\hat{\xi}(k;k_F) - \sqrt{\hat{\xi}^2(k;k_F) + \Delta_{\mathrm{p}}^2(k;k_F)}\right] - \frac{J_z}{4\pi^2}\left(k_F^2 - \sin^2 k_F\right). \quad (3.65)$$

and the total spin along the z-direction is

$$s_{\mathrm{tot}}^z = \frac{N}{4}\left[1 - \int_{-\pi}^{\pi} \frac{\mathrm{d}k}{2\pi} \frac{\hat{\xi}(k;k_F)}{\sqrt{\hat{\xi}^2(k;k_F) + \Delta_{\mathrm{p}}^2(k;k_F)}}\right]. \quad (3.66)$$

The excitation gap is given by

$$E_{\mathrm{gap}} = \min_k \sqrt{\hat{\xi}^2(k;k_F) + \Delta_{\mathrm{p}}^2(k;k_F)}. \quad (3.67)$$

It remains to discuss the p-wave pairing. There are two contributions to $\Delta_{\mathrm{p}}(k)$ in the presence of Rashba spin-orbit coupling ($\propto \alpha\sigma_y$): a direct contribution due to spin-orbit coupling and a contribution mediated by virtual spin flips and singlet pairing. The latter is equivalent to the mechanism by which spin-orbit-coupled nanowires proximity couple to an s-wave superconductor and acquire a p-wave gap (in the strong-field limit). To derive this contribution, we assume a large mean field along the positive z-direction,

$$\frac{J_z s_{\mathrm{tot}}^z}{N} \simeq \frac{J_z k_F}{2\pi}. \quad (3.68)$$

Treating the pairing terms in perturbation theory and expanding for small $\alpha\tilde{t}/J_z k_F$, we obtain the effective p-wave pairing

$$\Delta_{\mathrm{p}}(k;k_F) = 4i\tilde{\Delta}\alpha \sin k\left[1 + \frac{2\pi\tilde{t}}{J_z k_F}\cos k\right]. \quad (3.69)$$

The results of this section are illustrated in Fig. 3.12 along with the exact diagonalization data. Panel (a) includes the p-wave gap as determined from Eqs. (3.67) and (3.69) (black, dot-dashed), while panel (b) includes $|s_{\mathrm{tot}}^z|$ and n_{holes} ($= |s_{\mathrm{tot}}^z|/2$ within the spin-polarized ansatz) determined from Eqs. (3.66). k_F is determined by minimizing the normal state energy, Eq. (3.62).

3.3 CONCLUSION

Dilute YSR chains constitute a versatile platform for quantum magnetism. Even for spin-$\frac{1}{2}$ adatoms, we uncover a rich phase diagram described by an extended $t - J$ model. Unlike the standard $t - J$ model, there are no restrictions on the sign of J nor on its strength relative to

t. Tunneling spectra reflect its local spectral function, when accounting for additional pairing correlations.

Spin-$\frac{1}{2}$ impurities are directly realized for magnetic adatoms with one unpaired electron in the valence shell (e.g., Cerium). Importantly, however, the relevant spin is not identical to the bare spin S_0 of the magnetic adatom on the superconducting substrate. Adatoms can bind a quasiparticle in any of the $2S_0$ conduction-electron channels [121]. The effective spin is thus equal to $S_0 - Q/2$, where Q denotes the number of bound quasiparticles, and the extended $t-J$ model can apply to higher-spin impurities, if all but one channel robustly bind a quasiparticle.

More generally, our results exemplify the importance of treating dilute YSR chains as quantum spin chains. Their effective spin depends on the detailed coupling between adatom and substrate, and can conceivably be tuned even for a given system, for instance on gate-tunable superconductors [206] and on Moiré [11] or charge-density-modulated [II, 13] structures. The phenomenology of dilute YSR chains with higher spins is further refined by single-ion anisotropy as well as both intra- and interchannel YSR hybridization.

Unraveling the phenomenology of quantum YSR chains therefore promises important insights into the physics of magnetic adatoms on superconductors. While hybridizing subgap states form YSR bands in models with classical spin textures, we find that subgap spectra exhibit a plethora of qualitatively distinct behaviors depending on the magnetic phase. The quantum magnetism must also inform the search for topological superconductivity and Majorana zero modes in dilute YSR chains. In particular, we find that the parent metallic ferromagnet is limited in scope by competing insulating-ferromagnet and singlet-superconductor phases.

Finally, the physics of dilute YSR chains is not limited to magnetic adatoms, but can also be realized in chains of Coulomb-blockaded quantum dots coupled to a superconductor. Previous theoretical work focused on classical spins [213–215], but recent experiments on double quantum dots construct the elementary unit of quantum YSR chains [216, 217]. When the quantum dots are tuned to odd Coulomb blockade islands, they realize $S = \frac{1}{2}$ spins which can be coupled via a superconducting bulk. This provides a promising complement to recent work [218] on quantum dot arrays as quantum simulators of quantum magnetism.

4 CURRENT-BIASED JOSEPHSON DIODES

The results of this chapter have been published in Refs. [IV, V]. A further publication is in preparation [VI].

Nonreciprocity[1] is essential for many applications in electronics, not least for logical circuits. The fundamental nonreciprocal circuit element is the diode [219, 220], characterized by high resistance for one current direction and low resistance for the other.

Recently nonreciprocal behavior has been demonstrated in a range of experiments on layered superconductors [128–135]. In particular, it was shown that the bulk critical current may depend on the direction of the current flow if the system breaks time-reversal and inversion symmetries [221–225]. This development has potential to boost superconducting electronics applications [128, 136].

Josephson junctions are of particular interest for applications e.g. in a superconducting quantum computing architecture [127]. Indeed, nonreciprocal behavior was observed in a number of different current-biased Josephson systems [136–144]. A version of the Josephson diode can already be understood in terms of the Josephson current-phase relation,

$$I_s(\varphi) = \frac{2e}{\hbar}\frac{\partial F}{\partial \varphi}. \tag{4.1}$$

We have seen in Sec. 2.2 that inversion or time-reversal symmetry implies an antisymmetric current-phase relation. If both of these symmetries are absent, the current-phase relation can in principle have a global maximum $I_{c,+} \equiv \max_\varphi I_s(\varphi)$ and minimum $I_{c,-} \equiv -\min_\varphi I_s(\varphi)$ of different magnitude. These are the maximum equilibrium currents that can be passed through the junction in positive or negative current direction. For bias currents outside this range equilibrium breaks down and a voltage develops. Thus, $I_{c,\pm}$ are the critical currents of the junction and generically nonreciprocal, $I_{c,+} \neq I_{c,-}$, once inversion and time-reversal symmetry are broken. This is the simplest manifestation of the Josephson diode effect. Previous theoretical work has discussed numerous situations in which both of these symmetries are broken, exploring microscopic mechanisms that lead to a nonreciprocal bulk supercurrent [145–152].

However, junctions in the weak-damping regime are hysteretic as shown in Fig. 4.1: When increasing (lowering) the bias current I_b from zero, the junction switches from the supercurrent state into the resistive state at the switching current $I_{\mathrm{sw},+}$ ($I_{\mathrm{sw},-}$). The resistive state is charac-

---

[1] In this context, by nonreciprocity we understand the dependence of properties of electronic elements on voltage sign or current direction.

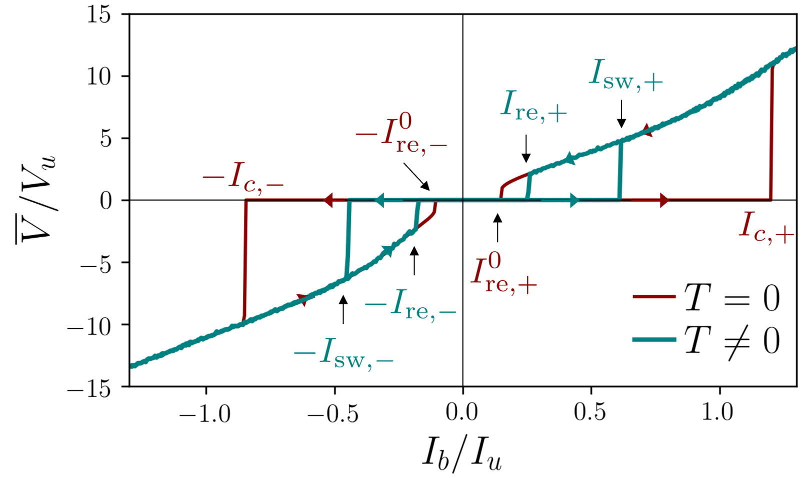

Figure 4.1: Hysteresis loop in the voltage signal as function of bias current sweep, both in the absence (temperature $T = 0$, red trace) and in the presence ($T = 0.1E_u$, green trace) of current noise. The bias current I_b is ramped up and down at rate $dI_b/dt = 10^{-5}I_u/t_u$ and the voltage $\overline{V}$ is averaged over a period of $600t_u$. The characteristic currents of the junction, i.e. the critical currents $I_{c,\pm}$, noiseless retrapping currents $I^0_{\mathrm{re},\pm}$, switching currents $I_{\mathrm{sw},\pm}$ and retrapping currents $I_{\mathrm{re},\pm}$, are in general nonreciprocal if the current-phase relation and dissipative current are asymmetric. Here, we used the asymmetric current-phase relation and asymmetric dissipative current shown in Fig. 4.2. Note that $I_{\mathrm{sw},\pm}$ and $I_{\mathrm{re},\pm}$ are stochastic quantities and fluctuate between sweeps. Here, we simply show a typical trajectory.

terized by a finite voltage $\overline{V} \neq 0$, where the bar denotes an appropriate time average. Due to fluctuation-induced transitions the switching currents are smaller than the critical currents, $I_{\mathrm{sw},\pm} < I_{c,\pm}$. Conversely, when decreasing (increasing) the bias level again the junction retraps into the supercurrent state with $\overline{V} = 0$ only at a smaller retrapping current $I_{\mathrm{re},+}$ ($I_{\mathrm{re},-}$). In such hysteretic junctions nonreciprocity can appear in both the switching and retrapping currents.

While in the majority of experiments on the Josephson diode effect nonreciprocity is more pronounced in the switching current [136, 140, 142, 144], a recent experiment of our collaborators in the Franke group exhibited dominant asymmetry in the retrapping currents of an atomic-scale Josephson junction [V]. The observed nonreciprocity was shown to be crucially dependent on the species of adatom placed in the junction region. We will discuss this in more detail in Sec. 4.5 below. Crucially, the single-atom junction is time-reversal symmetric, ruling out a description in terms of Eq. (4.1) alone. We demonstrate, that it is instead the particle-hole symmetry breaking induced by magnetic impurities which gives rise to the nonreciprocity. We note that Wu et al. [136] also report a Josephson diode effect absent any time-reversal breaking fields. It is at this point unclear what the origin or mechanism leading to nonreciprocity is in their case.

In order to determine the origin of nonreciprocity in the absence of time-reversal symmetry breaking, and in order to understand the distinct mechanisms leading to nonreciprocal switching and retrapping, we developed a general theory of current-biased Josephson diodes, describing in detail the microscopic origin of nonreciprocities and their effect on the diode behavior of the characteristic currents of the junction [IV]. In particular, we found that — as expected —

dominant nonreciprocity in the switching current results from an asymmetric current-phase relation, requiring broken time-reversal symmetry. Strikingly though, dominant nonreciprocity in the retrapping currents results from an asymmetric dissipative current, which may be traced back to broken particle-hole symmetry rather than time-reversal symmetry. Conversely, we show that in the limit of weak damping or low temperatures, asymmetry in the current-phase relation has only weak effect on the retrapping currents, and asymmetry in the dissipative current has only weak effects on the switching currents. This is against the common wisdom that if a symmetry is broken, generically all response is asymmetric. This correspondence is the main result of this chapter. We summarize it here:

$$I_s(\varphi) \neq -I_s(-\varphi) \text{ \& } I_d(V) = -I_d(-V) \quad \longleftrightarrow \quad I_{\text{sw},+} \neq I_{\text{sw},-} \text{ \& } I_{\text{re},+} \simeq I_{\text{re},-}, \tag{4.2a}$$

$$I_s(\varphi) = -I_s(-\varphi) \text{ \& } I_d(V) \neq -I_d(-V) \quad \longleftrightarrow \quad I_{\text{sw},+} \simeq I_{\text{sw},-} \text{ \& } I_{\text{re},+} \neq I_{\text{re},-}. \tag{4.2b}$$

Here, $I_d(V)$ is the dissipative current. The approximate equalities become exact in the low damping or low temperature regime.

Our analysis proceeds in several steps: First, we extend the RCSJ model, which was introduced in Sec. 2.2, to nonreciprocal expressions for the supercurrent as well as the dissipative current. We then demonstrate the correspondence given in Eq. (4.2) numerically, based on purely phenomenological expressions for I_s and I_d. In order to corroborate our numerical findings, we develop an analytical understanding of the Josephson diode effect in the absence (Sec. 4.2) and presence of fluctuations (Sec. 4.3), establishing the correspondence between current-phase asymmetry and nonreciprocal switching currents, as well as between asymmetric dissipation and nonreciprocal retrapping currents within the framework of the Fokker-Planck equation. In Sec. 4.4 we then derive the extended RCSJ equation from a microscopic model of a tunneling junction within a streamlined Ambegaokar-Eckern-Schön approach [226, 227], putting the previous phenomenological considerations on sound footing. Finally, in Sec. 4.5 we present in detail a physical example of a Josephson diode with dominant nonreciprocity in the retrapping currents: the single-atom Josephson junction featured in the experiment by Trahms et al. [V]. In particular, we present phenomenological simulations that, when accounting for frequency dependent damping [228], reproduce the experimental results and thereby demonstrate the quality of our theoretical considerations. Finally, we stress that, despite the fact that our considerations are motivated by the experiment on single-atom Josephson junctions, our theoretical results have general bearing and should prove useful for interpretation of experiments on Josephson diodes.

4.1 RCSJ MODEL FOR JOSEPHSON DIODES AND NUMERICAL RESULTS

The conventional RCSJ model was introduced in Sec. 2.2. It is completely symmetric with respect to negation of both currents and voltages and therefore predicts reciprocal characteristic currents. If the relevant symmetries are absent nonreciprocal behavior can enter through

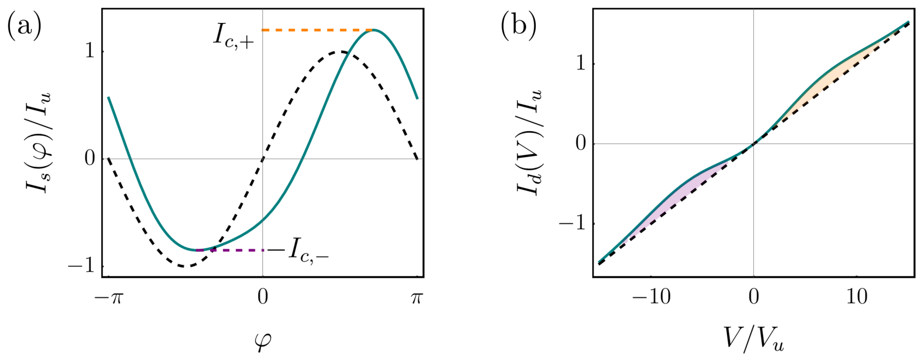

Figure 4.2: Dimensionless phenomenological (a) current-phase relations and (b) dissipative currents used in this section to illustrate effect of nonreciprocities on the behavior of the characteristic currents of a Josephson junction. Green traces correspond to asymmetric currents defined in App. B.2, while black curves correspond to standard RCSJ expressions [sinusoidal current-phase relation and ohmic dissipative current].

all components of the RCSJ model, i.e. through the capacitive I_{cap}, dissipative I_d, and supercurrent I_s terms in Eq. (2.13). Misaki and Nagaosa [153] considered nonlinear contributions to the quantum capacitance and demonstrated resulting nonreciprocities in the characteristic currents. However, asymmetric contributions to the quantum capacitance require differing density of states on the two sides of the junction. In practice it is to be expected that these contributions are dominated by the geometric capacitance (unless the densities of states are very small). Furthermore, current experimental platforms consider junctions with electrodes formed from identical materials, ruling out the aforementioned mechanism. Hence, we disregard this option here and concentrate on nonreciprocities originating in the supercurrent and the dissipative current by allowing for general (possibly asymmetric) current-phase relations $I_s(\varphi)$ and dissipative currents $I_d = I_d(V)$. The dynamics of the phase may then be described by a generalized RCSJ-Langevin equation [228, 229]

$$\tfrac{\hbar}{2e}C\ddot{\varphi} + I_d(\tfrac{\hbar}{2e}\dot{\varphi}) + I_s(\varphi) + \delta I = I_b. \tag{4.3}$$

The correlator of the current fluctuations

$$\langle \delta I(t)\delta I(t')\rangle = K(\tfrac{\hbar}{2e}\dot{\varphi}(t))\delta(t-t') \tag{4.4}$$

is related to the the dissipative current by the fluctuation-dissipation theorem. Provided temperatures are sufficiently low, this implies the nonlinear Johnson-Nyquist noise

$$K(V) = 2T\frac{I_d(V)}{V}. \tag{4.5}$$

For details, see Sec. 4.3.1 below. As the noise power depends on the voltage, Eq. (4.3) is ambiguous as is [230]. As we obtain the extended RCSJ equation from a stochastic field integral (see

Sec. 4.4) we have to employ the Ito definition of stochastic differential equations [231]. Eq. (4.3) describes the dissipative and diffusive motion of a phase particle in a tilted washboard potential

$$U(\varphi) = U_s(\varphi) - \frac{\hbar}{2e} I_b \varphi, \text{ with } I_s(\varphi) = \frac{2e}{\hbar}\frac{\mathrm{d}}{\mathrm{d}\varphi} U_s(\varphi). \tag{4.6}$$

We choose the integration constant such that $\int_0^{2\pi} \mathrm{d}\varphi \, U_s(\varphi) = 0$. Furthermore, to avoid unnecessary complications, we restrict attention to potentials $U_s(\varphi)$ with a single minimum (φ_s^{min}) and maximum (φ_s^{max}) per period $\varphi \in [0, 2\pi)$. This implies that also $U(\varphi)$ has one minimum (φ^{min}) and maximum (φ^{max}) per period as long as the absolute bias current is below the critical currents of the junction. More precisely, the minimum and maximum remain for

$$- I_{c,-} < I_b < I_{c,+}, \tag{4.7}$$

where $-I_{c,-} < 0$ is the minimum and $I_{c,+} > 0$ is the maximum of the current-phase relation $I_s(\varphi)$.

Before we proceed with the discussion of the extended RCSJ model, we introduce dimensionless variables. We will use lower-case letters to denote the dimensionless variables while dimensionful variables are denoted by upper-case letters (with the exception of time). We use the plasma frequency at zero bias as characteristic frequency scale. The plasma frequency is

$$\Omega_p = \sqrt{\frac{4e^2 U''(\varphi^{\mathrm{min}})}{\hbar^2 C}} = \Omega_p(I_b). \tag{4.8}$$

The units of time, energy, voltage and current are thus

$$t_u = \Omega_p^{-1}(0), \; E_u = U''(\varphi_0^{\mathrm{min}}) = \frac{\hbar^2 C}{4e^2}\Omega_p^2(0), \; V_u = \frac{\hbar\Omega_p(0)}{2e}, \; I_u = \frac{\hbar C}{2e}\Omega_p^2(0), \tag{4.9}$$

with corresponding times $\tau = t/t_u$, frequencies $\omega = \Omega/\Omega_p(0)$, energies $\varepsilon = E/E_u$, potentials $u = U/E_u$, temperature $\theta = T/E_u$, voltages (or phase velocities) $v = V/V_u$ and currents $i = I/I_u$. In these units, the extended RCSJ model becomes

$$\partial_\tau^2 \varphi + i_d(\partial_\tau \varphi) + i_s(\varphi) + \delta i = i_b, \tag{4.10}$$

where $i_d(v) = I_d(V = V_u v)/I_u$, with noise correlator

$$\langle \delta i(\tau) \delta(i\tau') \rangle = k(v(\tau))\delta(\tau - \tau'), \quad k(v) = 2\theta \frac{i_d(v)}{v}. \tag{4.11}$$

For a sinusoidal current-phase relation $I_s(\varphi) = (2eE_J/\hbar)\sin\varphi$, $E_u = E_J$, and hence energies are measured in terms of the Josephson energy E_J, while currents are measured in terms of the critical current $I_u = I_c = 2eE_J/\hbar$. Finally, an ohmic dissipative current has the dimensionless

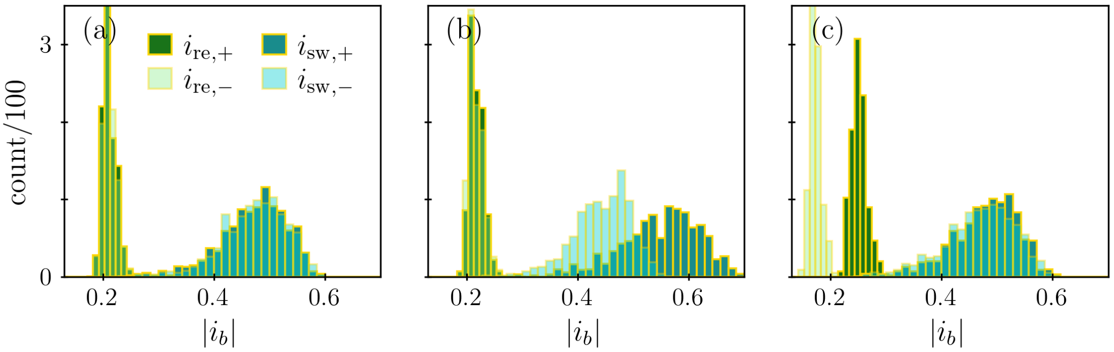

Figure 4.3: Histograms of switching and retrapping currents for 1000 bias current sweeps with (a) symmetric current-phase relation and dissipative current [conventional RCSJ model], (b) asymmetric current-phase relation, $i_s(\varphi) \neq -i_s(-\varphi)$, but symmetric dissipative current, $i_d(v) = -i_d(-v)$, and (c) asymmetric $i_d(v)$, but symmetric $i_s(\varphi)$. We use the ramprate $di/d\tau = 10^{-5}$ and the temperature $\theta = 0.1$. See Fig. 4.2 for the current-phase relations and dissipative currents used here, or see App. B.2 for an explicit definition of the functions $i_s(\varphi)$ and $i_d(v)$. Figure from [IV].

form $i_d(v) = gv$ in terms of the dimensionless conductance $g = [RC\Omega_p(0)]^{-1}$. See App. B.1 for more details.

First evidence for the correspondence between current-phase asymmetry and switching currents asymmetry as well as between dissipative current and retrapping currents given in Eq. (4.2) comes from straightforward numerical integration of the Langevin equation Eq. (4.10). To this end, we implement bias current sweeps such as the one shown in Fig. 4.1 within the Langevin equation, and extract the characteristic currents numerically. We perform this for the standard RCSJ model [$i_s(\varphi)$ and $i_d(v)$ given by black dashed traces in Fig. 4.2 (a) and (b), respectively], the case of asymmetric current-phase relation [$i_s(\varphi)$ given by green trace in Fig. 4.2 (a) and $i_d(v)$ given by black dashed trace in Fig. 4.2 (b)] and the case of asymmetric dissipation [$i_s(\varphi)$ given by black dashed trace in Fig. 4.2 (a) and $i_d(v)$ given by green trace in Fig. 4.2 (b)].

Resulting histograms for the switching and retrapping currents are shown in Fig. 4.3. As to be expected, the histograms are independent of the direction of the bias current i_b for the conventional RCSJ model [Fig. 4.3 (a)]. When the junction has an asymmetric current-phase relation but symmetric dissipative current, only the switching currents are nonreciprocal [Fig. 4.3 (b)]. Conversely, for asymmetric dissipative current, but symmetric current-phase relation, only the retrapping currents are nonreciprocal [Fig. 4.3 (c)].

4.2 DETERMINISTIC JOSEPHSON DIODES

We now aim to develop an analytical understanding of the switching and retrapping process within the extended RCSJ model. To this end, consider first deterministic motion. The pres-

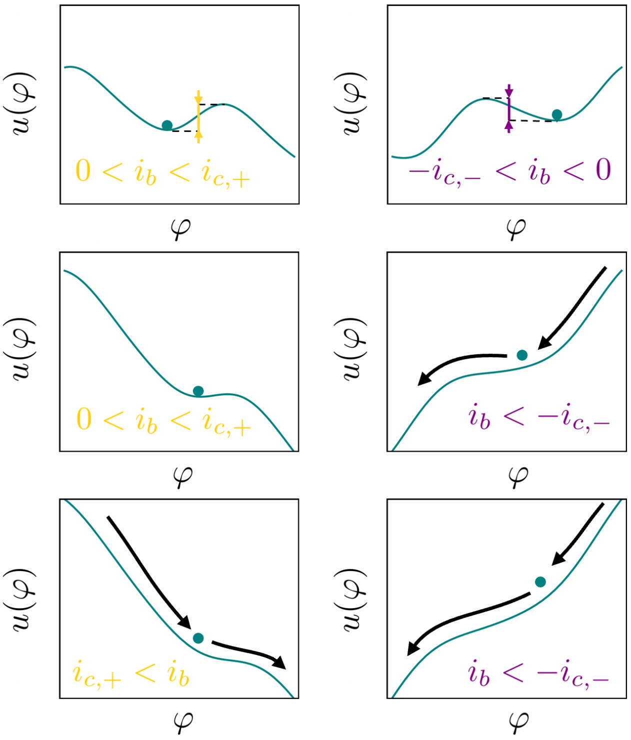

Figure 4.4: Mechanism of switching in the tilted washboard picture. The positive and negative bias cases are shown in the left and right columns. In the first line, the absolute bias level is smaller than the critical currents and the phase particle is trapped in a potential minimum for both bias directions. In the second line, the absolute bias level has been increased to the point where the minimum has appeared for negative bias direction, so that the phase particle is no longer trapped and develops an average velocity. In other words, the junction has switched to the resistive state. Due to asymmetry in the current-phase relation, the minimum still survives for positive bias direction, and the junction remains superconducting. In the third line the junction has switched also for positive bias.

ence of a minimum at finite bias implies that the junction can support a supercurrent: in the absence of noise Eq. (4.10) then has the stable zero-voltage solution

$$\varphi(\tau) = \varphi^{\min}, \quad v(\tau) = 0, \tag{4.12}$$

with $i_b = i_s(\varphi^{\min})$, where we used that $i_d(0) = 0$. The steady state solution Eq. (4.12) is also referred to as the *trapped state*, as it corresponds to a phase particle trapped in a minimum of the washboard potential. If the bias level i_b is increased adiabatically, the junction remains in the trapped state, until the bias reaches the critical currents. Here, the phase particle is released, and develops an average velocity, i.e. the junction switches to the resistive state. Thus in the noiseless case, the switching currents equal the critical currents. If $i_{c,+} \neq i_{c,-}$ at certain bias levels the junction can support a supercurrent only for one bias direction. This is the simplest realization of the Josephson diode effect that was discussed already in the introductory text to this chapter. We illustrate the mechanism within the tilted washboard picture in Fig. 4.4.

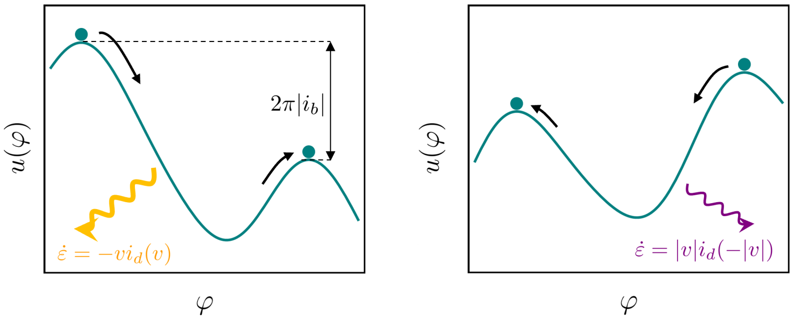

Figure 4.5: Mechanism of retrapping in the tilted washboard picture. Left panel corresponds to positive, right panel to negative bias level (of different magnitude). The bias levels are tuned to the points where the potential energy gain $2\pi|i_b|$ is exactly balanced by the dissipated energy $\int \mathrm{d}t\dot{\varepsilon}$ for the limiting trajectory that starts on a maximum with zero velocity. These points correspond to the retrapping currents $i^0_{\mathrm{re},\pm}$. Here, the dissipative current and hence the dissipation rate is asymmetric such that the limited balanced situation arises at different bias levels, corresponding to nonreciprocity in the retrapping currents.

For sufficiently large bias currents there is a distinct steady state characterized by nonvanishing average voltage. For $|i_b| \gg i_{c,\pm}$, we can neglect the supercurrent, and Eq. (4.3) has the finite-voltage steady state solution

$$\varphi(\tau) \simeq \varphi_0 + v_d\tau, \quad v(\tau) \simeq v_d, \tag{4.13}$$

with $i_d(v_d) = i_b$. This is referred to as *running state* as the phase particle is running down the washboard potential at a finite average speed. The running state persists also to lower bias levels but its trajectory deviates from the simple form given in Eq. (4.13). It is characterized by $v(\tau + \tau_P) = v(\tau)$ and $\varphi(\tau + \tau_P) = \varphi(\tau) \pm 2\pi$, where τ_P is the period of the motion and $\pm = \operatorname{sign} i_b$, and, as a consequence, by the balance of energy gain due to the tilted potential and the dissipated energy per period,

$$\varepsilon_d\big|_{\mathrm{run}} = -\int_0^{\tau_P} \mathrm{d}\tau \, \frac{\mathrm{d}}{\mathrm{d}\tau}\varepsilon = u(\varphi) - u(\varphi \pm 2\pi). \tag{4.14}$$

Here, $u(\varphi) - u(\varphi \pm 2\pi) = 2\pi|i_b|$, and the energy of the junction is defined as

$$\varepsilon = \frac{1}{2}v^2 + u(\varphi). \tag{4.15}$$

The first term is simply the dimensionless version of the capacitive term $CV^2/2$. Explicitly, in the running state ε_d takes the form

$$\varepsilon_d\big|_{\mathrm{run}} = \int_0^{\tau_P} \mathrm{d}\tau \, v_{\mathrm{run}}(\tau) i_d(v_{\mathrm{run}}(\tau)) = \int_0^{\pm 2\pi} \mathrm{d}\varphi \, i_d(v_{\mathrm{run}}(\varphi)), \tag{4.16}$$

where $v(\varphi)$ is the unique periodic solution to

$$\frac{\mathrm{d}v}{\mathrm{d}\varphi} = -\frac{u'(\varphi) + i_d(v)}{v}. \tag{4.17}$$

In App. B.3 we solve this equation in the regime of weak damping. The solution may be expanded as

$$v_{\mathrm{run}}(\varphi) = v_d - \frac{u_s(\varphi)}{v_d} + \mathcal{O}\big(v_d^{-3}\big). \tag{4.18}$$

The retrapping currents $i^0_{\mathrm{re},\pm}$ correspond to the positive/negative bias level at which the running state disappears. This point is reached when the running state trajectory passes through the unstable fixed point $[\varphi = \varphi^{\max}, v = 0]$. Now, if the phase particle is initialized at $\varphi^{\max}$ it only reaches $\varphi^{\max} \pm 2\pi$ after infinite time, $\tau_P \to \infty$. This gives the criterion

$$i^0_{\mathrm{re},\pm} = \int_0^{\pm 2\pi} \frac{\mathrm{d}\varphi}{2\pi}\, i_d(v_0(\varphi)), \tag{4.19}$$

where $v_0(\varphi)$ is the critical running state trajectory with $v_0(\varphi^{\max}) = 0$ and $\pm = \operatorname{sign} i_b = \operatorname{sign} v_0(\varphi)$. Note that also the right side of the equation implicitly depends on $i^0_{\mathrm{re},\pm}$ through the running state trajectory $v_0(\varphi)$. However, in the limit of weak damping, $i_d(v)/v \ll 1$, we may approximate

$$i^0_{\mathrm{re},\pm} \simeq \int_0^{\pm 2\pi} \frac{\mathrm{d}\varphi}{2\pi}\, i_d\Big(\pm\sqrt{2[u_s(\varphi_s^{\max}) - u_s(\varphi)]}\Big), \tag{4.20}$$

at leading order in i_d. Here, we used that to zeroth order in $i_d(v)$ and $i_b \sim i_d(v)$, the trajectory $v_0(\varphi)$ can be obtained through conservation of energy along the separatrix of the undamped problem at $i_b = 0$. Note that Eqs. (4.19) and (4.20) are manifestly asymmetric if the dissipative current is asymmetric as the velocity has definite sign. Furthermore, in the low damping regime, the asymmetry of the current-phase relation enters only through $u_s(\varphi)$ and hence is integrated out in the expression for the retrapping current. This corresponds to the time-reversal invariance of the mechanical equations of motion. The mechanism leading to retrapping is illustrated in Fig. 4.5.

With this we can establish a criterion for hysteresis. We call the junction *overdamped* if $i^0_{\mathrm{re},\pm} = i_{c,\pm}$. In this case, there is no hysteresis and switching and retrapping occur at the same point. Conversely, in *underdamped* junctions, the running state persists to bias currents lower than the critical current. Underdamped junctions are bistable in the bias ranges $i_{\mathrm{re},0,+} < i_b < i_{c,+}$ and $-i_{\mathrm{re},0,-} > i_b > i_{c,-}$: at the same bias level, the junction can either support a supercurrent without any voltage drop, or it supports a dissipative state, depending on the initialization. This implies hysteresis as seen for instance in Fig. 4.1.

Furthermore, we have established the correspondence between current-phase asymmetry and nonreciprocity in the switching currents as well as the correspondence between asymmetry in

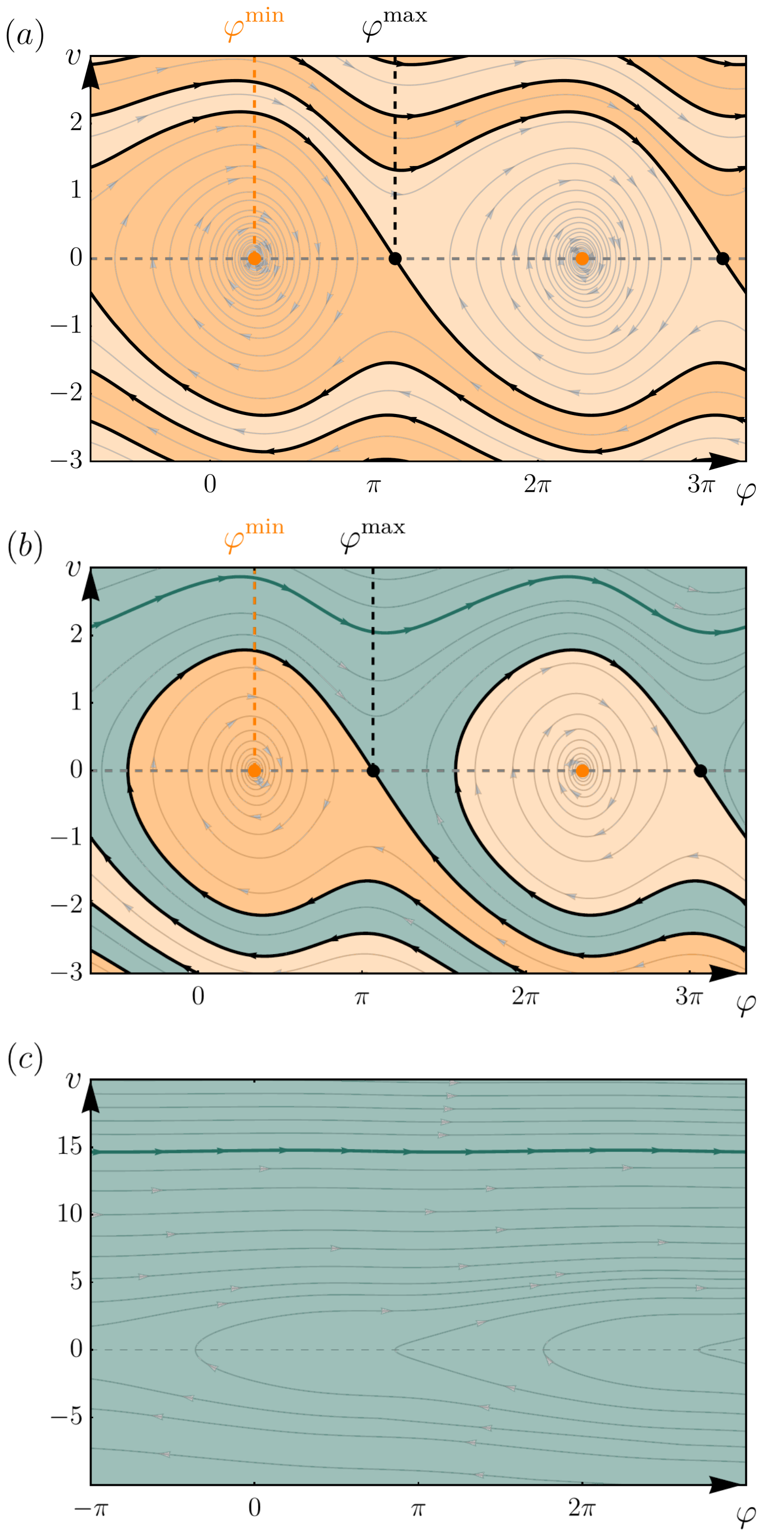

Figure 4.6: Phase space of extended RCSJ model for (a) $i_b = 0.05$, (b) $i_b = 0.3$, (c) $i_b = 1.5$, and asymmetric current-phase relation and dissipative current from Fig. 4.2.

the dissipation and nonreciprocity in the retrapping currents in the noiseless case (and provided the damping is weak). In the following we will show that these results are robust against noise. Before we consider the noisy dynamics, it is helpful to visualize the deterministic dynamics in phase space $[\varphi, v]$. This is shown in Fig. 4.6 for three positive bias levels, ignoring nonreciprocities for the moment.

For weak bias $I_b < I_{\mathrm{re}}^0$ [Fig. 4.6 (a)] the only fixed points of the dynamics are the trapped states $[\varphi^{\min} + 2\pi n, 0]$, with n integer. Each such point has an associated attractive region in phase space (colored orange, with lighter and darker shading), wherein any trajectory converges to the corresponding fixed point. The boundaries between these attractive regions are separatrices passing through the unstable fixed point $[\varphi^{\max}, 0]$ (black traces). Noise-induced transitions between the attractive regions correspond to phase diffusion.

Once the bias reaches $I_{\mathrm{re}}^0 < I_b$ [Fig. 4.6 (b)], the phase space topology abruptly changes and a new steady state emerges, the running state, drawn here in dark green. Its attractive region is shaded accordingly.[2] Now, the junction is bistable. If the temperature is sufficiently low, there is a separation of timescales and we may assume that the system equilibrates within a given attractive region. Everytime the noise drives the system across the separatrix it equilibrates in another trapped state. This transition corresponds to switching and retrapping in the noisy case. The rate is related to the probability current across the separatrix between trapped and running states (black traces). Note that this shows that phase diffusion is not compatible with hysteresis: Different trapped states are separated by the attractive region of the running state and hence no direct transition between the trapped states is possible without switching. This changes if the damping is strongly frequency dependent [228]. Furthermore, note that the separatrices still pass through the unstable fixed points. The critical trajectory in Eq. (4.19) is along such a separatrix at exactly the point when the bias is so low that two neighboring separatrices touch at an unstable fixed point. Here, the phase space picture resembles that of an undamped pendulum: damping and driving force exactly balance each other at the separatrix. In particular, in the weak damping approximation for the retrapping current, Eq. (4.20), the separatrix is thus just that of the undamped pendulum.

Finally, once $I_c < I_b$ [Fig. 4.6 (c)] the attractive regions of the trapped states have shrunk away, and the running state is the only steady state of the system.

4.3 NOISE-AFFECTED JOSEPHSON DIODES

We focus now on the bistable regime of Fig. 4.6 (b). In the presence of noise, the system transits between the trapped and running state. In order to extract the transition rates analytically we employ the Fokker-Planck equation associated to the stochastic dynamics of Eq. (4.10). It is

$$\frac{\partial}{\partial \tau} p = \left\{ -v \frac{\partial}{\partial \varphi} + \frac{\partial}{\partial v} \left[u'(\varphi) + i_d(v) + \frac{1}{2} \frac{\partial}{\partial v} k(v) \right] \right\} p \equiv \mathcal{L} p, \tag{4.21}$$

---

[2] We will use the terms trapped and running state for both the attractive region as well as the attractors, i.e. the steady states.

where $p = p(\tau; \varphi, v)$ is the probability density to find the system at the phase-space point (φ, v) at time τ, given initial data $p(\tau_0; \varphi_0, v_0)$. We also defined the forward Fokker-Planck operator $\mathcal{L}$. From the transition rates corresponding to the switching and retrapping process we can then infer the switching and retrapping current.

Before we get to that, we will briefly show that our choice of noise correlations $k(v) = 2\theta i_d(v)/v$ is consistent with detailed balance. This is relevant, as in the literature sometimes the static nonlinear conductance $g_s(v) = i_d(v)/v$ is replaced by the differential nonlinear conductance $g_d(v) = \mathrm{d}i_d(v)/\mathrm{d}v$ [228].

4.3.1 EQUILIBRIUM DISTRIBUTION AND DETAILED BALANCE

Consider $i_b = 0$, such that the washboard potential is untilted, $u(\varphi) = u_0(\varphi)$. The Fokker-Planck equation is a continuity equation in phase space,

$$\frac{\partial p}{\partial \tau} = -\nabla \cdot \mathbf{j}, \quad \nabla = \left(\frac{\partial}{\partial \varphi}, \frac{\partial}{\partial v}\right)^T, \tag{4.22}$$

with probability current density

$$j_\varphi = vp, \quad j_v = -\left[u_0'(\varphi) + i_d(v) + \frac{1}{2}\frac{\partial}{\partial v}k(v)\right]p. \tag{4.23}$$

One may separate the current density into a reversible and an irreversible contribution, $\mathbf{j} = \mathbf{j}^{\mathrm{rev}} + \mathbf{j}^{\mathrm{irr}}$, with

$$j_\varphi^{\mathrm{rev}} = vp,\ j_v^{\mathrm{rev}} = -u_0'(\varphi)p, \quad \text{and} \quad j_\varphi^{\mathrm{irr}} = 0,\ j_v^{\mathrm{irr}} = -\left[i_d(v) + \frac{1}{2}\frac{\partial}{\partial v}k(v)\right]p. \tag{4.24}$$

The stationary solution p_0 satisfies $\nabla \cdot \mathbf{j}_s = 0$. In equilibrium we expect the stationary solution to be of the Maxwell-Boltzmann type

$$p_0(\varphi, v) = \frac{1}{\mathcal{N}} \exp\left\{-\frac{1}{\theta}\left[\frac{1}{2}v^2 + u_0(\varphi)\right]\right\}. \tag{4.25}$$

(Note that such a global Maxwell-Boltzmann distribution would not be normalizable and hence not a valid solution for the tilted washboard potential, that is in the presence of a bias current $i_b \neq 0$.) This clearly satisfies $\nabla \cdot \mathbf{j}_s^{\mathrm{rev}} = 0$. The stationary Fokker-Planck equation then becomes $\nabla \cdot \mathbf{j}_s^{\mathrm{irr}} = 0$. Demanding that current densities vanish at $v \to \pm\infty$ this translates to $\mathbf{j}_s^{\mathrm{irr}} = 0$ or

$$\left[i_d(v) + \frac{1}{2}\frac{\partial}{\partial v}k(v)\right]p_0 = 0, \tag{4.26}$$

which is easily integrated to give

$$p_0(\varphi, v) \propto \exp\left\{-\int_0^v \mathrm{d}v' \left[\frac{2i_d(v') + k'(v')}{k(v')}\right]\right\}. \tag{4.27}$$

Consistency with Eq. (4.25) implies

$$k'(v) - \frac{vk(v)}{\theta} + 2i_d(v) = 0. \tag{4.28}$$

This is solved by

$$k(v) = 2e^{v^2/2\theta} \int_v^\infty \mathrm{d}v' e^{-v'^2/2\theta} i_d(v'), \tag{4.29}$$

where we have already specified an integration variable such that the result reduces to the familiar result for the case of Ohmic friction (see below). In the limit of small θ, the integral may be evaluated as

$$k(v) = 2\int_v^\infty \mathrm{d}v' e^{-(v'-v)(v'+v)/2\theta} i_d(v') \simeq 2\theta \frac{i_d(v)}{v}. \tag{4.30}$$

For Ohmic dissipation, $i_d(v) = gv$, where g is the dimensionless conductance, this is just the familiar Johnson-Nyquist noise $k = 2\theta g$.

The condition $\mathbf{j}_s^{\mathrm{irr}} = 0$ corresponds to detailed balance in the Fokker-Planck framework. It guarantees that the stationary distribution is given by Eq. (4.25). For low-temperatures detailed balance is satisfied if the noise correlation has the form in Eq. (4.30), while for higher temperature, one would have to use the modified noise correlator in Eq. (4.29). We assume detailed balance and low temperatures throughout, such that the noise amplitude is given by Eq. (4.30).

4.3.2 Distribution for large bias current

At finite bias current, the Maxwell-Boltzmann distribution is no longer an adequate description of the global steady state: If we take φ to be valued in $[0, 2\pi)$, the Maxwell-Boltzmann distribution is not periodic. If we instead to take φ to be valued in $\mathbb{R}$, the Maxwell-Boltzmann distribution is not normalizable. Furthermore, we expect a finite probability current in the φ direction, $J_\varphi = \int \mathrm{d}v\, j_\varphi$, due to phase diffusion, or if i_b is sufficiently large, due to the average velocity in the running state.

To gain intuition for the nonequilibrium running state we consider briefly the limit of large bias $i_b \gg u_s(\varphi)$, so that we can neglect the periodic potential. The corresponding steady state distribution is independent of φ, such that $\nabla \cdot \mathbf{j} = \partial_v j_v$. Demanding that current densities vanish at $v \to \pm\infty$, we obtain the steady state solution

$$p_0(v) \propto \exp\left\{-\int_0^v \mathrm{d}v' \left[\frac{2(i_d(v') - i_b) + k'(v')}{k(v')}\right]\right\}. \tag{4.31}$$

Employing detailed balance, the distribution simplifies to

$$p_0(v) \propto \exp\left\{-\frac{1}{\theta}\Phi(v)\right\}, \quad \Phi(v) = \int_0^v \mathrm{d}v' \left[1 - \frac{i_b}{i_d(v')}\right] v'. \tag{4.32}$$

The non-equilibrium potential Φ clearly has a minimum at v_d with $i_d(v_d) = i_b$. Furthermore, it diverges for $v \to \pm\infty$, and therefore the distribution is manifestly normalizable. For small temperatures the distribution is strongly peaked around this minimum. In particular, this implies the probability flux in φ-direction is

$$J_\varphi = \int \mathrm{d}v\, j_\varphi = \int \mathrm{d}v\, v p_0(v) \simeq v_d. \tag{4.33}$$

The mathematics are complicated drastically once a periodic potential is included as the current densities are then no longer constant along a given direction. Provided the temperature is sufficiently low, one can make progress with a WKB approximation. To this end, one uses the Ansatz

$$p_0(\varphi, v) \simeq A(\varphi, v) \exp\left\{-\frac{1}{\theta} W(\varphi, v)\right\}, \tag{4.34}$$

where $A(\varphi, v)$ is independent of θ. Expanding in powers of θ, the Hamilton-Jacobi-type equation for $W(\varphi, v)$ follows at order θ^{-1}. It is[3]

$$v\partial_\varphi W - \left[u'(\varphi) + i_d(v) - \frac{k(v)}{2\theta}\partial_v W\right]\partial_v W = 0. \tag{4.36}$$

Note that along any physical trajectory of the deterministic system W is decreasing, as

$$\frac{\mathrm{d}W(\varphi(t), v(t))}{\mathrm{d}t} = -\frac{k(v)}{2\theta}(\partial_v W)^2 < 0. \tag{4.37}$$

Thus, W is a Lyapunov function. In particular, this implies that W is minimal at the steady states (and by periodicity constant along the running state trajectory).

4.3.3 TRANSITION RATES IN THE BISTABLE REGIME

For i_b in the bistable regime, the above considerations for the steady state break down. Indeed, we are not interested in the true steady state but rather in the transition frequency between the metastable trapped and running states. Determination of the rate of transition events under general circumstances is a complicated but well-studied topic [232]. Importantly, the definition

---

[3] An equation for A is obtained at order 1, given by

$$\left[\frac{k(v)}{\theta}\partial_v W - u'(\varphi) - i_d(v)\right]\partial_v A + v\partial_\varphi A + \left[\frac{k'(v)}{\theta}\partial_v W - i_d'(v) - \frac{k(v)}{2\theta}(\partial_v W)^2\right] A = 0. \tag{4.35}$$

of transition rates requires a separation of time scales: the distinction of the metastable states breaks down if the transition rates are not slow compared to equilibration within the metastable states. Thus, temperatures need to be small compared to the characteristic energy barriers separating the metastable states. The foundational theory is due to Kramers [233] who studied the escape from a metastable well in the presence of ohmic friction and noise. Therefore, in the context of metastable states which have equilibrium nature, this topic is often referred to as Kramers escape. The switching process falls in this category, and we simply extend Kramers approach in a the weak damping limit to nonreciprocal dissipation and noise. The problem of escape from a metastable state with nonequilibrium character, such as the running state, is generically much harder. We will explain how to avoid these difficulties in the present problem below.

The most common approach to calculate the transition rates is the flux-over-population approach [232–234]. Here, one endows the Fokker-Planck equation with a (possibly extended) probability source in the metastable state of interest, or more precisely in the attractive region associated with that state. If the transition rate is much slower than the typical relaxation within the attractive region, the precise shape of the sources should not matter as the system relaxes to quasiequilibrium before a transition can be expected. The transition to another state is modeled by absorbing boundary conditions along the separatrix. By adjusting the strength of the source terms a non-equilibrium steady state is reached. The transition rate is then given by the ratio of the probability flux across the separatrix and the average population in the attractive region.

Specifying to the simpler case of the switching process, we may express this mathematically as,

$$\mathcal{L}p_{\mathrm{tr}} = -J\delta(\varphi - \varphi^{\mathrm{min}})\delta(v) \qquad \text{in } \Omega_{\mathrm{tr}}, \tag{4.38a}$$

$$p_{\mathrm{tr}} = 0 \qquad \text{on } \partial\Omega_{\mathrm{tr}}. \tag{4.38b}$$

where the subscript tr stands for trapped state, we denote the trapped state attractive region by Ω_{tr}, and the separatrix by $\partial\Omega_{\mathrm{tr}}$. Technically, p_{tr} is the Green function of the steady-state Fokker-Planck equation. The probability flux introduced by the source in the steady state has to satisfy $J = \int_{\partial\Omega_{\mathrm{tr}}} \mathrm{d}\mathbf{S} \cdot \mathbf{j}_{\mathrm{tr}}$, with probability current defined through $\mathcal{L}p_{\mathrm{tr}} = -\nabla \cdot \mathbf{j}_{\mathrm{tr}}$. The switching rate is then the ratio of flux over population, or

$$\gamma_{\mathrm{sw}} = \frac{\int_{\partial\Omega_{\mathrm{tr}}} \mathrm{d}\mathbf{S} \cdot \mathbf{j}_{\mathrm{tr}}}{\int_{\Omega_{\mathrm{tr}}} \mathrm{d}\varphi \mathrm{d}v \, p_{\mathrm{tr}}}. \tag{4.39}$$

This is still a difficult problem as the steady state distribution in presence of the fluxes, p_{tr}, remains to be determined. A solution can be obtained straightforwardly for one-dimensional Fokker-Planck equations. In the following section, we consider weak damping which allows one to reduce the two-dimensional Fokker-Planck equation [Eq. (4.21)] to an effective Fokker-Planck equation in the energy only. It is then a simple task to find switching rate and current.

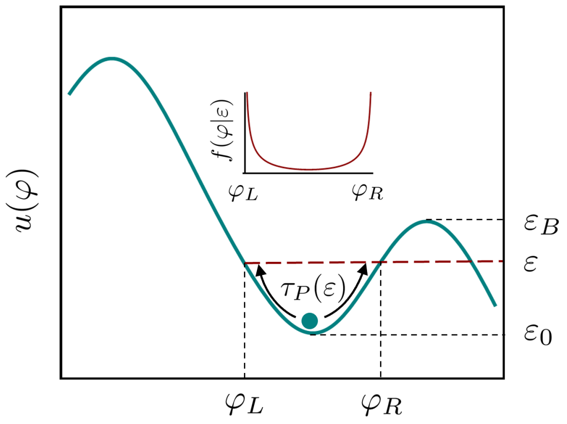

Figure 4.7: Switching or escape from the trapped state in the weak-damping regime. The phase particle has energy $\varepsilon_0 < \varepsilon < \varepsilon_0$ and is performing nearly undamped oscillations between $\varphi_L(\varepsilon)$ and $\varphi_R(\varepsilon)$. Its spatial distribution $f(\varphi|\varepsilon)$ is proportional to the inverse velocity and thus diverges at the turning points. Due to damping and thermal noise the energy of the particle fluctuates, eventually driving it across the barrier.

For general damping, due to the nonequilibrium nature of the running state, the retrapping rate is more difficult to obtain than the switching rate. The classic result for the retrapping rate is due to Ben-Jacob et al. [235], who employed a WKB approximation to construct a steady state solution for the running state. In the weak-damping regime, however, the retrapping rate can also be obtained within the flux-over-population approach [236]. We note that, as a side result of our calculation, we reproduce the Ben-Jacob result within the latter approach. To our knowledge this had not been done. Here, the calculation of the retrapping rate goes along the exact same line as that of the switching rate. In particular, we may introduce a source at some large velocity (of the same sign as the current bias, and spread out in φ),

$$\mathcal{L}p_{\text{run}} = -J'\delta(v \mp v_{\text{large}}) \qquad \text{in } \Omega_{\text{run}}, \tag{4.40a}$$

$$p_{\text{run}} = 0 \qquad \text{on } \partial\Omega_{\text{run}}. \tag{4.40b}$$

Here, $J' = J/2\pi$ is the flux density of the source. The retrapping rate is obtained in analogy to Eq. (4.39). For completeness, it is

$$\gamma_{\text{re}} = \frac{\int_{\partial\Omega_{\text{run}}} \mathrm{d}\mathbf{S} \cdot \mathbf{j}_{\text{run}}}{\int_{\Omega_{\text{run}}} \mathrm{d}\varphi \mathrm{d}v \, p_{\text{run}}}. \tag{4.41}$$

4.3.4 SWITCHING IN THE WEAK-DAMPING REGIME

In this section we will find an analytical expression for the switching rate and the resulting switching current in the weak-damping regime. We specify to the trapped state around a given minimum φ^{min} of $u(\varphi)$, say the one within $0 < \varphi^{\text{min}} < 2\pi$ for concreteness. The escape is over the next-in-energy maximum $\varphi^{\max} \gtrless \varphi^{\min}$ for $i_b \gtrless 0$. Furthermore, we assume bias current in the bistable regime, i.e. $|i_b|$ larger than $i^0_{\text{re},\pm}$. The barrier height

$$\Delta u = u(\varphi^{\max}) - u(\varphi^{\min}) \tag{4.42}$$

vanishes (and, naturally, the switching rate diverges) as the bias approaches the critical currents. We thus, consider only bias currents for which the temperature is small, $\theta \ll \Delta u$. As explained above, the system will then equilibrate to the Maxwell-Boltzmann distribution in proximity to the minimum, with occasional escape events over the barrier leading to a decrease in the local population.

Following to the flux-over-population approach we impose absorbing boundary conditions along the separatrix. We aim to find the retrapping rate at leading order in the damping. Specifically, we assume that $i_d(v)/v \ll 1$. The domain Ω_{tr} can then be approximated by the domain of bound or oscillatory motion of the undamped problem. While damping leads to corrections to the precise shape of the attractive region, this will only lead to higher order corrections in the final results. The domain of bound motion of the undamped problem can be specified solely by the (conserved) energy,

$$\varepsilon = \frac{1}{2}v^2 + u(\varphi). \tag{4.43}$$

We thus restrict our attention to energies $\varepsilon_0 \equiv u(\varphi^{\min}) < \varepsilon < \varepsilon_B \equiv u(\varphi^{\max})$ and $\varphi \in [\varphi_L(\varepsilon_B), \varphi_R(\varepsilon_B)]$. Here, we defined the left and right turning points of the motion, $\varphi_{L/R}(\varepsilon)$. This setting is sketched in Fig. 4.7 for positive bias. Of course, for $i_b > 0$ ($i_b < 0$) the right (left) turning point at ε_B is $\varphi^{\max}$. The absorbing boundary condition becomes simply $p_{\text{tr}}(\varphi, v) = 0$ if $\varepsilon(\varphi, v) = \varepsilon_B$.

ENERGY DIFFUSION EQUATION IN THE TRAPPED STATE

For weak damping $i_d(v)/v \ll 1$ the energy varies slowly with time,

$$\frac{\mathrm{d}}{\mathrm{d}\tau}\varepsilon = -v\, i_d(v) + \text{noise}. \tag{4.44}$$

Here, we use that $v \sim 1$ in the trapped state. In particular, the time scale associated with the dissipation and noise-induced diffusion of the energy is much longer than the period of the nearly undamped motion in the potential well. This suggests the following approximation scheme: treat the periodic motion as undamped, evaluate the dissipated energy (energy drift) and the noise induced energy gain or loss (energy diffusion) within a period of the undamped motion, and from this construct a Fokker-Planck equation for the energy alone. We used this literal construction in our paper [IV]. Here, we will present an equivalent but more formal derivation of the effective Fokker-Planck equation.

To this end, starting from Eq. (4.21), we first change variables from (φ, v) to (φ, ε) and then proceed to average the resulting equation over φ. Expressed in terms of the energy and phase, the velocity $v \gtrless 0$ is

$$v \equiv v_\pm(\varphi, \varepsilon) = \pm\sqrt{2(\varepsilon - u(\varphi))}. \tag{4.45}$$

We now write the probability distribution as piecewise defined function for positive and negative velocities, and express both parts as function of ε, i.e. we define $\tilde{f}_\pm(\varphi, \varepsilon) = p(\varphi, v_\pm(\varphi, \varepsilon))$. Note that this is not the new probability distribution yet, as we have not included the Jacobian factor. In the Fokker-Planck equation we may use the relation

$$-v_\pm \partial_\varphi \tilde{f}_\pm = -\left[v_\pm \partial_\varphi + v_\pm \frac{\partial v_\pm}{\partial \varphi} \partial_v\right] p = -v_\pm \partial_\varphi p + u' \partial_v p, \tag{4.46}$$

to eliminate $u'(\varphi)$. Taking into account also the Jacobian of the transformation, the new probability density

$$f_\pm(\varphi, \varepsilon) = \left|\frac{\partial v_\pm(\varphi, \varepsilon)}{\partial \varepsilon}\right| \tilde{f}_\pm(\varphi, \varepsilon) = \pm\frac{\tilde{f}_\pm(\varphi, \varepsilon)}{v_\pm(\varphi, \varepsilon)}, \tag{4.47}$$

satisfies the Fokker-Planck equation

$$\partial_\tau f_\pm = -\partial_\varphi(v_\pm f_\pm) + \partial_\varepsilon \left\{ \left[i_d(v_\pm) - \frac{k(v_\pm)}{2v_\pm} \right] (v_\pm f_\pm) + \partial_\varepsilon \left[\frac{v_\pm k(v_\pm)}{2} (v_\pm f_\pm) \right] \right\}, \tag{4.48}$$

for energies $\varepsilon_0 < \varepsilon < \varepsilon_B$. Note that $F_\pm = \int \mathrm{d}\varphi \, d\varepsilon \, f_\pm$ is the probability that the velocity is positive/negative. The domain of the new Fokker-Planck equation has the boundary $(\varphi, \varepsilon) = (\varphi, u(\varphi)) = (\varphi_{L/R}(\varepsilon), \varepsilon)$, where it satisfies the boundary condition $\tilde{f}_+ = \tilde{f}_-$ and hence $v_+ f_+ = -v_- f_-$. Using the detailed balance condition, Eq. (4.28), we can simplify this to

$$\partial_\tau f_\pm = -\partial_\varphi(v_\pm f_\pm) + \partial_\varepsilon\{i_d(v_\pm)[1 + \theta \partial_\varepsilon](v_\pm f_\pm)\}. \tag{4.49}$$

Similarly, the source term in Eq. (4.38) becomes

$$-J\delta(\varphi - \varphi^{\min})\delta(v - 0^+) \to -J\delta(\varphi - \varphi^{\min})\delta(\varepsilon - \varepsilon_0 - 0^+)\delta_{\pm,+}, \tag{4.50}$$

where we took the liberty to move the source to slightly positive velocities to avoid ambiguities.

In order to eliminate φ from Eq. (4.49), consider the following. In the undamped and noise-free case, given an energy ε, the distribution for φ is inversely proportional to the velocity at that point, or more precisely,

$$f(\varphi|\varepsilon) = \frac{2}{\tau_P(\varepsilon)\sqrt{2(\varepsilon - u(\varphi))}}, \qquad \varphi \in [\varphi_L(\varepsilon), \varphi_R(\varepsilon)]. \tag{4.51}$$

where we defined the period of the bound and undamped motion

$$\tau_P(\varepsilon) = \int_{\varphi_L(\varepsilon)}^{\varphi_R(\varepsilon)} \mathrm{d}\varphi \, \frac{2}{\sqrt{2(\varepsilon - u(\varphi))}} \equiv \oint \mathrm{d}\varphi \, \frac{1}{v(\varphi, \varepsilon)}. \tag{4.52}$$

This is in fact the steady-state solution to Eq. (4.49) if one sets $i_d = k = 0$. The contour integral is simply along the forward and backward branch of the periodic motion, i.e. we define

$$\oint \mathrm{d}\varphi \, g(\varphi, v(\varphi, \varepsilon)) = \int_{\varphi_L(\varepsilon)}^{\varphi_R(\varepsilon)} \mathrm{d}\varphi \, g(\varphi, v(\varphi, \varepsilon)) + \int_{\varphi_R(\varepsilon)}^{\varphi_L(\varepsilon)} \mathrm{d}\varphi \, g(\varphi, -v(\varphi, \varepsilon)), \tag{4.53}$$

for any function g on phase space. We proceed by making the ansatz

$$f_\pm(\varphi, \varepsilon) = F_\pm f(\varphi|\varepsilon) f(E), \tag{4.54}$$

i.e. we assume the system behaves as if undamped given its energy, but the energy is distributed according to $f(\varepsilon)$. Here, $F_\pm = 1/2$, as the undamped system spends the same amount of time moving forward and backward. This is due to the time-reversal symmetry of Newton's equation of motion. We now plug Eq. (4.54) into Eq. (4.49), sum over ± and integrate over $\varphi \in [\varphi_L(\varepsilon), \varphi_R(\varepsilon)]$. Using the Leibniz rule,

$$\partial_\varepsilon \int_{\varphi_L(\varepsilon)}^{\varphi_R(\varepsilon)} \mathrm{d}\varphi \, g(\varphi, \varepsilon) = \frac{\partial \varphi_R}{\partial \varepsilon} g(\varphi_R, \varepsilon) - \frac{\partial \varphi_L}{\partial \varepsilon} g(\varphi_L, \varepsilon) + \int_{\varphi_L(\varepsilon)}^{\varphi_R(\varepsilon)} \mathrm{d}\varphi \, \partial_\varepsilon g(\varphi, \varepsilon), \tag{4.55}$$

and the fact that $v(\varphi_{L/R}, \varepsilon) = 0$ as well as $i_d(0) = 0$, we obtain the desired Fokker-Planck equation for $f(\varepsilon)$,

$$\partial_\tau f(\varepsilon) = \partial_\varepsilon \left\{ \varepsilon_d(\varepsilon)[1 + \theta \partial_\varepsilon] \frac{f(\varepsilon)}{\tau_P(\varepsilon)} \right\}, \tag{4.56}$$

where we defined the dissipated energy per period of the oscillatory motion,

$$\varepsilon_d(\varepsilon) = \oint \mathrm{d}\varphi \, i_d(v(\varphi, \varepsilon)) = \int_0^{\tau_P(\varepsilon)} \mathrm{d}\tau \, v_\varepsilon(\tau) i_d(v_\varepsilon(\tau)). \tag{4.57}$$

As the integral includes forward and backward motion, any asymmetry in the dissipative current is ineffective and, as a consequence, Eq. (4.56) is completely invariant under $i_b \to -i_b$ if the potential u_s is symmetric. In particular, this implies that the switching rate determined from the effective Fokker-Planck equation (which determines the switching current) will be asymmetric only if the potential u_s is asymmetric, demonstrating the first part of the correspondence given in Eq. (4.2).

To make this more explicit, consider symmetric $u_s(\varphi) = u_s(-\varphi)$. It follows that the velocity and turning points satisfy

$$v(\varphi; i_b) = v(-\varphi; -i_b), \quad \varphi_L(i_b) = -\varphi_R(-i_b). \tag{4.58}$$

With this, it is straightforward to show that ε_d is manifestly symmetric in i_b,

$$\varepsilon_d(i_b) = \int_{-\varphi_R(-i_b)}^{-\varphi_L(-i_b)} \mathrm{d}\varphi\,[i_d(v(-\varphi; -i_b)) - i_d(-v(-\varphi; -i_b))] \tag{4.59a}$$

$$= \int_{\varphi_L(-i_b)}^{\varphi_R(-i_b)} \mathrm{d}\varphi\,[i_d(v(\varphi; -i_b)) - i_d(-v(\varphi; -i_b))] = \varepsilon_d(-i_b). \tag{4.59b}$$

We then conclude that to leading order in the weak-damping limit, the Eq. (4.56) and hence the switching rate and switching current is reciprocal even when the dissipative current is nonreciprocal.

SWITCHING RATE AND SWITCHING CURRENT

We now employ the flux-over-population method to calculate the switching rate, i.e. the rate of transitions from the potential well. The steady-state effective Fokker-Planck equation for ε including the source term introduced in Eq. (4.38) now takes the form

$$-J\delta(\varepsilon - \varepsilon_0 - 0^+) = \partial_\varepsilon \left\{ \varepsilon_d(\varepsilon)[1 + \theta\partial_\varepsilon] \frac{f(\varepsilon)}{\tau_P(\varepsilon)} \right\} \equiv -\partial_\varepsilon j_\varepsilon, \tag{4.60}$$

where in the second equality we defined the probability current in ε-direction, j_ε. Integrating with respect to ε once gives $J = j_\varepsilon(\varepsilon) - j_\varepsilon(\varepsilon_0)$. We assume that the probability flux originates from the source only, such that $j_\varepsilon(\varepsilon_0) = 0$. Thus, we have the equation

$$J = -\varepsilon_d(\varepsilon)[1 + \theta\partial_\varepsilon] \frac{f(\varepsilon)}{\tau_P(\varepsilon)}. \tag{4.61}$$

Translating the boundary condition $p_{\mathrm{tr}} = 0$ on $\partial\Omega_{\mathrm{tr}}$ to $f(\varepsilon_B) = 0$, we can solve this straightforwardly. The result is

$$f(\varepsilon) = J\tau_P(\varepsilon) \exp\left\{-\frac{\varepsilon}{\theta}\right\} \int_{\varepsilon}^{\varepsilon_B} \mathrm{d}\varepsilon' \, \frac{\exp\left\{\frac{\varepsilon'}{\theta}\right\}}{\theta\varepsilon_d(\varepsilon')} \simeq J \frac{\tau_P(\varepsilon)}{\varepsilon_d(\varepsilon_B)} \exp\left\{-\frac{\varepsilon - \varepsilon_B}{\theta}\right\}. \tag{4.62}$$

In the second step we assumed low temperatures, $\theta \ll \varepsilon_B$, so that the integral is dominated by its upper boundary. The inverse transition rate is given by the ratio population/flux [c.f. Eq. (4.39)], i.e. it is

$$\gamma_{\rm sw}^{-1} = \frac{1}{J}\int_{\varepsilon_0}^{\varepsilon_B} \mathrm{d}\varepsilon\, f(\varepsilon) \simeq \frac{\theta \tau_P(\varepsilon_0)}{\varepsilon_d(\varepsilon_B)} \exp\left\{\frac{\varepsilon_B - \varepsilon_0}{\theta}\right\}, \tag{4.63}$$

where in the second equality we again invoked $\theta \ll \varepsilon_B$. The period at energy ε_0 corresponds to motion right at the potential minimum and is thus given by the inverse plasma frequency $2\pi/\omega_p$ (here the dimensionless plasma frequency is $\omega_p = \Omega_p(i_b)/\Omega_p(0)$, note that $\omega_p \neq 1$ at finite i_b). The switching rate is thus

$$\gamma_{\rm sw} \simeq \frac{\varepsilon_d(\varepsilon_B)\omega_p}{2\pi\theta} \exp\left\{-\frac{\Delta u}{\theta}\right\}, \tag{4.64}$$

where ω_p, $\Delta u = u(\varphi^{\max}) - u(\varphi^{\min})$ and $\varepsilon_d(\varepsilon_B)$ depend on the bias i_b. One can further simplify this by approximating the potential well as quadratic in the expression for the velocity, $v_\pm(\varphi, \varepsilon_B) \simeq \pm\sqrt{2\Delta u - \omega_p^2 \delta\varphi^2}$ such that

$$\begin{aligned} \varepsilon_d(\varepsilon_B) &= \int_{v\ \text{real}} \mathrm{d}\varphi\, [i_d(v_+) - i_d(v_-)] && (4.65\text{a}) \\ &\simeq \int_{-\frac{1}{a}}^{\frac{1}{a}} \mathrm{d}(\delta\varphi) \left[i_d\left(\sqrt{2\Delta u}\sqrt{1 - a^2\delta\varphi^2}\right) - \ldots \right], && (4.65\text{b}) \end{aligned}$$

where we used the shorthand $a^2 = \omega_p^2/2\Delta u$. With this the switching rate becomes

$$\gamma_{\rm sw} \simeq \frac{g_{\rm eff}\Delta u}{\theta} \exp\left\{-\frac{\Delta u}{\theta}\right\}, \tag{4.66}$$

in terms of the effective dimensionless conductance

$$g_{\rm eff} = \int_0^\pi \frac{\mathrm{d}x}{\pi} \sin x \frac{\left[i_d\left(\sqrt{2\Delta u}\sin x\right) - i_d\left(-\sqrt{2\Delta u}\sin x\right)\right]}{\sqrt{2\Delta u}}. \tag{4.67}$$

Both Δu and hence $g_{\rm eff}$ depend on i_b. For an Ohmic junction $i_d(v) = gv$, it is $g_{\rm eff} = g$.

We now derive an analytical expression for the switching current. When ramping up (or down) the bias current i_b from zero at the ramp rate $a > 0$,

$$i_b(\tau) = \pm a\tau, \tag{4.68}$$

the junction will eventually escape from the trapped state and abruptly switch into the running state. The bias levels at which this is happening are the switching currents $i_{\mathrm{sw},\pm}$. The probability P_{tr} for the system to remain in the trapped state satisfies the rate equation

$$\frac{\mathrm{d}P_{\mathrm{tr}}}{\mathrm{d}\tau} = -\gamma_{\mathrm{sw}}(\tau)P_{\mathrm{tr}}. \tag{4.69}$$

The escape rate $\gamma_{\mathrm{sw}}(\tau)$ from the trapped to the running state depends on time, as the barrier height depends on the bias current. Solving for $P_{\mathrm{tr}}(\tau)$ with initial condition $P_{\mathrm{tr}}(\tau) = 1$ gives

$$P_{\mathrm{tr}}(\tau) = \exp\left\{-\int_0^\tau \mathrm{d}\tau'\,\gamma_{\mathrm{sw}}(\tau')\right\}. \tag{4.70}$$

In view of Eq. (4.68), we can replace the time argument by current,

$$P_{\mathrm{tr}}(i_b) = \exp\left\{\mp\frac{1}{a}\int_0^{i_b} \mathrm{d}i_b'\,\gamma_{\mathrm{sw}}(i_b')\right\} = \exp\left\{-\frac{1}{a}\int_0^{|i_b|} \mathrm{d}i\,\gamma_{\mathrm{sw}}(\pm i)\right\}. \tag{4.71}$$

This expression can be used to define the average switching currents $i_{\mathrm{sw},\pm} > 0$ through

$$P_{\mathrm{tr}}(i_b = \pm i_{\mathrm{sw},\pm}) = \frac{1}{2}. \tag{4.72}$$

Due to the exponential factor in Eq. (4.64), the integrand increases rapidly with increasing i due to the decreasing barrier, so that the integral is dominated by bias currents $i \sim i_{\mathrm{sw},\pm}$. This allows us to approximate

$$a\ln 2 \simeq \theta\left(\left|\frac{\mathrm{d}i_b}{\mathrm{d}\varepsilon_B}\right|\gamma_{\mathrm{sw}}\right)_{i_b=\pm i_{\mathrm{sw},\pm}}. \tag{4.73}$$

Solving for the exponent, this yields

$$\Delta u(\pm i_{\mathrm{sw},\pm}) = \theta \ln\left(\frac{\varepsilon_d(\varepsilon_B)\omega_p}{2\pi a \ln 2|\varphi^{\mathrm{max}} - \varphi^{\mathrm{min}}|}\right)_{i_b=\pm i_{\mathrm{sw},\pm}}. \tag{4.74}$$

where we used that

$$\left|\frac{\mathrm{d}\Delta u}{\mathrm{d}i_b}\right| = |\varphi^{\mathrm{max}} - \varphi^{\mathrm{min}}|. \tag{4.75}$$

To make analytical progress, we approximate the bias-current dependence of the potential barrier as

$$\Delta u(i_b) \simeq \Delta u_s\left(1 \mp \frac{i_b}{i_{c,\pm}}\right)^{\mu_\pm}, \tag{4.76}$$

where we defined the exponent

$$\mu_\pm = \left|\varphi_s^{\max} - \varphi_s^{\min}\right|_\pm \frac{i_{c,\pm}}{\Delta u_s}, \tag{4.77}$$

with $|\varphi_s^{\max} - \varphi_s^{\min}|_\pm = \lim_{i_b\to 0^\pm} |\varphi^{\max} - \varphi^{\min}|$. This expression interpolates between Δu_s at zero bias and $\Delta u = 0$ at the critical currents, and correctly reproduces the linear term in the small - i_b expansion. It is moreover a rather accurate approximation to set $i_{\text{sw},\pm} \simeq 0$ under the logarithm (so that $\omega_p = 1$ in particular). We then find

$$i_{\text{sw},\pm} \simeq i_{c,\pm}\left\{1 - \left[\frac{\theta}{\Delta u_s}\ln\left(\frac{\varepsilon_d(u_s(\varphi_s^{\max}))}{2\pi a \ln 2|\varphi_s^{\max} - \varphi_s^{\min}|_\pm}\right)\right]^{1/\mu_\pm}\right\}. \tag{4.78}$$

This is the central result of this section (together with the expression for the retrapping current, Eq. (4.101) below). We note again that this expression is non-reciprocal only if u_s and hence the current-phase relation is asymmetric. In particular, it is completely independent of the asymmetry of $i_d(v)$. Indeed, from the definition of $\varepsilon_d = \oint \mathrm{d}\varphi\, i_d(v)$ it follows that only the anti-symmetric part of i_d enters in the switching current Eq. (4.78).

We finally comment on the requirements for the validity of the weak damping approximation. Writing a differential equation for the distribution function $f(\varepsilon)$ requires that it must be smooth on the scale of the dissipated energy ε_d per period. Provided we consider configurations sufficiently close to equilibrium, this is guaranteed as long as $\varepsilon_d \ll \theta$.

4.3.5 RETRAPPING IN THE WEAK-DAMPING REGIME

We now consider the retrapping process in the weak-damping regime [$i_d/v \ll 1$]. In order to have a well defined metastable running state we furthermore require the temperature to be sufficiently low compared to a characteristic energy to be specified below. As above, we impose absorbing boundary conditions along the separatrix. Noting that the typical bias levels are already first order in the damping (as this is where the retrapping typically occurs) we may approximate the running domain Ω_{run} as that of the undamped and undriven system. In particular, this implies that the domain of the running state is specified only by the energy of the undriven system,

$$\epsilon = \frac{v^2}{2} + u_0(\varphi). \tag{4.79}$$

Alternatively, one may view ϵ as the true energy of the system and the bias current as an external force dragging the phase particle along the periodic landscape. This is illustrated in Fig. 4.8. In this picture, the running state corresponds to rotational motion, i.e. to energies $\epsilon > \epsilon_B = u_s(\varphi_s^{\max})$. The boundary condition becomes $p_{\text{run}}(\varphi, v) = 0$ for $\epsilon(\varphi, v) = \epsilon_B$.

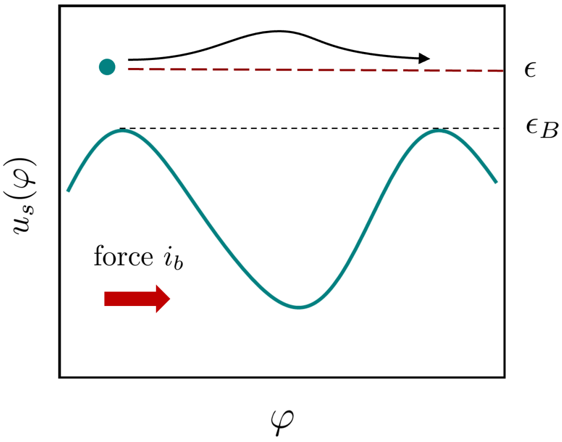

Figure 4.8: Retrapping process in the weak-damping regime (untilted washboard picture). The phase particle is dragged along a periodic potential landscape by the constant force i_b. Its energy (red-dashed line) is almost constant as the dissipated energy and the work done on the particle by the external force nearly cancel each other. The velocity (black line) is a weak function of position, with maximum where the potential energy is minimal. The energy drifts and diffuses due to the frictional and noise forces. Once it reaches the barrier ϵ_B, the particle does not have any kinetic energy at the maxima and becomes trapped.

ENERGY DIFFUSION EQUATION IN THE RUNNING STATE

In the running state the energy $\varepsilon = \frac{1}{2}v^2 + u(\varphi)$ is no longer a slow variable, as $\mathrm{d}\varepsilon/\mathrm{d}\tau \sim v_d i_d(v_d) \sim v_d i_b \sim i_b^2/g \gg 1$ in the weak-damping regime. However, ϵ is a slowly varying quantity due to the near cancellation of the frictional and driving forces,

$$\frac{\mathrm{d}}{\mathrm{d}\tau}\epsilon = v(i_b - i_d(v)) + \text{noise}. \tag{4.80}$$

Here, we derive an effective Fokker-Planck equation for ϵ in the running state, i.e. for energies $\epsilon > \epsilon_B = u_0(\varphi_0^{\max})$. The Fokker-Planck equation is derived as in the previous section, but due to the altered definition of the energy, a term due to the bias current remains. The transformed Fokker-Planck equation is

$$\partial_\tau f_\pm = -\partial_\varphi[v_\pm f_\pm] + \partial_\epsilon\left\{\left[i_d(v_\pm) - i_b - \frac{k(v_\pm)}{2v_\pm}\right]v_\pm f_\pm + \partial_\epsilon\left[\frac{v_\pm k(v_\pm)}{2}v_\pm f_\pm\right]\right\}, \tag{4.81}$$

where the velocity is now a function of φ and ϵ, $v_\pm(\varphi,\epsilon) = \pm\sqrt{2(\epsilon - u_0(\varphi))}$. We are interested in the distribution around the (deterministic) running state i.e. we assume the velocity has the same sign as i_b. Furthermore, as the energy varies much slower than φ, we can assume that the the distribution of the position given the energy is again just the inverse velocity. We hence make the ansatz

$$f_\pm(\varphi,\epsilon) = F_\pm f(\varphi|\epsilon)f(\epsilon). \tag{4.82}$$

We neglect the probability for velocities opposite to the bias, i.e. $F_\pm = 1$ if $\text{sign}(i_b) = \pm$ and $F_\pm = 0$ if not. The normalized conditional distribution for φ is

$$f(\varphi|\epsilon) = \frac{1}{\tau_P(\epsilon)\sqrt{2(\epsilon - u_0(\varphi))}}, \quad \tau_P(\epsilon) = \int_0^{2\pi} \mathrm{d}\varphi \, \frac{1}{\sqrt{2(\epsilon - u_0(\varphi))}}. \tag{4.83}$$

Note that φ now takes values in $[0, 2\pi)$: the motion is no longer oscillatory (or bound) but rotational (or unbound). Integrating Eq. (4.81) with respect to φ and summing over $\pm$, we obtain

$$\partial_\tau f(\epsilon) = \partial_\epsilon \{\varepsilon_d(\epsilon)[1 + \theta\partial_\epsilon] - 2\pi|i_b|\} \frac{f(\epsilon)}{\tau_P(\epsilon)}. \tag{4.84}$$

Here, we again assumed that the noise satisfies detailed balance and defined the dissipated energy per period in the running state,

$$\varepsilon_d(\epsilon) = \int_0^{\pm 2\pi} \mathrm{d}\varphi \, i_d(\pm v(\varphi, \epsilon)), \; \pm = \text{sign}(i_b). \tag{4.85}$$

Note that the dissipated energy is positive and in particular $\varepsilon_d(\epsilon_B) = 2\pi i^0_{\text{re},\pm}$. Eq. (4.84) is now manifestly asymmetric in i_b if $i_d(v) \neq -i_d(-v)$ and $u_0(\varphi) = u_0(-\varphi)$. Furthermore, an anti-symmetric dissipative current $i_d(v) = -i_d(-v)$ implies that $\varepsilon_d(i_b) = \varepsilon_d(-i_b)$. In this case Eq. (4.84) is invariant under a sign change of the bias current, no matter the shape of the potential, or in other terms no matter the current-phase asymmetry.

RETRAPPING RATE AND RETRAPPING CURRENT

In order to find the retrapping rate, we need to solve the effective Fokker-Planck equation (4.84) in the steady state with probability flux J introduced at a large energy, c.f. Sec. 4.3.3. The resulting equation is

$$J = \{\varepsilon_d(\epsilon)[1 + \theta\partial_\epsilon] - 2\pi|i_b|\} \frac{f(\epsilon)}{\tau_P(\epsilon)} \tag{4.86}$$

for $\epsilon > \epsilon_B$ subject to absorbing boundary $f(\epsilon_B) = 0$. This is readily solved as

$$f(\epsilon) = J\tau_P(\epsilon) \exp\left\{-\frac{F(\epsilon)}{\theta}\right\} \int_{\epsilon_B}^{\epsilon} \mathrm{d}\epsilon' \, \frac{1}{\theta\varepsilon_d(\epsilon')} \exp\left\{\frac{F(\epsilon')}{\theta}\right\}, \tag{4.87}$$

where the potential function F is defined as

$$F(\epsilon) = \int_{\epsilon_0}^{\epsilon} \mathrm{d}\epsilon' \left[1 - \frac{2\pi|i_b|}{\varepsilon_d(\epsilon')}\right]. \tag{4.88}$$

Here, we define the energy ϵ_0 via

$$\varepsilon_d(\epsilon_0) = 2\pi|i_b|. \tag{4.89}$$

Hence, ϵ_0 is the energy of the undamped and unforced trajectory for which the dissipation function balances the external force i_b. In other words, it characterizes the steady state in the weak-damping regime. We make the assumption, that there is only one such energy, i.e. that $i_d(v)$ allows only one steady state. This means that F has only one minimum at ϵ_0. Furthermore, this implies that F is a monotonously decreasing function for $\epsilon_B < \epsilon < \epsilon_0$ and monotonously increasing function for $\epsilon > \epsilon_0$.

The inverse retrapping rate is given by the ratio population/flux $= \int \mathrm{d}\epsilon f/J$, i.e. by

$$\gamma_{\text{re}}^{-1} = \int_{\epsilon_B}^{\infty} \mathrm{d}\epsilon\, \tau_P(\epsilon) \exp\left\{-\frac{F(\epsilon)}{\theta}\right\} \int_{\epsilon_B}^{\epsilon} \mathrm{d}\epsilon'\, \frac{1}{\theta \varepsilon_d(\epsilon')} \exp\left\{\frac{F(\epsilon')}{\theta}\right\}. \tag{4.90}$$

For low temperatures this can be evaluated straightforwardly. The integral over ϵ receives its main contribution from the minimum of F, i.e. from ϵ_0, while the integral over ϵ' receives its main contribution from maxima of F. The the maxima are at the boundary of the integration domain. As the first integral is dominated by $\epsilon = \epsilon_0$, the second integral will be dominated by its lower boundary. This gives the expression

$$\gamma_{\text{re}}^{-1} \simeq \tau_P(\epsilon_0) \sqrt{\frac{2\pi\theta}{F''(\epsilon_0)}} \frac{\exp\left\{\frac{F(\epsilon_B)}{\theta}\right\}}{\varepsilon_d(\epsilon_B)[-F'(\epsilon_B)]}. \tag{4.91}$$

In order to obtain a compact expression for general $i_d(v)$ we make the following simplifications. First, we rewrite $F(\epsilon_B)$ as an integral over the current $i(\epsilon) = \varepsilon_d(\epsilon)/2\pi \in [i^0_{\text{re},\pm}, i_b]$ (note that ε_d increases monotonically from ϵ_B to ϵ_0). This gives,

$$F(\epsilon_B) = 2\pi \int_{i_b}^{i^0_{\text{re},\pm}} \mathrm{d}i\, [\varepsilon_d'(\epsilon(i))]^{-1} \left[1 - \frac{|i_b|}{i}\right] \simeq \frac{2\pi}{\varepsilon_d'(\epsilon_0)|i_b|} \frac{(i_b \mp i^0_{\text{re},\pm})^2}{2}. \tag{4.92}$$

Second, we may find expressions for $\tau_P(\epsilon_0)$ and $\varepsilon_d'(\epsilon_0)$ in terms of the approximate running state trajectory $v_{\text{run}}(\varphi) \simeq v_d - u_0(\varphi)/v_d$. At leading order in $v_d = i_d^{-1}(i_b)$ this gives

$$\tau_P(\epsilon_0) \simeq \frac{2\pi}{v_d},\ \varepsilon_d'(\epsilon_0) \simeq \frac{2\pi i_d'(v_d)}{v_d}. \tag{4.93}$$

Altogether we have the closed form expression for the retrapping rate,

$$\gamma_{\text{re}} = \sqrt{\left[\frac{g_{\text{d}}}{g_{\text{s}}}\right]_{v_d} \frac{(i_b \mp i^0_{\text{re},\pm})^2}{2\pi\theta}} \exp\left\{-\left[\frac{1}{g_{\text{d}}\, g_{\text{s}}}\right]_{v_d} \frac{(i_b \mp i^0_{\text{re},\pm})^2}{2\theta}\right\}. \tag{4.94}$$

Here, we defined the static and differential conductances,

$$g_{\text{d}}(v) = \frac{\mathrm{d}i_d}{\mathrm{d}v}(v), \quad g_{\text{s}}(v) = \frac{i_d(v)}{v}. \tag{4.95}$$

respectively. Asymmetric damping may enter in several ways. First, it may enter through the noisefree retrapping current $i^0_{\mathrm{re},\pm}$ which is manifestly asymmetric in damping. Second, it may enter through the conductances $g_\mathrm{d}(\pm|v_d|)$ and $g_\mathrm{s}(\pm|v_d|)$. For ohmic friction $i_d(v) = gv$, the noisefree retrapping current can be approximated as $i^0_\mathrm{re} \simeq 4g/\pi$ and we reproduce the classic result [235],

$$\gamma_\mathrm{re} = \sqrt{\frac{(i_b/g - 4/\pi)^2}{2\pi\theta}} \exp\left\{ -\frac{(i_b/g - 4/\pi)^2}{2g^2\theta} \right\}. \tag{4.96}$$

The retrapping currents $i_{\mathrm{re},\pm}$ may be defined in a similar manner as the switching currents. The bias current is now ramped down (up) from a sufficiently large starting value $\pm i_0$ with $i_0 \gg i_{\mathrm{re},\pm}$, i.e.

$$i_b(\tau) = \pm(i_0 - a\tau). \tag{4.97}$$

The average retrapping currents are defined as the bias level at which the probability for having retrapped reaches $1/2$. This gives

$$\frac{1}{2} = \exp\left\{ \frac{1}{a} \int_{i_0}^{\pm i_{\mathrm{re},\pm}} \mathrm{d}i\, \gamma_\mathrm{re}(\pm i) \right\}, \tag{4.98}$$

Due to the exponential factor in γ_re the main contribution to the integral stems from $i_b \sim i_{\mathrm{re},\pm}$. This allows one to approximate $[v_d = i_d^{-1}(\pm i_{\mathrm{re},\pm})]$

$$a \ln 2 \simeq \frac{1}{\sqrt{2\pi\theta}} \sqrt{\left[\frac{g_\mathrm{d}}{g_\mathrm{s}}\right]_{v_d}} \int_{i_{\mathrm{re},\pm}}^{\infty} \mathrm{d}i\, (i \mp i^0_{\mathrm{re},\pm}) \exp\left\{ -\left[\frac{1}{g_\mathrm{d} g_\mathrm{s}}\right]_{v_d} \frac{(i \mp i^0_{\mathrm{re},\pm})^2}{2\theta} \right\} \tag{4.99}$$

$$= \sqrt{\frac{\theta}{2\pi} [g_\mathrm{d}^3 g_\mathrm{s}]_{v_d}} \exp\left\{ -\left[\frac{1}{g_\mathrm{d} g_\mathrm{s}}\right]_{v_d} \frac{(i_{\mathrm{re},\pm} - i^0_{\mathrm{re},\pm})^2}{2\theta} \right\}. \tag{4.100}$$

Setting $i_{\mathrm{re},\pm} \to i^0_{\mathrm{re},\pm}$ in the preexponential factor and solving for $i_{\mathrm{re},\pm}$ gives

$$i_{\mathrm{re},\pm} = i^0_{\mathrm{re},\pm} + \left[\sqrt{\theta g_\mathrm{d} g_\mathrm{s} \ln\left(\frac{\theta g_\mathrm{d}^3 g_\mathrm{s}}{2\pi (a \ln 2)^2} \right)} \right]_{v_d = i_d^{-1}(\pm i^0_{\mathrm{re},\pm})}. \tag{4.101}$$

This is the central result of this section (together with the expression for the retrapping current, Eq. (4.78) above). An asymmetric dissipative current clearly leads to nonreciprocity $i_{\mathrm{re},+} \neq i_{\mathrm{re},-}$ in Eq. (4.101). Conversely, symmetric dissipation gives reciprocal retrapping currents even if the current-phase relation is asymmetric. This is inherited from the expression for $i^0_{\mathrm{re},\pm}$ in the weak damping limit, Eq. (4.20).

The weak-damping approximation of the running state Fokker-Planck equation is well controlled provided that $(\varepsilon_d - 2\pi|i_b|)^2/\varepsilon_d \ll \theta$. In the low-damping regime, the relevant bias levels are also linear in ε_d, such that the condition of validity again is $\varepsilon_d \ll \theta$.

We have thus established analytical evidence that confirms the numerical picture of Sec. 4.1: in the weak-damping regime the correspondence given in Eq. (4.2) is exact. We also believe that the correspondence holds also in the regime of low temperatures. In this case, the switching rate prefactor (the exponential factor remains the same) is controlled by the population near the trapped state attractor, as well as the phase space flow in the proximity of the unstable fixed point. If temperature is sufficiently low, this warrants linearization of the frictional forces, rendering nonlinearities irrelevant [232, 233]. We do not have a clear picture of the retrapping process though: while it is clear that it will be manifestly asymmetric if the dissipative current is asymmetric, it is hard to establish the independence of the retrapping rate with respect to the potential shape.

4.4 Phase action

In the previous sections we have developed a phenomenological theory of Josephson diode effects in current-biased junctions. In particular, based on the extended RCSJ model we have established a correspondence between asymmetry in the current-phase relation and nonreciprocal switching currents, and asymmetry in the dissipative current and nonreciprocal retrapping currents, see Eq. (4.2).

We now develop a microscopic theory of the Josephson diode effect in a tunneling junction, with the aim of explicitly demonstrating the origin of asymmetry in the current-phase relation and the dissipative current. While we already established in Sec. 2.2 that an asymmetric current-phase relation can be obtained in an equilibrium calculation provided broken time reversal symmetry, we have not touched upon the microscopic origin of the dissipative current and the requirements for its asymmetry. Indeed, the dissipative current in a tunneling junction receives contributions from several sources: First, at finite voltages the superconducting electrodes may exchange individual quasiparticles. This gives rise to a dissipative normal current, I_{qp}. We will derive explicitly how this contribution enters the RCSJ equation of motion within a streamlined Ambegaokar-Eckern-Schön theory [226, 227], including also higher order processes such as multiple Andreev reflection. Second, the electromagnetic environment contributes to the dissipative current. We will not explicitly include this into our microscopic theory and instead augment the resulting extended RCSJ equation by a phenomenological environmental impedance $Z(\omega)$ and its associated current $I_{\text{em}}(t) = \int \mathrm{d}t' \, [\int \mathrm{d}\omega \, Z^{-1}(\omega) e^{-i(t-t')\omega}] V(t')$.

We may state the central results of this section as follows. The dissipative current that enters the extended RCSJ equation may be written as

$$I_d(t) = I_{\text{qp}}(\tfrac{\hbar}{2e}\dot{\varphi}(t)) + I_{\text{em}}(t), \tag{4.102}$$

where $I_{\text{qp}}(V)$ is the *voltage-biased* quasiparticle current, provided that the rate of change of the voltage is slow compared to the typical time scales of the superconducting electrodes. This is guaranteed if the capacitance of the junction is sufficiently large. Furthermore, the current-phase relation entering the RCSJ equation receives voltage dependent corrections to its equilibrium form. We argue that these are unimportant for a qualitative picture. Finally, we establish the nonlinear fluctuation-dissipation theorem Eq. (4.5) at leading order in the tunnel coupling. We give explicit expressions for quasiparticle current, the current-phase relation, and the noise correlator to all orders in the tunneling coupling.

An equation of motion for the dynamics of the phase difference involves voltages and as such necessitates a nonequilibrium description. For the problem at hand, the Keldysh field integral technique [170, 231] is appropriate: it allows one to isolate the phase difference as the low energy degree of freedom describing the dynamics of the tunneling junction, and provides seamless integration with the Green function formalism necessary to formulate the complicated tunneling processes in a compact manner. This section is structured as follows. In Sec. 4.4.1 we define the microscopic Hamiltonian and sketch how the Keldysh field integral is constructed. We proceed by deriving an effective action for the phase difference, which we then simplify within a semiclassical expansion, in Secs. 4.4.2-4.4.5. Finally, in Secs. 4.4.6 and 4.4.7 we obtain a time-local description of the phase dynamics through an adiabatic approximation and in Sec. 4.4.9 evaluate the resulting expressions in the tunneling regime.

4.4.1 MICROSCOPIC MODEL AND KELDYSH FORMALISM

We model a Josephson junction by two tunnel coupled superconductors. The full Hamiltonian may be decomposed as

$$H = H_L + H_R + H_{\text{tun}} + H_{\text{cap}}, \tag{4.103}$$

where the superconducting electrodes are described by ($\alpha = L/R$)

$$H_\alpha = \int \mathrm{d}^3x \left[\sum_{\sigma\sigma'} \psi^\dagger_{\alpha,\sigma}(x) h_{\sigma\sigma'}(\hat{k}) \psi_{\alpha,\sigma'}(x) - g\, \psi^\dagger_{\alpha,\uparrow}(x) \psi^\dagger_{\alpha,\downarrow}(x) \psi_{\alpha,\downarrow}(x) \psi_{\alpha,\uparrow}(x) \right], \tag{4.104}$$

where $\hat{k} = -i\nabla$ and the tunnel coupling is described by

$$H_{\text{tun}} = \sum_\sigma \left[\vartheta\, \psi^\dagger_{L,\sigma}(0) \psi_{R,\sigma}(0) + \text{h.c.} \right]. \tag{4.105}$$

We specified to simple s-wave singlet pairing to avoid unnecessary complications. Note that our results extend straightforwardly to superconductors with single component order parameter. In contrast to our considerations in Chapter 2, we now explicitly include the spin-orbit coupling of the superconducting electrodes as this represents an essential ingredient for asymmetric current-phase relations in the tunneling model. We model the effects of Coulomb repulsion due to charge imbalances between the electrodes within a capacitive approximation,

$$H_{\text{cap}} = \frac{1}{8C} (Q_L - Q_R)^2. \tag{4.106}$$

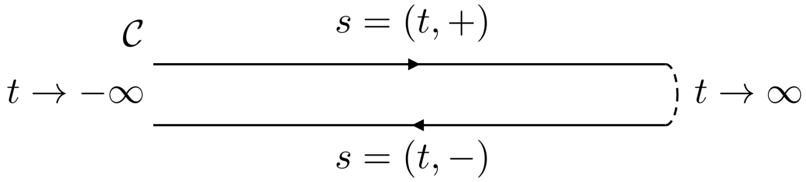

Figure 4.9: Contour $\mathcal{C}$ used in Keldysh formalism. We denote the position along $\mathcal{C}$ by s. The latter can be taken apart into a forward branch and a backward branch, each parametrized by time $t \in \{-\infty, \infty\}$.

Here, the total charge in electrode α is given by

$$Q_\alpha = e \int \mathrm{d}^3x \sum_\sigma \psi^\dagger_{\alpha,\sigma}(x)\psi_{\alpha,\sigma}(x), \tag{4.107}$$

and C denotes the geometric capacitance of the junction. The operator measuring the current across the junction is

$$\mathcal{I} = ie \sum_\sigma \Big[\vartheta\, \psi^\dagger_{L,\sigma}(0)\psi_{R,\sigma}(0) - \text{h.c.}\Big]. \tag{4.108}$$

Note that this can be obtained from H_{tun} by differentiating with respect to the phase of ϑ. Letting $\vartheta \to \vartheta e^{\frac{i}{2}a}$, it is

$$\mathcal{I} = 2e \frac{\partial}{\partial a} H_{\text{tun}}(a)\bigg|_{a=0}. \tag{4.109}$$

The Keldysh field integral formalism extends the functional integral formalism to non-equilibrium many-body systems. As usual one defines a generating functional from which expectation values and correlation functions of observables can be inferred. Here, the generating functional is defined as

$$\mathcal{Z}[\eta] = \mathrm{tr}\left[\mathrm{T}_\mathcal{C} \exp\left\{-i \int_\mathcal{C} \mathrm{d}s\, H_\eta(s)\right\}\rho(t_i \to -\infty)\right], \tag{4.110}$$

where the $\rho(t_i \to -\infty)$ is the initial density matrix in Fock space, s parametrizes the Keldysh contour $\mathcal{C}$ shown in Fig. 4.9, and $T_\mathcal{C}$ is the associated contour ordering symbol. We can decompose the Keldysh contour into a forward and a backward branch parametrized only by time, i.e. we write $s = (\pm, t)$. The moments of a (Schrödinger picture) observable $\mathcal{O}$ can be obtained by coupling the Hamiltonian to a source field η with opposite signs on the two branches of the contour,

$$H_\eta(s) = H + \eta(s)\mathcal{O} = H + \frac{1}{2}\lambda(s)\eta(t)\mathcal{O}. \tag{4.111}$$

Here, we introduced the function $\lambda(s)$ which equals to one on the forward branch, and minus one on the backward branch, $\lambda(s = (\pm, t)) = \pm 1$. The expectation value of $\mathcal{O}$ at time t is then simply

$$\langle \mathcal{O}(t) \rangle = i \frac{\delta}{\delta \eta(t)} \ln \mathcal{Z}[\eta] \bigg|_{\eta=0} . \tag{4.112}$$

Note that the generating functional is normalized such that $\mathcal{Z}[0] = 1$. Higher derivatives of $\ln \mathcal{Z}$ yield symmetrized connected correlation functions of the observable $\mathcal{O}$ (see also App. B.4).

In our case, the Hamiltonian $H(t)$ describes the two coupled superconductors in terms of fermion fields, $\psi \equiv \psi_{L/R,\sigma}(x)$. It is then possible to write the generating function as a Grassmann functional integral [231]

$$\mathcal{Z}[\eta] = \int \mathcal{D}\psi \mathcal{D}\overline{\psi} \, \exp\{iS_\eta[\psi, \overline{\psi}]\} \tag{4.113}$$

with Keldysh action (suppressing the field indices)

$$S_\eta[\psi, \overline{\psi}] = \int_{\mathcal{C}} \mathrm{d}s \left\{ \overline{\psi}(s) i \frac{\partial}{\partial s} \psi(s) - H_\eta(\psi(s), \overline{\psi}(s)) \right\}. \tag{4.114}$$

Note that we have dropped the dependence on the initial density matrix here. To see why we can safely do so, consider the following. We expect on physical grounds that the microscopic degrees of freedom relax on a timescale set by the inverse superconducting gap. In particular, we will not be interested in the microscopic transients but rather in the slow evolution of the phase difference, and hence, only the initial value of the phase difference should be of importance. This can be implemented easily once a classical equation of motion has been derived.

4.4.2 HUBBARD-STRATONOVICH DECOUPLING AND EFFECTIVE PHASE ACTION

In order to proceed, we now decouple those terms in the action which are quartic in the fermion operators by means of a Hubbard-Stratonovich transformation. Consider first the attractive interaction in the superconducting leads. It may be decoupled by introducing the fluctuating complex order parameter field $\Delta_\alpha(x, s) = |\Delta_\alpha|(x, s) \exp\{i\theta_\alpha(x, s)\}$ for both superconductors. This gives

$$\begin{aligned} &\exp\left\{ ig \int_{\mathcal{C}} \mathrm{d}s \int \mathrm{d}^3x \, \overline{\psi}_{\alpha,\uparrow}(x, s) \overline{\psi}_{\alpha,\downarrow}(x, s) \psi_{\alpha,\downarrow}(x, s) \psi_{\alpha,\uparrow}(x, s) \right\} \\ &\propto \int \mathcal{D}\Delta \mathcal{D}\overline{\Delta} \exp\left\{ -i \int_{\mathcal{C}} \mathrm{d}s \int \mathrm{d}^3x \left[\frac{|\Delta_\alpha|^2}{g} + \overline{\Delta}_\alpha \psi_{\alpha,\downarrow} \psi_{\alpha,\uparrow} + \overline{\psi}_{\alpha,\uparrow} \overline{\psi}_{\alpha,\downarrow} \Delta_\alpha \right] \right\}. \end{aligned} \tag{4.115}$$

By gauge invariance, only fluctuations of the phase difference

$$\phi(s) = \theta_L(s) - \theta_R(s) \tag{4.116}$$

are physical. The Jacobian associated with the transformation $\mathcal{D}\Delta\mathcal{D}\overline{\Delta} \to \mathcal{D}|\Delta|\mathcal{D}\phi$ is trivial. Following the discussion in Sec. 2.2, we ignore fluctuations of the order parameter magnitude as well as spatial fluctuations of the order parameter phase, i.e. $\Delta_\alpha(x,s) = \Delta\exp\{i\theta_\alpha(s)\}$, where we set $\Delta \equiv |\Delta| > 0$ and constant. Similarly, the capacitive interaction may be decoupled by introducing a Hubbard-Stratonovich field $V(s)$. With $Q = (Q_L - Q_R)/2$, it is

$$\exp\left\{-i\int_{\mathcal{C}} \mathrm{d}s\, \frac{Q^2(s)}{2C}\right\} \propto \int \mathcal{D}V\, \exp\left\{-i\int_{\mathcal{C}} \mathrm{d}s \left[-\frac{C}{2}V^2(s) - V(s)Q(s)\right]\right\}. \tag{4.117}$$

$V(s)$ describes the voltage fluctuations associated with the charging term.

Now, the action is quadratic in the fermion fields. After performing the associated Grassmann integrals the partition function is (see App. B.5 for details on Grassmann Gaussian integrals in the four-component Nambu framework)

$$\mathcal{Z} \propto \int \mathcal{D}\phi \int \mathcal{D}V\, \exp\left\{i\int_{\mathcal{C}} \mathrm{d}s\, \frac{C}{2}V^2(s) + \frac{1}{2}\,\mathrm{Tr}\ln\left[i\mathcal{G}^{-1}\right]\right\}, \tag{4.118}$$

where the contour-ordered Nambu Green function $\mathcal{G}$ includes the coupling between both leads, and depends on the Hubbard-Stratonovich fields $\phi(s)$ and $V(s)$. We also define the Green function diagonal in the leads, $\mathcal{G}_0 = \mathrm{diag}(\mathcal{G}_{0L}, \mathcal{G}_{0R})$. Setting $\theta_L + \theta_R = 0$, we may write $\mathcal{G}_0$ as

$$\mathcal{G}_0^{-1} = i\frac{\partial}{\partial s} - \left\{\tilde{h}(\hat{k}) + \Delta e^{i\rho_z\frac{\phi(s)}{2}}\tau_+ + e^{-i\rho_z\frac{\phi(s)}{2}}\tau_- - \frac{1}{2}eV(s)\rho_z\tau_z\right\}, \tag{4.119}$$

where we introduce the particle-hole diagonal part of the Bogoliubov-de Gennes Hamiltonian $\tilde{h}(k)$,[4] and define a set of Pauli matrices ρ_i in electrode space (L,R). The trace Tr is over the Keldysh contour, position, electrode space, particle-hole space and spin. It will prove useful to eliminate the phase ϕ from the pairing term by means of a unitary transformation $\mathcal{G}_0^{-1} \to U\mathcal{G}_0^{-1}U^\dagger$ with $U(s,s') = \exp\{-i\rho_z\tau_z\phi(s)/4\}\delta_{\mathcal{C}}(s-s')$. The transformed $\mathcal{G}_0$ takes the form

$$\mathcal{G}_0^{-1} = i\frac{\partial}{\partial s} - \left\{h_{\mathrm{BdG}}(\hat{k}) - \frac{1}{2}\left[eV(s) - \frac{1}{2}\frac{\partial}{\partial s}\phi(s)\right]\rho_z\tau_z\right\}. \tag{4.120}$$

The full Green function $\mathcal{G}$ is related to $\mathcal{G}_0$ via the Dyson equation

$$\mathcal{G} = (1 - \mathcal{G}_0\mathcal{T})^{-1}\mathcal{G}_0 = \mathcal{G}_0 + \mathcal{G}_0\mathcal{T}\mathcal{G}. \tag{4.121}$$

---

[4] Expanding in spin Pauli matrices σ_i, the particle-hole diagonal part of the Bogoliubov-de Gennes Hamiltonian is $\tilde{h}(k) = h_0(\tau_z k)\tau_z + \boldsymbol{h}(\tau_z k)\cdot\boldsymbol{\sigma}$.

In the transformed frame, the tunneling operator $\mathcal{T}$ explicitly depends on the phase difference,

$$\mathcal{T}(x,x';s-s') = \mathcal{T}(s)\delta(x)\delta(x')\delta_C(s-s'), \quad \mathcal{T}(s) = \vartheta e^{\frac{i}{2}\phi(s)\tau_z}\tau_z\rho_+ + \text{h.c.}\,. \tag{4.122}$$

Here, we absorbed any complex phase of ϑ into ϕ such that ϑ is real.

Plugging the Dyson equation into the trace-log part of the action gives two terms. The first term is given by $\operatorname{Tr}\ln[i\mathcal{G}_0^{-1}]$. This is simply the part of action which describes the two superconductors individually. We will only be interested in its dependence on V and ϕ. The leading order term in an expansion in powers of $eV - \frac{1}{2}\partial_s\phi$ is given by

$$\delta S \simeq \frac{1}{2}\text{Vol.} \times \nu_0 \int_C \mathrm{d}s \left[eV(s) - \frac{1}{2}\frac{\partial}{\partial s}\phi(s)\right]^2. \tag{4.123}$$

This essentially pins the voltage $V(s)$ to the phase difference by bulk energies, resulting in the Josephson relation $V = \frac{1}{2e}\dot{\phi}$ (mathematically, this corresponds to evaluating the $\mathcal{D}V$ integral in the stationary phase approximation). The second term is $\operatorname{Tr}\ln[1-\mathcal{G}_0\mathcal{T}]$. This gives rise to the quasiparticle and supercurrent contributions to the action and will be discussed in detail below. At this stage the phase-dependent part of the partition function is

$$\mathcal{Z} \propto \int \mathcal{D}\phi\, \exp\left\{ i\int_C \mathrm{d}s\, \frac{C}{8e^2}\left[\frac{\partial}{\partial s}\phi(s)\right]^2 + \frac{1}{2}\operatorname{Tr}\ln[1-\mathcal{G}_0\mathcal{T}] \right\} \tag{4.124a}$$

$$\equiv \int \mathcal{D}\phi\, \exp\{iS[\phi]\}. \tag{4.124b}$$

Note that in the absence of source fields, once the normalization has been accounted for, it is still $\mathcal{Z} = 1$.

4.4.3 SEMICLASSICAL MEAN-FIELD EQUATIONS

We will now investigate the mean field behavior of $S[\phi]$, i.e. we treat the integration over $\mathcal{D}\phi$ within a stationary phase approximation. We will find that this procedure gives the deterministic classical equation of motion for the phase difference across the Josephson junction.[5] To proceed, we split $\phi(s)$ into even and odd components with respect to the Keldysh contour,

$$\phi(s) = \varphi(t) + \frac{1}{2}\lambda(s)\chi(t). \tag{4.125}$$

Within the classical approximation, φ becomes the degree of freedom associated with the Josephson junction, while χ is a purely quantum object. To see this, note that quantum probabilities

---

[5] Indeed, one may show that this corresponds to the classical limit $\hbar \to 0$ upon reintroducing $s \to s/\hbar$ and rescaling $\chi \to \hbar\chi$, where χ is the quantum component of the phase difference field to be introduced below [170, 231]. Note that $\hbar$ still enters in the capacitive term, but "disappears" once this is expressed in terms of the voltage V.

involve products of amplitudes corresponding to differing forward and backward (conjugate) processes, while classical probabilities involve only the diagonal terms in this expansion. One therefore refers to φ as the classical component and to χ as the quantum component of ϕ, even though both fields receive quantum corrections. Expressed in these variables, the capacitive term in the action becomes

$$\delta S_{\text{cap}} = \frac{C}{4e^2}\int \mathrm{d}t\, \dot{\chi}(t)\dot{\varphi}(t). \tag{4.126}$$

Varying the action with respect to φ and χ gives the mean field equations

$$\frac{C}{4e^2}\ddot{\chi} = -\frac{i}{2}\frac{\delta}{\delta\varphi(t)}\operatorname{Tr}\ln[1-\mathcal{G}_0\mathcal{T}] = \frac{1}{4}\operatorname{tr}\left[\mathcal{G}(t,t)\mathcal{T}(t)\tau_z\rho_z\lambda_z\right], \tag{4.127a}$$

$$\frac{C}{4e^2}\ddot{\varphi} = -\frac{i}{2}\frac{\delta}{\delta\chi(t)}\operatorname{Tr}\ln[1-\mathcal{G}_0\mathcal{T}] = \frac{1}{8}\operatorname{tr}\left[\mathcal{G}(t,t)\mathcal{T}(t)\tau_z\rho_z\right]. \tag{4.127b}$$

Here, we dropped the spatial arguments of the local Green function $\mathcal{G}(t,t') \equiv \mathcal{G}(x=0,x'=0;t,t')$. We also introduced a set of Pauli matrices λ_i encoding the Keldysh contour information, with $\lambda_z = 1$ corresponding to the forward branch and $\lambda_z = -1$ corresponding to the backward branch for a given convolution. In particular, Green functions are now a matrix in Keldysh space,

$$\mathcal{G}(s,s') \equiv \begin{pmatrix} \mathcal{G}^{\mathrm{T}}(t,t') & \mathcal{G}^{<}(t,t') \\ \mathcal{G}^{>}(t,t') & \mathcal{G}^{\tilde{\mathrm{T}}}(t,t') \end{pmatrix}, \tag{4.128}$$

in terms of the time-ordered (s, s' forward), lesser (s forward, s' backward), greater (s backward, s' forward) and anti-time-ordered Green functions (s, s' backward) [237]. We note the identities

$$[AB](s,s') = \int_{\mathcal{C}} \mathrm{d}s''\, A(s,s'')B(s'',s') \equiv \int \mathrm{d}t\, A(t,t'')\lambda_z B(t'',t'), \tag{4.129a}$$

$$\operatorname{Tr}[A] = \int_{\mathcal{C}} \mathrm{d}s\, \operatorname{tr}[A(s,s)] \equiv \int \mathrm{d}t\, \operatorname{tr}[A(t,t)\lambda_z], \tag{4.129b}$$

where in the final expressions A and B are considered matrices in Keldysh space. The tunneling operator may now be expressed as (dropping the delta functions in real space)

$$\mathcal{T}(t) = \vartheta e^{\frac{i}{2}\tau_z(\varphi(t)+\frac{1}{2}\lambda_z\chi(t))}\tau_z\rho_+ + \text{h.c.}\,. \tag{4.130}$$

The Green function $\mathcal{G}$ depends on φ and χ at all times, rendering Eqs. (4.127) highly nonlocal in time. After expanding the trace in Keldysh space, the mean field equations involve the combinations

$$\mathcal{G}^{\mathrm{T}}(t,t) \mp \mathcal{G}^{\tilde{\mathrm{T}}}(t,t). \tag{4.131}$$

It is a rather general fact that at equal times the time-ordered and anti-time ordered Green functions coincide with $\mathcal{G}^{>}(t,t)$ [231]. Employing further the facts that $\mathcal{T}$ is off-diagonal in electrode space, and that off-diagonal components of the greater and lesser Green function coincide, the mean field equations become

$$\ddot{\chi} = 0, \qquad \frac{C}{4e^2}\ddot{\varphi} = \frac{1}{4}\,\mathrm{tr}\,[\mathcal{G}^<(t,t)\mathcal{T}(t)\tau_z\rho_z]. \tag{4.132}$$

By construction, the quantum component χ vanishes at the turning point of the Keldysh contour, i.e. $\chi(T/2) = 0$, where for convenience we restricted the Keldysh contour to the interval $t \in [-T/2, T/2]$ with $T \to \infty$. However, the phase field can wind along the contour, $\phi_{\text{final}} = \phi_{\text{initial}} + 2\pi W$, where $W \in \mathbb{Z}$ is the winding number. With $\ddot{\chi} = 0$ this implies $\chi(-T/2) = -2\pi W$ or $\chi(t) = 2\pi W(t - T/2)/T$. The winding of χ encodes the quantization of the transferred charge.[6] For $T \to \infty$ it leads to a near constant phase shift in $\mathcal{T}$ and, consequently, in $\mathcal{G}$, which can safely be ignored [170]. The mean field equation for φ corresponds to a time-nonlocal version of the noiseless RCSJ equation. This is not what we are interested in, yet. In order to obtain the Langevin term, we need to expand the action in the fluctuations of the quantum component χ around its mean field value, zero.

4.4.4 Mean-field current and current-current correlation function

In order to identify the form of physical observables in terms of the phase difference $\phi(s)$, we introduce source fields. Consider first the current operator. Naively, we would introduce a source term $\delta H_\eta(s) = \lambda(s)\eta(t)\mathcal{I}$. Instead, we introduce the source field in the phase of ϑ and make use of Eq. (4.109). Specifically, we let $\vartheta \to \vartheta \exp\{\frac{i}{4}\lambda(s)\eta(t)\}$. In the phase action this amounts to a shift $\chi(t) \to \chi(t) + \eta(t)$. Up to contact terms, this leads to the same correlation functions as the source term $\delta H_\eta(s) = \lambda(s)\eta(t)\mathcal{I}$. The corresponding (unnormalized) generating functional is

$$\mathcal{Z}[\eta] = \int \mathcal{D}\varphi\mathcal{D}\chi\ \exp\{iS[\varphi, \chi + \eta]\}. \tag{4.134}$$

We now evaluate this within the mean field approximation. The stationary phase approximation gives

$$\mathcal{Z}[\eta] \simeq \exp\{iS[\varphi_{\text{mf}}, \chi_{\text{mf}} + \eta]\}, \tag{4.135}$$

---

[6] To motivate this, consider the following. First, note that the partition function $\mathcal{Z}$ receives contributions from all windings, i.e. it involves a sum over W. Next, plug the mean field solution for $\chi(t)$ into δS_{cap}. This gives

$$\sum_W \exp\left\{\frac{2\pi i W}{T}\int_{-T/2}^{T/2} \mathrm{d}t\,\frac{C\dot{\varphi}}{4e^2}\right\} = \sum_W \exp\left\{2\pi i W\frac{C\overline{V}}{2e}\right\}, \tag{4.133}$$

where we used the second Josephson relation and denoted the time-averaged voltage $\overline{V}$. This sum receives significant contributions only if the mean transferred charge is $\overline{Q} = C\overline{V}$ is quantized in units of $2e$. This argument may be extended to the instantaneous charge $Q(t)$ [170].

where φ_{mf} and χ_{mf} are the solutions to the mean field Eqs. (4.132). In particular, $\chi_{\mathrm{mf}} \simeq 0$, giving $\mathcal{Z}[\eta] \simeq \exp\{iS[\varphi_{\mathrm{mf}}, \eta]\}$. Connected correlation functions are obtained from $\ln \mathcal{Z}[\eta] = iS[\varphi_{\mathrm{mf}}, \eta]$. Expanding in powers of η thus gives the mean, variance and higher cumulants of the mean field current,

$$S[\varphi, \eta] = -\frac{1}{2e} \int \mathrm{d}t\, I[\varphi](t)\eta(t) + \frac{i}{8e^2} \int \mathrm{d}t \int \mathrm{d}t'\, \eta(t) K[\varphi](t, t')\eta(t') + \dots . \tag{4.136}$$

There is no zeroth order in η as the evolution along the forward and backward contours cancel in the absence of η or χ (this corresponds to the normalization condition of the original Keldysh generating functional, Eq. (4.110)). The mean field cumulants depend on the full history of, that is, are functionals of $\varphi(t)$. Such dependence is denoted by the argument in rectangular brackets. In order to proceed, we have to expand the tunneling operator $\mathcal{T}(t)$ in powers of $\chi + \eta$,

$$\mathcal{T} = \mathcal{T}_0 + \mathcal{T}_1(\chi + \eta) + \frac{1}{2}\mathcal{T}_2(\chi + \eta)^2 + \dots = \mathcal{T}_0 \sum_{n=0} \frac{1}{n!} \left[-\frac{i}{4} \tau_z \rho_z \lambda_z (\chi + \eta) \right]^n . \tag{4.137}$$

Here, the leading order tunneling operator $\mathcal{T}_0(t)$ is obtained from $\mathcal{T}(t)$ by setting χ and η to zero. Correspondingly, the trace-log term in the mean field action becomes

$$-\frac{i}{2} \operatorname{Tr} \ln \left[1 - \mathcal{G}_0 \mathcal{T}\right] = = \frac{i}{2} \operatorname{Tr} \left[\mathcal{G}\mathcal{T}_1 \eta + \frac{1}{2} \mathcal{G}\mathcal{T}_2 \eta^2 - \frac{1}{2} \mathcal{G}\mathcal{T}_1 \eta \mathcal{G}\mathcal{T}_1 \eta \right] + \dots . \tag{4.138}$$

Here, the full Green function is now redefined via

$$\mathcal{G} = (1 - \mathcal{G}_0 \mathcal{T}_0)^{-1} \mathcal{G}_0 = \mathcal{G}_0 + \mathcal{G}_0 \mathcal{T}_0 \mathcal{G} . \tag{4.139}$$

In particular, it no longer depends on χ or η.

We now investigate Eq. (4.138) term by term. The linear order evaluates to

$$\operatorname{Tr} \{\mathcal{G}\mathcal{T}_1 \eta\} = -\frac{i}{2} \int \mathrm{d}t\ \operatorname{tr} \{\mathcal{G}^{<}(t, t) \mathcal{T}_0(t) \tau_z \rho_z\} \eta(t) . \tag{4.140}$$

From this the mean field current expectation value may be read off as

$$I[\varphi](t) \equiv \langle \mathcal{I}(t) \rangle_{\mathrm{mf}} = \frac{C}{2e} \ddot{\varphi} - \frac{e}{2} \operatorname{tr} \{\mathcal{G}^{<}(t, t) \mathcal{T}_0(t) \tau_z \rho_z\} = I_{\mathrm{cap}} + I_{\vartheta} . \tag{4.141}$$

The mean field equation for φ thus simply corresponds to $I[\varphi](t) = 0$. In the second equality, we have separated the current into a capacitive contribution, I_{cap}, and a tunneling contribution, I_{ϑ}, for later convenience. The mean field tunneling current I_{ϑ} can be viewed as the expectation value of the current operator $\mathcal{I}(t)$ with enforced time dependent phase difference given by $\varphi(t)$. To see this, we expand in electrode space,

$$I_\vartheta = \frac{e\vartheta}{2}\,\mathrm{tr}\left\{\mathcal{G}^<_{RL}(t,t)e^{\frac{i}{2}\varphi(t)\tau_z} - \mathcal{G}^<_{LR}(t,t)e^{-\frac{i}{2}\varphi(t)\tau_z}\right\}. \tag{4.142}$$

In the Heisenberg picture, the current operator in the presence of the applied phase difference $\varphi(t)$ is given by [238]

$$\mathcal{I}_\varphi(t) = ie\vartheta\sum_\sigma\left[e^{\frac{i}{2}\varphi(t)}\psi^\dagger_{L,\sigma}(0,t)\psi_{R,\sigma}(0,t) - e^{-\frac{i}{2}\varphi(t)}\psi^\dagger_{R,\sigma}(0,t)\psi_{L,\sigma}(0,t)\right]. \tag{4.143}$$

Noting that $\mathcal{G}^<_{ab} = i\langle\Psi^\dagger_b\Psi_a\rangle$ it becomes clear that the expectation value of $\mathcal{I}_\varphi$ clearly reproduces Eq. (4.142).

We investigate now the quadratic order terms which give rise to the symmetrized or classical current-current correlation function

$$K[\varphi](t,t') \equiv \frac{1}{2}\langle\mathcal{I}(t)\mathcal{I}(t') + \mathcal{I}(t')\mathcal{I}(t)\rangle_{\mathrm{mf}}. \tag{4.144}$$

Consider first the term $\frac{i}{4}\,\mathrm{Tr}\{\mathcal{G}\mathcal{T}_2\eta^2\}$. Upon evaluating the Keldysh trace, this contains the equal time combination $\mathcal{G}^T(t,t) - \mathcal{G}^{\tilde{T}}(t,t)$ and thus vanishes. The second quadratic order term, $\mathrm{Tr}\,\{\mathcal{G}\mathcal{T}_1\eta\mathcal{G}\mathcal{T}_1\eta\}$, evaluates to

$$-\frac{1}{16}\int \mathrm{d}t\int \mathrm{d}t'\,\eta(t)\,\mathrm{tr}\,\{\mathcal{G}(t,t')\mathcal{T}_0(t')\tau_z\rho_z\mathcal{G}(t',t)\mathcal{T}_0(t)\tau_z\rho_z\}\eta(t'). \tag{4.145}$$

We can simplify this further by expanding in Keldysh indices. Expressing the time-ordered and anti-time-ordered Green functions in terms of $\mathcal{G}^>$ and $\mathcal{G}^<$ and using the cyclicity of the trace, we obtain

$$K[\varphi](t,t') = \frac{e^2}{4}\,\mathrm{tr}\,[\mathcal{G}^<(t,t')\mathcal{T}_0(t')\tau_z\rho_z\mathcal{G}^>(t',t)\mathcal{T}_0(t)\tau_z\rho_z + \,t \longleftrightarrow t'\,]. \tag{4.146}$$

As in the case of $I_\vartheta[\varphi](t)$ above, $K[\varphi](t,t')$ precisely corresponds to the symmetrized noise correlator one would obtain in the presence of an externally applied time-dependent phase difference $\varphi(t)$ [239]. In other words, the functional $K[\varphi]$ may be written as $K[\varphi](t,t') = \frac{1}{2}\langle\mathcal{I}_\varphi(t)\mathcal{I}_\varphi(t') + \mathcal{I}_\varphi(t')\mathcal{I}_\varphi(t)\rangle$.

4.4.5 Semiclassical expansion and Langevin equation

The mean field equation $I[\varphi](t) = 0$ provides an equation governing the evolution of the phase difference φ but it captures neither quantum nor thermal fluctuations. We would like a classical (Langevin) equation of motion which includes the fluctuations described by the Gaussian current fluctuations, i.e. by K. To this end, we need to expand around the classical mean field saddle point for the quantum component of the phase difference field, $\chi_{\mathrm{mf}} = 0$. In the previous section we have seen that an expansion in χ is equivalent to expanding in the source term conjugate to the current operator η. Thus, an expansion to second order in $\delta\chi = \chi - \chi_{\mathrm{mf}} = \chi$ achieves the desired classical equation including Gaussian fluctuations. Writing the time integrals as matrix multiplication, the action is

$$S[\varphi, \chi + \eta] = -\frac{1}{2e} I^T[\varphi](\chi + \eta) + \frac{i}{8e^2}(\chi + \eta)^T K[\varphi](\chi + \eta) + \dots . \tag{4.147}$$

To proceed, we introduce the Langevin current $\xi(t)$ via the Hubbard-Stratonovich decoupling

$$\exp\left\{-\frac{1}{8e^2}\chi^T K[\varphi]\chi\right\} \propto \int \mathcal{D}\xi \, \exp\left\{-\frac{1}{2}\xi^T K^{-1}[\varphi]\xi - \frac{i}{2e}\xi^T \chi\right\}. \tag{4.148}$$

Note that $\xi(t)$ has units of a current. This replaces the χ^2-term in the action. Now χ features only linearly in the action and we would like to perform the associated functional integral. However, it is of advantage to first simplify the cross terms $\eta^T K \chi + \chi^T K \eta = 2\eta^T K \chi$ using the identity

$$\exp\left\{-\frac{1}{4e^2}\eta^T K \chi\right\} \exp\left\{-\frac{i}{2e}\xi^T \chi\right\} = \exp\left\{-\frac{i}{2e}\eta^T K \frac{\delta}{\delta\xi}\right\} \exp\left\{-\frac{i}{2e}\xi^T \chi\right\}. \tag{4.149}$$

The integration over χ now results in a functional delta function involving no source terms. With this the (unnormalized) generating functional becomes

$$\mathcal{Z}[\eta] = \int \mathcal{D}\varphi \mathcal{D}\xi \, \delta[I[\varphi] + \xi] \exp\{iS_{\mathrm{source}}[\eta]\} \exp\left\{-\frac{1}{2}\xi^T K^{-1}[\varphi]\xi\right\}. \tag{4.150}$$

The exponential involving the source action is

$$\exp\{iS_{\mathrm{source}}[\eta]\} = \exp\left\{-\frac{i}{2e}\left(I[\varphi] - K[\varphi]\frac{\delta}{\delta\xi}\right)\eta - \frac{1}{8e^2}\eta^T K[\varphi]\eta\right\}, \tag{4.151}$$

where we integrated by parts once so that the $\delta/\delta\xi$ derivative acts on $e^{-\frac{1}{2}\xi^T K^{-1}\xi}$. Within our approximation, this has to be expanded to second order in η. Careful evaluation gives

$$\exp\{iS_{\mathrm{source}}[\eta]\} = 1 - \frac{i}{2e}(I[\varphi] + \xi)^T \eta - \frac{1}{8e^2}(I[\varphi] + \xi)^T \eta (I[\varphi] + \xi)^T \eta + \dots . \tag{4.152}$$

Note that the $\eta^T K\eta$-term has dropped out. The noise correlations are now encoded in the fluctuating current ξ alone. We finally arrive at the main result of this section,

$$\mathcal{Z}[\eta] = \int \mathcal{D}\varphi \left\langle \delta\left[\frac{C}{2e}\ddot{\varphi}(t) + I_\vartheta[\varphi](t) + \xi(t)\right] \exp\{iS_{\text{source}}[\eta]\} \right\rangle_\xi . \tag{4.153}$$

The delta function enforces that partition function receives contributions only from trajectories $\varphi(t)$ which obey the classical equation of motion

$$\frac{C}{2e}\ddot{\varphi}(t) + I_\vartheta[\varphi](t) + \xi(t) = 0. \tag{4.154}$$

Of course, this is simply the condition that the junction conserves the current. Furthermore, the trajectories need to be averaged with respect to the fluctuating current $\xi(t)$. Note that the correlations of ξ depend on the trajectory $\varphi(t)$. A bias current can readily included by an additional source term

$$S_{\text{bias}}[\phi] = \frac{1}{2e}\int_C \mathrm{d}s\, I_b(t)\phi(s) = \frac{1}{2e}\int \mathrm{d}t\, I_b(t)\chi(t). \tag{4.155}$$

In this case the right hand side of Eq. (4.154) is given by I_b. While similar to the extended RCSJ equations used in the first sections of this chapter, this equation is not yet very useful as it is highly time-nonlocal due to the dependence on the history of $\varphi(t)$. In the next section, we will perform an adiabatic approximation to remedy this.

4.4.6 GREEN FUNCTIONS IN ADIABATIC APPROXIMATION

In order to derive a time-local equation of motion, we assume that φ and $\dot{\varphi}$ vary sufficiently slowly compared to the decay of the uncoupled Green function $\mathcal{G}_0$. This assumption will have to be checked a posteriori.

Before we get to the adiabatic approximation, we define a number of useful expressions. First, we split $\mathcal{G}$ into diagonal and off-diagonal parts in electrode space,

$$\mathcal{G} = \mathcal{G}^{\text{d}} + \mathcal{G}^{\text{od}}, \quad \mathcal{G}^{\text{d}} = \begin{pmatrix} \mathcal{G}_{LL} & 0 \\ 0 & \mathcal{G}_{RR} \end{pmatrix}, \quad \mathcal{G}^{\text{od}} = \begin{pmatrix} 0 & \mathcal{G}_{LR} \\ \mathcal{G}_{RL} & 0 \end{pmatrix}. \tag{4.156}$$

The diagonal Green function now involves only even powers in $\mathcal{T}_0$ and hence satisfies the Dyson equation

$$\mathcal{G}^{\text{d}} = \mathcal{G}_0 + \mathcal{G}_0\Sigma\mathcal{G}^{\text{d}}, \quad \Sigma = \mathcal{T}_0\mathcal{G}_0\mathcal{T}_0. \tag{4.157}$$

The self energy Σ renormalizes the motion within a given electrode due to detours into the other electrode. It is diagonal in electrode space. The off-diagonal Green function can be expressed in terms of $\mathcal{G}^{\mathrm{d}}$ and Σ via

$$\mathcal{G}^{\mathrm{od}} = \mathcal{G}_0 \mathcal{T}_0 \mathcal{G}^{\mathrm{d}}. \tag{4.158}$$

The mean field current involves the off-diagonal Green function. Exploiting the cyclicity of the trace it now may be written compactly as

$$I_\vartheta[\varphi](t) = \frac{e}{2} \operatorname{tr} \Big\{ \big[\Sigma \mathcal{G}^{\mathrm{d}}\big]^<(t,t) \tau_z \rho_z \Big\}. \tag{4.159}$$

We also introduce a dressed self-energy,

$$\boldsymbol{\Sigma} = \mathcal{T}_0 \mathcal{G} \mathcal{T}_0, \tag{4.160}$$

as this allows to write the noise correlation function in a compact manner, given by

$$K[\varphi](t,t') = \frac{e^2}{4} \operatorname{tr} \{ \boldsymbol{\Sigma}^<(t,t') \tau_z \rho_z \mathcal{G}^>(t',t) \tau_z \rho_z + \, t \longleftrightarrow t' \}. \tag{4.161}$$

We now come to the adiabatic expansion. To this end we transform the Green functions to the Wigner representation. This amounts to a Fourier transform with respect to the time difference $\delta = t - t' \to \omega$, while the center of mass time $\tau = (t + t')/2$ is left as is. In the Wigner representation the self energy is given by

$$\Sigma(\tau;\omega) = \int \mathrm{d}\delta \, e^{i\omega\delta} \, \Sigma(\tau + \tfrac{\delta}{2}, \tau - \tfrac{\delta}{2}) \tag{4.162a}$$

$$= \int \mathrm{d}\delta \, e^{i(\omega-\epsilon)\delta} \, \mathcal{T}_0\big(\tau + \tfrac{\delta}{2}\big) \mathcal{G}_0(\epsilon) \mathcal{T}_0\big(\tau - \tfrac{\delta}{2}\big). \tag{4.162b}$$

We assume that $\mathcal{G}_0(\delta)$ decays sufficiently fast compared to the variation of φ, so that the integral receives contributions only from small δ. We can therefore approximate

$$\varphi(\tau \pm \tfrac{\delta}{2}) \simeq \varphi(\tau) \pm \frac{\delta}{2} \dot{\varphi}(\tau). \tag{4.163}$$

With this, the Wigner representation self energy becomes

$$\Sigma_L(\tau;\omega) \simeq \vartheta^2 \begin{pmatrix} G^e_{0R}(\omega_+) & -F^{eh}_{0R}(\omega) e^{i\varphi(\tau)} \\ -F^{he}_{0R}(\omega) e^{-i\varphi(\tau)} & G^h_{0R}(\omega_-) \end{pmatrix}, \tag{4.164}$$

with Σ_R obtained by $R \to L$, $\omega_\pm \to \omega_\mp$ and $\varphi \to -\varphi$. Here, we defined $\omega_\pm = \omega \pm \frac{\dot{\varphi}(\tau)}{2} \equiv \omega \pm eV(\tau)$, and introduced the normal and anomalous components G (G_0) and F (F_0) of the Nambu Green function $\mathcal{G}$ ($\mathcal{G}_0$), respectively. Note that they are still matrices in spin-space.

Importantly the slow τ dependence enters of Σ enters solely through the phase difference $\varphi(\tau)$, as well as the voltage $V(\tau) = \frac{1}{2e}\dot{\varphi}(\tau))$. We emphasize this by writing

$$\Sigma(\tau;\omega) \simeq \Sigma(\varphi(\tau), V(\tau);\omega), \tag{4.165}$$

where the right hand side is defined by the adiabatic approximation goven in Eq. (4.164). It is useful to expand the self energy in powers of $e^{i\varphi}$, i.e.

$$\Sigma(\varphi, V;\omega) = \sum_m \Sigma_m(V;\omega)e^{im\varphi},\ \Sigma_m(V;\omega) = \int \frac{\mathrm{d}\varphi}{2\pi}\,\Sigma(\varphi, V;\omega)e^{-im\varphi}. \tag{4.166}$$

Clearly, the only nonzero terms are $m = -1, 0, 1$.

We now want to argue that, at the same level of approximation, also the full Green function depends only on τ through φ and V. We can do so order by order in pertubation theory. To this end note that the Dyson equation, Eq. (4.157), has the perturbative solution

$$\mathcal{G}^{\mathrm{d}} = \sum_{n=0}^{\infty}(\mathcal{G}_0\Sigma)^n\mathcal{G}_0. \tag{4.167}$$

To evaluate the convolutions in the Wigner picture we employ the Moyal product

$$[ab](\tau;\omega) = a(\tau;\omega)\lambda_z \exp\Big\{\tfrac{i}{2}\overleftrightarrow{\mathcal{D}}\Big\}b(\tau;\omega),\quad \overleftrightarrow{\mathcal{D}} = \frac{\overleftarrow{\partial}}{\partial\omega}\frac{\overrightarrow{\partial}}{\partial\tau} - \frac{\overleftarrow{\partial}}{\partial\tau}\frac{\overrightarrow{\partial}}{\partial\omega}. \tag{4.168}$$

The τ dependence of Eq. (4.167) originates solely from $\varphi(\tau)$ and $V(\tau)$ in Σ. We systematically neglect $\ddot{\varphi}$ and higher derivatives. This translates to

$$\overleftrightarrow{\mathcal{D}} \simeq 2eV(\tau)\left(\frac{\overleftarrow{\partial}}{\partial\omega}\frac{\overrightarrow{\partial}}{\partial\varphi(\tau)} - \frac{\overleftarrow{\partial}}{\partial\varphi(\tau)}\frac{\overrightarrow{\partial}}{\partial\omega}\right). \tag{4.169}$$

Using the definition of the shift operator $\exp\{a\frac{\partial}{\partial_x}\}f(x) = f(x{+}a)$, we then may approximate the first order term in the expansion Eq. (4.167), $[\mathcal{G}_0\Sigma\mathcal{G}_0](\tau;\omega)$, as

$$\begin{aligned}\sum_m \mathcal{G}_0(\omega)\lambda_z \exp\Big\{ieV\tfrac{\overleftarrow{\partial}}{\partial\omega}\tfrac{\overrightarrow{\partial}}{\partial\varphi}\Big\}\Sigma_m(V;\omega)e^{im\varphi}\exp\Big\{-ieV\tfrac{\overleftarrow{\partial}}{\partial\varphi}\tfrac{\overrightarrow{\partial}}{\partial\omega}\Big\}\lambda_z\mathcal{G}_0(\omega)&\\ = \sum_m \mathcal{G}_0(\omega - meV)\lambda_z\Sigma_m(V;\omega)\lambda_z\mathcal{G}_0(\omega + meV)e^{im\varphi}&\end{aligned} \tag{4.170}$$

Again, τ-dependence enters only via φ and V, so that we may write

$$[\mathcal{G}_0\Sigma\mathcal{G}_0](\tau;\omega) \simeq [\mathcal{G}_0\Sigma\mathcal{G}_0](\varphi(\tau), V(\tau);\omega). \tag{4.171}$$

The same arguments go through for higher orders. Eq. (4.167) thus implies that within the adiabatic approximation also the Wigner picture $\mathcal{G}^{\mathrm{d}}$ depends on τ only implicitly through the phase and the voltage, i.e.

$$\mathcal{G}^{\mathrm{d}}(\tau;\omega) \equiv \mathcal{G}^{\mathrm{d}}(\varphi(\tau), V(\tau);\omega). \tag{4.172}$$

In particular, this implies that it can also be expanded as

$$\mathcal{G}^{\mathrm{d}}(\varphi, V;\omega) = \sum_m \mathcal{G}^{\mathrm{d}}_m(V;\omega)e^{im\varphi}. \tag{4.173}$$

By evaluating the current and the noise correlator in terms of the adiabatic Green function, the equation of motion Eq. (4.154) is rendered time-local. In order to solve the Dyson equation in the adiabatic approximation at all orders one has to resort to numerics (see App. B.6).

4.4.7 CURRENT AND NOISE IN ADIABATIC APPROXIMATION

We now derive a time-local expression for the current, i.e. an expression

$$I_\vartheta[\varphi](t) \equiv I_\vartheta(\varphi(t), V(t)). \tag{4.174}$$

From Eq. (4.159) it follows that (suppressing the voltage dependence in the arguments of the right hand side)

$$I_\vartheta(\varphi, V) = \frac{e}{2}\int \frac{\mathrm{d}\omega}{2\pi}\sum_{mn} \mathrm{tr}\left\{\left[\Sigma_m(\omega - meV)\lambda_z\mathcal{G}^{\mathrm{d}}_n(\omega + neV)\right]^<\tau_z\rho_z\right\}e^{i(m+n)\varphi}. \tag{4.175}$$

Importantly, if one sets $\varphi = 2eVt + \varphi_0$, this is just the voltage-bias expression for the tunneling current [238, 240]. We see that in the adiabatic approximation the tunneling current entering the classical equation of motion for the phase difference φ is the voltage-bias current evaluated for the instantaneous voltage and phase difference. The tunneling current satisfies the Fourier expansion (where we shifted $\omega \to \omega - meV$)

$$I_\vartheta(\varphi, V) = \sum_m I_m(V)e^{im\varphi}, \tag{4.176a}$$

$$I_m(V) = \frac{e}{2}\int \frac{\mathrm{d}\omega}{2\pi}\sum_n \mathrm{tr}\left\{\left[\Sigma_{m-n}(\omega - meV)\lambda_z\mathcal{G}^{\mathrm{d}}_n(\omega)\right]^<\tau_z\rho_z\right\}. \tag{4.176b}$$

The reality of the tunneling current manifests in $I_m = I^*_{-m}$.

We treat the noise correlator K in a similar fashion. In the adiabatic approximation, K depends explicitly only on the time difference δ, while all slow τ dependence enters only through the dependence on $\varphi(\tau)$ and $V(\tau)$, i.e.

$$K[\varphi](t,t') \simeq K(\varphi(\tau), V(\tau); \delta). \tag{4.177}$$

In the Wigner picture the noise correlator is

$$K(\varphi, V; \omega) = \frac{e^2}{4} \sum_{\pm} \int \frac{\mathrm{d}\epsilon}{2\pi} \operatorname{tr}\left\{\mathbf{\Sigma}^<(\varphi, V; \epsilon \pm \omega)\tau_z\rho_z \mathcal{G}^>(\varphi, V; \epsilon)\tau_z\rho_z\right\}. \tag{4.178}$$

Note that K involves only symmetric in frequency noise. Indeed, odd frequency noise is related to quantum statistics of the environment and thus disappears in the classical approximation [195]. Here, the Wigner picture dressed self-energy in the adiabatic approximation, $\mathbf{\Sigma}(\varphi, V; \omega)$, takes the form

$$\vartheta^2 \begin{pmatrix} G^e_{RR}(\omega + eV) & -F^{eh}_{RR}(\omega)e^{i\varphi} & G^e_{RL}(\omega)e^{i\varphi} & -F^{eh}_{RL}(\omega + eV) \\ -F^{he}_{RR}(\omega)e^{-i\varphi} & G^h_{RR}(\omega - eV) & -F^{he}_{RL}(\omega - eV) & G^h_{RL}(\omega)e^{-i\varphi} \\ G^e_{LR}(\omega)e^{-i\varphi} & -F^{eh}_{LR}(\omega - eV) & G^e_{LL}(\omega - eV) & -F^{eh}_{LL}(\omega)e^{-i\varphi} \\ -F^{he}_{LR}(\omega + eV) & G^h_{LR}(\omega)e^{i\varphi} & -F^{he}_{LL}(\omega)e^{i\varphi} & G^h_{LL}(\omega + eV) \end{pmatrix}. \tag{4.179}$$

Note that the Fourier expansion of $\mathbf{\Sigma}$ does not truncate like the one of Σ. Furthermore, as $\mathcal{G}$ includes terms with odd powers of $\mathcal{T}_0$, the Fourier expansions of $\mathcal{G}$ and Ω include half-integer m. However, due to the trace, the noise correlator is even-powered in $\mathcal{T}$, and its Fourier series involves only integer terms. It is given by

$$K(\varphi, V; \omega) = \sum_m K_m(V; \omega) e^{im\varphi}, \tag{4.180a}$$

$$K_m(V; \omega) = \frac{e^2}{4} \sum_{\pm} \int \frac{\mathrm{d}\epsilon}{2\pi} \sum_n \operatorname{tr}\left\{\mathbf{\Sigma}^<_{m-n}(V; \epsilon \pm \omega)\tau_z\rho_z \mathcal{G}^>_n(V; \epsilon)\tau_z\rho_z\right\}. \tag{4.180b}$$

Finally, in order to obtain a truly time-local equation of motion, the noise needs to be memoryless. This amounts to the Markovian approximation

$$K(\varphi, V; t - t') \simeq K(\varphi, V)\delta(t - t'), \; K(\varphi, V) = K(\varphi, V; \omega = 0). \tag{4.181}$$

This is the white noise approximation to the voltage-bias noise of the tunneling current [239].

4.4.8 INTERIM SUMMARY

We briefly summarize the result of this extended calculation. We have shown that, within the adiabatic approximation, the classical equation of motion governing a tunneling Josephson contact is given by a Langevin-type equation for the phase difference φ,

$$\frac{C}{2e}\ddot{\varphi}(t) + I_\vartheta(\varphi(t), \tfrac{1}{2e}\dot{\varphi}(t)) + \delta I(t) = I_b(t). \tag{4.182}$$

Here, the fluctuating force is the generalized Johnson-Nyquist noise [we renamed $\xi \to \delta I$ in order to adapt to the notation of Secs. 4.1]. It satisfies

$$\langle \delta I(t) \delta I(t') \rangle = K(\varphi(t), \tfrac{1}{2e}\dot{\varphi}(t))\delta(t - t'). \tag{4.183}$$

The tunneling current $I_\vartheta = I_\vartheta(\varphi, V)$ is given by the voltage-bias expectation value of the tunneling current operator [238],

$$I_\vartheta(\varphi, V) = \langle \mathcal{I}_{\varphi=2eVt}(t) \rangle \Big|_{t \to \frac{\varphi}{2eV}}. \tag{4.184}$$

Similarly, the noise power $K(\varphi, V)$ is given by the zero-frequency component of the symmetrized current-current correlation function with voltage-bias V [239].

Eq. (4.182) provides a microscopic basis for the phenomenological extended RCSJ model in Eq. (4.3). To see this, consider the expansion of the tunneling current, $I_\vartheta = \sum_m I_m(V)e^{im\varphi}$. Clearly, the φ independent part of the current gives rise to the dissipative current

$$I_d(V) = I_0(V) \equiv I_{\mathrm{qp}}(V). \tag{4.185}$$

We thus identify I_0 with the quasiparticle current across the junction. Similarly, at zero voltage, the phase dependent part of the current defines the current-phase relation,

$$I_s(\varphi) \equiv \sum_{m \geq 1} I_m(0)e^{im\varphi}. \tag{4.186}$$

The question arises what should be made of the mixed, i.e. phase and voltage dependent, contribution

$$\sum_{m \geq 1} [I_m(V) - I_m(0)]e^{im\varphi}. \tag{4.187}$$

Here, we take the radical approach and neglect them. We base this on the following observations: In the trapped state voltage is absent and the mixed contribution vanishes. In the running state, exponents involving φ become quickly oscillating terms and their effect is averaged out. Of course, this is a very coarse picture. In particular, thermal excitations lead to a small oscillating voltage in the trapped state. Furthermore, the potential landscape at some mean running state voltage is affected by the mixed terms. Thus, while they are not expected to affect the physical mechanisms governing the Josephson tunnel junction the mixed terms should be included if quantitative predictions are necessary. Note that the current noise needs to be approximated accordingly, leaving only the phase-independent component $K_0(V)$.

Our calculation extends the Ambegaokar-Eckern-Schön theory [226, 227] in several essential ways: First, we derived the tunneling action to all orders in ϑ, thereby capturing higher order processes such as multiple Andreev reflections which become relevant at larger normal state conductance [238, 240]. Second, we showed that the full voltage-bias nonlinear quasiparticle current enters the RCSJ equation provided the voltage varies sufficiently slowly. Finally, our considerations show that the nonlinear noise kernel is linked to the nonlinear quasiparticle current. In the following section we will make this statement more precise.

So far we have not commented on the validity of the adiabatic approximation. It is well-controlled provided that $\ddot{\varphi}\delta^2 \ll 1$, where the time scale δ is set by the decay of $\mathcal{G}_0$. Ignoring fluctuations, the acceleration of the phase difference satisfies $\delta^2\ddot{\varphi} = \delta^2(I_\vartheta - I_b)/C$. Thus, we can always guarantee that the adiabatic approximation is accurate by demanding sufficiently large capacitance C. This is consistent with the classical picture as well as the low temperature expansion of the noise correlator in Sec. 4.3.1.

4.4.9 TUNNELING REGIME

We have not yet investigated how nonreciprocity enters into the quasiparticle current or into the current-phase relation. To gain further insight into these questions we will now apply our theory to the tunneling regime: If the dimensionless tunnel coupling

$$\gamma = (\nu_0 \pi \vartheta)^2 \tag{4.188}$$

is sufficiently small only processes involving few transfers of electrons and holes contribute significantly to the tunneling current. Here, we keep terms only to the leading order γ^1, corresponding to the incoherent transfer of a single electron or hole, or the coherent transfer of a Cooper pair.

In order to find the tunneling current we may thus replace $\mathcal{G}^{\mathrm{d}}$ by $\mathcal{G}_0$ in Eq. (4.159). Employing the adiabatic approximation and expanding in Fourier modes this gives

$$\begin{aligned} I_m(V) &= \frac{e}{2}\int \frac{\mathrm{d}\omega}{2\pi}\,\mathrm{tr}\left\{[\Sigma_m(\omega - meV)\lambda_z\mathcal{G}_0(\omega)]^<\tau_z\rho_z\right\} && (4.189\text{a})\\ &= \frac{e}{2}\int \frac{\mathrm{d}\omega}{2\pi}\,\mathrm{tr}\left\{[\Sigma^r_m(\omega - meV)\mathcal{G}^<_0(\omega) + \Sigma^<_m(\omega - meV)\mathcal{G}^a_0(\omega)]\tau_z\rho_z\right\}. && (4.189\text{b})\end{aligned}$$

Here, $m \in \{-1, 0, 1\}$ as a maximum of two $\varphi/2$ factors may be collected by the tunneling fermions at this order. In the second line we expanded in Keldysh indices using the Langreth rule. To this end, we defined the retarded and advanced components of the Green function and the self energy, which are denoted by r and a, respectively. Before we proceed, it is useful to define the BCS spectral matrix in dimensionless units as the anti-hermitian part of the Green function,

$$\mathcal{A}_\alpha(\omega) = \frac{i}{2\pi\nu_0}\Big\{\mathcal{G}^r_{0\alpha}(\omega) - [\mathcal{G}^r_{0\alpha}(\omega)]^\dagger\Big\} = -\frac{i}{2\pi\nu_0}\Big\{\mathcal{G}^a_{0\alpha}(\omega) - [\mathcal{G}^a_{0\alpha}(\omega)]^\dagger\Big\}, \tag{4.190}$$

where $\alpha \in \{L, R\}$. $\mathcal{A}$ is a hermitian matrix in particle-hole as well as spin space. We assume that the superconducting electrodes remain in equilibrium. Under this circumstance, the greater and lesser Green functions are related to the retarded and advanced Green functions via

$$\mathcal{G}^>_{0\alpha}(\omega) = -2\pi\nu_0 i\,[1 - n_F(\omega)]\mathcal{A}_\alpha(\omega), \tag{4.191a}$$

$$\mathcal{G}^<_{0\alpha}(\omega) = 2\pi\nu_0 i\, n_F(\omega)\mathcal{A}_\alpha(\omega). \tag{4.191b}$$

Here, $n_F(\omega)$ is the Fermi occupation function. We also define the hermitian part of the Green function in dimensionless units

$$\mathcal{B}_\alpha(\omega) = \frac{1}{2\pi\nu_0}\Big\{\mathcal{G}^r_{0\alpha}(\omega) + [\mathcal{G}^r_{0\alpha}(\omega)]^\dagger\Big\} = \frac{1}{2\pi\nu_0}\Big\{\mathcal{G}^a_{0\alpha}(\omega) + [\mathcal{G}^a_{0\alpha}(\omega)]^\dagger\Big\}. \tag{4.192}$$

We aim to express the current in terms of $\mathcal{A}$ and $\mathcal{B}$.

It is now straightforward to find compact expressions for the tunneling current components. Consider first the quasiparticle current $I_{\text{qp}}(V) = I_0(V)$. It is

$$I_0(V) = 2e\gamma \int \frac{\mathrm{d}\omega}{2\pi}[n_F(\omega) - n_F(\omega + eV)] \\ \times \operatorname{tr}_{\text{spin}}\left[\mathcal{A}^e_L(\omega)\mathcal{A}^e_R(\omega + eV) + \mathcal{A}^h_L(\omega + eV)\mathcal{A}^h_R(\omega)\right]. \tag{4.193}$$

Importantly, if both inversion symmetry (exchange of L and R) and particle-hole symmetry (exchange of e and h) are absent, this current may be nonreciprocal, i.e. $I_0(V) \neq -I_0(-V)$. Note that this corresponds to particle-hole symmetry in the normal metal sense,[7] and not the constraint on the single-particle Hilbert space related to the Nambu formalism. To illustrate how broken particle-hole symmetry gives rise to nonreciprocity consider tunneling between two normal metals [$\mathcal{A}_\alpha = \sigma_0\nu_\alpha(\omega\tau_z)$]. The quasiparticle current then takes the form

$$I_0(V) = \frac{4e\gamma}{\pi}\int \mathrm{d}\omega\,[n_F(\omega) - n_F(\omega + eV)]\frac{\nu_L(\omega)\nu_R(\omega + eV)}{\nu_0^2}. \tag{4.194}$$

---

[7] Indeed, the Nambu constraint relates the particle and hole spectra at opposite energies, $\mathcal{A}^e_\sigma(\omega) = \mathcal{A}^h_\sigma(-\omega)$. Here, by broken particle-hole symmetry we understand that the physical spectral function obeys $A_\sigma(\omega) \neq A_\sigma(-\omega)$. This translates to the condition $\mathcal{A}^e_\sigma(\omega) \neq \mathcal{A}^h_\sigma(\omega)$ given in the main text. [Note the ordering of elements in our convention of Nambu spinors: diag($\mathcal{A}$) $=$ ($\mathcal{A}^e_\uparrow, \mathcal{A}^e_\downarrow, \mathcal{A}^h_\downarrow, \mathcal{A}^h_\uparrow$).] For nonreciprocal $I_0(V)$ it suffices that particle-hole symmetry is broken in one of the electrodes. Furthermore, since we are considering spin-independent tunneling, it may also be necessary to have $A_\sigma(\omega) \neq A_{-\sigma}(-\omega)$ or $\mathcal{A}^e_\sigma(\omega) = \mathcal{A}^h_{-\sigma}(\omega)$. See App. B.7 for details.

Here, $\nu_\alpha(\omega)$ is the density of states per unit volume of electrode α as a function of energy measured from the Fermi level. In the presence of either inversion symmetry $[\nu_L(\omega) = \nu_R(\omega)]$ or particle-hole symmetry in the normal metal sense $[\nu_\alpha(\omega) = \nu_\alpha(-\omega)]$ the quasiparticle current satisfies $I_0(V) = -I_0(-V)$. In the absence of both, $I_0(V)$ is nonreciprocal. Of course, particle-hole symmetry is only ever an approximate symmetry, present only on energy scales much smaller than the Fermi energy E_F. Nonetheless, it is precisely these energy scales, $\omega \sim \Delta \ll E_F$, which are relevant in the present problem, and one usually approximates $\nu_\alpha(\omega) = \nu_0 =$ constant. This reproduced the well known Ohmic expression $I_0(V) = GV$ in terms of the tunneling resistance $R^{-1} = 4e^2\gamma/\pi$. We shall see below that magnetic impurities provide a mechanism which leads to broken particle-hole symmetry on energy scales $\omega \lesssim \Delta$.

As advertised above, we will neglect the mixed terms which depend on both the phase difference and the voltage. This amounts to setting $V = 0$ in $I_{\pm 1}$. We note that the combinations $I_{s,1} = i(I_1 - I_{-1})$ and $I_{c,1} = I_1 + I_{-1}$ multiply the $\sin\varphi$ and $\cos\varphi$ terms, respectively. We obtain for these prefactors

$$I_{s,1}(V=0) = 2e\gamma \int \frac{\mathrm{d}\omega}{2\pi}\, n_F(\omega)\, \mathrm{tr}_{\mathrm{spin}} \Big[\mathcal{A}_L^{he}(\omega)\mathcal{B}_R^{eh}(\omega) + \mathcal{A}_L^{eh}(\omega)\mathcal{B}_R^{he}(\omega) \\ + \mathcal{B}_L^{he}(\omega)\mathcal{A}_R^{eh}(\omega) + \mathcal{B}_L^{eh}(\omega)\mathcal{A}_R^{he}(\omega)\Big], \quad (4.195a)$$

as well as

$$I_{c,1}(V=0) = -2e\gamma i \int \frac{\mathrm{d}\omega}{2\pi}\, n_F(\omega)\, \mathrm{tr}_{\mathrm{spin}} \Big[\mathcal{A}_L^{he}(\omega)\mathcal{B}_R^{eh}(\omega) - \mathcal{A}_L^{eh}(\omega)\mathcal{B}_R^{he}(\omega) \\ + \mathcal{B}_L^{he}(\omega)\mathcal{A}_R^{eh}(\omega) - \mathcal{B}_L^{eh}(\omega)\mathcal{A}_R^{he}(\omega)\Big]. \quad (4.195b)$$

In particular, in the presence of time-reversal symmetry $\sigma_y h^*_{\mathrm{BdG}}(-k)\sigma_y = h_{\mathrm{BdG}}(k)$ in both electrodes [and assuming that the pairing is s-wave, i.e. that Δ is a unit matrix, as we have done throughout], the electron-hole and hole-electron blocks of $\mathcal{G}^{\mathrm{ret}}$ are identical and $I_{c,1}$ vanishes. This implies $I_s(\varphi) = -I_s(-\varphi)$. We have already argued in Sec. 2.2 that time-reversal symmetry leads to antisymmetric current-phase relations as a consequence of the equilibrium expression $I_s(\varphi) = (2e/\hbar)\partial F/\partial\varphi$. While, in the absence of time-reversal symmetry, the $\cos\varphi$ term leads to an asymmetric current-phase relation, the tunneling limit does not suffice to achieve nonreciprocal critical currents as the latter require the contribution of higher harmonics $e^{im\varphi}$, $m > 2$, in addition.

We can evaluate the noise correlator in a similar fashion. In the tunneling regime, its Fourier components are

$$K_m(V;\omega) = \frac{e^2}{4}\sum_{\pm}\int \frac{\mathrm{d}\epsilon}{2\pi}\, \mathrm{tr}\,\{\Sigma_m^{<}(V;\epsilon+\omega)\tau_z\mathcal{G}_0^{>}(\epsilon)\tau_z\}. \quad (4.196)$$

Employing the identity (n_B is the Bose occupation function)

$$n_F(\epsilon \pm eV + \omega)[1 - n_F(\epsilon)] = n_B(\pm eV + \omega)[n_F(\epsilon) - n_F(\epsilon \pm eV + \omega)], \tag{4.197}$$

one readily finds for the $m = 0$ component

$$K_0(V;\omega) = \frac{e}{2}\sum_{\pm} \coth\left(\frac{eV \pm \omega}{2T}\right) I_0(V \pm \tfrac{\omega}{e}) \tag{4.198}$$

To understand the noise associated with the components $m = \pm 1$ we make the simplifying assumption $F^{eh} = F^{he}$ corresponding to time-reversal symmetric leads. The $K \sim \sin\varphi$ term involves the particle-hole antisymmetric combination $\Sigma_1(\epsilon + \omega) - \Sigma_{-1}(\epsilon + \omega)$. Employing in addition the fact that $\Sigma_{\pm 1}$ anticommutes with τ_z and the symmetry of $\mathcal{G}_0$ with respect to particle-hole space, we see that the $\sin\varphi$ contribution to K exactly vanishes,

$$K_{s,1}(V;\omega) = 0. \tag{4.199}$$

This shows, to leading order in the tunneling, that there is no noise associated with the supercurrent. The noise associated with the $\cos\varphi$ current does not vanish at finite frequency. It can be obtained as

$$K_{c,1}(V;\omega) = e\coth\left(\frac{\omega}{2T}\right) I_{c,1}(\omega). \tag{4.200}$$

Here, $I_{c,1}(V)$ is now given by

$$\begin{aligned} I_{c,1}(V) = 2e\gamma \int \frac{\mathrm{d}\omega}{2\pi}[n_F(\omega) - n_F(\omega + eV)] \\ \times \mathrm{tr}_{\text{spin}}\left[\mathcal{A}_L^{eh}(\omega)\mathcal{A}_R^{eh}(\omega + eV) + \mathcal{A}_L^{eh}(\omega + eV)\mathcal{A}_R^{eh}(\omega)\right]. \end{aligned} \tag{4.201}$$

This is manifestly antisymmetric in V and thus vanishes at $V = 0$. Indeed, this is consistent with Eq. (4.195b), which vanishes for $F^{eh} = F^{he}$. In particular, this implies that $K^{\pm}_{c,1}$ disappears in the white noise approximation.

In summary, the extended RCSJ equation governing the phase dynamics of a junction in the tunneling regime involves the dissipative current $I_d(V) = I_0(V)$ and the current-phase relation $I_s(\varphi) = I_{s,1}\sin\varphi + I_{c,1}\cos\varphi$. Furthermore, the noise power is related to the dissipative current through the fluctuation-dissipation relation

$$K(V) = K_0^+(V;0) = e\coth\left(\frac{eV}{2T}\right) I_0(V). \tag{4.202}$$

At large temperatures[8] one may expand the right hand side to reproduce the nonlinear Johnson-Nyquist noise employed in the phenomenological approach in Secs. 4.2 and 4.3.

4.5 SINGLE-ATOM JOSEPHSON JUNCTIONS

In the previous section, we have seen that particle-hole symmetry breaking in the normal density of states $\nu(E = eV)$ leads to nonreciprocity in the quasiparticle current. However, this nonreciprocity is appreciable only on scales $eV \sim E_F$. Here, we will consider a tunnel junction involving a single magnetic adatom. It is well known, that such junctions have asymmetric tunnel currents for bias voltages $eV \sim \Delta$ due to the difference in particle and hole weights of the YSR wavefunction (see Sec. 2.3.2).

Indeed, a Josephson diode effect was recently observed in such single-atom Josephson junctions in an experiment conducted by our collaborators Trahms et al. [V]. Here, adatoms are manipulated on a superconducting Pb surface. The second electrode of the Josephson junction is provided by a superconducting Pb scanning tunneling microscope tip. The Josephson diode effect manifests dominantly in nonreciprocal retrapping currents, while the switching currents are nearly symmetric. Importantly, nonreciprocity is observed only when magnetic adatoms (Cr and Mn) are placed in the junction, but not for a nonmagnetic Pb adatom. This behavior is summarized in Figs. 4.10 and 4.11 with the former figure showing individual traces and the latter histograms. Note that the traces exhibit a finite slope in the supercurrent branch. The slope is due to noise induced transitions between neighboring minima, a phenomenon known as phase diffusion.

In view of the correspondence Eq. (4.2) and the particle-hole symmetry broken quasiparticle currents associated with magnetic adatoms, we expect an explanation of the nonreciprocity in terms of the dissipative current. In the following, we will first demonstrate this for a microscopic model of magnetic adatoms in the tunneling regime. We then present phenomenological simulations, which use experimental $I - V$ curves as input, and accurately reproduce the qualitative features of the experimental data.

4.5.1 YU-SHIBA-RUSINOV TUNNEL JUNCTIONS AND PARTICLE-HOLE SYMMETRY BREAKING DUE TO IMPURITIES

As in Sec. 2.3.2, we model the magnetic impurity as a delta-scatterer carrying the classical magnetic moment $\mathbf{S} = -S\hat{z}$. Assuming that the impurity is located precisely at the impurity site,

---

[8] In Sec. 4.3.1 we instead assumed low temperatures. There, the temperature was compared to the kinetic energy of the junction, $CV^2/2$. Thus, we require that the capacitance is sufficiently large so that the hierarchy $CV^2 \gg T \gg eV$ may be satisfied.

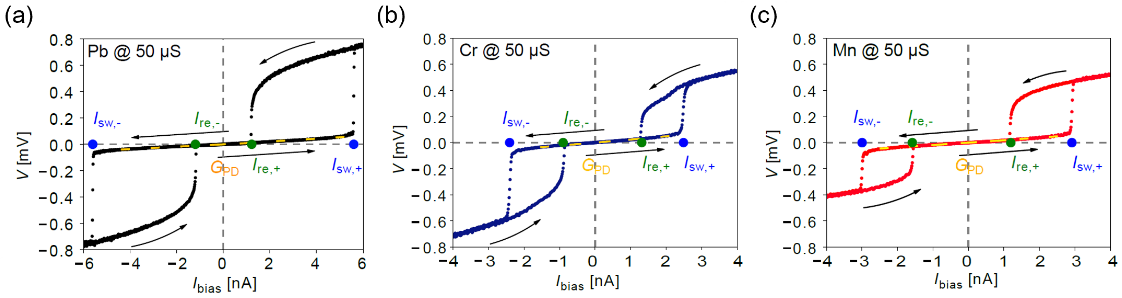

Figure 4.10: Hysteresis traces of current-biased tunneling junctions including a (a) Pb, (b) Cr, and (c) Mn atom. The measurements are performed at a normal-state conductance of 50μS. In contrast to Fig. 4.1 the supercurrent branch has a small slope due to phase diffusion. Figure adapted from [V].

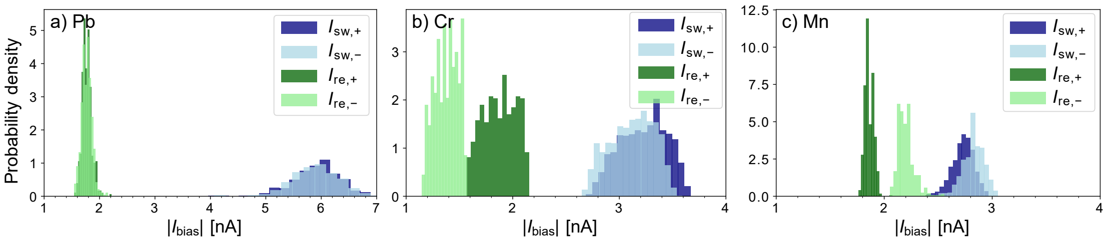

Figure 4.11: Histograms of absolute values of switching and retrapping currents for the two bias directions, as extracted from individual hysteresis traces for (a) Pb, (b) Cr, and (c) Mn junctions. The junction conductances were set at 10 mV to 50 μS. Figure from supplemental material of [V].

but couples only to one of the electrodes (the substrate in an STM setup), the new Hamiltonian is obtained via $H \to H + H_{\text{imp}}$

$$H_{\text{imp}} = \sum_{\sigma} \psi^{\dagger}_{R,\sigma}(0)[V - K_0\sigma_z]\psi_{L,\sigma}(0). \tag{4.203}$$

We furthermore assume the superconductors to be unstructured in all other regards. With these assumptions, the local Green functions [which enter the expressions for the quasiparticle current and noise correlator] are given by

$$\mathcal{G}_{0,L}(\omega) = -\pi\nu_0\sigma_0\frac{\omega + \Delta\tau_x}{\sqrt{\Delta^2 - \omega^2}}, \tag{4.204a}$$

$$\mathcal{G}_{0,R}(\omega) = -\pi\nu_0\frac{\omega + \Delta\tau_x + (\alpha\sigma_z + \beta\tau_z)\sqrt{\Delta^2 - \omega^2}}{(1 - \alpha^2 + \beta^2)\sqrt{\Delta^2 - \omega^2} - 2\alpha\sigma_z\omega}, \tag{4.204b}$$

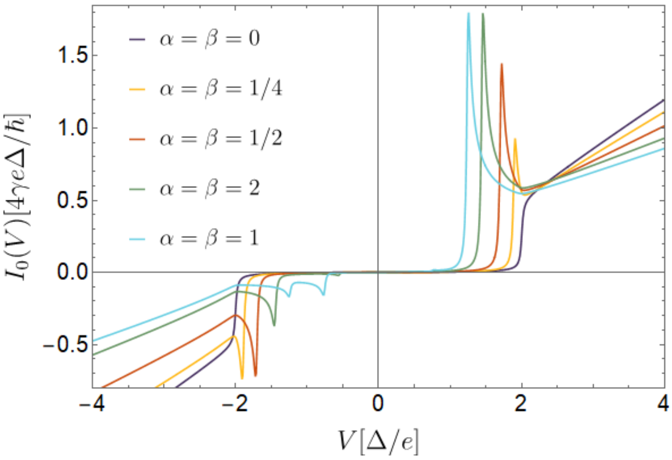

Figure 4.12: Zeroth Fourier component of the tunneling current in the tunneling regime as a function of the voltage V. For $\alpha \neq 0 \neq \beta$ the current is clearly asymmetric, $I_0(V) \neq -I_0(-V)$. Parameters: $T = 0.1\Delta$, $\eta = 0.01\Delta$, and $\alpha = \beta \in \{0, \frac{1}{4}, \frac{1}{2}, 1, 2\}$.

where we introduced the dimensionless couplings $\alpha = \pi\nu_0 K_0$ and $\beta = \pi\nu_0 V$. As was discussed in Sec. 2.3.2, the substrate Green function $\mathcal{G}_{0,R}$ has poles at $\pm E_{\text{YSR}}$, where

$$E_{\text{YSR}} = \Delta\frac{1-\alpha^2+\beta^2}{\sqrt{(1-\alpha^2+\beta^2)^2+4\alpha^2}}. \tag{4.205}$$

This is the signature of the YSR bound state induced by the magnetic adatom. More precisely, the $(\tau_z, \sigma_z) = (+,+)$ and $(-,-)$ components of $\mathcal{G}_{0,R}$ have a pole at $+E_{\text{YSR}}$ with weights u^2 and v^2, respectively. Conversely, the $(+,-)$ and $(-,+)$ components of $\mathcal{G}$ have a pole at $-E_{\text{YSR}}$ with weights v^2 and u^2, respectively. Here, u and v are given by

$$u, v = 2\Delta\frac{\sqrt{\alpha[1+(\alpha\mp\beta)^2]}}{[(1-\alpha^2+\beta^2)^2+4\alpha^2]^{3/2}}. \tag{4.206}$$

Noting that only the $(+,+)$ and $(+,-)$ components are physical, we may identify the pole at $E_{\text{YSR}} \gtrless 0$ with the possibility to excite the unoccupied (occupied) YSR bound state by tunneling in/out of a spin-up electron [weight u^2], and the pole at $-E_{\text{YSR}} \lessgtr 0$ with the possibility to excite the unoccupied (occupied) YSR bound state by tunneling out/in of a spin-down electron [weight v^2].

Exploiting the simplicity of the tip Green function, which manifests as $\mathcal{A}_L(\omega) \equiv \mathcal{A}_L^e(\omega) = \mathcal{A}_L^h(\omega) = \mathcal{A}_L(-\omega) = |\omega|(\omega^2-\Delta^2)^{-1/2}\Theta(|\omega|-\Delta)$, the quasiparticle current may be simplified to

$$I_0(V) = 2e\gamma\int\frac{\mathrm{d}\omega}{2\pi}[n_F(\omega-eV)-n_F(\omega)]\mathcal{A}_L(\omega-eV)\,\mathrm{tr}\,[\mathcal{A}_R(\omega\tau_z)]. \tag{4.207}$$

Invoking the Nambu constraint the trace factor becomes $\mathrm{tr}\left[\mathcal{A}_R(\omega\tau_z)\right] = 2\sum_\sigma A_R^\sigma(\omega) = A_R(\omega)$, where A^σ $[A]$ is the spin-[non]resolved normal spectral function [see Eq. (2.20) and App. B.7 for the definitions]. The current is asymmetric in V provided that $A(\omega) \neq A(-\omega)$ which, based on the observations in the previous paragraph, is clearly the case for $u \neq v$. To be explicit, we set $E_{\mathrm{YSR}} > 0$ for concreteness, and focus on the subgap current $V \lesssim 2\Delta$, where $A_R(\omega) = u^2\delta(\omega - E_{\mathrm{YSR}}) + v^2\delta(\omega + E_{\mathrm{YSR}})$, as well as temperatures $T \ll E_{\mathrm{YSR}}$. This yields the expression

$$I_0(V) \simeq \frac{2e\gamma}{\pi}\left[u^2 n_F(\omega - eV)\mathcal{A}_L(\omega - eV) - v^2 n_F(\omega + eV)\mathcal{A}_L(\omega + eV)\right]. \tag{4.208}$$

For $u \neq v$ this is explicitly nonreciprocal on the small energy scale $eV \sim \Delta$. The full range of $I_0(V)$ is shown in Fig. 4.12 for several values of $\alpha = \beta$.

Let us investigate how the particle-hole asymmetry $A(\omega) \neq A(-\omega)$ arises. To this end, note that $u \neq v$ requires finite potential scattering, or $\beta \neq 0$. In order to understand this, consider the Anderson impurity model,

$$H_{\mathrm{imp}} = \epsilon \sum_\sigma n_\sigma + U n_\uparrow n_\downarrow - t \sum_\sigma \left[d_\sigma^\dagger \psi_{R,\sigma}(0) + \mathrm{h.c.}\right]. \tag{4.209}$$

Here, d_σ annihilates a localized electron with spin σ and $n_\sigma = d_\sigma^\dagger d_\sigma$. For large repulsive interaction U and large and negative orbital energy ϵ, the orbital is occupied at all times and only its spin degree of freedom remains. Virtual deoccupation and double occupation of the orbital leads to interactions with the substrate. Formally, this can be implemented through a Schrieffer-Wolff transformation, producing impurity Hamiltonian used in this section (albeit with a quantum spin degree of freedom, c.f. Sec. 2.3.1 and Chapter 3). In terms of the Anderson model parameters, the potential and exchange scattering couplings are

$$\alpha = \pi\nu_0 t^2\left(\frac{1}{|\epsilon|} + \frac{1}{\epsilon + U}\right), \quad \beta = \pi\nu_0 t^2\left(\frac{1}{|\epsilon|} - \frac{1}{\epsilon + U}\right). \tag{4.210}$$

In particular, β vanishes for $\epsilon = -U/2$. This corresponds to the situation in which the Anderson impurity is particle-hole symmetric (in the normal metal sense). Conversely, $\beta \neq 0$ corresponds to broken particle-hole symmetry and thus enables $A(\omega) \neq A(-\omega)$ and $I_0(V) \neq -I_0(-V)$.

This begs the question why exchange scattering is necessary to observe nonreciprocal quasiparticle current between superconductors. The answer lies in Anderson's theorem [176]: a potential impurity is without effect to the low energy spectrum of the superconductor. While it may induce a bound state above (below) the upper (lower) band edge [depending on dimensionality as well as the sign and magnitude of β] which indeed leads to $A(\omega) \neq A(-\omega)$ at $\omega \sim D$, where D is the bandwidth, here we are interested only in energies $\omega \sim \Delta$. For such energies, $A(\omega) = A(-\omega)$ in the absence of exchange scattering. We also comment on the clas-

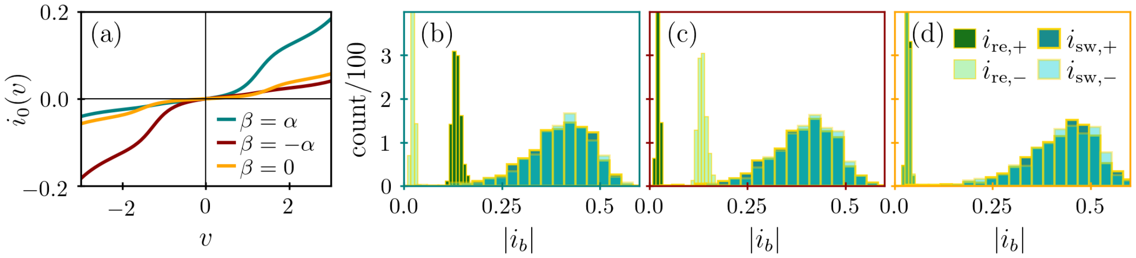

Figure 4.13: Josephson diode effect in YSR tunnel junction. (a) dissipative quasiparticle current $i_d(v) = i_0(v)$ for different values of the potential scattering β. Note that, in contrast to Fig. 4.12, the range of the dimensionless voltage is much reduced [$eV = \Delta v/4$] so that only the subgap dissipation relevant to the retrapping current [$v < 2$ in Eq. (4.20) provided the junction is sinusoidal] is shown. Furthermore, note the factor of ten difference in η. (b)-(d) Histograms of switching and retrapping currents corresponding to $i_0(v)$ in (a) (note color-coded box). In the particle-hole asymmetric cases (b) and (c) the retrapping currents are strongly nonreciprocal. The sign of the asymmetry is determined by the sign of β. In the particle-hole symmetric case (d) the retrapping currents are symmetric. Parameters: $\Delta = 2\hbar\Omega_p$ [this fixes C], $T = 0.01\Delta$, $\alpha = 1.5$, $\gamma = 0.2$, $\eta = 0.1\Delta$, and $\beta \in \{\pm\alpha, 0\}$. Figure from [IV].

sical spin approximation used here. In Chapter 3 we discussed the zero bandwidth model as complimentary approach to the classical spin approximation, highlighting the quantum nature of the impurity spin at the cost of the accurate representation of the quasiparticle continuum. For deep YSR states this should provide an accurate picture. For a $S = \frac{1}{2}$ impurity, we can explicitly find the subgap spectral function in the zero bandwidth model as

$$A(\omega) = \frac{1}{4}\sum_{\pm}\left[1 \pm \frac{V}{\sqrt{\Delta^2 + V^2}}\right]\delta(\omega \mp E_{\mathrm{YSR}}). \tag{4.211}$$

In the presence of potential scattering, $V \neq 0$, this is manifestly asymmetric. This suggests that asymmetric $A(\omega)$ at $\omega \sim \Delta$ is a general feature of YSR states. Indeed, this is confirmed by NRG studies [18].

The presence of the magnetic impurity also affects the supercurrent $I_s(\varphi)$. One might expect an artificial $\cos\varphi$ contribution stemming from the time-reversal breaking associated with the classical spin approximation. However, this would further require spin-orbit coupling which we neglect in the present discussion. The prefactor of the $\sin\varphi$ term may be evaluated explicitly. Restoring $\hbar$, we obtain $I_s(\varphi) = (2eE_J/\hbar)\sin\varphi$, where

$$E_J = \frac{\gamma\Delta}{\sqrt{(1-\alpha^2+\beta^2)^2 + 4\alpha^2}}. \tag{4.212}$$

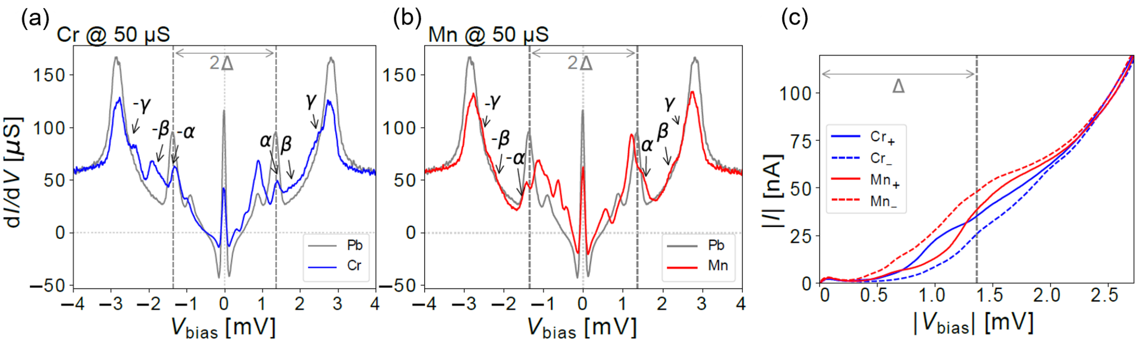

Figure 4.14: (a-b) Voltage bias dI/dV at normal conductance of 50μS for junctions including (a) Cr and (b) Cr adatom. There is significant subgap spectral weight at voltages $|eV| < 2\Delta$ stemming from multiple Andreev reflections as well as processes involving YSR excitations. (c) Corresponding voltage-bias $I-V$ traces for Cr (blue) and Mn (red) junctions showing the absolute current at positive (solid) and negative (dashed) voltages. Figure adapted from [V].

Finally, we consider the phase dynamics of the YSR tunnel junction via numerical integration of the extended RCSJ equation. We use the dimensionless units introduced in Sec. 4.1. The plasma frequency of the junction (at zero bias) is now determined by microscopic parameters,

$$\Omega_p = \left(\frac{\pi^2}{(1-\alpha^2+\beta^2)^2+4\alpha^2}\right)^{1/4}\sqrt{\frac{\Delta}{\hbar RC}}, \tag{4.213}$$

where $R^{-1} = 4e^2\gamma/\pi$. The free parameters of the model are $\Delta, T, \eta, C, \gamma, \alpha$ and β. In order to obtain appreciable subgap structure, which is important for sizeable nonreciprocal retrapping currents, we consider a strongly hybridized YSR impurity characterized by large η. Note, that the lack of subgap spectral weight is an artefact of the tunneling regime. At higher orders in the tunneling, multiple Andreev reflections redistribute spectral weight into the tunneling gap. Histograms of the switching and retrapping currents for the YSR tunneling junction are presented in Fig. 4.13. As expected, particle-hole symmetry breaking due to $\beta \neq 0$ leads to nonreciprocal retrapping currents, while switching currents remain unaffected.

4.5.2 Modeling the single-atom Josephson diode

While the histograms in Fig. 4.13 exhibit asymmetry in the retrapping distributions depending on the impurity parameters, the microscopic theory based on the tunneling regime has several shortcomings. First, the histograms in Fig. 4.11 are obtained at a normal state conductance of 50μS. This is clearly not in the tunneling regime: Fig. 4.14 (a) and (b) show the dI/dV signals at this conductance for the Mn and Cr junctions, respectively. There is no well defined gap in the spectrum, and peaks corresponding to multiple Andreev reflections are observable at $eV = \Delta$ and less clearly at other voltages. The subgap spectral weight gives rise to the dissipative current, and therefore leads to sizeable retrapping currents. Achieving retrapping currents of similar magnitude as the switching currents in the tunneling regime necessitated unnatural assumptions such as large η and $\hbar\Omega_p \sim \Delta$. In particular, the classical approximation relies on $E_J \gg \hbar\Omega_p$ which is inconsistent with the assumptions $\Omega_p \sim \Delta$ and $\gamma \ll 1$. Finally, the traces shown in Fig. 4.10 show phase diffusion in the trapped state. It is well known that the coexistence of phase diffusion and hysteresis in a Josephson junction implies frequency dependent damping [228]. We will see that the lack of frequency dependent damping can explain the qualitative differences between the experimental histograms in Fig. 4.11 and the tunneling regime histograms in Fig. 4.13, such as the narrow shape and small asymmetry of the switching current distributions, as well as the relative magnitude of the retrapping currents for positive and negative bias.

In order to amend these issues, instead of relying on a microscopic model, we use the measured quasiparticle current $I_{\mathrm{qp}}(V)$ as input to the phenomenological RCSJ equation. Fig. 4.14 (c) shows the measured (voltage-bias) $I-V$ characteristics for Cr and Mn. This includes both the quasiparticle current as well as a Josephson contribution. Only the latter contributes to the dissipative current. We isolate the quasiparticle contribution by fitting the Josephson contribution to its functional form. The procedure is detailed in App. B.8. Moreover, to account for the observed phase diffusion in the trapped state, we also incorporate frequency-dependent friction. Following Kautz and Martinis [228], we shunt the junction by an additional RC element with Ohmic resistor $\tilde{R}$ and capacitor $\tilde{C}$ to model dissipation induced by the electromagnetic environment. The total dissipative current is then the sum of the quasiparticle current and the current flowing via the RC element,

$$I_d(V) = I_{\mathrm{qp}}(V) + \frac{V-\tilde{V}}{\tilde{R}}, \quad \delta I = \delta I_{\mathrm{qp}} + \delta I_{\tilde{R}}, \tag{4.214}$$

where $\tilde{V}$ is the voltage drop across the capacitor which satisfies the equation

$$\frac{\mathrm{d}}{\mathrm{d}t}\tilde{V} = \frac{1}{\tilde{R}\tilde{C}}\Big(V - \tilde{V} + \tilde{R}\,\delta I_{\tilde{R}}\Big). \tag{4.215}$$

The RC element is inconsequential at low frequencies (running state), so that damping is dominated by the quasiparticle current. In contrast, it dominates friction at high frequencies (trapped state), allowing for phase diffusion. We assume $V/\tilde{R} \gg I_{\mathrm{qp}}(V)$, so that the quasiparticle current is effectively shorted at high frequencies, $I_d(V) \simeq V/\tilde{R}$. Following the discussion in Sec. 4.3.1, we assume that the noise associated with the quasiparticle current has correlator $\langle \delta I_{\mathrm{qp}}(t)\delta I_{\mathrm{qp}}(t')\rangle = 2T[I_{\mathrm{qp}}(V)/V]\delta(t-t')$, while the noise associated with the resistor $\tilde{R}$ has correlator $\langle \delta I_{\tilde{R}}(t)\delta I_{\tilde{R}}(t')\rangle = 2\tilde{T}\tilde{R}^{-1}\delta(t-t')$, where $\tilde{T}$ is the effective temperature of the shunt circuit. Finally, we comment on the current-phase relation. While the presence of spectral features due to multiple Andreev reflections suggest a significant $\sin(2\varphi)$ contribution, we will assume a simple $\sin\varphi$ current-phase relationship to keep the number of undetermined parameters under control.

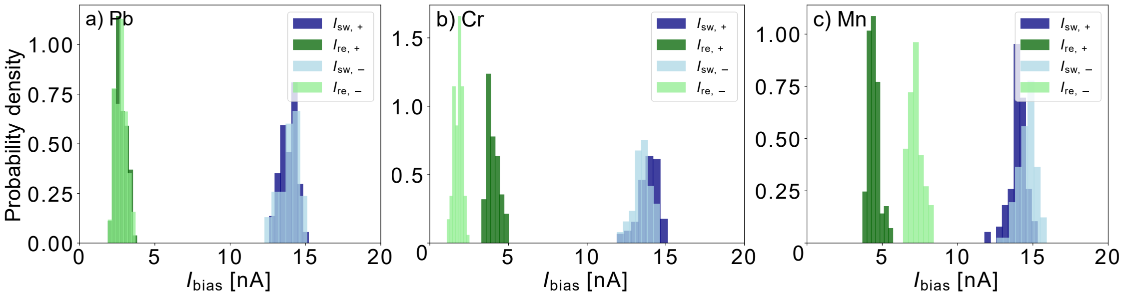

Figure 4.15: Statistics of switching and retrapping currents (theoretical simulations based on $I-V$ measurements). (a-c) Histograms of absolute values of switching and retrapping currents for the two bias directions, as extracted from individual $V-I$ curves from simulation of Eq. (4.216) with $I_{\mathrm{qp}}(V)$ obtained from experimental $I-V$ curves of a (a) Pb, (b) Cr, and (c) Mn junction at 50 μS (c.f. App. B.8). Each histogram includes data extracted from 100 sweeps for each current direction. For parameters, see text below Eq. (4.216). Figure from supplemental material of [V].

In the dimensionless units which were introduced in Sec. 4.1, the resulting RCSJ equations become

$$\frac{\mathrm{d}}{\mathrm{d}\tau}\varphi = v, \tag{4.216a}$$

$$\frac{\mathrm{d}}{\mathrm{d}\tau}v = i_{\mathrm{b}} - i_s(\varphi) - \left[i_{\mathrm{qp}}(v) + \frac{v-\tilde{v}}{\tilde{Q}}\right] - \sqrt{\frac{2\theta i_{\mathrm{qp}}(v)}{v}}\xi_1 - \sqrt{2\tilde{\theta}\tilde{g}}\xi_2, \tag{4.216b}$$

$$\frac{\mathrm{d}}{\mathrm{d}\tau}\tilde{v} = \frac{1}{\tilde{\tau}}\left[v - \tilde{v} + \sqrt{2\tilde{\theta}\tilde{g}^{-1}}\xi_2\right]. \tag{4.216c}$$

Here, in addition to the quantities defined in Sec. 4.1, we introduced the dimensionless voltage $\tilde{v} = 2e\tilde{V}/\hbar\Omega_p$, the dimensionless conductance $\tilde{g} = [\tilde{R}C\Omega_p]^{-1}$, as well as the reduced temperature $\tilde{\theta} = \tilde{T}/E_J$ describing the RC shunt. We also defined dimensionless Langevin currents ξ_1 and ξ_2 with normalized correlations $\langle\xi_i(\tau)\xi_j(\tau')\rangle = \delta_{ij}\delta(\tau-\tau')$ corresponding to δI_{qp} and $\delta I_{\tilde{R}}$, respectively. For the simulation, we estimate the experimental parameters as $R_{\mathrm{N}} \sim 20$ kΩ, $\Delta \sim 1.5$ meV, $T \sim 0.1$ meV and $C \sim 10^{-15}$ F. This gives $I_c \sim 100$ nA, $E_J \sim 0.2$ meV and $\hbar\Omega_p \sim 0.3$ meV. The reduced temperature is thus $\theta = 0.5$. For the RC element we choose parameters $\tilde{Q} = 10$, $\tilde{\tau} = 1000$, and $\tilde{\theta} = \theta$. We sweep the bias current with a rate $\mathrm{d}I_{\mathrm{bias}}/\mathrm{d}t = 10^{-7}I_c\Omega_p \sim 1$ nA/μs. The experimental sweep rate is smaller by about a factor of 10^{-3}, but this would make the numerical simulations forbidding. Along with the simplified current-phase relation and the order-of-magnitude estimates of experimental parameters, this implies that one can only expect qualitative, but not quantitative agreement between simulations and experiment.

The results of the theoretical simulations are summarized in Fig. 4.15, which shows histograms of the absolute values of switching and retrapping currents extracted from 100 sweeps in each current direction. Note that the panels only differ in the precise form of $I_{\mathrm{qp}}(V)$ which is ex-

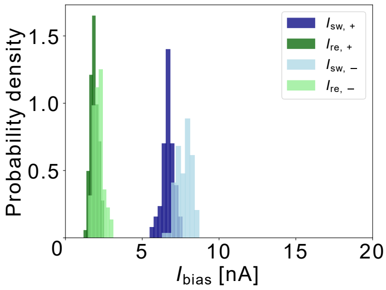

Figure 4.16: Simulated statistics of switching and retrapping currents with symmetric quasiparticle current and asymmetric current-phase relation. Histograms of absolute values of switching and retrapping currents for the two bias directions, as extracted from individual $V - I$ curves in simulations of Eq. (4.216). $I_{\mathrm{qp}}(V)$ is obtained from experimental $I - V$ curves of a Pb junction at $G_{\mathrm{N}} = 50\,\mu$S. The asymmetric current-phase relation is defined in the final paragraph of Sec. 4.5.2. Each histogram includes data extracted from 98 sweeps for each current direction. Other parameters as in Fig. 4.15. Figure from supplemental material of [V].

tracted from the $I - V$ curves of Pb, Cr and Mn, respectively. The simulations based on the $I_{\mathrm{qp}}(V)$ of Pb do not show asymmetry in the switching or the retrapping currents. The simulations based on the $I_{\mathrm{qp}}(V)$ of Cr and Mn exhibit weak asymmetry in the switching currents and strong asymmetry in the retrapping currents, correctly reproducing the qualitative features of the experimental histograms in Fig. 4.11.

To rule out the possibility that the observed asymmetry stems from the current-phase relation $I_s(\varphi)$ rather than from the dissipative quasiparticle current, we now demonstrate that an asymmetric current-phase relation leads to strong asymmetry in the switching currents and weak asymmetry in the retrapping currents, contrasting with our experimental observations. To this end, we simulate Eq. (4.216) using Pb $I - V$ data for $I_{\mathrm{qp}}(V)$ together with an asymmetric current-phase relation $I_s(\varphi) = I_0[\sin(\varphi - \varphi_0) + b\sin(2\varphi)]$. We choose $\varphi_0 = 0.5 = b$ and fix $I_0 \simeq 54.2$ nA by requiring that the current entering the definition of the plasma frequency, i.e., the slope of I_s around the stable minimum, is still 100 nA (which we continue to use as the unit of current). The critical current now depends on direction, with $I_{c,+} \simeq 53.3$ nA and $I_{c,-} \simeq 80.0$ nA. Histograms of switching and retrapping currents obtained by simulating Eq. (4.216) with the current-phase relation $I_s(\varphi)$ are presented in Fig. 4.16. The asymmetry of the switching currents is clearly much greater than that of the retrapping currents. Thus, a symmetric dissipative current together with an asymmetric current-phase relation cannot explain the phenomenology of strongly asymmetric retrapping currents and weakly asymmetric switching currents observed for the Cr and Mn Josephson junctions.

4.6 Conclusion

In this chapter, we have developed a phenomenological theory of nonreciprocity in current-biased Josephson junctions, focusing on the hysteretic behavior of weakly damped junctions.

The main finding of this chapter is the correspondence given in Eq. (4.2): a nonreciprocal switching current originates from nonreciprocity of the current-phase relation. In contrast, a nonreciprocal retrapping current originates from asymmetric dissipation. Moreover, these different sources of nonreciprocity have different symmetry requirements. While nonreciprocal switching currents require breaking of time reversal symmetry, nonreciprocity of the retrapping currents does not. While these observations are based on a phenomenological extension to the well known RCSJ model, we have also provided a microscopic derivation of the classical equation of motion for the phase difference across a tunnel contact. This allowed us to identify broken particle-hole symmetry (in the normal metal sense) as a requirement for nonreciprocity in the dissipation and thus also in the retrapping currents. Our theory comes very timely, as it helps explain and assess recent experiments on weakly damped, time-reversal symmetric Josephson junctions [V, 136]. In particular, it explains the dominant nonreciprocity in the retrapping currents that was observed in atomic scale Josephson junctions involving magnetic adatoms in terms of the particle-hole symmetry breaking associated with YSR states.

Our work opens several new avenues for theoretical and applied research. First, within our streamlined Ambegaokar-Eckern-Schön approach we have focused on the tunneling regime thus far, where we established intuitive expressions as well as a generalized fluctuation-dissipation theorem. However, it is precisely the inclusion of higher order processes which sets our approach apart from the established Ambegaokar-Eckern-Schön framework. It is therefore of immediate importance to extend our analysis to higher orders, or, if it proves possible, to establish such results at all orders in the tunneling. Second, the Josephson diode effect has been observed in a range of extended junctions for which the tunnel contact description is not appropriate. It should be straightforward to extend our approach to such systems. Moreover, explicit integration with the scattering matrix approach [241] would allow to more directly interpret the expressions for the current and current-current correlations. Finally, there are now a number of systems that exhibit a Josephson diode effect. Nonetheless, it is still a question of fundamental interest how nonreciprocal response in superconductors interfaces with other components, such as the propagating bosonic modes in superconducting circuits. Our work provides the foundation upon which such applications can be based.

5 READOUT OF MAJORANA QUBITS

This chapter is based on Ref. [VII].

Qubits based on Majorana bound states promise key advantages for quantum computing, including long intrinsic lifetimes deriving from the nonlocal encoding of quantum information [41, 44, 242] and topologically protected single-qubit gates based on braiding or, alternatively, on exploiting measurements in all Pauli bases. A popular Majorana qubit – known as Majorana box qubit [154] or tetron and hexon [45] – is based on semiconductor quantum wires proximity coupled to a superconductor [50, 51, 187]. These qubits are believed to be within experimental reach [243] and quantum computing architectures have been developed on their basis [45, 46, 156, 244, 245]. Quantum computation with Majorana qubits is expected to rely heavily on projective qubit measurements, with all Clifford gates implemented using single and two-qubit measurements [45, 156, 246]. Indeed, these schemes can be referred to as measurement-based topological quantum computing and good readout fidelities are absolutely central to their performance. This makes it essential to develop a detailed theoretical understanding of the proposed readout schemes for Majorana-based topological qubits.

While a blessing for their characteristics as a quantum memory, the nonlocal nature of topological qubits complicates the readout of the encoded quantum information. Readout requires to make the nonlocally encoded quantum information available locally. This can be achieved by exploiting interference effects which are sensitive to the Majorana parity operator of interest [45, 154, 247]. A schematic Majorana qubit is shown in Fig. 5.1 and involves four Majorana bound states located at the ends of two proximity-coupled semiconductor quantum wires. The Pauli operators associated with the Majorana qubit are parity operators involving products of two Majorana operators. Here, we focus on a readout procedure which measures these Majorana parity operators by tunnel coupling a quantum dot to the relevant pair of Majoranas as shown in Fig. 5.1. Virtual tunneling processes between Majorana qubit and quantum dot shift the energy levels of the quantum dot in a manner that depends on the Majorana parity. As a result, the coupled time evolution of Majorana qubit and quantum dot entangles the two, and the charge state of the quantum dot becomes correlated with the Majorana parity. Measurements of the quantum dot charge, for instance by a nearby quantum point contact, can thus be used to read out the Majorana qubit.

In principle, it is possible to design parity-to-charge conversion procedures which allow for a projective measurement of the Majorana parity based on a single-shot projective measurement of the charge $\hat{n}$ of the quantum dot [154]. However, these schemes are not robust and require fine tuning and rapid manipulation of system parameters. More generically, the charge state

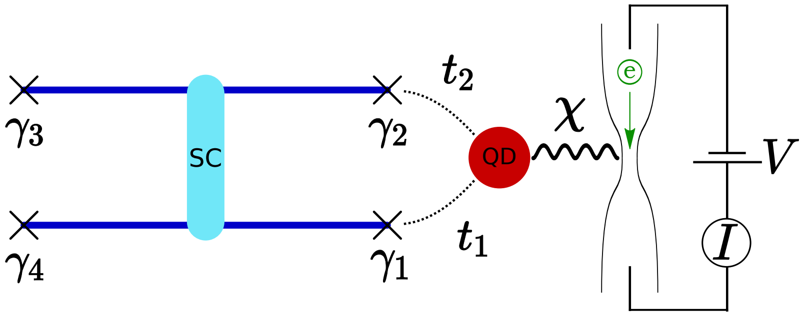

Figure 5.1: Setup for readout of Majorana qubit. A quantum dot (QD) is tunnel coupled to a Majorana qubit consisting of two topological superconducting wires (dark blue) with four Majorana bound states $\hat{\gamma}_1, \ldots, \hat{\gamma}_4$. The wires are connected by a conventional superconducting bridge (SC) allowing charge to move freely between the wires, so that only the overall charge of the Majorana qubit is fixed by the charging energy. The Majorana parity $\hat{Z} = -i\hat{\gamma}_1\hat{\gamma}_2$ defines the Pauli-Z operator of the Majorana qubit, and can be read out by tunnel coupling the two Majoranas $\hat{\gamma}_1$ and $\hat{\gamma}_2$ to the quantum dot. The quantum dot charge is measured by capacitively coupling (with strength $k \propto |\chi|^2$) the dot to a quantum point contact. Figure from [VII].

of the quantum dot becomes only weakly correlated with the state of the Majorana qubit, and qubit readout requires multiple measurements. This can be achieved by repeatedly coupling and decoupling qubit and quantum dot, with intervening projective measurements of $\hat{n}$ and resets of the qubit charge state.

In practice this coupling, decoupling, and resetting is challenging and prone to errors. It would be preferable and more natural to keep Majorana qubit and quantum dot coupled during the entire readout procedure and to *monitor* the charge of the quantum dot continuously. Here, we show that a projective readout of the Majorana qubit can indeed be robustly implemented in this manner. In particular, our strategy significantly relaxes the requirements on dynamical control over system parameters, and obviates the need for resets of the quantum dot charge state.

To describe the dynamics of the quantum measurement, we include the measurement device in the theoretical description. The continuous measurement decoheres the system in the basis of the quantum dot charge and outputs the noisy measurement signal $j(t)$ of the quantum point contact [248]. The task is then twofold. First, one needs to show that the system of Majorana qubit and quantum dot decoheres in the actual basis of interest associated with the parity operator of the Majorana qubit. Second, one needs to ascertain that the measurement outcome can be extracted from the signal $j(t)$. Both criteria must be satisfied to effectively implement a projective (Born rule) readout of the Majorana qubit which can be employed for measurement-based topological quantum computation.

This chapter is structured as follows. In section 5.1, we introduce the system under consideration, a Majorana qubit with two of the four Majorana bound states tunnel coupled to a quantum dot as illustrated in Fig. 5.1, and discuss how under idealized assumptions, quantum dot charge measurements can be used for single-shot readout of the Majorana qubit. We then turn to more realistic readout protocols which rely on continuous monitoring of the quantum dot charge, collecting our central results in Sec. 5.2. The basic master-equation formalism describing weak measurements of the quantum dot charge by a quantum point contact is described in Sec. 5.2.1. As a backdrop, we first illustrate the formalism in Sec. 5.2.2 by reviewing charge monitoring of a quantum dot in the absence of coupling to a Majorana qubit. We then include the coupling to the Majorana qubit in Sec. 5.2.3 and show how a two-Majorana parity (Pauli operator) of the Majorana qubit can be read out. While it suffices to monitor the average quantum-point-contact current for charge readout of an uncoupled quantum dot, we find that in general, readout of the Majorana qubit requires one to measure noise correlations of the current. Readout based on noise correlations can be avoided by tuning to a sweet spot in parameter space or, as shown in Sec. 5.2.4, by including additional processes which cause relaxation of the coupled Majorana qubit-quantum dot system to its ground state. In both of these cases, it suffices in principle to monitor the average quantum-point-contact current. In Sec. 5.2.5, we discuss various processes which are detrimental to the readout protocol. Most importantly, the previous sections assume that the residual Majorana hybridizations of the qubit are negligible, and we show here how these hybridizations affect the measurement protocol. Finally, Sec. 5.2 closes with a discussion of alternative readout schemes which rely on coupling the Majorana qubit to double quantum dots, see Sec. 5.2.6. We find that this readout scheme adds flexibility in designing the coupling between Majorana qubit and quantum dots. We also discuss readout of Majorana parity operators involving more than two Majoranas, which represent two-qubit parities or stabilizer operators of topological quantum error correcting codes. While our results are mostly analytical in nature, we illustrate the various measurement protocols by simulations of the stochastic master equation. In addition to our analytical estimates throughout Sec. 5.2, these simulations also illustrate the required measurement times. Sec. 5.3 discusses the measurement protocols from a more general point of view. We emphasize that the underlying mechanism – which we term symmetry-protected readout – is quite general and has further implications for both, Majorana and non-Majorana systems. We finally summarize and conclude in Sec. 5.4. We focus on the principal arguments and results here. Explicit calculations and background material are relegated to a series of appendices.

5.1 Majorana qubits and quantum dot readout

5.1.1 Majorana qubit coupled to quantum dot

Majorana qubits are Coulomb-blockaded islands hosting $2m$ Majorana bound states $\hat{\gamma}_j$ as described by the Hamiltonian

$$\hat{H}_{\mathrm{M}} = E_C\left(\hat{N} - N_g\right)^2 + i\sum_{i<j}^{2m} \varepsilon_{ij}\hat{\gamma}_i\hat{\gamma}_j. \tag{5.1}$$

The first term reflects the charging energy E_C of the device, which depends on the total charge $\hat{N}$ as well as a gate-controlled offset N_g. For a fixed charge and well-separated Majorana bound states, the ground state of the system is 2^{m-1}-fold degenerate. Residual splittings are included in H_M through the ε_{ij}. Above-gap excitations of the Majorana wires are ignored by virtue of a sufficiently large gap. Note that in this chapter we denote operators which act in the Fock space with a hat.

The minimal number of Majoranas required for a single qubit is four, in which case the Majorana island realizes a Majorana box qubit or tetron. Figure 5.1 shows such a Majorana qubit assembled from a pair of topological superconducting quantum wires hosting two Majorana bound states each. The superconducting bridge between the quantum wires provides a sufficiently large mutual capacitance so that the charging energy depends on the charges of the individual wires only via the total charge of the device [45]. For definiteness, we choose $N_g = 0$, so that the ground-state manifold has even fermion parity, $\hat{P} = (-i\hat{\gamma}_1\hat{\gamma}_2)(-i\hat{\gamma}_3\hat{\gamma}_4) = 1$. We can then define the Pauli operators

$$\hat{Z} = -i\hat{\gamma}_1\hat{\gamma}_2 \tag{5.2a}$$
$$\hat{X} = -i\hat{\gamma}_2\hat{\gamma}_3 \tag{5.2b}$$
$$\hat{Y} = -i\hat{\gamma}_3\hat{\gamma}_1 \tag{5.2c}$$

of the qubit. Fermion parity conservation implies that one can alternatively use the operators $\hat{Z}' = \hat{P}\hat{Z}$ (with $\hat{X}'$ and $\hat{Y}'$ defined analogously).

Readout of the qubit operators (say, $\hat{Z}$ for definiteness) can be effected by connecting the Majorana island to a quantum dot via tunnel junctions as depicted in Fig. 5.1 [45, 154]. We assume that the quantum dot has a single nondegenerate level ϵ, which is spin resolved due to the magnetic field required for realizing topological superconductivity (see also [249]). Then, the quantum dot is described by the Hamiltonian

$$\hat{H}_{\mathrm{QD}} = \epsilon\hat{n}, \tag{5.3}$$

where the quantum dot occupation $\hat{n} = \hat{d}^\dagger\hat{d}$ involves the annihilation operator $\hat{d}$ of the gate-tunable dot level. We assume that the quantum dot is unoccupied in the ground state, $n = 0$.

Tunneling between quantum dot and Majorana qubit is described by

$$\hat{H}_{\mathrm{T}} = (t_1\hat{\gamma}_1 + t_2\hat{\gamma}_2)e^{i\hat{\phi}/2}\hat{d} + \text{h.c.} \tag{5.4}$$

Electrons tunneling into or out of the Majorana island affect the state of the system within the ground-state manifold and change its charge. We describe the first effect through the Majorana operators γ_j (which leave the charge state of the system unchanged, $[\hat{\gamma}_i, \hat{N}] = 0$), and the second through a charge shift operator $e^{i\hat{\phi}/2}$ (with $[\hat{\phi}, \hat{N}] = 2i$ and $[\hat{\gamma}_i, \hat{\phi}] = 0$). In this formulation, physical states must satisfy the total parity constraint $(-i)^m \prod_{i=1}^{2m} \hat{\gamma}_i = (-1)^{\hat{N}}$.

For a topological qubit, we assume that the hybridizations ε_{ij} are negligible, so that the Majorana bound states are true zero-energy modes of the Majorana island. This implies that in addition to the fermion parity $\hat{P}$ of the qubit, also all two-Majorana parities $i\hat{\gamma}_i\hat{\gamma}_j$ are good quantum numbers. In particular, this is the case for the Pauli-$\hat{Z}$ operator of the Majorana qubit. The resulting degeneracy is partially lifted when tunnel coupling the Majorana qubit to the quantum dot. It is important to notice, however, that unlike the Pauli-$\hat{Z}$ operator, the combined fermion parity operator

$$\hat{\pi} = \hat{Z}(-1)^{\hat{n}} \tag{5.5}$$

remains a conserved quantity [157]. Restricting ourselves to states which have total fermion parity $P(-1)^n = 1$ and can thus be reached from the ground state with $n = N = 0$ by tunneling, the Hamiltonian $\hat{H} = \hat{H}_{\mathrm{M}} + \hat{H}_{\mathrm{QD}} + \hat{H}_{\mathrm{T}}$ becomes block diagonal in the subspaces of the combined fermion parity $\hat{\pi}$,

$$\hat{H} = \begin{pmatrix} h_+ & 0 \\ 0 & h_- \end{pmatrix}. \tag{5.6}$$

Here, we choose the basis $\{|\uparrow, 0\rangle, |\downarrow, 1\rangle, |\downarrow, 0\rangle, |\uparrow, 1\rangle\}$ with the first entry distinguishing the eigenstates of $\hat{Z}$ and the second entry denoting the occupation of the quantum dot level, see App. C.1 for details. We use lower-case letters without hats to denote operators within subspaces of fixed combined parity $\hat{\pi}$. The corresponding 2×2 blocks take the explicit form

$$h_\pi = \begin{pmatrix} 0 & t_1 - i\pi t_2 \\ t_1^* + i\pi t_2^* & \varepsilon \end{pmatrix} = \frac{\varepsilon}{2} + \Omega_\pi \boldsymbol{h}_\pi \cdot \boldsymbol{\sigma}, \tag{5.7}$$

where $\boldsymbol{\sigma}$ denotes a vector of Pauli matrices and $\varepsilon = \epsilon + E_C$ the detuning (which depends on both, the level energy ϵ of the quantum dot and the charging energy E_C of the Majorana island). We also defined a Bloch vector

$$\boldsymbol{h}_\pi = (\sin\theta_\pi \cos\phi_\pi, \sin\theta_\pi \sin\phi_\pi, \cos\theta_\pi) \tag{5.8}$$

with $\cos\theta_\pi = -\varepsilon/2\Omega_\pi$ and $\sin\theta_\pi e^{i\phi_\pi} = (t_1^* + i\pi t_2^*)/\Omega_\pi$, as well as the Rabi frequency $\Omega_\pi^2 = \varepsilon^2/4 + |t_1^* + i\pi t_2^*|^2$. The eigenenergies and Rabi frequencies of the two subspaces are different provided that $\mathrm{Im}\,(t_1 t_2^*) \neq 0$.

5.1.2 Basic measurement protocols

The tunnel couplings entangle the Pauli-$\hat{Z}$ operator of the Majorana qubit with the charge of the quantum dot. The entanglement emerges from processes in which an electron virtually occupies the Majorana island through one Majorana involved in $\hat{Z}$ and leaves it through the other. This makes the quantum information stored nonlocally in the Majorana qubit accessible locally in the quantum dot. We first discuss to which degree a single projective measurement of the charge of the quantum dot realizes a measurement of $\hat{Z}$.

We begin with a protocol in which the tunnel coupling between dot and Majorana qubit is turned on adiabatically on the scale of the system dynamics. We assume that prior to turning on the tunnel couplings, the Majorana qubit is in an arbitrary qubit state and the quantum dot is initialized in the $n=0$ state,

$$|\psi\rangle = (\alpha|\uparrow\rangle + \beta|\downarrow\rangle)|0\rangle. \tag{5.9}$$

Adiabatically turning on the tunnel couplings t_1 and t_2, this state evolves into the corresponding eigenstate of the coupled system,

$$|\psi'\rangle = \alpha|g_+\rangle + \beta e^{i\chi}|g_-\rangle. \tag{5.10}$$

Here, the relative phase χ depends on details of the protocol, and we defined the exact ground states

$$|g_+\rangle = \sin\frac{\theta_+}{2}|\uparrow,0\rangle - \cos\frac{\theta_+}{2}e^{i\phi_+}|\downarrow,1\rangle, \tag{5.11a}$$

$$|g_-\rangle = \sin\frac{\theta_-}{2}|\downarrow,0\rangle - \cos\frac{\theta_-}{2}e^{i\phi_-}|\uparrow,1\rangle \tag{5.11b}$$

of $h_\pm$. Notice that $\theta_\pm = \pi$ in the absence of the tunnel couplings. Then, a subsequent projective measurement of the charge n of the quantum dot either yields $n=0$ and the state

$$|\psi'_0\rangle = \frac{1}{\sqrt{p'_0}}\left(\alpha\sin\frac{\theta_+}{2}|\uparrow\rangle + \beta e^{i\chi}\sin\frac{\theta_-}{2}|\downarrow\rangle\right)|0\rangle, \tag{5.12}$$

with probability

$$p'_0 = |\alpha|^2\sin^2\frac{\theta_+}{2} + |\beta|^2\sin^2\frac{\theta_-}{2}, \tag{5.13}$$

or $n=1$ and

$$|\psi'_1\rangle = \frac{1}{\sqrt{p'_1}}\left(\alpha\cos\frac{\theta_+}{2}e^{i\phi_+}|\downarrow\rangle + \beta e^{i\chi}\cos\frac{\theta_-}{2}e^{i\phi_-}|\uparrow\rangle\right)|1\rangle, \tag{5.14}$$

with probability $p'_1 = 1 - p'_0$.

Unfortunately, such charge measurements provide only partial information on the qubit state. One can arrange perfect correlation between the measurement outcome $n = 0$ and, say, the $|{\uparrow}\rangle$ state of the qubit by fine tuning $\sin \frac{\theta_-}{2} = 0$. However, one readily proves that

$$\left|\sin^2 \frac{\theta_+}{2} - \sin^2 \frac{\theta_-}{2}\right| \leq \frac{1}{2}. \tag{5.15}$$

This implies that a measurement outcome of $n = 1$ remains compatible with both qubit states even if $n = 0$ is perfectly correlated with the $|{\uparrow}\rangle$ state.

In principle, a projective measurement can be implemented when turning on the quantum dot-Majorana qubit tunneling instantaneously. In this case, the initial state $|\psi\rangle$ is no longer an eigenstate, and its unitary evolution under the Hamiltonian $\hat{H}$ entangles qubit and quantum dot. Depending on the measurement outcome, a projective charge measurement after a waiting time T yields the states

$$|\psi_0''\rangle = \frac{1}{\sqrt{p_0''}}[\alpha A_+(T)|{\uparrow}\rangle + \beta A_-(T)|{\downarrow}\rangle]|0\rangle, \tag{5.16a}$$

$$|\psi_1''\rangle = \frac{1}{\sqrt{p_1''}}[\alpha B_+(T)|{\downarrow}\rangle + \beta B_-(T)|{\uparrow}\rangle]|1\rangle. \tag{5.16b}$$

with probabilities $p_0'' = |\alpha A_+|^2 + |\beta A_-|^2$ and $p_1'' = 1 - p_0''$, respectively. Here, we defined the amplitudes $A_\pm(T) = \cos \Omega_\pm T + i \cos \theta_\pm \sin \Omega_\pm T$ and $B_\pm(T) = -i \sin \theta_\pm e^{i\phi_\pm} \sin \Omega_\pm T$, where $|A_\pm|^2 + |B_\pm|^2 = 1$. This scheme implements a projective measurement of $\hat{Z}$, when these coefficients satisfy, say, $|A_-|^2 = |B_+|^2 = 0$, with the remaining two coefficients being equal to unity. This can be realized for $t_1 = it_2$, $|t_{1,2}|^2 \gg \varepsilon^2/4$, and $T = \pi/2\Omega_-$. As such, the qubit is left in the $|{\uparrow}\rangle$ state for both measurement outcomes. Thus, for the outcome $n = 1$, this protocol would need to be followed by another waiting period to rotate the state back to $|{\downarrow}\rangle$, before turning off the tunnel couplings.

While in principle this allows for single-shot projective measurements of $\hat{Z}$, the protocol relies on fine-tuned waiting periods and a hierarchy of time scales which would be challenging to fulfill in experiment. Most importantly, we need to assume that the charge measurement is fast compared to internal time scales of the coupled Majorana qubit-quantum dot system. This requirement derives from the fact that the measurement operator $\hat{n}$ does not commute with the Hamiltonian of the system. Alternatively, we can abruptly turn off the tunnel couplings after entangling Majorana qubit and quantum dot state, and measure the quantum dot charge only subsequently. Then, the charge measurement is quantum nondemolition. Under realistic circumstances, a single projective charge measurement would presumably provide only partial information on $\hat{Z}$. This can be remedied by repeating the above protocol sufficiently many times until the measurement outcome is certain (see App. C.2).

Implementing this protocol is clearly challenging and requires detailed and fast control. One may also worry that the fast switching excites the qubit in unwanted ways. It would be preferable to implement a projective measurement of $\hat{Z}$ by monitoring the quantum dot charge *while* the quantum dot is coupled to the Majorana qubit. This obviates the need for repeated switching, ideally without compromising on the achievable measurement times. We now turn to describe such continuous measurement procedures.

5.2 Majorana-qubit readout via quantum dot charge monitoring

5.2.1 Continuous charge measurements

To describe the readout dynamics, we need to include a measurement device for the quantum dot charge in the microscopic description. We assume that the quantum dot is capacitively coupled to a voltage-biased quantum point contact in such a way that the transmission amplitude $\mathcal{T}$ of the quantum point contact depends on the charge state of the quantum dot [250, 251],

$$\hat{\mathcal{T}} = \tau + \chi\hat{n}. \tag{5.17}$$

The current through the quantum point contact will then depend on the quantum dot charge, taking the values $I_0 \propto |\tau|^2$ when the quantum dot is empty and $I_1 \propto |\tau + \chi|^2$ when the quantum dot is occupied. (For simplicity, we assume that τ and χ have relative phase π.) Provided that the voltage applied to the quantum point contact is sufficiently large, $eV \gg \Omega_\pi$, this setup decoheres the system in the quantum dot charge basis (see App. C.3.1).

When $I_0 \gg |\delta I| = |I_1 - I_0|$, the fluctuating current through the quantum point contact becomes a Gaussian random process (see App. C.3.3),

$$I(t) = I_0 + \delta I\langle\hat{n}(t)\rangle + \sqrt{I_0}\xi(t), \tag{5.18}$$

involving the Langevin current $\xi(t)$ with $\mathbb{E}[\xi(t)] = 0$ and $\mathbb{E}[\xi(t)\xi(t+\tau)] = \delta(\tau)$. Here, $\mathbb{E}[.]$ denotes an ensemble average over many realizations of the measurement procedure. It will prove useful to work with a dimensionless measurement signal

$$j(t) = \frac{I(t) - I_0}{\delta I} = \langle\hat{n}(t)\rangle + \frac{1}{\sqrt{4k}}\xi(t) \tag{5.19}$$

relative to the measured background current I_0, with $k \propto |\chi|^2$. The first term contains information on the quantum dot charge and the second is the noise added by the quantum point contact. Within the Born-Markov approximation, the state of the system evolves according to the stochastic master equation [250, 251] (see App. C.3 for a derivation)

$$\frac{\mathrm{d}}{\mathrm{d}t}\hat{\rho}_c(t) = \underbrace{-i\Big[\hat{H},\hat{\rho}_c(t)\Big] + k\mathcal{D}[\hat{n}]\hat{\rho}_c(t)}_{\equiv\mathcal{L}\hat{\rho}_c(t)} + \sqrt{k}\xi(t)\mathcal{H}[\hat{n}]\hat{\rho}_c(t). \tag{5.20}$$

The term involving the superoperator $\mathcal{D}[\hat{L}]\hat{\rho} = \hat{L}\hat{\rho}\hat{L}^\dagger - (\hat{L}^\dagger\hat{L}\hat{\rho} + \hat{\rho}\hat{L}^\dagger\hat{L})/2$ causes decoherence in the eigenbasis of $\hat{n}$, and the term with the superoperator $\mathcal{H}[\hat{L}]\hat{\rho} = \hat{L}\hat{\rho} + \hat{\rho}\hat{L}^\dagger - \langle\hat{L} + \hat{L}^\dagger\rangle\hat{\rho}$ describes the information gain by the measurement. The latter is a Langevin term due to the stochastic nature of the measurement. The stochastic master equation (5.20) describes the state of the system *conditioned* on the measurement signal $j(t)$, as denoted by the subscript c. The ensemble-averaged – and thus *unconditioned* – evolution of the system simply follows by dropping the stochastic term, $\mathrm{d}\hat{\rho}(t)/\mathrm{d}t = \mathcal{L}\hat{\rho}(t)$.

5.2.2 QUANTUM-DOT CHARGE MEASUREMENT

To recall how this formalism describes standard projective measurements, consider first a simple quantum dot charge readout with $\hat{H}_T = 0$. The deterministic terms in Eq. (5.20) lead to a decay of the off-diagonal components of the density matrix $\hat{\rho}$ in the charge basis, but preserve the diagonal components. The action of the stochastic terms can be understood from the equation of motion for $n(t) \equiv \langle\hat{n}(t)\rangle = \mathrm{tr}[\hat{n}\hat{\rho}_c(t)]$,

$$\frac{\mathrm{d}}{\mathrm{d}t}n(t) = \sqrt{4k}[n(t) - n^2(t)]\xi(t). \tag{5.21}$$

Its two fixed points $n = 0$ and $n = 1$ correspond to the two possible measurement outcomes. Conservation of the diagonal components of the ensemble-averaged density matrix ensures that these outcomes occur with the correct probabilities. At the fixed point n, the quantum-point-contact current $j(t)$ becomes stationary, $j_n(t) = n + \xi(t)/\sqrt{4k}$, and directly reveals the measurement outcome n after an integration time τ_m. The latter is determined by the requirement that the integrated signal dominate over the integrated noise, which happens for $\tau_m \gg (4k)^{-1}$. We note that we use the steady-state measurement signal when estimating measurement times. While transients may also provide information in principle, we assume that in practice, typical measurement times will exceed the time scale on which the system decoheres.

This time-resolved description of a projective measurement of $\hat{n}$ is illustrated in Fig. 5.2 based on a numerical solution of Eq. (5.20). We show sample trajectories of the expectation value of the quantum dot charge (experimentally inaccessible) as well as the corresponding measurement currents through the quantum point contact. While the instantaneous measurement current fluctuates strongly, its time average reveals the quantum dot charge.

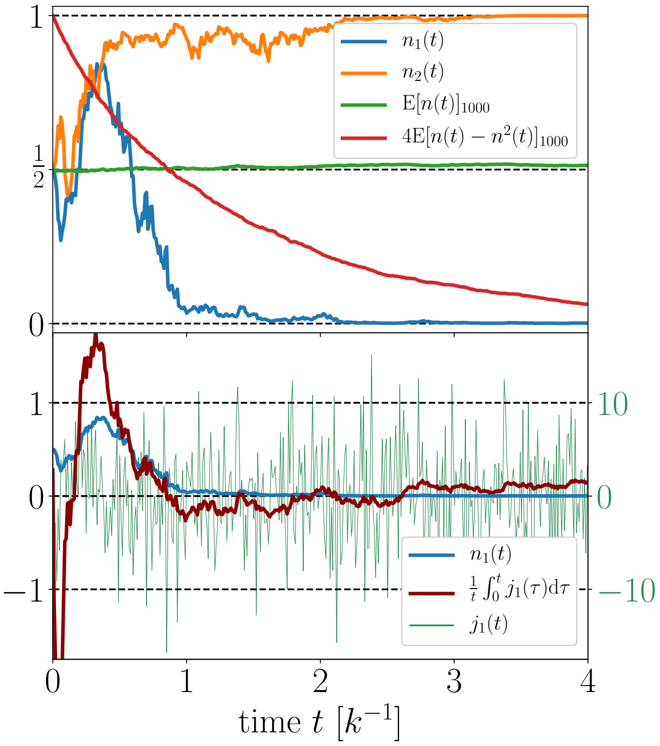

Figure 5.2: Continuous measurement of the quantum dot charge for $H_T = 0$, with initial state $(|\uparrow, 0\rangle + |\downarrow, 1\rangle)/\sqrt{2}$ corresponding to $n(0) = 1/2$. (a) Two sample trajectories $n_1(t)$ (blue) and $n_2(t)$ (orange) corresponding to measurement results $n = 0$ and $n = 1$, respectively. The ensemble averaged evolution of the quantum dot charge (green, obtained from 1000 trajectories) stays near 1/2. The ensemble average of $4\big(n(t) - n^2(t)\big)$ (red) equals unity for uncertain charge and zero when a fixed point has been reached, and therefore quantifies the advance of the measurement process. (b) Instantaneous (green, right y-axis labels) and time-averaged (dark red, left y-axis labels) measurement current for sample trajectory $n_1(t)$ (blue, same as in top panel). Figure from [VII].

5.2.3 MAJORANA-QUBIT READOUT

Including the tunnel coupling $\hat{H}_T$ between quantum dot and Majorana qubit, the dot occupation is no longer a good quantum number. While the measurement tries to project the state of the system into charge eigenstates, tunneling continuously rotates it out of this basis. This can be seen explicitly from the equation of motion for the charge expectation value,

$$\frac{\mathrm{d}n}{\mathrm{d}t} = i\Big\langle \Big[\hat{H}, \hat{n}\Big] \Big\rangle + \sqrt{4k}[n - n^2]\xi. \tag{5.22}$$

As a result of the nonzero commutator on the right hand side, the evolution of $n(t)$ no longer tends towards fixed points. Similarly, $\langle \hat{Z}(t) \rangle$ also does not evolve towards fixed points as $\hat{Z}$ does not commute with $\hat{H}$, as well. At first sight, this seems to imply that quantum dot charge measurements will not suffice to read out the state of the qubit. Remarkably, we find that one may still read out $\hat{Z}$ from a measurement of the quantum dot charge, but the procedure is more subtle.

The key observation is that the evolution governed by Eq. (5.20) implements a quantum nondemolition measurement of the combined local parity $\hat{\pi}$, which is in one-to-one correspondence with $\hat{Z}$ for the initial state in Eq. (5.9). Under quantum dot charge measurements, the evolution of $\pi(t) = \langle\hat{\pi}(t)\rangle$ is a bistable process with fixed points $\pi = \pm 1$, which are reached with the correct probabilities $|\alpha|^2$ and $|\beta|^2$, respectively. This does not yet guarantee a projective measurement of $\hat{Z}$. First, as a consequence of the tunneling Hamiltonian, the measurement does not properly project the state of the system, but leaves it in an equal mixture of the two eigenstates with combined local parity π. However, once the measurement outcome π is determined, the readout device can be decoupled and the state of the quantum dot-Majorana qubit system appropriately reset (see App. C.2.2). Second, one needs to specify how to read out π and thus Z from the measurement current. Unlike for pure quantum dot charge measurements, the average measurement current in general no longer distinguishes between the two measurement outcomes. Instead, a measurement readout generally requires one to analyze the frequency-dependent noise of the measurement current.

We now discuss these claims in more detail. We first show that under quantum dot charge measurements, the unconditioned evolution of the density matrix $\hat{\rho}(t)$ generically tends towards

$$\hat{\rho}^{\infty} = \frac{1}{2}\mathrm{diag}(|\alpha|^2, |\alpha|^2, |\beta|^2, |\beta|^2) \tag{5.23}$$

for the initial state in Eq. (5.9). This follows because the evolution preserves the weight of the two π subspaces and the set of steady states of $\mathcal{L}$ is spanned by $\hat{\rho}_+^{\infty} = \mathrm{diag}(1,1,0,0)/2$ and $\hat{\rho}_-^{\infty} = \mathrm{diag}(0,0,1,1)\,/2$. To see this, we decompose $\hat{\rho}$ into 2×2 blocks $\rho_{\pi,\pi'}$ according to the combined parity eigenvalues. Since $\hat{\pi}$ is a good quantum number and commutes with the quantum dot charge operator, the evolution equation for $\hat{\rho}$ decouples into independent equations

$$\dot{\rho}_{\pi,\pi} = -i[h_\pi, \rho_{\pi,\pi}] + k\mathcal{D}[n]\rho_{\pi,\pi} = \mathcal{L}_{\pi,\pi}\rho_{\pi,\pi}, \tag{5.24a}$$

$$\dot{\rho}_{+-} = -i(h_+\rho_{+-} - \rho_{+-}h_-) + k\mathcal{D}[n]\rho_{+-} = \mathcal{L}_{+-}\rho_{+-}. \tag{5.24b}$$

for the diagonal and off-diagonal blocks of $\hat{\rho}$.

The equations for the diagonal blocks have themselves Lindblad form and preserve the trace. As h_π does not commute with the quantum dot charge n (unless $t_1 = \pm i t_2$ in which case the tunneling Hamiltonian vanishes for one of the blocks; we will comment on this case below) and as n is hermitian, their only zero mode is the completely mixed state. Then, preservation of the trace implies that the diagonal blocks of the density matrix do indeed tend towards the fixed points

$$\rho_{++}^{\infty} = \frac{|\alpha|^2}{2}\mathbb{1} \quad \text{and} \quad \rho_{--}^{\infty} = \frac{|\beta|^2}{2}\mathbb{1}, \tag{5.25}$$

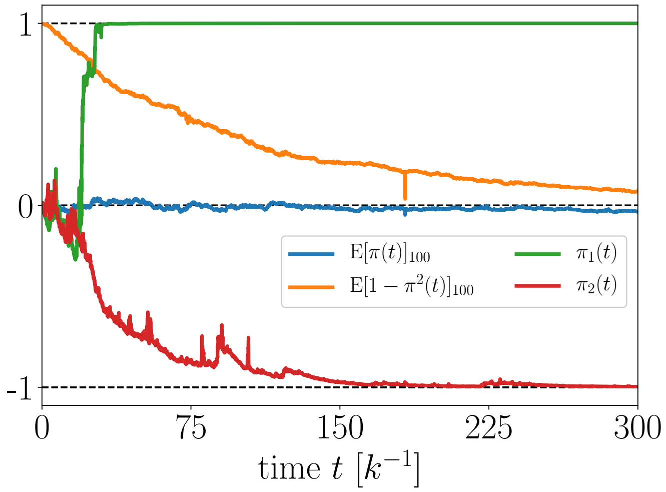

Figure 5.3: Continuous readout of Majorana qubit, with initial state $(|\uparrow,0\rangle + |\downarrow,0\rangle)/\sqrt{2}$ corresponding to $n(0) = 0$. Two sample trajectories $\pi_1(t)$ (green) and $\pi_2(t)$ (red) show different measurement outcomes $\pi = 1$ and $\pi = -1$, respectively. The ensemble average of $\pi(t)$ (blue, computed for 100 trajectories) remains close to zero for all times. The ensemble average of $1 - \pi^2(t)$ (orange) quantifies the distance from the fixed points $\pi = \pm 1$. Parameters: $\varepsilon = 20k$, $t_1 = e^{-i\varphi}t_2 = 2k$ with $\varphi = \pi/4$. Figure from [VII].

respectively. (We analyze the complete set of eigenvalues $\lambda_{\pi,n}$ and eigenmodes of $\mathcal{L}_{\pi,\pi}$ in App. C.4.1.) Anticipating that the off-diagonal blocks generically decay to zero, we obtain the correct Born-rule probabilities for $\hat{Z}$. The final state has weight $|\alpha|^2$ in the $\pi = +1$ subspace and $|\beta|^2$ in the $\pi = -1$ subspace, which just corresponds to the probabilities of finding $Z = +1$ or $Z = -1$, as required.

The equation for the off-diagonal block deviates from Lindblad form since the first term on the right hand side involves both Hamiltonians h_+ and h_-. We analyze the eigenvalues $\tilde{\lambda}_n$ of $\mathcal{L}_{+-}$ in App. C.4.2 and find that they generically correspond to decaying modes. Then, the off-diagonal blocks decay to zero and the two π subspaces decohere, $\rho^{\infty}_{+-} = 0$. The only exception occurs when $\mathrm{Im}\{t_1 t_2^*\} = 0$. In this case, the off-diagonal block supports a nondecaying mode since the characteristic frequencies coincide for the $\pi = +1$ and $\pi = -1$ eigenspaces and we find $\rho^{\infty}_{+-} = \alpha^* \beta \mathbb{1}/2$.

Consistent with these results, the conditional evolution of $\hat{\rho}$ is a bistable process for $\pi(t)$ and a projective measurement of $\hat{\pi}$. We can readily derive the stochastic evolution equation for $\pi(t)$,

$$\dot{\pi} = \sqrt{4k}\xi(\langle \hat{n}\hat{\pi}\rangle - n\pi). \tag{5.26}$$

Clearly, $\pi = \pm 1$ are fixed points of this equation. This is illustrated in Fig. 5.3, where we show two representative sample trajectories of $\pi(t)$ for measurement outcomes $\pi = +1$ and $\pi = -1$. We find numerically that provided $\mathrm{Im}\{t_1 t_2^*\} \neq 0$, these are the only fixed points, cp. $\mathbb{E}[1 - \pi^2(t)] \to 0$ in Fig. 5.3. We analyze the stochastic evolution in more detail in App. C.5.

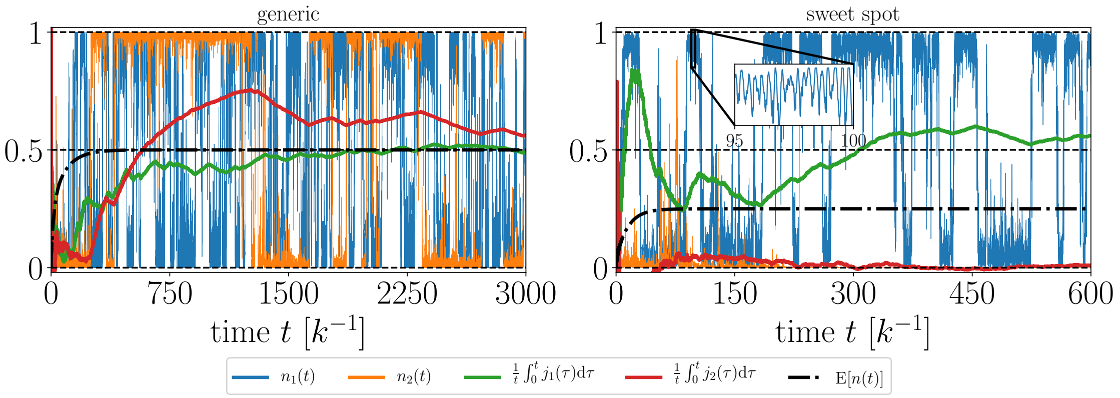

Figure 5.4: Continuous readout of Majorana qubit, with initial state $(|\uparrow,0\rangle + |\downarrow,0\rangle)/\sqrt{2}$ corresponding to $n(0) = 0$. The panels show the (experimentally accessible) time-averaged measurement currents for two different combined-parity outcomes $\pi = 1$ (index 1) and $\pi = -1$ (index 2) and the (experimentally inaccessible) expectation value of the quantum dot charge. (a) Generic parameters as in Fig. 5.3 ($\varphi = \pi/4$). Average measurement currents converge to $1/2$ for both $\pi = +1$ (dark green) and $\pi = -1$ (dark red), reflecting $\mathbb{E}[n(t)] \to 1/2$ (dash-dotted line), and the measurement outcome cannot be deduced from the time-averaged measurement current in the long-time limit. The charge expectation value $n_i(t)$ remains close to the charge eigenvalues, with occasional transitions occurring more frequently for outcome $\pi = +1$ (blue trace) than for outcome $\pi = -1$ (orange trace), reminiscent of telegraph noise. For suitable parameters, it may be feasible to base readout on extracting the transition rate between $n \simeq 0$ and $n \simeq 1$ from the measurement current. Moreover, the integrated current relaxes more slowly to $1/2$ in the low-frequency sector (here $\pi = -1$) which may also help readout in some instances. (b) Same for the sweet spot $t_1 = -it_2$ ($\varphi = \pi/2$), where the system Hamiltonian h_π commutes with the quantum dot charge $\hat{n}$ for $\pi = -1$. The time-averaged measurement current now converges to $1/2$ for outcome $\pi = +1$ (dark green, $\hat{n}$ not conserved) and to zero for outcome $\pi = -1$ (dark red, $\hat{n}$ conserved), so that π is accessible from the time-averaged measurement current. This is a limiting case of the readout based on transition rates between $n \simeq 0$ and $n \simeq 1$, which become increasing unequal as parameters approach the sweet spot. The ensemble average of $n(t)$ (dash-dotted line) now converges to $1/4$. The inset shows the coherent charge oscillations at frequency Ω_+. Figure from [VII].

The decay of the off-diagonal block to zero implies that π can be extracted from the measurement current $j(t)$. Once the measurement current becomes stationary, $j(t) = j_\pi(t)$, the system explores the full subspace with fixed π in an ergodic manner. This follows from the fact that the ensemble average over all trajectories with outcome π yields a completely mixed state on the subspace. Importantly, this implies that the ensemble (or time) average of $j_\pi(t)$ does not carry information on π,

$$\mathbb{E}[j_\pi(t)] = \mathrm{tr}[\hat{n}\mathbb{E}[\hat{\rho}_c(t)|_\pi]] + \frac{\mathbb{E}[\xi(t)]}{\sqrt{4k}} = n_\pi^\infty = \frac{1}{2}. \tag{5.27}$$

In agreement with Eq. (5.27) and in contrast to the simple quantum dot charge readout (see Sec. 5.2.2), the integrated measurement currents converge to $1/2$ irrespective of the measurement outcome. This is shown in Fig. 5.4 (left panel).

Nonetheless, information on π is generically encoded in the noise correlations of the measurement current,

$$S_\pi(\tau) = \mathbb{E}[j_\pi(t) j_\pi(t+\tau)]. \tag{5.28}$$

In the stationary (long-time) limit, the corresponding power spectrum $S_\pi(\omega)$ can be readily computed for the two values of π (see App. C.6). In the limit of weak measurements, $k \ll \Omega_\pi$, we find that in addition to a white-noise background, which is just the shot noise power of the quantum point contact, the power spectrum exhibits Lorentzian peaks at $\omega = 0$ and $\omega = \pm 2\Omega_\pi$, which reflect the dynamics of the Majorana qubit-quantum dot system. Explicitly, we find

$$S_\pi(\omega) = \frac{1}{4k} + \frac{\cos^2\theta_\pi}{2} \frac{\kappa_\pi}{\omega^2 + \kappa_\pi^2} + \frac{\sin^2\theta_\pi}{4} \sum_\pm \frac{\tilde{\kappa}_\pi}{(\omega \pm 2\Omega_\pi)^2 + \tilde{\kappa}_\pi^2}, \tag{5.29}$$

where we introduced the widths

$$\kappa_\pi = \frac{\sin^2\theta_\pi}{2} k, \; \tilde{\kappa}_\pi = \frac{(1+\cos^2\theta_\pi)}{4} k \tag{5.30}$$

of the Lorentzians. The measurement result for π can be read off in particular from the location of the Lorentzians in frequency. This is illustrated in Fig. 5.5 which shows the power spectrum for a numerically generated measurement current and compares it to Eq. (5.29).

Physically, the zero-frequency peak in Eq. (5.29) is associated with the telegraph noise of the charge expectation value shown in Fig. 5.4. In principle, the width of this peak also encodes the measurement outcome. Indeed, Fig. 5.4 illustrates that the dwell time near $n = 0$ and $n = 1$ depends on the π subspace. For suitable parameters, it may also be possible to monitor the transition rate directly by means of an appropriately smoothened measurement current, or to extract information on the measurement outcome from associated transients in the time-averaged measurement current. The peak at finite frequency originates from Rabi oscillations, which are seen in Fig. 5.4 as the small deviations of the quantum dot charge from its eigenvalues $n = 0$ and $n = 1$ (see inset of right panel). The measurement pushes the system into a charge eigenstate and thus a superposition of energy eigenstates, which then leads to oscillations as a result of the Hamiltonian dynamics.

It is interesting to consider two special parameter choices. First, for $\mathrm{Im}\{t_1 t_2^*\} = 0$, the off-diagonal block ρ_{+-} of the density matrix does not decay. Indeed, in this case, not only the average measurement signal, but also its noise correlations are independent of π. More generally, the failure to decohere in the $\hat{\pi}$ basis reflects the fact that the measurement signals for the two subspaces are indistinguishable.

While the measurement fails for $\mathrm{Im}\{t_1 t_2^*\} = 0$, it can be simplified at the sweet spot $t_1 = -it_2$ ($t_1 = it_2$ is analogous). In this case, the Hamiltonian commutes with $\hat{n}$ in the $\pi = -1$ block and charge conservation in this block makes all density matrices which are diagonal in the charge basis into zero modes of $\mathcal{L}_{--}$. In this fine-tuned situation, it is not necessary to

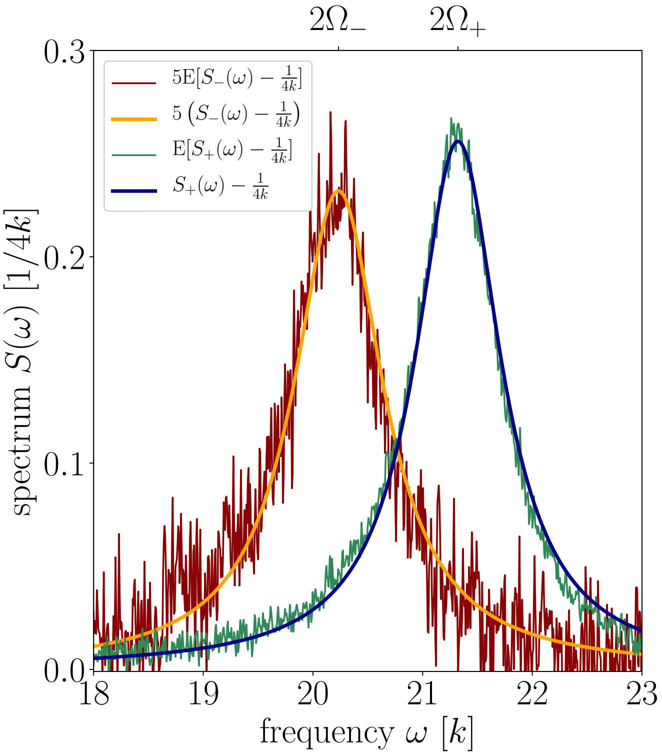

Figure 5.5: Power spectra of the measurement signal corresponding to outcomes $\pi = +1$ and $\pi = -1$. Numerical simulations based on Eq. (5.20) (green and red traces) are in excellent agreement with the analytical expression in Eq. (5.29) (blue and orange traces). The numerical power spectra were obtained by generating measurement signals for long time intervals of $T \sim 10^7 k^{-1}$. The long integration time is necessitated by the small weight of the finite-frequency Lorentzians when $\sin\theta_\pi \ll 1$. Other parameters as in Fig. 5.3. The power spectrum for $\pi = -1$ is scaled up by a factor of five for better visibility. Figure from [VII].

measure noise correlations. Instead, the measurement outcome for $\hat{\pi}$ and hence $\hat{Z}$ can be extracted from the ensemble-averaged charge alone, which yields $\mathbb{E}[n] = 1/2$ for $\pi = +1$ and $\mathbb{E}[n] = 0$ for $\pi = -1$. For small deviations from the fine-tuned point, $t_1 = -it_2 + \delta$ with $\delta \ll |t_1|$, charge is no longer conserved in both blocks and $\mathbb{E}[n] = 1/2$ regardless of π. However, the relaxation rate to the stationary state will be smaller in the $\pi = -1$ block by a factor $|\delta|^2/|t_1|^2$. For a sufficiently high measurement efficiency, it might then be possible to resolve π from transient differences in the average charge. Figure 5.4 (right panel) shows corresponding simulations (with $\delta = 0$), which confirm that in principle, the integrated measurement signals suffice to identify the measurement outcome in a measurement time $\tau_m \sim k^{-1}$.

An important characteristic of the measurement is the measurement-induced decoherence time (see Refs. [188–194] for discussions of Majorana qubit decoherence unrelated to measurements). The decoherence time is closely related to (and in fact upper bounded by) the inverse of the real part of the slowest decaying eigenvalue $\tilde{\lambda}_{\text{slow}}$ of $\mathcal{L}_{+-}$. Figure 5.6 shows numerical

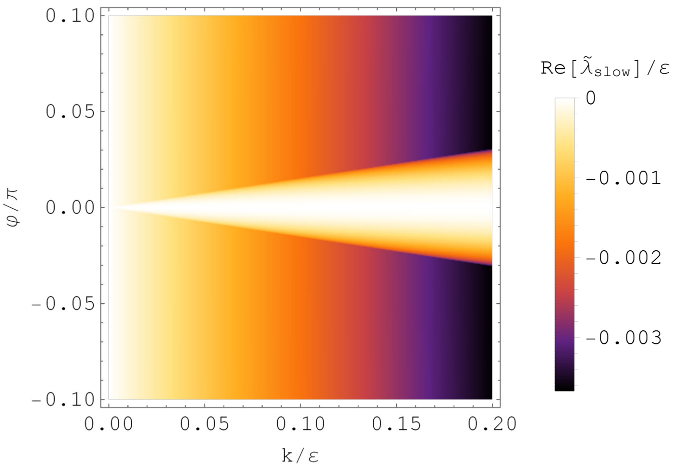

Figure 5.6: Decoherence rate as characterized by the real part of the slowest decaying eigenvalue of $\mathcal{L}_{+-}$, $\mathrm{Re}\{\tilde{\lambda}_{\rm slow}\}$ as a function of the measurement strength k and φ defined through $t_1 = e^{-i\varphi}t_2 = 0.1\varepsilon$. Figure from [VII].

results for $\mathrm{Re}\{\tilde{\lambda}_{\rm slow}\}$. We focus on weak measurements, $k, |t_1|, |t_2| \ll \varepsilon$, and nonzero but possibly small φ defined through $t_1 = e^{-i\varphi}t_2$. We observe that there is no decoherence along the line $\varphi = 0$ where $\mathrm{Im}\{t_1 t_2^*\} = 0$. At fixed k, $\mathrm{Re}\{\tilde{\lambda}_{\rm slow}\}$ grows quadratically in φ up until discontinuous lines, where $\tilde{\lambda}_{\rm slow}$ and the corresponding eigenmatrix coalesce with another eigenvalue-eigenmatrix pair. Then, the eigenmatrices of $\mathcal{L}_{+-}$ fail to span the space of 2×2 complex matrices along these *exceptional* lines emanating from $(\varphi, k) = (0, 0)$. At fixed φ and to leading order in k, we observe a linear decrease as k increases towards the discontinuity. The measurement is more efficient when tuning to the large-$|\varphi|$ side of the exceptional lines. In this region, $\mathrm{Re}\{\tilde{\lambda}_{\rm slow}\}$ depends only weakly on φ, which is why we only display the region of small φ in Fig. 5.6. Note that the discontinuities are regularized by relaxation terms, such as those discussed in the following Sec. 5.2.4.

5.2.4 MAJORANA-QUBIT READOUT IN THE PRESENCE OF RELAXATION

The results of the previous section may be surprising in that the quantum point contact does not detect the dependence of the ground-state expectation value of the quantum dot charge on the parity sector π. Instead, the information on π can generically only be extracted from noise correlations of the measurement current $j(t)$. Experimentally, however, it would be preferable if π could be extracted from the average measurement signal.

The underlying reason for the insensitivity to the quantum dot charge in the ground state is that under the continuous measurement, the density matrix generically becomes proportional to the unit matrix within the subspace with fixed π [see Eq. (5.25)]. Then, the expectation value of the quantum dot charge is just equal to 1/2, independent of the parity π. The difference in quantum dot charge between the ground states is compensated by the opposite difference between the excited states.

It is then natural to expect that the average measurement current distinguishes between the two subspaces once one includes additional relaxation processes from the excited state $|e_\pi\rangle$ to the ground state $|g_\pi\rangle$. Unlike the measurement which leads to relaxation in the basis of the quantum dot charge, this additional relaxation should operate within the eigenbasis of h_π. We now show that this expectation is indeed correct.

There are various processes which induce relaxation within the eigenstate basis. One relevant example are effective measurements of the Majorana-qubit charge by the environment. For definiteness, we effect relaxation within the eigenstate basis by coupling to the electromagnetic environment. Within the Born-Markov approximation and focusing on $T = 0$ for simplicity, this leads to an additional dissipation term in Eq. (5.20) (see App. C.3.4 for details),

$$\frac{\mathrm{d}}{\mathrm{d}t}\hat{\rho}|_{\mathrm{relax}} = \Gamma_- \sum_\pi \mathcal{D}\left[\frac{\sin\theta_\pi}{2}\hat{\tau}_-^\pi\right]\hat{\rho} \equiv \mathcal{L}'\hat{\rho}. \tag{5.31}$$

Here, we defined the lowering operator in the energy basis for subspace π, $\hat{\tau}_-^\pi = |g_\pi\rangle\langle e_\pi|$ and the zero-temperature relaxation rate $\Gamma_- = 2\pi J(2\Omega_\pi)$ governed by the spectral density $J(\omega)$ of the electromagnetic environment. While Γ_- may depend on π in principle, we assume $J(2\Omega_+) \simeq J(2\Omega_-)$ for simplicity. Note that at finite temperatures, there is an additional dephasing term $\Gamma_0\mathcal{D}[\cos\theta_\pi\hat{\tau}_z^\pi/2]\hat{\rho}$ in the eigenstate basis, where $\Gamma_0 = 2\pi\lim_{\omega\to 0} J(\omega)b(\omega)$ with the Bose distribution $b(\omega)$. However, for $k, \Gamma_-, \Gamma_0 \ll \Omega_\pi$, this term does not affect the results, cp. App. C.4.1.

Importantly, Eq. (5.31) also conserves $\hat{\pi}$ and the total unconditioned master equation [obtained by incorporating Eq. (5.31) into Eq. (5.20)] still decouples into blocks. The off-diagonal block obeys

$$\dot{\rho}_{+-} = (\mathcal{L}_{+-} + \mathcal{L}'_{+-})\rho_{+-}. \tag{5.32}$$

Here, $\mathcal{L}'_{+-} = \frac{1}{4}\Gamma_- \sin\theta_+ \sin\theta_- \mathcal{D}[\tau_-]$ has Lindblad form and a negative semidefinite real part. Since $\mathcal{L}_{+-}$ generically has only decaying eigenvalues, $\mathcal{L}_{+-} + \mathcal{L}'_{+-}$ is also decaying. The only exception occurs when $\mathrm{Im}\{t_1 t_2^*\} = 0$, as in the absence of relaxation. In this special case, $\mathcal{L}_{+-}$ and thus also $\mathcal{L}_{+-} + \mathcal{L}'_{+-}$ as a whole have Lindblad form and preserve the trace. Thus, the condition for the measurement to work remains unchanged in the presence of relaxation.

The evolution of the diagonal blocks tends to

$$\rho_{\pi,\pi}^\infty = \frac{1}{2}(\tau_0^\pi + R\tau_z^\pi) \tag{5.33}$$

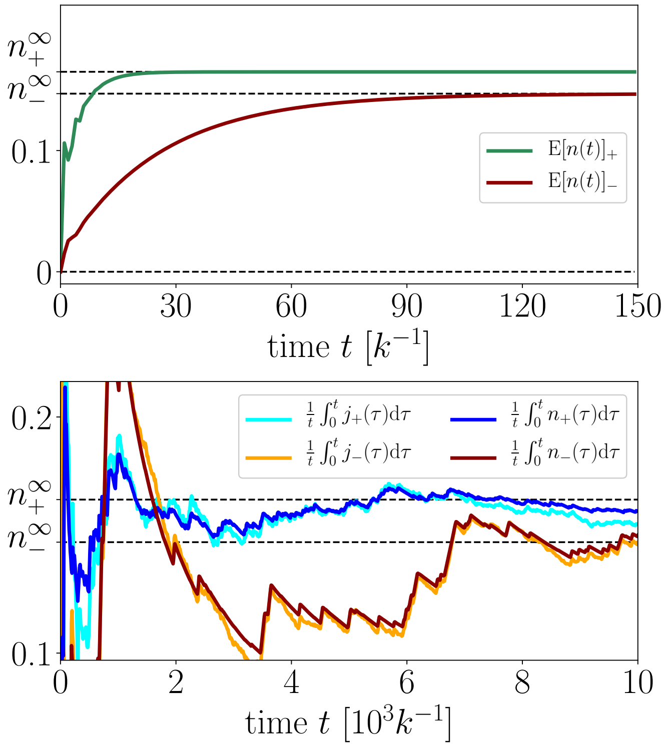

Figure 5.7: Continuous readout of Majorana qubit in the presence of relaxation with rate $\Gamma_- = 5k$ (other parameters as in Fig. 5.3). (a) Ensemble-averaged quantum dot occupations $n(t)$, restricted to the subspaces $\pi = +1$ (green trace) and $\pi = -1$ (red trace), as obtained from the unconditioned master equation (starting in the ground state with $n = 0$). $\mathbb{E}[n(t)]_\pi$ converges to distinct expectation values n_π^∞ for the two subspaces, so that π can be read out from the time-averaged measurement current of a quantum dot charge measurement. (b) Time averaged measurement signals for trajectories in the $\pi = +1$ (cyan trace) and $\pi = -1$ (orange) sectors, converging to n_π^∞. Readout requires integration times which are significantly longer than convergence times of the ensemble-averaged quantum dot occupations in the top panel. From Eq. (5.39), the measurement time can be estimated as $\tau_m \sim 10^4/k$ for the given parameters. This estimate is based on the fluctuations in the $\pi = -1$ sector, where fluctuations are larger since $\cot\theta_- \gg \cot\theta_+$. We also show the time average of the charge expectation value (not accessible in experiment). The similarity of the curves indicates that fluctuations of the measurement current are dominated by fluctuations of the charge expectation value. Figure from [VII].

in the energy basis to leading order in $\Omega_\pi \gg k, \Gamma_-$. Here we defined the ratio

$$R = \frac{\Gamma_-}{\Gamma_- + 2k} \tag{5.34}$$

characterizing the strength of the additional relaxation. The associated ensemble average of the quantum dot charge becomes

$$n_\pi^\infty = \frac{1}{2}(1 + R\cos\theta_\pi). \tag{5.35}$$

When the measurement is stronger than dissipation, we have $R \ll 1$ and the quantum dot charge is close to $1/2$, independent of π. However, in the opposite limit, when dissipation is stronger than the measurement and R approaches unity, the average charge is approximately given by the ground-state expectation value of the charge in the respective sector, $\langle g_\pi|\hat{n}|g_\pi\rangle = (1+\cos\theta_\pi)/2$. In this limit, the time-averaged measurement signal depends on π, in agreement with the heuristic arguments given above.

We illustrate these considerations by the numerical simulations shown in Fig. 5.7. Including the relaxation process in Eq. (5.31) in the simulations of the unconditioned master equation, we compute the time-averaged measurement currents and find that indeed, they converge towards n_π^∞, albeit slowly.

The corresponding measurement time is determined by the requirement to resolve the difference

$$\left|n_+^\infty - n_-^\infty\right| = 4R\left|\frac{\mathrm{Im}\{t_1 t_2^*\}}{\varepsilon^2}\right| \tag{5.36}$$

in quantum dot occupations. The time-averaged measurement current

$$j_{\mathrm{int},\pi}(T) = \frac{1}{T}\int_0^T \mathrm{d}t\, j_\pi(t) \tag{5.37}$$

fluctuates around n_π^∞, with decreasing magnitude of the fluctuations as T grows. The fluctuations can be estimated via the variance

$$\mathbb{V}[j_{\mathrm{int},\pi}(T)] = \frac{1}{4kT} + \cot^2\theta_\pi R^2\,\frac{4k}{\Gamma_-^2 T}. \tag{5.38}$$

The first term reflects the white noise background, whereas the second originates from fluctuations of $n(t)$. The latter depends on the sector π. The measurement time can then be estimated by comparing the variance with the resolution necessary to distinguish the two possible measurement outcomes. This gives

$$\tau_m \sim \frac{\varepsilon^4}{16|\mathrm{Im}\{t_1 t_2^*\}|^2}\left(\frac{1}{4kR^2} + C\frac{4k}{\Gamma_-^2}\right), \tag{5.39}$$

where we use the variance of the sector with larger fluctuations, defining

$$C = \max_\pi \cot^2\theta_\pi. \tag{5.40}$$

We observe that a large splitting resulting from a large $|\mathrm{Im}\{t_1 t_2^*\}|$ and a small ε are advantageous for a fast measurement. (Note, however, that there is a tradeoff since a small ε enhances quasiparticle poisoning rates.) Moreover, the terms in the brackets have interesting structure. They diverge for both $k \to 0$ and $k \to \infty$. Thus, at a given Γ_-, there is an optimal mea-

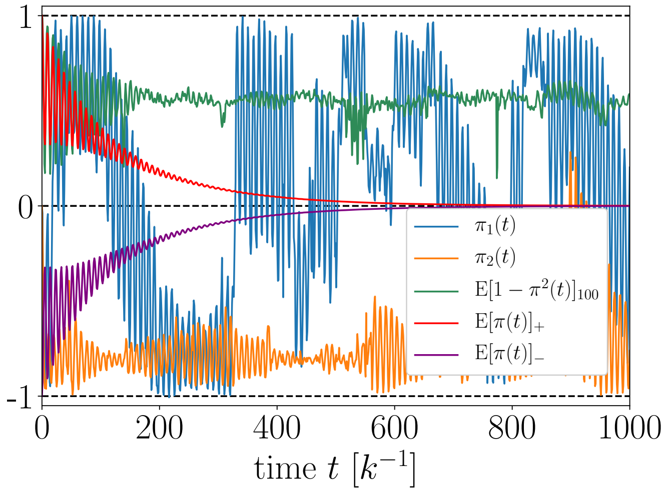

Figure 5.8: Effect of Majorana hybridization $\epsilon_{23} = 0.2k$ on Majorana-qubit readout (in the absence of relaxation, $\Gamma_- = 0$). Blue and orange traces: Sample trajectories of $\pi(t)$, clearly not reaching a fixed point. Red and purple traces: Ensemble-averaged evolution of $\pi(t)$ for states initialized in the $\pi = +1$ (red) and $\pi = -1$ (purple) sectors. Both curves converge towards $\mathbb{E}[\pi] = 0$, corresponding to an equal mixture of the two sectors, regardless of initial condition. Similarly, $\mathbb{E}[1 - \pi^2(t)]$ (green) does not approach 0, so that $\pi \neq \pm 1$. Other parameters as in Fig. 5.3. Figure from [VII].

surement strength $k_{\text{opt}} = \Gamma_-/2\sqrt{1+4C}$ to identify the measurement outcome based on the time-averaged signal. The corresponding optimal measurement time becomes

$$\tau_{m,\text{opt}} \sim \frac{\varepsilon^4\left(1+\sqrt{1+4C}\right)}{16\Gamma_-|\mathrm{Im}\{t_1 t_2^*\}|^2}. \tag{5.41}$$

5.2.5 CHARGE NONCONSERVATION AND MAJORANA HYBRIDIZATIONS

An essential assumption underlying the readout of the Majorana qubit is that the combined parity $\hat{\pi}$ is a good quantum number. In practice, there can be processes which do not conserve $\hat{\pi}$. First, the combined parity does not commute with the residual Majorana hybridizations ε_{ij} in Eq. (5.1) (except for ε_{12}). Second, $\hat{\pi}$ is no longer conserved in the presence of leakage of the quantum dot charge, say into additional reservoirs.

It is natural to expect that these processes spoil the measurement by allowing weight to move between the π subspaces and thereby scrambling the probabilities associated with the measure-

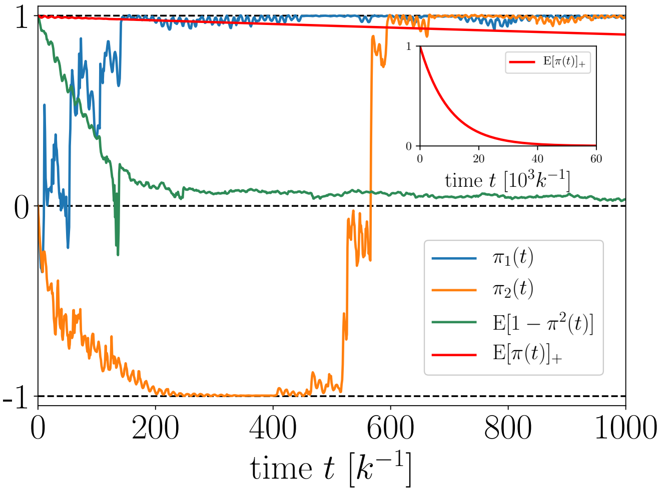

Figure 5.9: Effect of a weak Majorana hybridization $\epsilon_{23} = 0.02k$ on Majorana-qubit readout. For this hybridization strength, the measurement evolution, which tries to project π onto an eigenvalue of $\hat{\pi}$, is stronger than the evolution due to $\hat{H}_{23}$. Thus, in contrast to Fig. 5.8, individual $\pi_i(t)$ traces (blue and orange) remain predominantly near the fixed points $\pi = \pm 1$. This is also reflected in the fact that $\mathbb{E}[1-\pi^2]$ (green trace) reaches a steady state value which is different from but still close to zero. At short times, individual trajectories reach the fixed points with a probability reflecting the initial weights $|\alpha|^2$ and $|\beta|^2$ associated with the $\hat{\pi}$ eigenspaces. Eventually, hybridization flips $\pi(t)$ between 1 to -1, as illustrated by trajectory $\pi_2(t)$. These jumps cause a decay of the ensemble average of $\pi(t)$ over trajectories initialized within one fixed point, see red trace for $\mathbb{E}[\pi]_+$ (enlarged in inset). Correspondingly, the initial weights are lost and in the long-time limit, trajectories are close to either fixed point with equal probability (as quantified by the decay of $\mathbb{E}[\pi]_+$) . For good readout fidelity, the measurement outcome must be identifiable as long as $\mathbb{E}[\pi]_+ \simeq 1$. Other parameters as in Fig. 5.3. Figure from [VII].

ment outcomes. We analyze this in more detail for the Majorana hybridizations. For definiteness, we focus on ε_{23} with the corresponding contributions

$$\hat{H}_{23} = -i\varepsilon_{23}\hat{\gamma}_2\hat{\gamma}_3 \tag{5.42}$$

$$= \varepsilon_{23}\sum_n \left(|\uparrow, n\rangle\langle\downarrow, n| + |\downarrow, n\rangle\langle\uparrow, n|\right) \tag{5.43}$$

to the Hamiltonian and $\mathcal{L}_{23}\hat{\rho} = -i[\hat{H}_{23}, \hat{\rho}]$ to the Liouvillian. In the absence of relaxation and for $\mathrm{Im}\{t_1 t_2^*\} \neq 0$, the new total Liouvillian $\mathcal{L} + \mathcal{L}_{23}$ has $\hat{\rho}^\infty = \mathrm{diag}(1,1,1,1)/4$ as the only zero mode and, consequently, does not preserve information on the weights $|\alpha|^2$ and $|\beta|^2$ of the initial Majorana-qubit state in the long-time limit (see App. C.7).

This is illustrated in Fig. 5.8 which shows $\mathbb{E}[\pi(t)]_\pm$, the ensemble-averaged evolution of $\pi(t)$ for initial states $\pi(0) = \pm 1$. For significant values of ϵ_{23}, $\mathbb{E}[\pi(t)]_\pm$ relaxes to 0 faster than the measurement can project $\hat{\pi}$, as indicated by the fact that $\mathbb{E}[1-\pi^2(t)]$ remains large for all times t. This implies that the system forgets the weights associated with the π eigensectors too fast to perform a measurement. In contrast, Fig. 5.9 shows data for a much smaller value of ϵ_{23}.

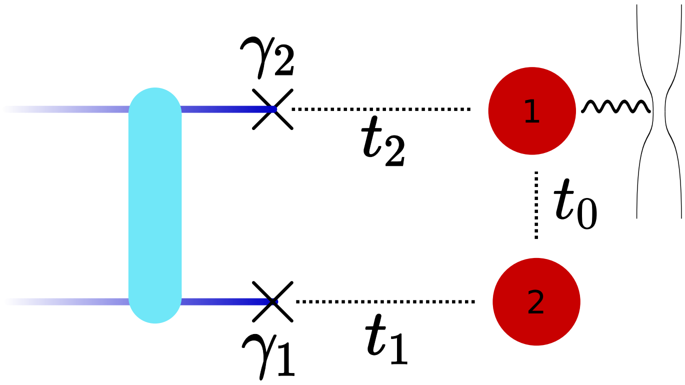

Figure 5.10: Majorana qubit readout by means of a double quantum dot (with inter-dot tunneling t_0), with charge monitoring by a quantum point contact of one (as shown) or both quantum dots. Symbols as in Fig. 5.1. Figure from [VII].

Here, $\varepsilon_{23} \ll \tau_m^{-1}$ and the information on the weights is retained transiently. Still, in the long-time limit, this information is lost and Majorana hybridizations set an upper limit for the time a measurement may take. Including relaxation does not change this qualitatively. In this case, the steady state will no longer be completely mixed, but importantly, there is only one steady state and information on the qubit state is lost in the long time limit.

5.2.6 READOUT VIA DOUBLE QUANTUM DOT

READOUT OF TWO-MAJORANA PARITIES

It is interesting to compare the scheme discussed so far with a modified readout setup which couples the Majorana qubit to a double quantum dot, such that Majoranas $\hat{\gamma}_1$ and $\hat{\gamma}_2$ entering into $\hat{Z}$ are coupled to one quantum dot each, see Fig. 5.10. In this case, the effective hopping amplitude between the quantum dots equals

$$t_{\hat{Z}} = t_0 + \frac{i t_1 t_2^*}{E_c} \hat{Z}. \tag{5.44}$$

Here, t_0 denotes direct hopping, while the second term originates from indirect hopping via the Majorana qubit. We consider the subspace in which a single electron in the double quantum dot can reside in either of the two quantum dots, with basis states $|1,0\rangle$ and $|0,1\rangle$. The Hamiltonian of the system, written in the basis $\{|1,0;\uparrow\rangle, |0,1;\uparrow\rangle, |1,0;\downarrow\rangle, |0,1;\downarrow\rangle\}$ becomes block-diagonal,

$$\hat{H} = \begin{pmatrix} h_\uparrow & 0 \\ 0 & h_\downarrow \end{pmatrix}, \tag{5.45}$$

where the 2×2 blocks take the form

$$h_Z = \begin{pmatrix} \epsilon/2 & t_Z \\ t_Z^* & -\epsilon/2 \end{pmatrix}. \tag{5.46}$$

Unlike the single-dot case, the block-diagonal structure is now directly related to the operator of interest, $\hat{Z}$. At first sight, this may seem to simplify readout based on monitoring the charge of one of the quantum dots.

However, this is not the case and our analysis of the readout via a single quantum dot carries over to the present case with only small changes. In particular, the time-averaged measurement signal of the quantum point contact does not distinguish between the two Z values, unless there is relaxation in the energy eigenbasis. This is because the measurement attempts to project the quantum dot into a charge eigenstate of one of the quantum dots, which is not an eigenstate, thus causing Rabi oscillations of the charge between the quantum dots. In the stationary limit, the system explores both charge states, $|1, 0\rangle$ and $|0, 1\rangle$, with equal probability and the ensemble-averaged charge becomes equal to 1/2, independent of Z. The similarities with the single-dot setup are, of course, rooted in the fact that the Hamiltonians (5.7) and (5.46) for the single and double-dot setups, respectively, are closely analogous.

Despite these similarities, the present setup may have some advantages which could compensate for the additional effort. First, the diagonal elements of the Hamiltonian (5.46) can now be tuned by a gate, making a wider parameter range accessible. Second, the double quantum dot presumably couples efficiently to the electromagnetic environment, which induces relaxation in the energy basis and enables readout of the qubit via the average measurement current. Third, the setup obviates the need for resetting the qubit as electrons enter the Majorana qubit only virtually.

READOUT OF FOUR-MAJORANA PARITIES

Universal quantum computing requires a gate which entangles qubits such as the controlled NOT. For Majorana qubits, the entangling gate can be implemented using measurements of two-qubit Pauli operators [45, 156, 246], say $\hat{Z}_1\hat{Z}_2$, where $\hat{Z}_1 = -i\hat{\gamma}_1\hat{\gamma}_2$ and $\hat{Z}_2 = -i\hat{\gamma}_3\hat{\gamma}_4$, cf. Fig. 5.11. This requires measurements of products of four Majorana operators. Measurements of Majorana parities with even more operators are required to read out stabilizer operators of various topological error correcting codes [242].

Measurements of four-Majorana parities can be implemented using double quantum dots as in Sec. 5.2.6, replacing the tunneling path through a single Majorana qubit in Fig. 5.10 by a tunneling path through a sequence of two Majorana qubits, as shown in Fig. 5.11. If the path involves all four Majoranas included in $\hat{Z}_1\hat{Z}_2$, the corresponding tunneling amplitude becomes

$$t_{\hat{Z}_1\hat{Z}_2} = t_0 + \frac{t_1 t_{23} t_4^*}{E_c^2}\hat{Z}_1\hat{Z}_2. \tag{5.47}$$

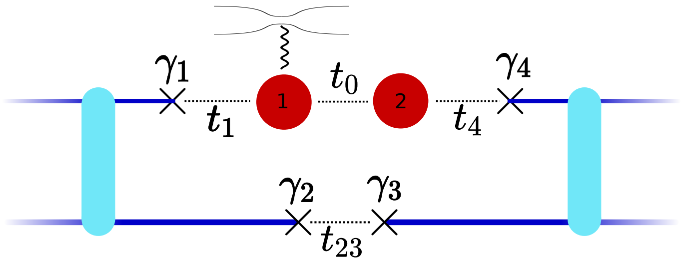

Figure 5.11: Four-Majorana readout by charge measurements on a double quantum dot. The Majorana bound states $\hat{\gamma}_2$ and $\hat{\gamma}_3$ are tunnel coupled directly via the tunneling link t_{23}. Symbols as in Fig. 1. Figure from [VII].

By analogy with our discussion in Sec. 5.2.6, the quantum dot charge measurement leads to decoherence in the eigenbasis of $\hat{Z}_1\hat{Z}_2$. At the same time, the density matrix remains unaffected within the diagonal blocks of fixed two-qubit parity $\hat{Z}_1\hat{Z}_2$, so that no information is gained on $\hat{Z}_1$ or $\hat{Z}_2$. Clearly, this can, at least in principle, be extended to the measurement of larger products of Majorana operators.

5.3 SYMMETRY-PROTECTED READOUT

We found in Sec. 5.2.3 that even though $\hat{Z}$ was not a conserved quantity and the measurement device was coupled to $\hat{n}$, we could read out $\hat{Z}$ by effectively extracting the combined local parity $\hat{\pi}$ which is a symmetry of both the system and the measurement Hamiltonian. This is a special case of a more general result (see, e.g., [252, 253]). If an operator $\hat{\Pi}$ commutes with both, the Hamiltonian, $[\hat{H}, \hat{\Pi}] = 0$, and the full set of jump operators describing the measurement and decoherence channels, $[\hat{L}_\alpha, \hat{\Pi}] = 0$, the system generically decoheres in the $\hat{\Pi}$ basis. In particular, decoherence occurs as long as the measurement current distinguishes between the eigenspaces of $\hat{\Pi}$ [254]. Before justifying the validity of this statement, we further illustrate its usefulness by additional applications to Majorana qubits.

It was shown by Akhmerov [157] that coupling Majorana zero modes $\hat{\gamma}_i$ to other fermionic quasiparticles $\hat{\alpha}_{i,k}$ localized in their vicinity is not detrimental to topological protection. Due to their localized nature, the quasiparticles do not couple distant Majoranas and the operators

$$\hat{\gamma}_i' = \hat{\gamma}_i(-1)^{\hat{N}_i} \tag{5.48}$$

with $\hat{N}_i = \sum_k \hat{\alpha}_{i,k}^\dagger \hat{\alpha}_{i,k}$ are dressed but protected zero modes of the system which commute with the Hamiltonian. This was recently studied further for a specific model in Ref. [255].

For these dressed zero modes to be useful for topological quantum computation, we need to be able to use them in Majorana qubits and to perform projective measurements of corresponding qubit operators such as $\hat{Z}' = -i\hat{\gamma}_1'\hat{\gamma}_2'$ [156]. The general statement mentioned above implies that this is indeed possible. Consider a measurement of $\hat{Z}$ by coupling $\hat{\gamma}_1$ and $\hat{\gamma}_2$ to a quantum dot as before. We can define a modified combined local parity

$$\hat{\pi}' = \hat{Z}(-1)^{\hat{n}+\hat{N}_1+\hat{N}_2} = \hat{Z}'(-1)^{\hat{n}}, \tag{5.49}$$

which includes the localized quasiparticles. Unlike $\hat{\pi}$, the modified combined parity $\hat{\pi}'$ is a symmetry of the system in the absence of processes coupling to other Majorana bound states or changing the charge $\hat{n} + \hat{N}_1 + \hat{N}_2$. A measurement which distinguishes between the two eigenspaces of $\hat{\pi}'$ will then no longer decohere the system in the eigenbasis of $\hat{\pi}$, but in the eigenbasis of $\hat{\pi}'$, as required for a projective readout of a qubit based on the dressed zero modes. There may, however, be a reduction in the readout speed, as the coupling to other localized modes reduces the hybridization of the zero mode with the quantum dot.

Our description of the measurement process in terms of the stochastic master equation (5.20) assumes a large bias applied to the quantum point contact, which might cause unnecessary heating of the quantum dot-Majorana qubit system as a consequence of the measurement. The general statement above implies that this assumption, although technically convenient, is unnecessary. Inspecting the derivation of the stochastic master equation in App. C.3, we see that relaxing this assumption will change the argument of the decoherence operator $\mathcal{D}[\hat{n}]$ in Eq. (5.20). Nevertheless, $\hat{\pi}$ is conserved by all interactions and thus necessarily by the argument of $\mathcal{D}$, as well. Then, the system still decoheres in the $\hat{\pi}$ eigenbasis. It is worthwhile noting, however, that for smaller bias voltages the argument of $\mathcal{D}$ will in general no longer be hermitian and the associated steady state will not be completely mixed within each π subspace.

Now we turn to justifying the general statement. If, for simplicity, the symmetry squares to one, $\hat{\Pi}^2 = \mathbb{1}$, the unconditional master equation decouples into blocks labeled by the eigenvalues of $\hat{\Pi}$ (cp. Sec. 5.2.3),

$$\dot{\rho}_{\pi\pi} = -i[h_\pi, \rho_{\pi\pi}] + \sum_\alpha k_\alpha \mathcal{D}[l^\alpha_\pi]\rho_{\pi\pi} = \mathcal{L}_{\pi\pi}\rho_{\pi\pi}, \tag{5.50a}$$

$$\dot{\rho}_{+-} = -i(h_+\rho_{+-} - \rho_{+-}h_-) + \sum_\alpha \tilde{\mathcal{D}}[l^\alpha_+, l^\alpha_-]\rho_{+-} = \mathcal{L}_{+-}\rho_{+-}. \tag{5.50b}$$

Here, we use the notation $\tilde{\mathcal{D}}[A, B]\rho = A\rho B^\dagger - (A^\dagger A\rho + \rho B^\dagger B)/2$ and decompose $\hat{L}_\alpha = \mathrm{diag}[l^\alpha_+, l^\alpha_-]$ as well as $\hat{H} = \mathrm{diag}[h_+, h_-]$. Just as in Sec. 5.2.3, the diagonal blocks have Lindblad form and the evolution preserves the weights in the respective blocks.

We then need to understand when $\mathcal{L}_{+-}$ leads to a decay of ρ_{+-}. Baumgartner and Narnhofer [252] show that nontrivial off-diagonal steady states exist if and only if there is a unitary

$$\hat{U} = \begin{pmatrix} 0 & u^\dagger \\ u & 0 \end{pmatrix} \tag{5.51}$$

connecting the two subspaces, $\hat{U}\hat{P}_+ = \hat{P}_-\hat{U}^\dagger$, which commutes with the Hamiltonian and all the $\hat{L}^\alpha$. Here, $\hat{P}_\pm$ denotes the projectors onto the two eigenspaces of $\hat{\Pi}$ and u is a unitary acting on the $\hat{\Pi}$ eigenspaces. Then, one has

$$h_- = u^\dagger h_+ u \ , \ l_-^\alpha = u^\dagger l_+^\alpha u, \tag{5.52}$$

so that both the spectra of the Hamiltonians and the algebras formed by $\left\{h_\pm, l_\pm^\alpha\right\}$ are identical. This implies that the two sectors are unitarily equivalent and the associated measurement currents are indistinguishable. The existence of such a unitary U requires finetuning. Generically, the subspaces are not related in this manner and the measurement signals distinguish between the two sectors. Then, decoherence occurs in the eigenbasis of $\hat{\Pi}$.

This holds true regardless of the details of the measurement procedure. For instance, one could alternatively base the charge measurement on circuit-QED reflectometry, where the coupling to the quantum dot charge takes the form

$$\hat{H}_{\mathrm{cQED}} = g\,\hat{n}\left(\hat{a}_0^\dagger + \hat{a}_0\right). \tag{5.53}$$

Here, $\hat{a}_0$ annihilates a bosonic resonator mode and g quantifies the coupling strength. Since the coupling respects the symmetry $[\hat{H}_{\mathrm{cQED}}, \hat{\pi}] = 0$, this generically decoheres the system in the eigenbasis of $\hat{\pi}$. This emphasizes that it is really the symmetry that counts, not the details of the measurement, and we refer to this mechanism as symmetry protected decoherence or symmetry protected readout.

While decoherence generically occurs in the eigenbasis of $\hat{\pi}$, the decoherence rates depend on the specifics of the measurement and can be linked to the rate at which it is possible to distinguish the measurement signals of the two sectors [254]. In particular, $|\mathrm{tr}\rho_{+-}(t)|^2$ is closely related to the probability to correctly identify the measurement outcome from the measurement signal up to time t. Since this assumes an ideal measurement, the decay of ρ_{+-} generally provides only bounds on the measurement time.

5.4 Discussion

Readout of Majorana-based topological qubits is an important problem and has attracted much attention in the literature for qubit designs based on Coulomb-blockaded superconducting islands [45, 154, 256, 257] or alternative settings [258–264]. Its importance is rooted in the fact that promising schemes for Majorana-based quantum computation [45, 156, 242] rely on measurements as an integral part of quantum information processing. This implies that the measurements must not only provide the measurement outcome, but also reliably project the qubit into the corresponding eigenstate.

A variety of techniques have been proposed to read out Majorana qubits, including interferometry of transport currents passed through the Majorana qubit [154, 257, 264], techniques borrowed from circuit quantum electrodynamics [45, 154, 256, 259, 260], or measurements relying on charge sensing [45, 154, 258, 261, 262, 265]. Techniques borrowed from circuit quantum electrodynamics can frequently be treated theoretically in close analogy to the description for (nontopological) superconducting qubits [266]. At the same time, these schemes involve a substantial hardware overhead and may significantly increase the effective dimensions of each qubit. Therefore, we focused here on readout of Majorana qubits based on coupling to a quantum dot whose charge is measured by means of a quantum point contact. This approach combines suitability to the basic design of Majorana qubits with conceptual simplicity, and thus relevance for near-term devices with accessibility of a thorough theoretical analysis at an analytical level.

Despite its apparent simplicity, this scheme poses nontrivial questions. In particular, we discuss charge-based readout protocols of parity-protected Majorana qubits which are distinctly different from charge-based readout protocols of other types of qubits. Spin qubits (by spin-charge conversion) [267] or Majorana qubits without parity protection [261] (by parity-to-charge conversion) can also be effected by charge measurements. In these cases, the computational basis of the qubit is robustly brought into one-to-one correspondence with the charge basis. In contrast, the charge-based readout of parity-protected Majorana qubits projects in the charge basis, while the qubit operator enters through a tunneling Hamiltonian which does not commute with the charge. Generically, this makes a single projective charge measurement insufficient to identify the qubit state. Moreover, readout by repeated charge measurements would necessitate very high levels of control. Instead, the readout process is a weak continuous measurement and its theoretical description requires a time-resolved description of the measurement.

A systematic measurement theory of this readout scheme for (parity-protected) Majorana qubits is the central contribution of the work presented in this chapter. Our theory reveals under which conditions a measurement of the quantum dot charge constitutes a projective measurement of the Majorana parity of the qubit, describes the time it takes to decohere the system in the measurement basis, and includes the noisy measurement signal which can be analyzed to estimate required measurement times.

Our central insight is that generically, one does not directly measure the Majorana parity but rather a combined parity which includes the quantum dot charge in addition to the Majorana parity of the qubit. We find that this is not detrimental to the readout as the combined parity can eventually be converted into the desired Majorana parity. Importantly, this observation generalizes and our theory also applies more generally. In particular, this implies that other local charges which the Majorana might couple to are not a hindrance to topological protection. Topological quantum computation, including qubit readout, can be based on dressed zero modes which include these additional local charges. In its general form, the underlying result states that decoherence generically occurs in the eigenbasis of operators which commute with the system and readout Hamiltonians, which we refer to as symmetry protected decoherence or readout.

The theory also describes how to extract the measurement outcome from the measurement current through the quantum point contact. We find that generically, the measurement outcome cannot be reconstructed from the average measurement current, but only from its noise correlations. This can only be avoided when including additional dissipative processes, or by exploiting transient signals in fine-tuned situations. This surprising result can be traced back to the fact that the quantity to be read out enters into a tunneling amplitude which does not commute with the measured quantity, namely the quantum dot charge. We emphasize that for readout based on a single quantum dot, the Majorana qubit is in an excited state for a significant fraction of the measurement time. This may make the procedure susceptible to qubit errors by uncontrolled electron tunneling. This can be avoided in a measurement setup using a double quantum dot, which may thus promise better readout fidelities.

Finally, the theory naturally provides estimates of the measurement time. We find that the measurement times for Majorana qubit readout based on setups with a single quantum dot are consistently considerably larger than those for a conventional quantum dot charge readout at the same measurement strength. The reason for this is twofold. First, the decoherence rates are no longer simply controlled by the measurement strength $\sim k$ but involve the small tunnel couplings between quantum dot and Majorana qubit, $\sim |t|^2 k/\varepsilon^2 \ll k$. Second, one generically cannot access the entire information contained in the measurement signal. Instead, typical experiments will only have access to its mean and two-point correlations. Thus, actual measurement times can be large compared to the decoherence time. However, slow readout should not be a generic feature of Majorana qubit readout. In fact, readout setups with two quantum dots can access an increased parameter range and should be less restricted. Investigating the double-dot setup in greater detail represents an interesting direction for future work.

We note also the related paper [268], which was published at a similar time as the work presented here, and which contains a partly complementary analysis and reaches similar conclusions where overlapping.

6 SURFACE PHOTOGALVANIC EFFECT IN WEYL SEMIMETALS

This chapter is based on Ref. [VIII].

In the past decade, Weyl semimetals (WSMs) have attracted great attention, from theoretical prediction [56] to experimental realization [90–92, 269]. Of particular interest are the peculiar transport phenomena [61, 270] due to the presence of Weyl fermions, the associated chiral anomaly [59, 271, 272], and topological Fermi-arc surface states [56, 273]. For instance, WSMs are considered a promising platform for optoelectronic applications [101, 158] because chirality and the topologically protected linear dispersion of Weyl fermions generally tend to enable and enhance the response to incident light [274]. The relevant light frequencies lie typically in the mid- and far-infrared region, bounded from below by the typically small but finite chemical potential at the Weyl nodes and from above by the onsetting non-linear corrections to the Weyl dispersion.

Most discussed is the photogalvanic effect (PGE) in non-centrosymmetric WSMs—a *dc* current response to light irradiation [69–71, 73, 74, 161–165]. Generally, the photogalvanic current density may be expanded as [160, 275]

$$\mathbf{J} = \sum_{i,j=x,y,z} \mathbf{\Gamma}_{ij} \mathcal{E}_i \mathcal{E}_j^*, \tag{6.1}$$

where $\boldsymbol{\mathcal{E}}$ is the polarization vector of the light field and $\mathbf{\Gamma}$ is the photogalvanic response tensor. One distinguishes between a ballistic current, induced by asymmetric in momentum photogeneration (or injection following the terminology of [276]), which is proportional to the relaxation time and dominates in clean samples, and the shift current, which is finite even in the absence of relaxation processes. Notably, in non-centrosymmetric WSMs a quantized photogeneration induced by circularly polarized light was predicted [72]. WSMs that in addition to inversion also break time-reversal symmetry may further exhibit a ballistic response to linearly polarized light which may be giant [71, 165, 277–280].

Besides the bulk PGE that can be understood in terms of infinite-system models, the PGE has been explored at the surfaces of metals [281–283] and topological insulators [284–287], in which case the surface-normal component of $\mathbf{\Gamma}$ (but not that of $\mathcal{E}$) vanishes. In the field of WSMs, recently there was evidence from experiments and first principles calculations that Fermi arc states might play an important role in the photogalvanic response [166, 167], a contribution

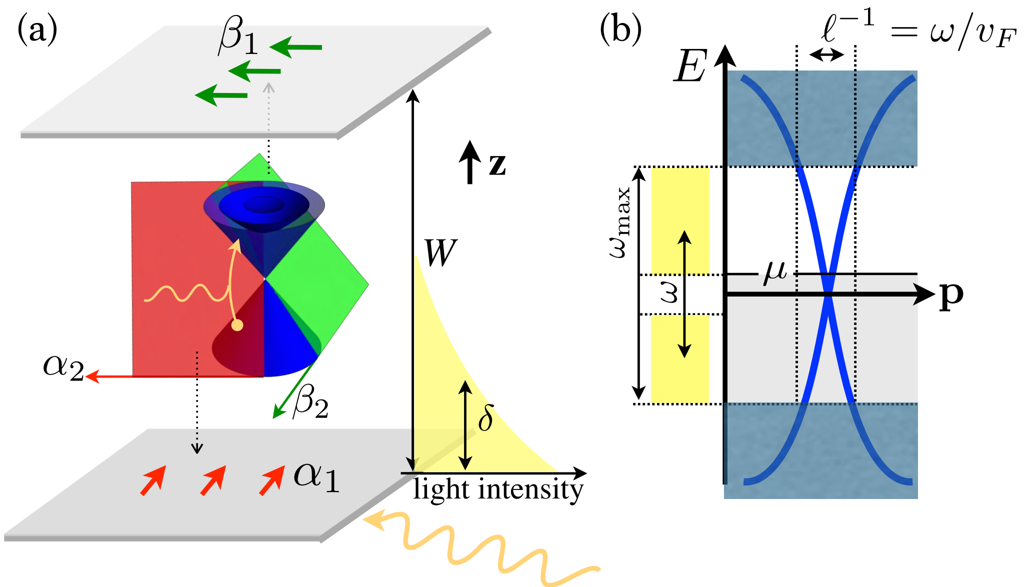

Figure 6.1: (a) Dispersion (energy vs. in-plane momenta) of Weyl fermions confined to a slab of thickness W. The plot shows bulk states (blue) and surface states of bottom surface (red) and top surface (green). The surface states are tightly *glued* to the bulk Weyl cone and emanate in the direction $\boldsymbol{\alpha}_2$ ($-\boldsymbol{\beta}_2$) for bottom (top) surface. The figure also shows the directions of Fermi-arc motion ($\boldsymbol{\alpha}_1$ and $\boldsymbol{\beta}_1$), as well as the photon penetration depth δ. (b) Low-energy band structure at the Weyl node. The Fermi energy μ and the energy range of the linear-dispersion regime, $\omega_{\max}$, determine the range of considered photon frequencies $2\mu < \omega < \omega_{\max}$. Figure from [VIII].

that was neglected in previous theories. In particular, [167] have shown that the contribution of surface states to the PGE due to excitations between the surface states of the same surface are possible in chiral crystals due to high Chern numbers and a non-linear dispersion of those surface states.

The mere presence of surface states, however, does not capture the full peculiarity of a WSM. Importantly, the *two*-dimensional Fermi-arc surface states, constituting in some sense the reaction of a pair of chiral Weyl fermions to confinement, are tightly glued to the *three*-dimensional Weyl fermions [288], as illustrated in Fig. 6.1(a). This *connectivity* distinguishes Fermi arcs from surface states of metals and topological insulators and was shown to give rise to a number intriguing, counter-intuitive linear-response effects [78–80, 82–89]. Understanding its role also for the photogalvanic response is highly desirable. The theoretical challenge to capture the effect of the connectivity is the requirement to go beyond an effective surface theory and consider a full three-dimensional, yet spatially confined model.

Here, we present a theory of ballistic photogalvanic response of Weyl fermions spatially confined in one direction with general boundary conditions, relevant for Weyl-semimetal slabs with an arbitrary configuration of Weyl nodes *and arbitrary orientations of Fermi arcs at the bottom and top surfaces, which need not be the same.*

Specifically, the orientation of the bottom (top) Fermi arc is defined by the direction of its velocity, $\boldsymbol{\alpha}_1$ ($\boldsymbol{\beta}_1$), or the perpendicular direction at which the arc emanates from the Weyl node, $\boldsymbol{\alpha}_2$ (-$\boldsymbol{\beta}_2$), see Fig. 6.1(a). We show that this symmetry-breaking directionality gives rise to a vastly richer response behavior compared to an unconfined WSM. In particular, the confinement enables the otherwise vanishing linear and circular PGE in centrosymmetric WSMs. Furthermore, the response is crucially determined by the orientations of the Fermi arcs. The latter may be adjusted by choosing different surface terminations [289, 290] or surface doping [168]. In principle, this allows control over the photogalvanic response by modification of the surface only.

To focus on Weyl physics, we consider a photon frequency range for which excitations can take place only close to Weyl nodes where the bulk and arc dispersions are linear, see Fig. 1(b). The total response is then the sum of the responses of individual Weyl nodes. Further, we focus on the semimetallic regime, in which the Fermi level μ is close to the Weyl node and smaller than the photon energy, such that Pauli blocking as well as screening may be neglected. In this regime, intra-surface (arc-arc) excitations are forbidden,[1] but bulk-bulk excitations as well as arc-bulk excitations exist.

Most strikingly, for a centrosymmetric WSM confined to a slab, the photogalvanic response is fully determined by the Fermi-arc orientation. Considering the current density in Eq. (6.1) as the current density averaged over the slab width, the response tensor can be decomposed into a confinement-independent bulk-bulk contribution $\boldsymbol{\Gamma}^{\mathrm{bb}}$ and confinement-induced contributions, which in turn consist of bulk-bulk $\delta\boldsymbol{\Gamma}^{\mathrm{bb}}$ as well as arc-bulk $\boldsymbol{\Gamma}^{\mathrm{ab}}$ parts,

$$\boldsymbol{\Gamma} = \boldsymbol{\Gamma}^{\mathrm{bb}} + \delta\boldsymbol{\Gamma}^{\mathrm{bb}} + \boldsymbol{\Gamma}^{\mathrm{ab}}. \tag{6.2}$$

For a centrosymmetric WSM, $\boldsymbol{\Gamma}^{\mathrm{bb}}$ vanishes according to general symmetry considerations [160]. The response is thus given by

$$\boldsymbol{\Gamma}^{\mathrm{centrosymm.}} = \delta\boldsymbol{\Gamma}^{\mathrm{bb}} + \boldsymbol{\Gamma}^{\mathrm{ab}}, \tag{6.3}$$

where both contributions are fully determined by the Fermi-arc orientations since the orientation of the arcs and modification of the bulk-state wavefunctions are both defined by the boundary conditions. Moreover, a centrosymmetric WSM necessarily breaks time-reversal symmetry, which implies that $\boldsymbol{\Gamma}^{\mathrm{centrosymm.}}$ will include a ballistic response to linearly polarized light of the type discussed in [278]. This is directly relevant to magnetic WSMs, such as $\mathrm{Co_3Sn_2S_2}$ [93], RhSi [95], and GdPtBi [94]. Table 6.1 summarizes which types of photogalvanic response are possible in unconfined and confined WSMs, depending on the mechanism and the presence of time-reversal and inversion symmetry.

---

[1] Arc-arc transitions may play a role in some special situations. For instance, large Chern numbers $|C| > 1$ imply the presence of several arc sheets and thus energy and momentum conserving arc-arc transitions become a possibility. Similarly, unscreened surface potentials may lead to strongly dispersing Fermi arcs [168] which may in principle enable intra-arc transitions. We preclude these issues by assuming $C = \pm 1$ and linear arc dispersion.

symmetry	time reversal (broken inversion)	inversion (broken timereversal)	neither
ballistic current (injection)	bCPGE, *sCPGE*	*sCPGE*, *sLPGE*	bCPGE, bLPGE, *sCPGE*, *sLPGE*
shift current	bLPGE, sLPGE	(sCPGE, sLPGE)	(bCPGE, bLPGE, sCPGE, sLPGE)

Table 6.1: Allowed types of photogalvanic response in WSMs, bCPGE, sCPGE, bLPGE, and sLPGE, distinguished by light polarization, circular (CPGE) and linear (LPGE), and origin (b for bulk) and (s for surface). Setups are categorized by mechanism (ballistic/shift current) and presence/absence of time-reversal and inversion symmetry of the WSM material. Terms in parentheses give subdominant response in clean systems. Italic text marks contributions first discussed in this work. In the presence of inversion symmetry, the bulk photogalvanic response vanishes and only surface contributions remain. In this case, the response is fully determined by the directionality of the Fermi arcs. In particular, there is a surface induced ballistic LPGE enabled by broken time-reversal symmetry.

Finally, the confinement-induced PGE is categorized depending on the slab thickness. For a sufficiently thick slab or sufficiently high frequency the light field does not penetrate the whole slab. This is the case when the penetration depth δ, which for photon energies $\hbar\omega \sim 1\,\mathrm{meV}$ to $1\,\mathrm{eV}$ lies in the range $1\,\mu\mathrm{m}$ to $1\,\mathrm{mm}$, is much smaller than the slab thickness W. For light incident at the bottom surface, see Fig. 6.1(a), the top surface no longer contributes to the response. This changes the symmetry of the response tensor. We refer to this limit as the *thick slab*. In the opposite limit, referred to as the *thin slab*, $\delta \gg W$, both surfaces contribute. Technically, the two limits require substantially different calculations, we will thus mostly consider the thick- and thin-slab regimes separately, using different analytical and numerical techniques.

This chapter is organized as follows. In Sec. 6.1 we introduce the model of a WSM in the slab geometry for which we perform our calculations. We also briefly discuss the decay of light waves in WSMs. Finally, we present the semiclassical formulae for the photogalvanic current that we employ. In Sec. 6.2 we classify the different contributions to the photogalvanic response tensor and estimate their magnitude. Further, we comment on the irrelevance of finite light momentum. In Sec. 6.3 we discuss the symmetry constraints on the response tensor. Finally, in Sec. 6.4 we present analytical results for the different contributions to the response tensor for a single Weyl cone in the different regimes. We further present a lattice simulation in the thin limit which confirms the analytical results. At the end of this section we apply our results to WSMs with several Weyl cones by considering a centrosymmetric WSM with two nodes. We conclude in Sec. 6.5. Technical details are delegated to the appendices.

6.1 Model

6.1.1 Weyl semimetal

We consider a WSM slab with a set of Weyl nodes which are close to the Fermi level. We also assume that the projections of the Weyl points to the surface Brillouin zone are well-separated. Since we consider the response to excitations occurring close to the Weyl nodes only, it suffices to consider the response of a single Weyl node, from which the response of a WSM with several Weyl nodes will follow by combining the single-Weyl-node response tensors, transformed according to the specific Weyl-node arrangement.

In order to evaluate the matrix elements relevant for the photogalvanic response tensors we seek explicit expressions for the wave-functions in the slab geometry (see Appendix A for a detailed derivation). To this end, we model a single Weyl fermion confined to $0 < z < W$ with the Hamiltonian (we set $\hbar = 1$)

$$H = \chi\, v\, \mathbf{p} \cdot \boldsymbol{\sigma}, \tag{6.4}$$

where $\mathbf{p}$ is the momentum (with $p_z = -i\partial_z$), $\boldsymbol{\sigma}$ the spin, $\chi = \pm$ the chirality, and v the velocity. For better transparency of the following calculations we here assume isotropic velocity of the Weyl fermion; in Appendix D.2 we generalize the results to an anisotropic Weyl node, which leads to a simple transformation of the response tensor. In the absence of a tilt, the Weyl Hamiltonian Eq. 6.4 commutes with the operator $\mathcal{T} = i\sigma_y K$, where K is complex conjugation. By analogy with relativistic theory we refer to this intra-node symmetry as time reversal (TR) symmetry. Note that it does not correspond to the time reversal operation acting on the whole crystal, as this connects different Weyl nodes. Thus the intra-node TR symmetry allows to constrain the response due to a single Weyl node only. A WSM with several Weyl nodes at generic points in momentum space clearly does not need to satisfy TR symmetry.

Using translation invariance parallel to the surface we seek energy eigenstates in the form of plane waves in the xy plane with the continuous in-plane momenta $\mathbf{p}_{||} = (p_x, p_y) \equiv p_{||}(\cos\phi, \sin\phi)$. Their dependence on z is given by the solutions to the Weyl equation $H\psi(z) = E\psi(z)$, which may be written as

$$\psi(z) \propto \exp\{i\mathcal{P}_z z\}\psi(0) \propto [p_z \cos(p_z z) + i \sin(p_z z)\mathcal{P}_z]\psi(0), \tag{6.5}$$

where $p_z = \sqrt{E^2 - p_{||}^2}$ and the generalized momentum operator reads

$$\mathcal{P}_z = \left(ip_y, -ip_x, \frac{\chi E}{v}\right) \cdot \boldsymbol{\sigma}. \tag{6.6}$$

The discrete energy eigenvalues of the slab (at fixed $\mathbf{p}_{||}$) are to be determined by boundary conditions. A generic boundary condition on the wavefunction is a vanishing current j_z across the boundaries. Since $j_z \propto \partial_{p_z} H \propto \sigma_z$ this corresponds to $\psi^\dagger \sigma_z \psi = 0$. Accounting for the possibility of differing boundary conditions for the bottom and top surfaces, a general boundary condition thus reads

$$\psi(0) \propto \begin{pmatrix} 1 \\ e^{i\alpha} \end{pmatrix}, \qquad \psi(W) \propto \begin{pmatrix} 1 \\ e^{i\beta} \end{pmatrix}, \tag{6.7}$$

parametrized by two independent angles α and β. Surface inhomogeneities would correspond to a spatial dependence of α and β. Here we assume translation invariance at the surface (up to a relaxation mean free path that will be introduced perturbatively below) and thus consider α and β to be constant.

The boundary conditions lead to the equation

$$\sin\frac{\beta-\alpha}{2} = \frac{\tan(p_z W)}{p_z}\left[p_\| \cos\left(\phi - \frac{\beta+\alpha}{2}\right) \mp \chi p \cos\frac{\beta-\alpha}{2}\right], \tag{6.8}$$

which determines the quantized eigenvalues p_z. Solutions with real p_z correspond to bulk states, imaginary solutions correspond to surface "arc" states. For details and explicit expressions of the arc and bulk states see App. D.1. Note that α and β define the velocity of the Fermi arcs localized at the bottom (b) and top (t) surfaces,

$$\mathbf{v}^{\mathrm{b}}_{\mathrm{arc}} = \chi v \boldsymbol{\alpha}_1, \ \mathbf{v}^{\mathrm{t}}_{\mathrm{arc}} = \chi v \boldsymbol{\beta}_1. \tag{6.9}$$

as well as the direction at which they emanate from the Weyl node, given by the constraint

$$\mathbf{p}\cdot\boldsymbol{\alpha}_2 \equiv \kappa_{\mathrm{b}} > 0, \quad \mathbf{p}\cdot(-\boldsymbol{\beta}_2) \equiv \kappa_{\mathrm{t}} > 0, \tag{6.10}$$

for bottom and top arc, respectively, where we defined the vectors

$$\boldsymbol{\alpha}_1 = \begin{pmatrix} \cos\alpha \\ \sin\alpha \\ 0 \end{pmatrix}, \ \boldsymbol{\alpha}_2 = \begin{pmatrix} -\sin\alpha \\ \cos\alpha \\ 0 \end{pmatrix}, \ \boldsymbol{\beta}_1 = \begin{pmatrix} \cos\beta \\ \sin\beta \\ 0 \end{pmatrix}, \ \boldsymbol{\beta}_2 = \begin{pmatrix} -\sin\beta \\ \cos\beta \\ 0 \end{pmatrix}. \tag{6.11}$$

The quantities κ_{t} and κ_{b} introduced in Eq. (6.10) have the meaning of inverse decay lengths of the evanescent wave functions of arc states at the top and bottom surfaces, respectively.

In order to analyze symmetries in the presence of the boundary conditions, it proves helpful to define an equivalent multilayer setup, which reproduces the same spectrum and wavefunctions as the boundary conditions Eq. (6.7). Note that this is a fictitious system only intro-

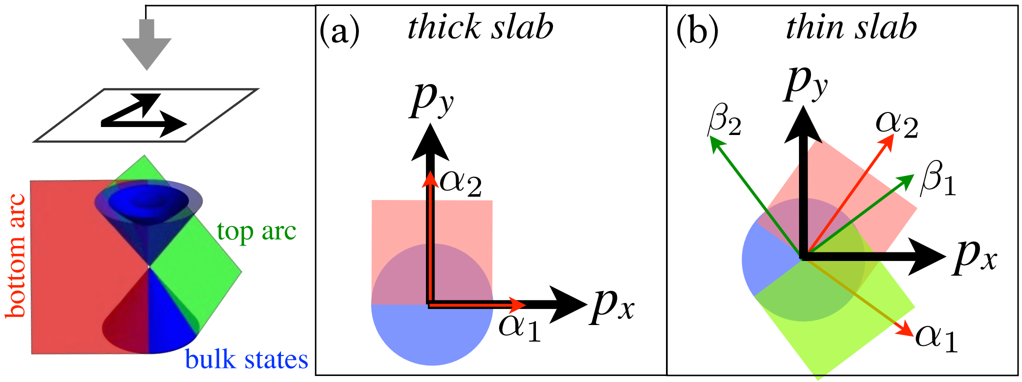

Figure 6.2: Top view on the slab dispersion (left, see also Fig. 6.1) showing the choice of coordinate axes p_x and p_y to lie along high-symmetry directions in (a) the thick-slab ($W \gg \delta$) and (b) the thin-slab case ($W \ll \delta$). The slab dispersion features bulk states (blue), surface states of bottom (red) and top (green) surfaces. In (a) only the bottom surface matters since the light penetrating over the depth δ at the bottom surface does not reach the top arc. Figure from [VIII].

duced to assist in understanding the response of a single Weyl node. The equivalent multilayer setup is defined by the Hamiltonian

$$H_{\chi m} = \chi v \mathbf{p} \cdot \boldsymbol{\sigma} + \begin{cases} -\chi m\, \boldsymbol{\sigma} \cdot \boldsymbol{\alpha}_2 & z < 0 \\ 0 & 0 < z < W \\ \chi m\, \boldsymbol{\sigma} \cdot \boldsymbol{\beta}_2 & z > W \end{cases}, \tag{6.12}$$

with $m \to \infty$ [169, 291]. Under TR the multilayer Hamiltonian transforms like

$$\mathcal{T}^{-1} H_{\chi m} \mathcal{T} = H_{\chi -m}. \tag{6.13}$$

The mass terms of the boundary conditions thus behave like TR-breaking magnetizations in the directions $-\chi\boldsymbol{\alpha}_2$ and $\chi\boldsymbol{\beta}_2$ at the two boundaries. Note that this does not imply TR-breaking of the WSM with several Weyl nodes.

Furthermore, note that the directions of the boundary spinors can be additionally controlled by TR-*preserving* boundary potentials [168]. One can easily check that adding a boundary potential $\delta H_\text{b} = \delta(z)\mu_0 + \delta(z-W)\mu_W$ to the Hamiltonian (6.12), rotates the boundary spinors like $\alpha \to \alpha + \chi 2\mu_0$ and $\beta \to \beta - \chi 2\mu_W$. Boundary potentials are typically disregarded in minimal models of Weyl-semimetal slabs, which corresponds to straight arcs connecting the Weyl cones, i.e., $\beta = \alpha + \pi$. Here we instead consider the general case that the Fermi arcs can emanate in any direction, considering the boundary spinors (6.7) to be given by two independent variables α and β. The resulting curvature of Fermi arcs, which is necessary to connect pairs of Weyl nodes and is often observed in experiments, is irrelevant in the close vicinity of the Weyl nodes to which the optical transitions that we consider are bound.

The directionality introduced by the boundary conditions will crucially determine the direction of the response. It is therefore convenient to define the coordinate axes along the emergent high-symmetry directions. Those depend on whether current is induced at a single surface (thick-slab case) or in the whole slab (thin-slab case). Figure 6.2 illustrates the geometry and the high-symmetry axes in these two cases.

6.1.2 ELECTROMAGNETIC WAVES IN WEYL SEMIMETALS

For frequencies $\omega \gtrsim \mu$ the conductivity in WSMs is given by [IX, 61]

$$\sigma(\omega) = N \frac{e^2}{24\pi\epsilon_\infty v}|\omega| = N\frac{\xi}{24\pi}|\omega|, \tag{6.14}$$

Here, N is the total number of Weyl nodes in the system, $\epsilon_\infty \sim 10$ is the permittivity due to inert bands and we let $e^2 \to e^2/\epsilon_\infty$ to account for screening. Finally, we defined the dimensionless coupling constant

$$\xi = \frac{e^2}{\epsilon_\infty v} = \frac{1}{137} \times \frac{c}{v} \times \frac{1}{\epsilon_\infty} \sim 0.1. \tag{6.15}$$

Note that $\mathcal{N} = N\xi/6$ takes values between $1/30$ and 1 in a WSM, depending on the number of nodes. The imaginary part of σ has only weak frequency dependence and has been absorbed into ϵ_∞. The frequency dependent permittivity then reads

$$\epsilon(\omega) = \epsilon_\infty \left[1 + \frac{4\pi i}{\omega}\sigma(\omega)\right] = \epsilon_\infty\left[1 + i\frac{N\xi}{6}\text{sign}(\omega)\right]. \tag{6.16}$$

We consider light entering the WSM at the $z = 0$ surface. The field *inside* the WSM has the form,

$$\mathbf{E}(\mathbf{r}, t) \propto \exp\{i(\mathbf{k}\cdot\mathbf{r} - \omega t)\}\exp\{-z/\delta\}, \tag{6.17}$$

where $\mathbf{k}$ is the momentum inside the medium and δ is the penetration depth. In terms of the vacuum wavenumber $k_v = \omega/c$ and to leading order in $\mathcal{N}$, they are given by

$$|\mathbf{k}| = \sqrt{\epsilon_\infty}k_v\left(1+\mathcal{N}^2\right)^{1/4}\cos\frac{\arctan\mathcal{N}}{2} \simeq \sqrt{\epsilon_\infty}k_v, \tag{6.18a}$$

$$\frac{1}{\delta} = \sqrt{\epsilon_\infty}k_v\left(1+\mathcal{N}^2\right)^{1/4}\sin\frac{\arctan\mathcal{N}}{2} \simeq \frac{\sqrt{\epsilon_\infty}\mathcal{N}}{2}k_v. \tag{6.18b}$$

With the above estimate of $\mathcal{N}$, depending on the number of Weyl nodes, we thus obtain $k\delta \sim 1\ldots10$.

6.1.3 Photogalvanic response tensor

We consider the response of the Weyl slab to the weak external oscillating electric field

$$\mathbf{E}(\mathbf{r},t) = \left[\boldsymbol{\mathcal{E}} e^{i\mathbf{k}\cdot\mathbf{r}-i\omega t} + \text{c.c.}\right] e^{-z/\delta}. \tag{6.19}$$

In the temporal gauge $\mathbf{E} = -\partial_t \mathbf{A}$, the perturbation to the Hamiltonian reads

$$\delta H = \mathbf{j}\cdot\mathbf{A}(\mathbf{r},t) = i\chi e\ell \boldsymbol{\mathcal{E}}\cdot\boldsymbol{\sigma} e^{-i\omega t} e^{i\mathbf{k}\cdot\mathbf{r}-z/\delta} + \text{h.c.}, \tag{6.20}$$

where $\mathbf{j} = -e\chi v\boldsymbol{\sigma}$ is the current operator and $\ell = v/\omega$ is the smallest length scale of our model. In the following we will use dimensionless length and momenta, denoted with a tilde,

$$\tilde{\mathbf{r}} = \frac{\mathbf{r}}{\ell}, \quad \tilde{\mathbf{p}} = \mathbf{p}\,\ell, \tag{6.21}$$

in units of ℓ and ℓ^{-1}, respectively.

The ballistic PGE can be described within the framework of the Boltzmann kinetic equation by balancing asymmetric photogeneration and impurity-induced relaxation. Using the standard perturbation theory and relaxation-time approximation, one can express the photogalvanic response in terms of the momentum relaxation time τ in the form [71, 276]

$$\boldsymbol{\Gamma}_{ij} = \frac{8\pi\eta\tau}{\tilde{W}} \int d^2\tilde{p}_{\|} \sum_{q_z p_z} \left(\frac{\mathbf{v}_{\mathbf{p}+}}{v} - \frac{\mathbf{v}_{\mathbf{q}-}}{v}\right) \delta\left(1 - \frac{E_{\mathbf{p}}}{\omega} - \frac{E_{\mathbf{q}}}{\omega}\right) \left(\mathbf{M}_{\mathbf{pq}} \otimes \mathbf{M}^*_{\mathbf{pq}}\right)_{ij} \tag{6.22}$$

where $\otimes$ denotes the dyadic product, $\mathbf{p} = (\mathbf{p}_{\|}, p_z)$, $\mathbf{q} = (\mathbf{p}_{\|} - \mathbf{k}_{\|}, q_z)$, $d^2\tilde{p}_{\|} = \ell^2 d\mathbf{p}_{\|}$, and we introduced the matrix elements

$$\mathbf{M}_{\mathbf{pq}} = \langle +, \mathbf{p}|\boldsymbol{\sigma} e^{i\mathbf{k}\cdot\mathbf{r}-z/\delta}|-, \mathbf{q}\rangle, \tag{6.23}$$

and the constant (restoring $\hbar$, which is set to one)

$$\eta = \frac{e^3}{16\pi^2\hbar^2}. \tag{6.24}$$

Note that $4\pi\eta$ is the quantum of the CPGE trace and may be assumed large compared to ordinary PGE magnitudes [72]. These expressions hold for both bulk-bulk and and arc-bulk excitations. To avoid overcounting of states, for bulk states the sum runs only over $p_z > 0$ while for arc states it runs over $\mathrm{Im}\{p_z\} > 0$. Note that $\Gamma_z = 0$ as $v_z = 0$ for all states due to the boundary conditions.

The relaxation-time approximation of Eq. (6.22) neglects energy and momentum dependencies, as well as forward-scattering corrections. Especially in the interplay of surface and bulk states, those can lead to potentially interesting quantitative refinements [89] of the results, which

	thick slab $W \gg \delta$	thin slab $\delta \gg W$
$\mathbf{\Gamma}^{\mathrm{bb}}$	$\frac{\delta}{W} = \frac{\tilde{\delta}}{\tilde{W}}$	1
$\delta\mathbf{\Gamma}^{\mathrm{bb}}, \mathbf{\Gamma}^{\mathrm{ab}}$	$\frac{\ell}{W} = \frac{1}{\tilde{W}}$	$\frac{\ell}{W} = \frac{1}{\tilde{W}}$

Table 6.2: Scaling of the confinement-independent contribution $\mathbf{\Gamma}^{\mathrm{bb}}$ and the confinement-induced contributions $\delta\mathbf{\Gamma}^{\mathrm{bb}}$, $\mathbf{\Gamma}^{\mathrm{ab}}$ with relevant length scales of the system (W, ℓ, δ) in the cases of a thin and thick slab.

is left for future work. We also neglect interaction effects, which are known to modify the PGE quantitatively [292].

Note that the three 3×3 matrices $\mathbf{\Gamma}$ are hermitian. According to standard terminology, the imaginary anti-symmetric part is associated with the circular PGE, which is present only if the incident light is elliptically polarized (the inverse implication is not true: elliptically polarized light can give rise to photogalvanic response stemming from the real symmetric part). The real symmetric part is referred to as the linear photogalvanic response, which exists even for linearly polarized radiation.

6.2 Classification and estimate of response contributions

There are three relevant length scales in the problem,[2] the v/c-weighted light wavelength $\ell = v/\omega$, the light penetration depth δ, and the slab thickness W, whereby the weighted light wavelength is always much smaller than the penetration depth, $\ell/\delta \sim v/c \sim 10^{-2}$. The width W is considered in two limits, the *thick-slab case* $W \gg \delta$ and the *thin-slab case* $\delta \gg W$. In the thick-slab case the light completely decays inside the slab and only a single slab surface is excited. In the thin-slab case the light penetrates nearly homogeneously the whole slab such that both surfaces are equally excited. In this limit, for simplicity of analytical calculations we introduce a lower bound for the width, $W \gg \ell$, so that energy quantization of slab modes is small compared to the light frequency. The ultrathin case $W \sim \ell$ will be considered numerically on a lattice model.

Before coming to the detailed calculation, it is useful to classify the response contributions according to their dependencies on the relevant length scales (ℓ, δ, W), separating confinement-independent from confinement-induced contributions and distinguishing contributions due to arc-bulk and bulk-bulk excitations as given in (6.2). The result is summarized in Table 6.2 and is explained in the following.

To estimate the magnitudes of contributions it suffices to disregard the spin degree of freedom and consider the bulk wavefunctions to be of the form $|\mathbf{q}\rangle = \exp(iq_z z)/\sqrt{W}$ and that of arc states of the form $|\mathbf{q}\rangle = \exp(-z/\ell)/\sqrt{l}$. In the latter, the inverse decay length κ, given in

---

[2] Here we neglect one length scale of the problem, which is the mean free path τv given by the relaxation time τ. Within the semiclassical approach described in Sec. 6.1.3 the mean free path is assumed long compared to essentially all other relevant scales, which makes the mean free path itself irrelevant for the following discussion.

(6.10), has been approximated by the typical inverse distance from the Weyl node in the active region of excitations, which is set by $\ell^{-1} \equiv \omega/v$. Neglecting the in-plane light momentum $\mathbf{k}$ (will be justified below), the matrix elements (6.23) for the thick-slab case can be estimated as

$$|\mathbf{M}|^2 \sim \begin{cases} \left(\frac{\delta}{W}\right)^2 \frac{1}{1+[(q_z-p_z)\delta]^2} & \text{bulk-bulk} \\ \frac{\ell}{W}\frac{1}{1+(q_z\ell)^2} & \text{arc-bulk.} \end{cases} \tag{6.25}$$

The momentum separation of modes is $1/W$, hence the number of modes within the active range around the node is W/ℓ. The summation over p_z and q_z thus gives

$$\sum_{p_z q_z} |\mathbf{M}|^2 \sim \begin{cases} \frac{\delta}{\ell} & \text{bulk-bulk} \\ 1 & \text{arc-bulk} \end{cases} \tag{6.26}$$

and the magnitude of the response tensor will thus scale like

$$\Gamma^{\text{bb}} \sim \frac{\delta}{W}, \qquad \Gamma^{\text{ab}} \sim \frac{\ell}{W}, \tag{6.27}$$

for bulk-bulk and arc-bulk excitations, respectively.

Since $\delta \gg \ell$, bulk-bulk excitations will give the dominant current contribution, while the confinement-induced correction due to arc-bulk excitations give the finite-size correction with the small parameter ℓ/δ. Importantly, there are also contributions due to bulk-bulk excitations possible that scale like those from arc-bulk excitations,

$$\delta\Gamma^{\text{bb}} \sim \Gamma^{\text{ab}}. \tag{6.28}$$

To see this, note that the contribution Γ^{bb} stems from approximating the peaked behavior of the bulk-bulk matrix elements in (6.25) at $q_z = p_z$ by a delta function, the correction to setting $q_z = p_z$ is of the order ℓ/δ because the peak width is $1/\delta$ and the effective integration range $1/\ell$. Hence the leading correction scales like the arc-bulk contribution, and needs to be taken into account.

Upon changing the scales from the thick-slab case, $W \gg \delta$, to the thin-slab case, $\delta \gg W$, the scaling of the contribution of arc-bulk excitations does not change because the localization length of most arc states, κ^{-1} given in (6.10), is set by ℓ and hence much smaller than both W and δ.

For bulk-bulk excitations, the matrix elements are now the overlaps of wavefunctions over the whole slab width,

$$|\mathbf{M}|^2 \sim \frac{1-\cos\left[(q_m-q_n)W\right]}{\left[(q_m-q_n)W\right]^2}. \tag{6.29}$$

Summation over p_z and q_z gives $\sum_{p_z q_z} |\mathbf{M}|^2 \sim \tilde{W}$ and the magnitude of the current thus scales like

$$\Gamma^{\mathrm{bb}} \sim 1, \tag{6.30}$$

missing the factor δ/W as compared to the limit $W \gg \delta$ given in (6.27), since transitions are now produced across the full width of the slab.

As before, the matrix elements are peaked at $q_m = q_n$; the correction $\delta\Gamma^{\mathrm{bb}}$ to the $q_m = q_n$ contribution Γ^{bb} is of order l/W because the peak width is now $1/W$, while the integration range is still $1/\ell$. Thus $\delta\Gamma^{\mathrm{bb}} \sim \Gamma^{\mathrm{ab}}$ remains valid also in the thin-slab limit. This concludes the explaination of the scaling summarized in Table 6.2.

6.2.1 IRRELEVANCE OF THE LIGHT MOMENTUM

The momentum transfer due to a finite light momentum has the magnitude $k \sim \omega/c$. The small parameter of corrections due to this momentum shift is k/p, where $p \sim 1/\ell = \omega/v$ is the typical momentum of excited states, hence $k/p \sim v/c \sim 0.01$. Comparing the smallness of corrections to the response, those due to a finite $\mathbf{k}$ are irrelevant for the thin-slab case but potentially relevant in the case of a thick slab, where they are on the same order as the finite-size corrections, cf. Table 6.2. It turns out, however, that corrections to leading order in $k/p \sim v/c$ vanish also for the thick-slab case, which we show explicitly for our slab model in Appendix D.5. An easier way to find the same result is to realize that considering the correction due to a finite k/p, one can neglect the finite-size corrections, which would give terms that are quadratic in the small parameter. Neglecting finite-size corrections, the result should thus coincide with that of an infinite system. In particular, the directionality introduced by the confinement becomes irrelevant. It is straightforward to verify that for a bulk Weyl cone the first-order k/p corrections vanish.

For the response tensor in Eq. (6.22) this means that $\mathbf{k}$ can be set to zero, the matrix elements become

$$\mathbf{M}_{\mathbf{pq}} = \langle +, \mathbf{p} | \boldsymbol{\sigma} e^{-z/\delta} | -, \mathbf{q} \rangle, \tag{6.31}$$

and the momenta have the same parallel component, $\mathbf{p} = (\mathbf{p}_{\|}, p_z)$, $\mathbf{q} = (\mathbf{p}_{\|}, q_z)$.

Finally, we comment on the spatial structure of the confinement induced response current. While our calculation considers only the spatial average of the current, we expect the spatial profile of the photogalvanic current to be uniform. This can be understood as follows. The total number of electrons in the surface Fermi arc states is unaffected by the perturbation, as just as many electrons are excited to positive energy Fermi arc states from the bulk as electrons are excited from negative energy Fermi arc states to the bulk. Close to the Weyl point all Fermi arc states have the same velocity. Hence, the net velocity due to Fermi arcs is unchanged. The non-equilibrium current stems from the asymmetric population of bulk states and hence is expected to be spatially uniform.

6.3 SYMMETRY CONSTRAINTS

As the last preliminary consideration before coming to the explicit results, we now consider symmetry constraints on the response tensor. Considering the transition matrix elements (6.31) we realize that since the band index $\pm$ enters the wavefunctions in the form $\pm\chi$, which can be explicitly seen in Appendix D.1, Eq. (D.9), we obtain the relation

$$\mathbf{M}^*_{\mathbf{pq}}\big|_\chi = \mathbf{M}_{\mathbf{qp}}\big|_{-\chi}. \tag{6.32}$$

Using this and that other terms in the response expression, Eq. (6.22), are symmetric in $\mathbf{p} \leftrightarrow \mathbf{q}$, we conclude that

$$\big(\boldsymbol{\Gamma} \pm \boldsymbol{\Gamma}^T\big)_\chi = \pm\big(\boldsymbol{\Gamma} \pm \boldsymbol{\Gamma}^T\big)_{-\chi}, \tag{6.33}$$

showing that the (anti)symmetric part of the response tensor is even (odd) in the chirality χ. Moreover, generally the (anti)symmetric part of the response tensor is odd (even) under TR [160], which, according to the transformation behavior (6.13) is given by $m \to -m$ (in the fictitious multilayer system) and thus

$$\big(\boldsymbol{\Gamma} \pm \boldsymbol{\Gamma}^T\big)_m = \mp\big(\boldsymbol{\Gamma} \pm \boldsymbol{\Gamma}^T\big)_{-m}. \tag{6.34}$$

For the thick-slab case, only the bottom surface is involved and $m \to -m$ corresponds to inversion of $\boldsymbol{\alpha}_2 \equiv \hat{\mathbf{y}}$, i.e., mirror reflection R_y with respect to the xz plane. Taking into account also symmetry with respect to R_x, the response tensor assumes the form

$$\boldsymbol{\Gamma}^{\text{thick}} = \hat{\mathbf{x}} \begin{pmatrix} 0 & \Gamma_{xxy} & 0 \\ \Gamma_{xxy} & 0 & \Gamma_{xyz} \\ 0 & -\Gamma_{xyz} & 0 \end{pmatrix} + \hat{\mathbf{y}} \begin{pmatrix} \Gamma_{yxx} & 0 & -\Gamma_{yzx} \\ 0 & \Gamma_{yyy} & 0 \\ \Gamma_{yzx} & 0 & \Gamma_{yzz} \end{pmatrix}. \tag{6.35}$$

For the thin-slab case, both surfaces are involved and combinations of two reflections leave the Hamiltonian invariant or time-reversed. In the thin-slab basis [Fig. 6.2(c)] we obtain

$$R_y R_z H_{\chi m} R_z R_y = H_{\chi m}, \tag{6.36a}$$

$$R_x R_y H_{\chi m} R_y R_x = H_{\chi -m}. \tag{6.36b}$$

The resulting transformation behavior of the response tensor dictates the form

$$\boldsymbol{\Gamma}^{\text{thin}} = \hat{\mathbf{x}} \begin{pmatrix} \Gamma_{xxx} & 0 & 0 \\ 0 & \Gamma_{xyy} & \Gamma_{xyz} \\ 0 & -\Gamma_{xyz} & \Gamma_{xzz} \end{pmatrix} + \hat{\mathbf{y}} \begin{pmatrix} 0 & \Gamma_{yxy} & -\Gamma_{yzx} \\ \Gamma_{yxy} & 0 & 0 \\ \Gamma_{yzx} & 0 & 0 \end{pmatrix}. \tag{6.37}$$

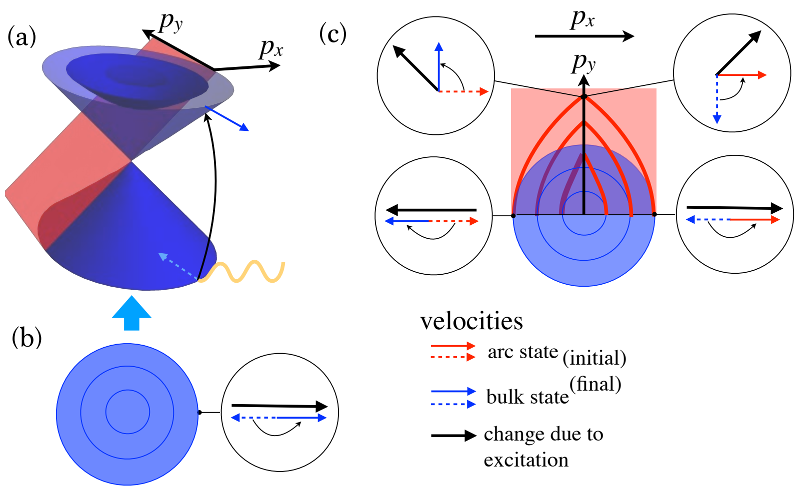

Figure 6.3: (a) Dispersion of Weyl fermions confined to a slab as function of in-plane momenta in the thick slab basis. Bulk states are colored blue and the Fermi-arc surface states red (only the bottom surface is shown). Velocities of initial (dashed arrow) and final state (solid arrow) of a photoexcitation are indicated. (b) Top view on bulk states in (a) showing the velocity change due to a bulk-bulk excitation. (c) Same as (b) but with indicated velocity change from arc-bulk excitations. Red contours indicate those states of the surface arc states that satisfy the energy-conservation constraint for arc-bulk excitations $\omega = \chi v p_x \pm v p$. Figure from [VIII].

A more detailed derivation of the tensor forms is given in Appendix D.3.

6.4 Results

6.4.1 PGE due to arc-bulk excitations

Arc-bulk excitations give rise to a current that is "automatically" a finite-size effect. Other finite-size corrections are negligible, which can be used to simplify the expression for the response tensor in Eq. (6.22); we can disregard the quantization of modes and replace the sums by integrals. The integration over z in the matrix elements of Eq. (6.31) may be extended to infinity since the decay of surface modes at most momenta is on the order of $\ell \ll \delta, W$, in both the thick-slab and thin-slab limits. Moreover we can neglect confinement-induced corrections of bulk states. A straightforward calculation (see Appendix D.4 for details) then gives

$$\boldsymbol{\Gamma}_{ij}^{\text{ab,thick}} = \frac{2\pi\eta\tau}{\tilde{W}} \left[i\chi \frac{8}{3} \varepsilon_{xij} \hat{\mathbf{x}} + \ln(2)\, \delta_{ij} (1 - \delta_{xi}) \hat{\mathbf{y}} \right] \tag{6.38}$$

for the bottom arc in the thick-slab basis $\hat{\mathbf{x}} = \boldsymbol{\alpha}_1$, $\hat{\mathbf{y}} = \boldsymbol{\alpha}_2$ [Fig. 6.2(b)]. The antisymmetric part is expressed using the Levi-Civita symbol ε_{ijk}. This is the only arc-bulk contribution in the thick-slab case.

In the thin-slab case we add the contribution of the top arc, which is equivalent to the bottom arc up to the changed directions, $\boldsymbol{\alpha}_1 \to \boldsymbol{\beta}_1, \boldsymbol{\alpha}_2 \to -\boldsymbol{\beta}_2$, see Fig. 6.2. Adding both contributions after appropriate rotation into the thin-slab basis [Fig. 6.2(c)] we obtain for $\frac{\tilde{W}}{4\pi\eta\tau}\boldsymbol{\Gamma}^{\text{ab,thin}}$

$$\hat{\mathbf{x}}\begin{pmatrix} \ln 2\, s_\Delta^3 & 0 & 0 \\ 0 & \ln 2\, s_\Delta c_\Delta^2 & i\frac{8}{3}\chi c_\Delta^2 \\ 0 & -i\frac{8}{3}\chi c_\Delta^2 & \ln 2\, s_\Delta \end{pmatrix} + \hat{\mathbf{y}}\, s_\Delta \begin{pmatrix} 0 & \ln 2\, c_\Delta^2 & -i\frac{8}{3}\chi s_\Delta \\ \ln 2\, c_\Delta^2 & 0 & 0 \\ i\frac{8}{3}\chi s_\Delta & 0 & 0 \end{pmatrix}, \tag{6.39}$$

where we defined

$$\Delta = \frac{\beta - \alpha}{2}, \tag{6.40}$$

as well as the shorthands $s_x = \sin x,\ c_x = \cos x$.

To understand this result, it suffices to understand the current production due to arc-bulk excitations at a single (bottom) surface, illustrated in Fig. 6.3. First we note that arc-bulk excitations vanish for the polarization component x because such a photon does not act on the spinor of the arc (which is an eigenspinor of σ_x) and thus cannot induce a transition to the orthogonal bulk state. This is circumvented when the linear polarization points in the other directions, y and z. The induced velocity due to arc-bulk excitations sum up to a total velocity pointing in the $\hat{\mathbf{y}}$ direction, see Fig. 6.3 (c), which explains the second term of (6.38).

Circular $y + iz$ polarization instead acts like a ladder operator on the σ_x eigenspinor and thus enhances the amplitude of spin-flip excitations where the spin is increased (at positive p_x in Fig. 6.3) and suppresses those where the spin is lowered (at negative p_x in Fig. 6.3), and vice versa for the opposite polarization handedness, $y - iz$, or chirality χ of the Weyl fermions. As is clear from Fig. 6.3, this asymmetry can produce velocity in the x direction, which sign depends on the polarization handedness and the chirality. This explains the first term of Eq. (6.38).

6.4.2 PGE DUE TO BULK-BULK EXCITATIONS

In contrast to the arc-bulk excitations, the contribution of excitations within the bulk bands (from the valence bulk band to the conduction bulk band) strongly differ for the thin- and thick-slab cases. We thus consider the two cases separately.

THICK SLAB LIMIT $W \gg \delta$

In this limit the light-induced excitations are produced at a single (bottom) surface in the finite strip of width δ. For the confinement-independent contribution $\boldsymbol{\Gamma}^{\text{bb}}$ we neglect all finite-size effects and obtain (see Appendix D.5.1 for details)

$$\boldsymbol{\Gamma}_{ij}^{\text{bb,thick}} = i\chi\frac{2\pi\eta\tau}{3}\frac{\delta}{W}\left(\varepsilon_{xij}\hat{\mathbf{x}} + \varepsilon_{yij}\hat{\mathbf{y}}\right). \tag{6.41}$$

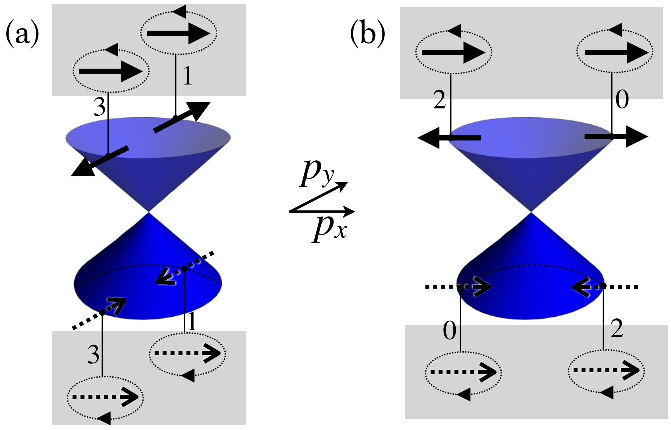

Figure 6.4: Characterization of bulk Weyl spinors in a semi-infinite spatial geometry. Spinors at the boundary are shown as arrows in the gray areas. They point in the x direction for all states. Going away from the boundary the spinors rotate so that the average spin, indicated as arrows at the cones, are like in an infinite system pointing parallel or antiparallel to the momentum, depending on the band and chirality (here positive). The numbers characterize the angle between the boundary and the average spinor (in units of $\pi/2$), which differ by π for opposite momenta. (a) and (b) show spinors at momenta perpendicular and parallel to the boundary spinor, respectively. Figure from [VIII].

Apart from the absence of current in the direction perpendicular to the boundary and the factor δ/W, this expression is identical to the circular PGE found in the infinite system model [71], which here has been re-derived using slab eigenstates. It is manifestly independent of the orientation of the Fermi arc. The prefactor δ/W correctly reflects the fact that excitations occur in the fraction of the penetration depth of the full sample width.

The leading corrections in the thick-slab limit are of a higher order in ℓ/δ, see Table 6.2. They stem from the z integration in the matrix elements (6.31), where we can still take the limit $W \to \infty$ but keep the finite light penetration depth. Other finite-size corrections are controlled by the small parameter ℓ/W and can thus be neglected. Expansion to leading order in ℓ/δ and numerical evaluation of the integral gives (see Appendix D.5.1 for details)

$$\frac{\delta\boldsymbol{\Gamma}^{\text{bb,thick}}}{\eta\tau/\tilde{W}} \simeq \hat{\mathbf{x}} \begin{pmatrix} 0 & 4.2 & 0 \\ 4.2 & 0 & -16.8i\chi \\ 0 & 16.8i\chi & 0 \end{pmatrix} + \hat{\mathbf{y}} \begin{pmatrix} -4.2 & 0 & 9.9i\chi \\ 0 & -4.2 & 0 \\ -9.9i\chi & 0 & -8.4 \end{pmatrix}, \tag{6.42}$$

written in the thick-slab basis, $\boldsymbol{\alpha}_1 = \hat{\mathbf{x}}, \boldsymbol{\alpha}_2 = \hat{\mathbf{y}}$. We estimate that these expressions are accurate to below 0.5%. Corrections to the circular PGE (antisymmetric part of the tensor) are in the same tensor components as the leading terms, as they should according to the symmetry constraints. The corrections are of opposite sign as the leading contribution because the tendency of the boundary to align the initial and final spinor suppresses the transition amplitude (circular

PGE needs spin-flip processes). A difference between x and y components is a manifestation of the boundary-condition-broken symmetry between the x and y directions.

The response to linearly polarized light (symmetric part of the tensor) is something that is not found for an infinite-system Weyl cone in the absence of tilt. This follows from the fact that a single unconfined tiltless Weyl node is intra-node TR symmetric and hence there is no linear PGE. The vanishing of the linear PGE in such a system is due to cancellation of the linearly-polarized-light-induced current from states at opposite momenta parallel to the polarization [71]. While the symmetry considerations have already shown that linear PGE contributions are possible in the presence of a boundary, (which breaks intra-node TR symmetry) it is peculiar that these contributions stem not only from arc-bulk but also from bulk-bulk excitations. To understand how the boundary breaks the symmetry between opposite momenta of bulk states, we consider the bulk-state spinor as a function of z, explicitly given in Eq. (D.9). At $z = 0$ the boundary condition forces the spinors at all momenta to coincide with $\psi(0) \propto (1, \exp[i\alpha])$. Going away from the boundary, the spinors rotate in the in-plane basis: At small z the spinor can be written as $(1, \exp[i\Phi(z)])$, with $\Phi(z) = -2\arctan[(\pm\chi p - p_x)z]$. Since $p > |p_x|$, the rotation handedness is the same for all momenta and is set only by the chirality and the band ($\pm$). The spin averaged over the whole slab width coincides with the spin of an infinite system—parallel or antiparallel to the momentum, depending on the band and chirality. As illustrated in Fig. 6.4, the angle between the spinor at $z = 0$ and the averaged spinor, measured in the direction of rotation, thus always differs by π for opposite momenta, which provides the crucial symmetry breaking and enables the response to linearly polarized radiation. Moreover, as can be seen from Eq. (D.9) and in Fig. 6.4(b), the x (i.e., $\boldsymbol{\alpha}_1$) component of the spinor is invariant under simultaneous band change and $\mathbf{p} \to -\mathbf{p}$, which explains the vanishing diagonal components for the response in the x direction.

THIN SLAB $\delta \gg W \gg \ell$

The confinement-independent contribution $\boldsymbol{\Gamma}^{\text{bb}}$ is obtained similarly to the thick-slab case by neglecting all finite-size corrections. The only difference is that the integration over z now extends over the whole slab width instead of δ. The result,

$$\boldsymbol{\Gamma}_{ij}^{\text{bb,thin}} = i\chi\frac{4\pi\eta\tau}{3}\left(\varepsilon_{xij}\hat{\mathbf{x}} + \varepsilon_{yij}\hat{\mathbf{y}}\right), \tag{6.43}$$

is, up to the missing factor $\delta/2W$, identical to the thick-slab case and, up to the vanishing current normal to the slab, identical to the known infinite-system result, as it should.

For the confinement-induced contributions we collect finite-size corrections of the type ℓ/W. They stem from the quantization of q_z and p_z as well as from corrections to the wave functions and the velocity of bulk states. We solve the problem numerically via discretizing the polar angle ϕ, and finding q_z, p_z pairs satisfying the energy conservation and Eq. (6.8) using standard numerical tools (see Appendix D.5.2 for details), yielding

$$\frac{\delta\Gamma_x^{\mathrm{bb,thin}}}{\eta\tau/\tilde{W}} \simeq \begin{pmatrix} -14.1s_\Delta + 4.7s_{3\Delta} & 0 & 0 \\ 0 & -21.5s_\Delta - 4.7s_{3\Delta} & -i\chi(26.7 + 6.9c_{2\Delta}) \\ 0 & i\chi(26.7 + 6.9c_{2\Delta}) & -23.0s_\Delta \end{pmatrix} \tag{6.44a}$$

for the x-direction and

$$\frac{\delta\Gamma_y^{\mathrm{bb,thin}}}{\eta\tau/\tilde{W}} \simeq \begin{pmatrix} 0 & 3.7s_\Delta - 4.7s_{3\Delta} & i\chi(26.5 - 6.9c_{2\Delta}) \\ 3.7s_\Delta - 4.7s_{3\Delta} & 0 & 0 \\ -i\chi(26.5 - 6.9c_{2\Delta}) & 0 & 0 \end{pmatrix} \tag{6.44b}$$

for the y-direction of the PG current. The numerical coefficients are accurate to the first decimal. Together with Eq. (6.38) and Eq. (6.42), Eq. (6.44) represents the central quantitative result of this work. Due to scale invariance of the Weyl Hamiltonian, these results are generic for any Weyl semimetal with untilted Weyl cones, up to straight-forward directional rescaling in case of anisotropic velocity, as discussed in Appendix D.2.

6.4.3 CONFINEMENT-INDUCED CONTRIBUTIONS AND LATTICE SIMULATION

The arc-bulk contribution Γ^{ab} and the confinement-induced bulk-bulk contribution $\delta\Gamma^{\mathrm{bb}}$ are intimately linked: They are of the same order of magnitude and they always occur in combination. Therefore, only the sum $\delta\Gamma^{\mathrm{bb}} + \Gamma^{\mathrm{ab}}$ is experimentally relevant.

In the thick-slab limit, the confinement-induced response tensor is

$$\frac{\delta\mathbf{\Gamma}^{\mathrm{bb,thick}} + \mathbf{\Gamma}^{\mathrm{ab,thick}}}{\eta\tau/\tilde{W}} \simeq \hat{\mathbf{x}} \begin{pmatrix} 0 & 4.2 & 0 \\ 4.2 & 0 & 0 \\ 0 & 0 & 0 \end{pmatrix} + \hat{\mathbf{y}} \begin{pmatrix} -4.2 & 0 & 9.9i\chi \\ 0 & 0.2 & 0 \\ -9.9i\chi & 0 & -4.0 \end{pmatrix}. \tag{6.45}$$

Note that since $\Gamma_{xyz}^{\mathrm{bb,thick}}$ and $\Gamma_{xyz}^{\mathrm{ab,thick}}$ cancel (within numerical accuracy), circularly polarized light may produce a sizeable current only parallel to the Fermi arc ($\boldsymbol{\alpha}_2 = \hat{\mathbf{y}}$), whereas linearly polarized light may produce currents perpendicular to the Fermi arc as well.

The thin slab limit result is plotted in Fig. 6.5 as a function of Δ. For $\beta = \alpha$ ($\Delta = 0$), the linear PGE vanishes because the second surface restores the symmetry between opposite momenta: With regard to the corresponding discussion for the thick-slab limit, the sense of rotation of spinors away from the $z = W$ boundary is opposite to $z = 0$ since z runs "backwards" there. For $\beta = \pm\pi + \alpha$ ($\Delta = \pm\pi/2$) the symmetric part of the response tensor is approxi-

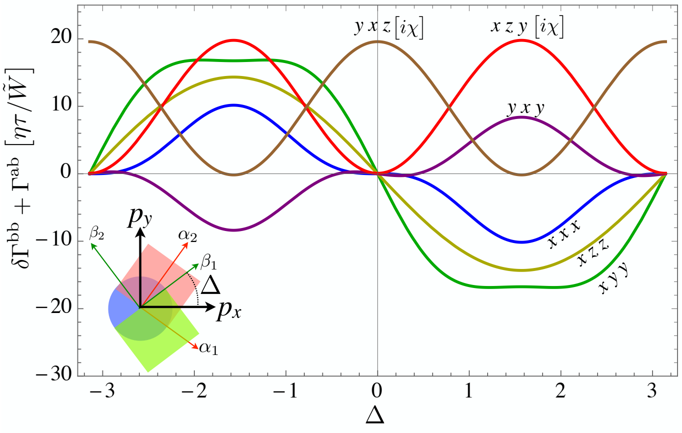

Figure 6.5: Confinement-induced response tensor $\delta\Gamma^{\text{bb,thin}}_{ijk} + \Gamma^{\text{ab,thin}}_{ijk}$ as a function of Δ. Only non-zero components are shown, labeled with ijk, the circular-PGE components have an additional prefactor $i\chi$ as indicated. Figure from [VIII].

mately maximized, while the weight of circular response is simply shifted from one component to the other. The Fermi arc orientations thus change the nature of the response completely.

More generally, one can understand that the (anti)symmetric part of the tensor, i.e., the linear (circular) PGE, must be odd (even) in Δ. In terms of Δ, the TR-breaking directions in (6.12) are given by $\boldsymbol{\alpha}_2 = (-\sin\Delta, \cos\Delta)$ and $\boldsymbol{\beta}_2 = (\sin\Delta, \cos\Delta)$. The transformation $\Delta \to -\Delta$ combined with the reflection R_x and $\chi \to -\chi$ leaves the Hamiltonian invariant. From the corresponding transformation of the tensor follows that components of the symmetric part are odd while components of the anti-symmetric part are even in Δ, as seen in Fig. 6.5.

Above we considered the thin-slab case while still assuming $W \gg \ell$. It is possible to relax this constraint and consider ultrathin slabs with $W \sim \ell$ resorting to numerical techniques. In this regime the confinement-induced and bulk contributions are of the same order. Furthermore, also transitions between arc states of the different surfaces become important. Here, we used a one-dimensional lattice realization of a single Weyl node (discretizing the z-direction while keeping $\mathbf{r}_\parallel$ continuous) to numerically evaluate the photogalvanic response tensor in Eq. (6.22). To this end we employ the lattice Hamiltonian,

$$H_{ij} = \frac{v}{2}[\sigma_x p_x + \sigma_y p_y + i\sigma_z \delta_{i,j+1} + \sigma_x(1 - \delta_{i,j+1})] + h.c., \tag{6.46}$$

where i, j denote the site index at fixed in-plane momenta p_x, p_y. This lattice version of the original infinite-system Weyl Hamiltonian (lattice constant set to one) has been constructed replacing

$$\sigma_z p_z \mapsto \sigma_z \sin p_z + \sigma_x(\cos p_z - 1), \tag{6.47}$$

such that the Hamiltonians coincide at small p_z (the second term removes a spurious Weyl cone at $p_z = \pm\pi$). Transformation into the site basis replaces

$$\sin p_z \mapsto i\tfrac{1}{2}(\delta_{i,j+1} - \delta_{i,j-1}), \qquad \cos p_z \mapsto \tfrac{1}{2}(\delta_{i,j+1} + \delta_{i,j-1}), \tag{6.48}$$

which leads to (6.46). The Hamiltonian (6.46) can be considered for a finite site number. The choice of the Pauli matrix σ_x for the second term in (6.47) sets the direction of the Fermi arc such that $\boldsymbol{\alpha}_2 = \hat{\mathbf{x}} = -\boldsymbol{\beta}_2$, corresponding to $\Delta = \pi/2$ of the thin-slab case considered above [169]. Numerical results for the PGE response tensor in Eq. (6.22) are obtained via discretizing parallel momenta, numerically diagonalizing the Hamiltonian (6.46), and summing over all pairs of states (one below and one above the Fermi level). The numerical discretization spacing and numerical broadening of the delta-function expressing energy conservation have been decreased until convergence of the results.

The results are shown in Fig. 6.6, demonstrating that our semi-analytical results can be reproduced in a lattice setting, and that the qualitative behaviour, such as sign and magnitude of the confinement induced contributions, extends down to $W \sim \ell$. For $W \lesssim 2\ell$, the finite-size gap of modes becomes larger than the photon energy and the response vanishes. To provide further insight in the mechanisms behind the confinement-induced response, in Fig. 6.7 we show the contributions resolved in the in-plane momentum. One can clearly see the cusp-like lines of the arc-bulk excitations and the circular lines of bulk-bulk excitations, c.f. Fig. 6.3. The signs of the contributions and the presence/absence of arc-bulk contributions is as discussed in the main text.

6.4.4 Surface PGE in centrosymmetric Weyl semimetals

Our results for a single Weyl node allow to infer on the response of a WSM with several nodes by adding the contributions of each node. Probably the most intersting case is that of centrosymmetric WSMs, for which the confinement-independent bulk-bulk contributions Γ^{bb} cancel and only the confinement-induced contributions, $\delta\Gamma^{\mathrm{bb}}$ and Γ^{ab}, survive. A minimal model of a centrosymmetric bulk WSM consists of a single pair of Weyl nodes with opposite chirality. Considering the multilayer Hamiltonian $H_{\chi m}$ in (6.12) as the Hamiltonian describing one of the Weyl nodes, for the Hamiltonian describing the second Weyl node of opposite chirality we take $H_{-\chi - m}$. In this case the Fermi arcs emanate in opposite directions, which happens when the Weyl nodes are connected in a straight line. However, we have seen in Sec. 6.1 that an additional boundary potential $\delta H_{\mathrm{b}} = \delta(z)\mu_0 + \delta(z - W)\mu_W$ rotates the spinors by $\alpha \to \alpha + \chi 2\mu_0$ and $\beta \to \beta - \chi 2\mu_W$. The generic situation is thus that there is a finite angle φ characterizing the deviation from an anti-parallel alignment, as shown in the inset of Fig. 6.8(a). Note that between the nodes, the Fermi arcs thus must be curved, as is typically seen in experiments; the curvature itself plays however no role for our results since excitations occur only close to the Weyl nodes.

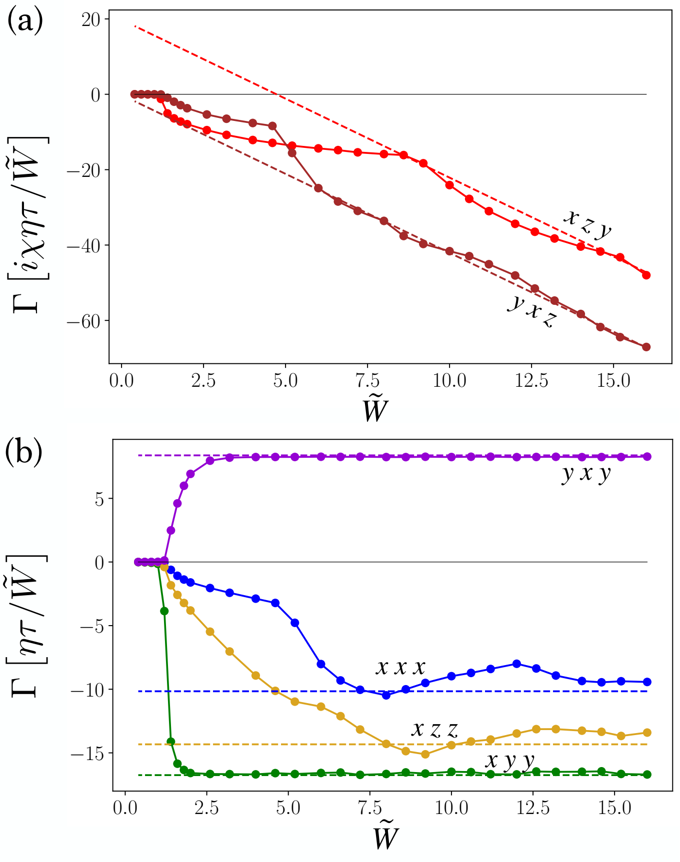

Figure 6.6: (a) Circular and (b) linear response tensor components in the ultra-thin limit $\tilde{W} = W/\ell \sim 1$ at $\Delta = \pi/2$. The data points correspond to the photogalvanic response tensor Eq. (6.22) numerically evaluated for a lattice realization of a single Weyl point. The dashed lines correspond to the semi-analytical results $\Gamma = \Gamma^{\mathrm{bb}} + \delta\Gamma^{\mathrm{bb}} + \Gamma^{\mathrm{ab}}$ in the limit $\tilde{W} \gg 1$. For $\tilde{W} \lesssim 2$, the lattice response vanishes as the frequency drops below the finite size gap. For $\tilde{W} \gtrsim 2$, the response converges towards the semi-analytical $\tilde{W} \gg 1$ results. Figure from [VIII].

The total response $\Gamma^{\mathrm{WSM}}_{abc}$ is obtained from the single-cone result $\Gamma_{ijk}(\chi, m)$ (now explicitly denoting the χ, m dependence),

$$\Gamma^{\mathrm{WSM}}_{abc} = R(\varphi)_{ai}R(\varphi)_{bj}R(\varphi)_{ck}\Gamma_{ijk}(\chi, m) + R(-\varphi)_{ai}R(-\varphi)_{bj}R(-\varphi)_{ck}\Gamma_{ijk}(-\chi, -m), \quad (6.49)$$

where $R(\varphi)$ is the spatial rotation matrix for a rotation around z by φ. The results are plotted in Fig. 6.8. From the transformation behavior of the response tensor discussed in Sec. 6.3 (symmetric part odd in m and even in χ, antisymmetric part odd in χ and even in m), the response of the two Weyl nodes cancel each other at $\phi = 0$. This means that in the thick-slab case the response vanishes when the Fermi arcs of the illuminated surface emanate from the Weyl nodes in

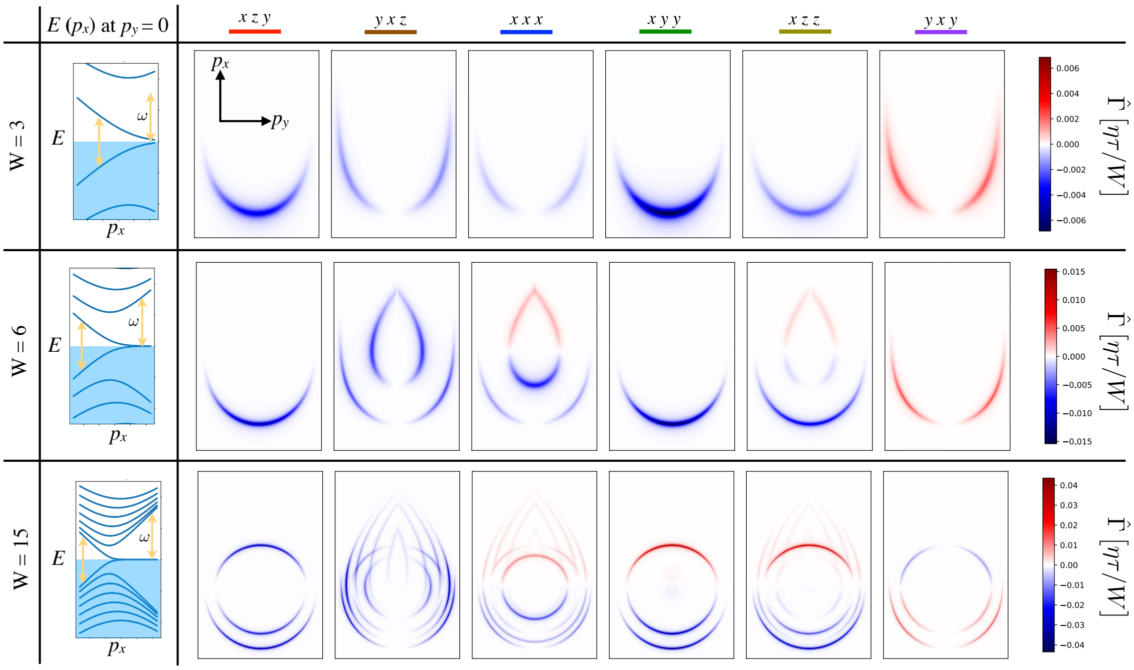

Figure 6.7: Parallel-momentum (p_x, p_y) resolved response tensor $\hat{\Gamma}$ ($\Gamma = \sum_{p_x,p_y} \hat{\Gamma}$) at three widths $W = 3, 6, 15$ for $v = 1$ and $\ell = 5$ sites. Left column indicates the dispersion at $p_y = 0$. Figure from [VIII].

exactly opposite directions. In the thin-slab case, the same applies but the emanation direction is replaced by the bisector of the top- and bottom-surface Fermi arcs.

For $\phi = \pi/2$ the directions just discussed (emanation direction for thick slab and bisector direction for thin slab) are parallel. This is equivalent to taking the contributions of the two Weyl nodes at the same m (instead of m and $-m$), while χ are still opposite. Since the (anti)symmetric part is even (odd) in χ, the antisymmetric parts cancel also here but the symmetric parts add up to twice the value of a single cone. This can be seen by comparison of Fig. 6.8(b) with the single-cone results shown in Fig. 6.5 for the thin-slab case and Fig. 6.8(a) with $\boldsymbol{\Gamma}^{\text{ab,thick}} + \delta\boldsymbol{\Gamma}^{\text{bb,thick}}$ from Eqs. (6.38) and (6.42) for the thick-slab case. (Note that the coordinate system is now rotated by $\pi/2$, i.e., $y \to x$ and $x \to -y$, compared to the single-cone case).

6.5 CONCLUSION

In conclusion, we have explored the PGE of a WSM spatially confined to a slab geometry. Symmetry breaking on the surfaces via the orientation of the Fermi arcs enables circular and linear photogalvanic response currents, which would otherwise not be possible, in particular, in centrosymmetric WSMs.

The magnitude of the confinement-enabled PGE inherits the topology-enhancement of unconfined Weyl fermions, based on the topologically protected band touchings [72, 277]. How-

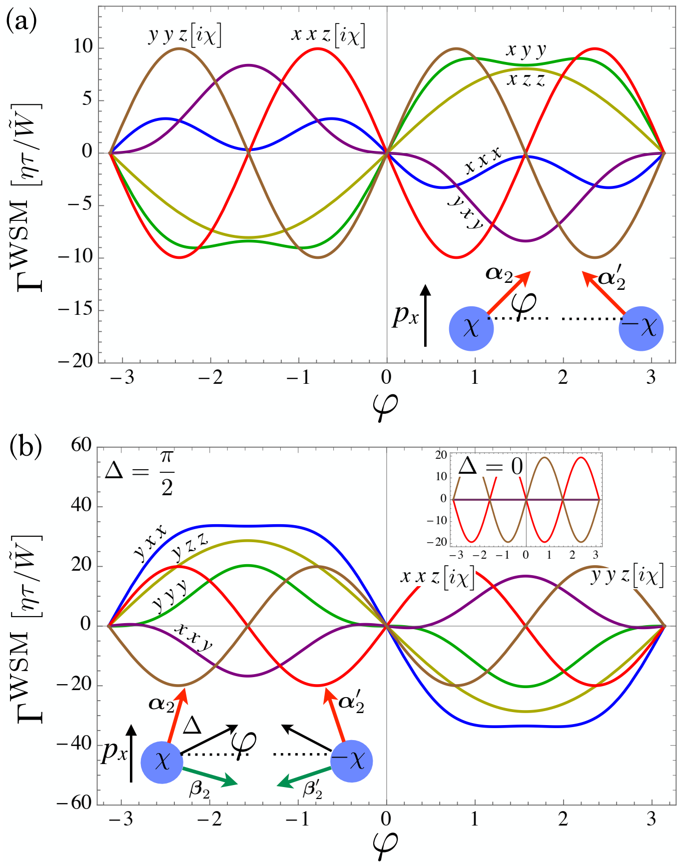

Figure 6.8: Response-tensor components for a centrosymmetric WSM in (a) the thick- and (b) the thin-slab case, as a function the angle φ. As shown in the lower insets, ϕ sets the deviation from antiparallel alignment of (a) the direction of bottom-surface Fermi arcs; and (b) the directions of bisectors of bottom- and top-surface Fermi arcs. In the thin-slab case (b) the angle between top and bottom arcs is chosen as $\Delta = \pi/2$; the inset in the right top shows the result for $\Delta = 0$, for which the linear PGE vanishes. Figure from [VIII].

ever, while in infinite systems those band touchings include only the chiral pairs of Weyl nodes, a confined system features topological surface states, which are tightly glued to the Weyl nodes.

The ratio of confinement-induced contributions to bulk contributions scales in case of a thin slab like $(v/c) \times (\lambda/W)$ and for the thick slab like v/c, where λ is the light wavelength, W the slab thickness, and $v/c \approx 0.01$ the node- vs. light-velocity. Considering the upper and lower bounds of λ set by the finite Fermi level and the band width of typical WSM materials, the confinement-induced PGE is on the order of bulk PGE for widths of order $W \sim 0.1 \ldots 1\,\mu$m. Surface-controlled PGE is thus found in such thin slabs even for non-centrosymmetric WSMs, which makes the experimental realization of thin WSM slabs or even stacks of those especially interesting.

One of the most remarkable properties of the confinement-induced PGE is that it is controlled by surface boundary conditions. We explicitly discussed the effect of a surface potential, which rotates the direction of Fermi arcs. Another interesting possibility, known from experiments, are layered WSMs for which the different surface terminations can not only change the directionality of Fermi arcs but even lead to different connectivities to the Weyl nodes [289, 290]. This Fermi-arc geometry is observable, e.g., via angle-resolved photoemission spectroscopy [91, 92, 269]; our work links this geometry with the photogalvanic response. In principle, a confinement-related photogalvanic response may exist also in regular metals due to Tamm surface states. However, such a response does not share the remarkable features of the confinement-induced PGE in WSMs. The difference is due to topology: while in a regular metal, the surface state wave-functions depend on microscopic details, in a WSM the Fermi arc wave functions are uniquely determined by the Fermi arc directionality. This fact enables the sensitivity to boundary conditions and hence the control of the confinement-induced PGE in WSM. Moreover, a confinement-related PGE in a regular metal would lack the aforementioned enhancement due to the band touchings in a WSM and should hence be much smaller than the effect discussed in this chapter.

With regard to the remarkable recent progress in device microstructuring [83, 293–296], our work might thus play an important role in identifying Weyl physics and shaping the photogalvanic response by designing the material surface.

7 SUMMARY AND PERSPECTIVE

This thesis discussed examples of the design and control of quantum matter and quantum devices that are engineered from subgap and boundary modes, as well as quantum response enabled and controlled by subgap and boundary modes. It thereby demonstrates the versatility and utility of subgap and boundary modes as building blocks for quantum engineering. The objectives of the quantum engineered systems and response characteristics considered in this work are multifold. They range from purposes of fundamental scientific merit, such as the design and simulation of novel quantum phases [I, II, III], to application-oriented purposes, relevant e.g. to superconducting electronics [IV, V, VI], topological quantum computing [VII], as well as optoelectronics [VIII]. In the following the novel aspects and relevance of the works presented here will be laid out and put into perspective.

Chains of magnetic adatoms on superconducting substrates are one of the primary experimental platforms in the search for one-dimensional topological superconductivity and its associated Majorana zero modes. Our results show that, contrary to the assumptions made in most theoretical works hitherto, the quantum nature of the adatom spin is of crucial importance in understanding the physics of these systems. Indeed, in the extreme case of spin-$\frac{1}{2}$ adatoms, the YSR excitation, which represents the local building block of the quantum engineered system, is neither a spinless nor a spinful fermion. It is instead an intrinsically strongly interacting degree of freedom. We arrived at this conclusion by taking an approach that is complimentary to the established theories of YSR chains: instead of simplifying the adatom spin, we simplify the superconducting substrate by considering the limit of vanishing bandwidth. While the resulting extended $t - J$ model is strongly interacting, it is one-dimensional and as such can be treated well with standard techniques such as exact diagonalization and DMRG. Here, we employed the former as it provides access to the experimentally relevant spectral function. We revealed rich many-body spectra governed by the interplay of separated spin and charge degrees of freedom, the hallmark of strongly correlated electron systems in one dimension. The possibility of emergent quantum magnetism in YSR chains had thus far eluded the theoretical community studying these systems. We further showed that a topological superconducting phase persists also in quantum YSR chains. However, due to competition with phases that do not have a counterpart in the classical picture, the topological region in parameter space is strongly suppressed. Finally, we identified a new nontopological mechanism unique to quantum YSR chains which leads to increased spectral weight at the chain ends and low bias. This is relevant to avoid misinterpretation of low-bias spectral features in terms of Majorana zero modes.

These results suggest several avenues for future studies. Most pressingly, the phase diagram of spin-$\frac{1}{2}$ quantum YSR chains needs to be understood more deeply. In particular, it is not yet clear what the precise phase boundaries within the overall singlet sector are. Preliminary considerations suggest that there is a continuous quantum phase transition which separates the fully screened phase and the fully unscreened antiferromagnetic chain. It is also not clear, whether the singlet superconductor is smoothly connected to the latter phase, or whether it forms a standalone phase. We have also seen in preliminary studies that addition of Dzyaloshinskii-Moriya interactions to the singlet superconductor phase leads to zero-bias spectral peaks localized at the chain ends. A possible explanation in terms of power law-localized Majorana zero modes induced by non-symmetry breaking spiral-like spin-spin correlations remains to be confirmed. It would also be interesting to apply the zero bandwidth approach to chains of spin-1 adatoms. Here, departure from $t-J$ physics is expected and single-ion anisotropy is relevant. Understanding of the spin-1 case may bridge between quantum and classical YSR chains. Exact diagonalization is not suitable to address these questions due to the excessive computational cost associated with scaling up the system size. Different numerical techniques such as DMRG, or analytical approaches such as bosonization methods should allow one to bypass these issues. Finally, their description in terms of $t-J$ fermions suggests that YSR assemblies may be used to simulate strongly correlated matter in a system that is designed from bottom-up, and that has lattice structure and couplings which are, at least in principle, under experimental control. As a first step, two-dimensional YSR assemblies should be considered: here, as opposed to the spin-charge separation in one dimension, the spin and charge carriers should exhibit confinement.

With single-atom Josephson diodes we have presented another fascinating application of YSR bound states: Instead of employing YSR states as building blocks for the engineering of novel quantum phases, here YSR states control the nonreciprocity of a nanoscale Josephson junction. We could explain this in terms of a novel mechanism leading to the Josephson diode effect: rather than current-phase asymmetry manifesting in nonreciprocal critical or switching currents, here asymmetric dissipation gives rise to nonreciprocity in the retrapping currents. This new mechanism has different symmetry requirements, and thus may be observed in time-reversal symmetric junctions provided that particle-hole symmetry in the normal metal sense is absent. We could establish the correspondence between current-phase asymmetry and nonreciprocity in the switching currents, asymmetric dissipation and nonreciprocity in the retrapping currents under rather general circumstances provided the damping is sufficiently weak. While these considerations were based on a phenomenological approach, we corroborated our results by microscopic considerations for a Josephson tunnel junction. Specifically, we streamlined and generalized the field-theoretic approach by Ambeaokar, Eckern and Schön, yielding an extended RCSJ equation that involves the voltage-bias expressions for the quasiparticle current as the dissipative contribution, and the voltage-bias expression for the current-current correlation function as noise correlator. In particular, these currents involve contributions at all orders in the tunneling, including multiple Andreev reflections. We then performed a numerical Monte-Carlo study of this RCSJ equation using experimental quasiparticle currents as input. With this we could reproduce the main features of the experiment on the magnetic atom Josephson junctions.

Thus far, the aim of our simulations has been qualitative understanding. However, we have arrived at a point where the RCSJ simulations could be used to fit and extract experimental parameters such as the critical current of the junction, or, more ambitiously, higher Fourier components of the current-phase relation. There are several issues which need to be addressed. First, the electromagnetic environment contributes significantly to the dynamics of the junction. By measuring the environmental impedance independently, e.g. by reflectometry techniques, the number of parameters needed to model the experiment could be reduced drastically. Similarly, our current procedure involves fitting and subtracting the voltage-bias Josephson current due to incoherent transfer of Cooper pairs. This introduces ambiguities in the model parameters that could be avoided if the quasiparticle current were measured at sufficiently high magnetic field suppressing the Josephson contribution. Progress is to be made also on the purely theoretical side. Our current theory describes only point contacts and therefore fails to describe a range of experiments on extended junctions [297, 298]. It is straightforward to incorporate this into our approach. In fact, it may prove useful to phrase the transport through the junction as a scattering problem and integrate this directly into the field-theoretic approach. This comes with the advantage that results are expressed in terms of directly measurable quantities such as transmission and reflection amplitudes, rather than microscopic parameters. As a last point, it remains to be shown under what circumstances the correspondence between an asymmetric current-phase relation and nonreciprocal switching currents as well as an asymmetric dissipative current and nonreciprocal retrapping currents breaks down. We have reason to believe it persists outside the weak-damping regime for sufficiently low temperatures but thorough analysis remains to be done.

The second example of subgap (and boundary) mode used for quantum engineering purposes in this thesis is the famously elusive Majorana zero mode. Its topological nature protects Majorana quantum devices against local noise, while also providing certain protected operations on its associated space of states. These features make Majorana zero modes particularly attractive for quantum computing applications. Here, we considered the simplest qubit formed from Majorana zero modes, the so called Majorana box qubit, which combines four Majorana zero modes on an electrostatically floating island. While these qubits are expected to be very long-lived their topological nature makes accessing the information they encode a complicated problem. Indeed, quantum computing based on Majorana Box Qubits relies heavily on quantum-non-demolition measurements to implement Clifford gates. A fast and robust readout protocol is therefore paramount to this quantum computing architecture. We developed a comprehensive theory of readout for Majorana Box Qubits based on the quantum trajectory approach. Our theory explains in detail not only decoherence but also the measurement signal, and thus provides strategies for optimal readout. For Majorana Box readout via charge sensing of a nearby quantum dot we found that there is an optimum for qubit-readout device coupling such that stronger coupling makes it harder to detect the measurement outcome. Finally, we show that the mechanism underlying our theory relies only on a conserved parity and as such should find application in many different platforms. We term this symmetry-protected readout.

The quantum trajectory approach is easily extended to include detrimental processes such as quasiparticle poisoning or Majorana hybridizations and thus may serve as a starting point for more sophisticated approaches describing real devices. It remains to be seen whether such devices will become a physical reality in the near future, though. Nonetheless, the intersection of decoherence, measurement and (symmetry-protected) topological order is a rich subject from a theoretical perspective and it should be fruitful to extend our considerations to more exotic topological excitations such as Fibonacci anyons.

The final example of boundary mode subject of this thesis is the topological Fermi arc that is associated with a Weyl semimetal bulk. Fermi arcs are responsible for a large number of exotic transport phenomena associated with their chiral and topological nature. Here, we studied the effect of Fermi arc surface states on the photoresponse. More specifically, we calculated the ballistic photogalvanic current for a Weyl semimetal slab, employing analytic semiclassical techniques augmented by lattice simulations. We show that the response is crucially determined by the Fermi arc orientations which may be affected through surface potentials. We argue that this allows for design of the photoresponse, e.g. for application in optoelectronics.

More broadly speaking, the control of response in Weyl semimetals is a field of active research. The aim of this program is the design of Weyl materials in which the topological and chiral anomaly related transport effects are the dominant response. We have provided merely one example of photocurrents dominated by the topological Fermi arcs. It would be interesting to see whether there are ways to extend this to other nonlinear response effects, such as second harmonic generation.

These examples represent the status quo of quantum engineering with subgap and boundary modes. Their embedding into the continua of condensed matter systems may put them at a disadvantage compared to atomic platforms such as cold atom quantum simulators and superconducting quantum computers, when it comes to coherence and programmability. But the scalability and comparable simplicity innate to condensed matter based technologies might well mean that the quantum simulators and computers of tomorrow are based on subgap and boundary modes.

Acknowledgments

This work would not have been possible without the support of a number of organizations and people.

Thanks go to the Quantera program of the EU, as well as the DFG through the SFB 910 for funding my research at the FU Berlin. Thanks also go to the CRC TR 183 which provided me with many opportunities to attend conferences and summer schools.

On the personal side, I want to thank my advisor Felix, who took me in when I was merely a disoriented master of science and formed me into the disoriented doctor of physics that I will soon be. While I never learned the discipline an aristocrat should expect from their subordinate, I learned enough from Felix to make up for it: lots of physics, a very straightforward way of thinking about physics, a healthy amount of skepticism, a healthy amount of optimism, the importance of a good story, and one or two math tricks. Felix was always open to discuss, whether it was physics ideas, physics gossip, or worldly going-ons. I thoroughly enjoyed the informal manner of these interactions which made me feel respected as a physicist. Thank you for all that.

I also want to thank my coadvisor Piet. Despite the fact that we never worked on a project together I learned many things from him, mostly in the infamous dice seminar. Not least, Piet taught me that physics hides behind the formalism as he always managed to find a simple picture for every phenomenon that we encountered, no matter how complicated it appeared on its formal surface. Beyond the physics, Piet was always kind and helpful and fun. It was a pleasure and honor to be coadvised by you.

My thanks also go to my other collaborators on the projects that make up this thesis. On the theory side, this encompasses Christophe, Maxim, Anton, Larissa and Harald. Thank you for teaching me many new techniques and for allowing me to gain a new perspective on the subjects through your minds. Special thanks go to Harald, who has helped me a great amount in polishing this thesis. I am particularly grateful also to my experimental collaborators Martina, Eva, and Katharina. It was a great joy and illuminating experience to work together with you on solving the riddles posed by your data. Through these projects I learned what I want my physics to be about. All of you, it was a pleasure to work with you and I hope to collaborate with some of you in the future!

Of course, my time at the FU was not solely about the science. The generalized condensed matter theory supergroup was always a fun environment and thanks go to all the people who helped make it that: the CMT boulder schmoulder connection, the old mensa schmensa gang, the new mensa gang, my Mitbürohners, the crossword crew, all the board game and chess enjoyers, and, last but not least, the special people who forget about time during coffee breaks.

Finally, my life beyond physics played a major role in keeping me sane-ish and generally well. This is mostly thanks to Sarah, who kept me grounded and made sure that I did not neglect the parts of life which are way more important than scribbling fantasy symbols and publications in glossy journals. Looking at this whole thing from a distance, there is one glaring omission: without my parents this thesis would not have come to be (I know, obvious, duh). They provided my brothers and myself with the happiest childhood and most well rounded upbringing one could imagine. I now pay back their parental love with this heap of paper filled with unintelligible gibberish. That's what you get for not making sure that I learn something proper like art or music. Before I conclude, I want to mention my friends and also my brothers, both here in Berlin and elsewhere, who always came to visit and made my years here in Berlin a great time.

APPENDIX A

A.1 ALGEBRA OF LOW ENERGY PROJECTED OPERATORS

In this Appendix we investigate the action of the projected Bogoliubov operators $P\gamma_\sigma P$, $P\gamma_\sigma^\dagger P$ as well as PS^iP on the low-energy subspace. We will find that they satisfy the same algebra as $t-J$ fermions (i.e., spinful electrons with the constraint that double occupancy is forbidden). Consider first the action of $P\gamma_\sigma P$ on the singlet,

$$P\gamma_\downarrow P|s\rangle = \frac{1}{\sqrt{2}}|+\rangle,\ P\gamma_\uparrow P|s\rangle = -\frac{1}{\sqrt{2}}|-\rangle. \tag{A.1}$$

Thus, the states $|\pm\rangle$ are created from $|s\rangle$ by application of $P\gamma_{\downarrow/\uparrow}P$ (up to normalization). Similarly, we have

$$P\gamma_\sigma^\dagger P|\pm\rangle = \begin{cases} 0 \text{ if } \sigma = \pm \\ \frac{\bar{\sigma}}{\sqrt{2}}|s\rangle \text{ if } \sigma = \mp \end{cases},\ P\gamma_\sigma^\dagger P|s\rangle = 0. \tag{A.2}$$

Thus, $P\gamma_\sigma^\dagger P$ acts as annihilator for the excitations with $\pm = \bar{\sigma}$, while $|s\rangle$ acts as the vacuum. Finally, consider the action of $P\gamma_\sigma P$ on the already occupied $|\pm\rangle$,

$$P\gamma_\sigma P|\pm\rangle = 0. \tag{A.3}$$

Following these observations, for $\sigma = \mp$ this corresponds to adding a second spin-σ electron into the already occupied state, which should indeed give 0. However, the above also implies $P\gamma_\uparrow P\gamma_\downarrow P|s\rangle = 0$, which corresponds to forbidden double occupation. This motivates the definition of new quasi-fermionic creation operators

$$\Gamma_\sigma^\dagger = \sigma\sqrt{2}P\gamma_{\bar{\sigma}}P, \tag{A.4}$$

which create the states $|\pm = \sigma\rangle$ from $|s\rangle$. They satisfy

$$\Gamma_\sigma^\dagger\Gamma_\sigma^\dagger = 0 = \Gamma_\sigma\Gamma_\sigma. \tag{A.5}$$

Due to the forbidden double occupation, these are not proper fermions. Their full anticommutation algebra on the low-energy subspace is given by

$$\left\{\Gamma_\uparrow,\Gamma_\uparrow^\dagger\right\}\begin{cases}|s\rangle\\|+\rangle\\|-\rangle\end{cases}=\begin{cases}|s\rangle\\|+\rangle\\0\end{cases},\quad\left\{\Gamma_\downarrow,\Gamma_\downarrow^\dagger\right\}\begin{cases}|s\rangle\\|+\rangle\\|-\rangle\end{cases}=\begin{cases}|s\rangle\\0\\|-\rangle\end{cases},\tag{A.6a}$$

$$\left\{\Gamma_\downarrow,\Gamma_\uparrow^\dagger\right\}\begin{cases}|s\rangle\\|+\rangle\\|-\rangle\end{cases}=\begin{cases}0\\0\\|+\rangle\end{cases},\quad\left\{\Gamma_\uparrow,\Gamma_\downarrow^\dagger\right\}\begin{cases}|s\rangle\\|+\rangle\\|-\rangle\end{cases}=\begin{cases}0\\|-\rangle\\0\end{cases},\tag{A.6b}$$

while

$$\left\{\Gamma_\uparrow^\dagger,\Gamma_\downarrow^\dagger\right\}=0=\{\Gamma_\uparrow,\Gamma_\downarrow\}.\tag{A.6c}$$

We now show explicitly that these operators satisfy the same algebra as the $t-J$ fermions. To this end, consider a single site, infinite-U Hubbard model described by fermionic operators d_σ, with states $|\mathrm{vac_H}\rangle$, $|\sigma_\mathrm{H}\rangle = d_\sigma^\dagger|\mathrm{vac_H}\rangle$ and the doubly occupied $|{\downarrow\uparrow}_\mathrm{H}\rangle = d_\downarrow^\dagger d_\uparrow^\dagger|\mathrm{vac_H}\rangle$, as well as the projector onto the empty and singly-occupied states, $P_\mathrm{H} = 1 - |{\downarrow\uparrow}_\mathrm{H}\rangle\langle{\downarrow\uparrow}_\mathrm{H}|$. Note that, for sake of simplicity, in the main text no distinction is made between the Hilbert space of the original model and that of the Hubbard model. As above we define the projected quasi-fermion operators as

$$D_\sigma = P_\mathrm{H} d_\sigma P_\mathrm{H}.\tag{A.7}$$

It is straightforward to check the anticommutation relations. As above

$$\left\{D_\uparrow, D_\uparrow^\dagger\right\}\begin{cases}|\mathrm{vac}_\mathrm{H}\rangle\\|{\uparrow}_\mathrm{H}\rangle\\|{\downarrow}_\mathrm{H}\rangle\end{cases}=\begin{cases}|\mathrm{vac}_\mathrm{H}\rangle\\|{\uparrow}_\mathrm{H}\rangle\\-P_\mathrm{H}d_\uparrow P_\mathrm{H}|{\downarrow\uparrow}_\mathrm{H}\rangle=0\end{cases}, \tag{A.8a}$$

$$\left\{D_\downarrow, D_\downarrow^\dagger\right\}\begin{cases}|\mathrm{vac}_\mathrm{H}\rangle\\|{\uparrow}_\mathrm{H}\rangle\\|{\downarrow}_\mathrm{H}\rangle\end{cases}=\begin{cases}|\mathrm{vac}_\mathrm{H}\rangle\\P_\mathrm{H}d_\downarrow P_\mathrm{H}|{\downarrow\uparrow}_\mathrm{H}\rangle=0\\|{\downarrow}_\mathrm{H}\rangle\end{cases}, \tag{A.8b}$$

$$\left\{D_\downarrow, D_\uparrow^\dagger\right\}\begin{cases}|\mathrm{vac}_\mathrm{H}\rangle\\|{\uparrow}_\mathrm{H}\rangle\\|{\downarrow}_\mathrm{H}\rangle\end{cases}=\begin{cases}0\\0\\-P_\mathrm{H}D_\downarrow d_\mathrm{H}|{\downarrow\uparrow}_\mathrm{H}\rangle+|{\uparrow}_\mathrm{H}\rangle=|{\uparrow}_\mathrm{H}\rangle\end{cases}, \tag{A.8c}$$

$$\left\{D_\uparrow, D_\downarrow^\dagger\right\}\begin{cases}|\mathrm{vac}_\mathrm{H}\rangle\\|{\uparrow}_\mathrm{H}\rangle\\|{\downarrow}_\mathrm{H}\rangle\end{cases}=\begin{cases}0\\P_\mathrm{H}d_\uparrow P_\mathrm{H}|{\downarrow\uparrow}_\mathrm{H}\rangle+|{\downarrow}_\mathrm{H}\rangle=|{\downarrow}_\mathrm{H}\rangle\\0\end{cases}, \tag{A.8d}$$

and

$$\left\{D_\uparrow^\dagger, D_\downarrow^\dagger\right\}=0=\{D_\uparrow, D_\downarrow\}. \tag{A.8e}$$

Thus, the low-energy projected superconductor may be described using the infinite-U Hubbard model instead, with $\gamma_\sigma\sim-\sigma d_{\bar{\sigma}}^\dagger/\sqrt{2}$. As mentioned above, we introduce the $\sim$-symbol to mean equivalence at the level of the low-energy projected theory. The corresponding Hamiltonian is

$$H_\mathrm{H}=-E_\mathrm{YSR}\sum_\sigma d_\sigma^\dagger d_\sigma+V-\frac{3}{4}K+Ud_\uparrow^\dagger d_\uparrow d_\downarrow^\dagger d_\downarrow,\ U\to\infty. \tag{A.9}$$

The merits of this identification will become clear when considering chains in the next section. We have not yet discussed the low-energy projected spin operators PS^iP. They act like the spin operators associated with the d fermions,

$$S^z\sim\frac{1}{2}\sum_\sigma\sigma d_\sigma^\dagger d_\sigma,\ S^+\sim d_\uparrow^\dagger d_\downarrow,\ S^-\sim d_\downarrow^\dagger d_\uparrow. \tag{A.10}$$

To see this, we explicitly consider their action on the low-energy states,

$$PS^zP|s\rangle\propto P(|{\Uparrow\downarrow}\rangle+|{\Downarrow\uparrow}\rangle)=0,\ PS^zP|\pm\rangle=\pm\frac{1}{2}|\pm\rangle, \tag{A.11a}$$

$$PS^+P|s\rangle\propto P|{\Uparrow\uparrow}\rangle=0,\ PS^\pm P|\pm\rangle=0,\ PS^\mp P|\pm\rangle=|\mp\rangle. \tag{A.11b}$$

The $\Gamma_{j,\sigma}$ have the same anticommutation algebra as $t-J$ fermions. The on-site algebra follows from the previous section. Furthermore, it is clear that $\{\Gamma_{j,\sigma}, \Gamma_{j',\sigma'}\} \propto P_j P_{j'} \{\gamma^\dagger_{j,\bar{\sigma}}, \gamma^\dagger_{j',\bar{\sigma}'}\} P'_j P_j = 0$ for $j \neq j'$ since $[P_j, P_{j'}] = 0$ and similarly for the anticommutator of creation and annihilation operators. There is one more issue to account for to make the mapping exact. The new vacuum is a product of local singlet states, and therefore has odd local fermion parities. Similarly, the single-occupied sites actually have even local fermion parity. Thus, acting with $\Gamma^\dagger_j$ on a basis state, there is an overall minus sign equal to the parity of the number of singlets on sites $i < j$, i.e. of the number of "unoccupied" rather than "occupied" states. To make this precise, consider the action of $\Gamma_{j,\sigma}$ on the product basis derived from $|s\rangle$ and $|\pm\rangle$. We write

$$|\mathbf{y}\rangle \equiv |y_1\rangle \otimes \ldots \otimes |y_N\rangle \tag{A.12}$$

in terms of $y_j \in \{-, s, +\}$. Then, we have

$$\begin{aligned} \Gamma_{j,\sigma}|\mathbf{y}\rangle = (-1)^{\sum_{i<n}(1+\sum_{\sigma'} n_{i,\sigma'})} \\ |y_1\rangle \otimes \ldots \otimes \Gamma_{j,\sigma}|y_j\rangle \otimes \ldots \otimes |y_N\rangle. \end{aligned} \tag{A.13}$$

Similarly, for the infinite-U Hubbard model

$$\begin{aligned} D_{j,\sigma}|\mathbf{x}\rangle = (-1)^{\sum_{i<n,\sigma'} n_{i,\sigma'}} \\ |x_1\rangle \otimes \ldots \otimes D_{j,\sigma}|x_j\rangle \otimes \ldots \otimes |x_N\rangle, \end{aligned} \tag{A.14}$$

where $x_j \in \{\mathrm{vac}_\mathrm{H}, \uparrow_\mathrm{H}, \downarrow_\mathrm{H}, \downarrow\uparrow_\mathrm{H}\}$ and $n_{j,\sigma} = d^\dagger_{j,\sigma} d_{,j\sigma}$. Hence, there is an additional factor of $(-1)^{n-1}$ that needs to be taken into account. With this, the equivalence Eq. (3.30) has been established.

A.2 FINITE SIZE EFFECTS IN THE PHASE DIAGRAM

One observes small apparent irregularities in the boundaries of the $S_\mathrm{tot} = 0$ phase at small $|J|$ in the quantum phase diagram in Fig. 3.7 (b). There are sawtooth-like dents between the ferromagnetic metal and the $S_\mathrm{tot} = 0$ phase and small regions with $S_\mathrm{tot} \neq 0$ within the $S_\mathrm{tot} = 0$ phase. Both of these are due to finite-size effects. The spin structure is depicted in Fig. 3.7 (b) as follows: The $S_\mathrm{tot} = 0$ phase is indicated by a tilted mesh, while the $S_\mathrm{tot} = N/2$ phase is indicated by a vertical/horizontal mesh. Boundaries of these phases are indicated by thick white lines. The ferromagnetic metal phase has $0 < S_\mathrm{tot} < N/2$ as indicated by the absence of a mesh.

Consider first the sawtooth-like dents between the ferromagnetic metal and the $S_\mathrm{tot} = 0$ phase. These may be understood in terms of the infinite-U Hubbard model, which our model maps to for $J = 0$ and $\tilde{\Delta} = 0$. The Bethe-ansatz solution for the infinite-U Hubbard model has a straightforward interpretation in terms of spin charge separation [211]. The eigenfunctions

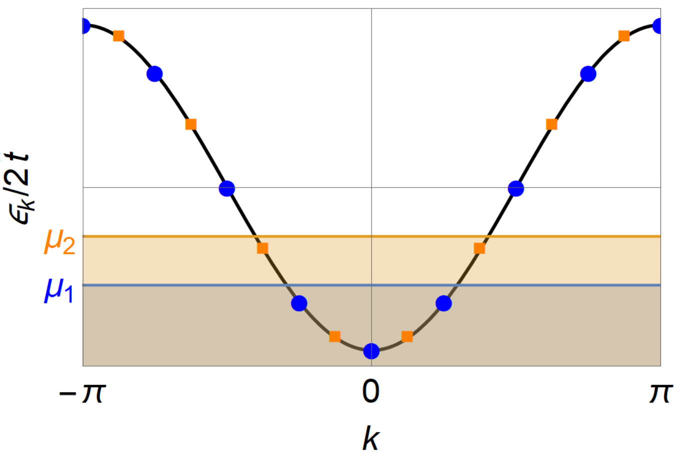

Figure A.1: Infinite-U Hubbard model. Depending on the spin state, the effective free fermion states obey periodic or antiperiodic boundary conditions. If the chemical potential is such that it is beneficial to host an even number of electrons (orange shading) antiperiodic boundary conditions are favorable. If an odd number of electrons is preferred, periodic boundary conditions are favorable. Figure from [I].

are comprised of an effectively spinless Slater determinant of plane-wave states with momenta $\{k_i\}$ and a spin wave function. The latter carries a spin-crystal momentum Λ, which depends on the spin configuration: $\Lambda = 0$ for $S_{\text{tot}} = Q/2$, and $\Lambda = \pi$ for $S_{\text{tot}} = 0$ (here, $Q = \sum_i n_i$ is the total charge). Then, the momenta satisfy the boundary condition

$$e^{iNk_i} = e^{i\Lambda} \tag{A.15}$$

and the total energy takes the free fermion form

$$E(\{n_i\}) = -2\tilde{t}\sum_i n_i \cos k_i. \tag{A.16}$$

Hence, for $S_{\text{tot}} = 0$, the allowed momenta correspond to antiperiodic boundary conditions, whereas for $S_{\text{tot}} = Q/2$, the allowed momenta correspond to periodic boundary conditions. To minimize the kinetic energy, an even number of fermions favors antiperiodic boundary conditions (for which $k = 0$ is not an allowed momentum) and hence a singlet-spin configuration, while an odd number favors periodic boundary conditions (where $k = 0$ is an allowed momentum) and hence a maximum-spin configuration. This is illustrated in Fig. A.1. For finite system sizes, a minimal RKKY coupling is needed to overcome this finite-size effect and one observes a shift of the phase boundary of the $S_{\text{tot}} = 0$ phase towards more negative J, whenever E_{YSR} is such that the system favors an even number of fermions. (Remember that E_{YSR} effectively acts as a chemical potential for the fermions.)

Importantly, this behavior is also observed in the absence of pairing and hence should not be confused with the competition between the ferromagnetic metal and singlet superconductor phases discussed in the main text. The latter is clearly not a finite-size feature. Pairing further stabilizes the $S_{\text{tot}} = 0$ phase for any number of fermions. This explains that the $S_{\text{tot}} = 0$ phase preempts the ferromagnetic metal phase at small, but negative J, regardless of the value of E_{YSR}.

Finally, consider the small islands of $S_{\text{tot}} \neq 0$ for $J > 0$, surrounded by the $S_{\text{tot}} = 0$ phase. In these regions, the ground state has an odd number of fermions and hence at least $S_{\text{tot}} = 1/2$. In thermodynamic limit this is irrelevant as the spin-density still vanishes.

APPENDIX B

B.1 DIMENSIONLESS VARIABLES

We will use lower-case letters to denote the dimensionless variables while dimensionful variables are denoted by upper-case letters (with the exception of time). To this end, we expand U about its minimum and maximum,

$$U(\varphi) = U(\varphi^{\min}) + \frac{1}{2} M\Omega_p^2(\varphi - \varphi^{\min})^2 + \ldots\,, \; M\Omega_p^2 = U''(\varphi^{\min}), \tag{B.1}$$

where the inertia M may be read off from the kinetic term $CV^2 = M\dot{\varphi}^2$, i.e. $M = \hbar^2 C/4e^2$. Thus, the frequency of the motion close to the minimum is given by the plasma frequency

$$\Omega_p = \sqrt{\frac{4e^2 U''(\varphi^{\min})}{\hbar^2 C}} = \Omega_p(I_b). \tag{B.2}$$

With this, we define dimensionless time

$$\tau = \Omega_p(0)t \tag{B.3}$$

in units of the inverse plasma frequency at zero bias, and accordingly the dimensionless phase velocity

$$v = \partial_\tau \varphi = \frac{2e}{\hbar\Omega_p(0)} V \equiv \frac{V}{V_u}. \tag{B.4}$$

It is then convenient to measure energies in units of $M\Omega_p^2(0) = U_s''(\varphi_s^{\min})$, such that the energy of the phase particle,

$$E = \frac{1}{2} CV^2 + U(\varphi), \tag{B.5}$$

becomes

$$\varepsilon = \frac{E}{M\Omega_p^2(0)} = \frac{1}{2} v^2 + u(\varphi),\; u(\varphi) = \frac{U(\varphi)}{M\Omega_p^2(0)}, \tag{B.6}$$

where the dimensionless potential $u(\varphi)$ satisfies the expansion

$$u(\varphi) = u(\varphi^{\min}) + \frac{1}{2}\omega_p^2(\varphi - \varphi^{\min})^2 + \ldots\,, \; \omega_p(i_b) = \frac{\Omega_p(i_b)}{\Omega_p(0)}. \tag{B.7}$$

Here, we also introduced dimensionless currents through

$$i_x = \frac{\hbar}{2eM\Omega_p^2(0)} I_x \equiv \frac{I_x}{I_u},\ x \in \{d, s, b, c,\ ...\}. \tag{B.8}$$

Note that it may be more convenient to measure microscopic energies in terms of $\hbar\Omega_p(0)$ or Δ and we will do that where appropriate. In these units, the extended RCSJ model becomes

$$\partial_\tau v + i_d(v) + i_s(\varphi) + \delta i = i_b,\ v = \dot{\varphi}. \tag{B.9}$$

where $i_d(v) = i_d(V = \hbar\Omega_p(0)v/2e)$, with noise correlator

$$\langle \delta i(\tau)\delta(i\tau')\rangle = k(v(\tau))\delta(\tau - \tau') \tag{B.10}$$

and

$$k(v) = 2\theta\frac{i_d(v)}{v},\ \theta = \frac{T}{M\Omega_p^2(0)}. \tag{B.11}$$

Finally, for a sinusoidal current-phase relation $I_s(\varphi) = (2eE_J/\hbar)\sin\varphi$, $M\Omega_p^2(0) = U_s''(\varphi_s^{\min}) = E_J$, and hence energies are measured in terms of the Josephson energy E_J, while currents are measured in terms of the critical current $I_c = 2eE_J/\hbar$.

B.2 PHENOMENOLOGICAL CURRENTS AND NUMERICAL SIMULATIONS

In order to illustrate the effect of nonreciprocities in the extended RCSJ model we use phenomenological current-phase relations and current-voltage characteristics. Specifically, we use the phenomenological current-phase relation

$$i_0(\varphi) = c_1[\sin(\varphi - \tilde{\varphi}) - c_2\sin(2\varphi)], \tag{B.12}$$

where c_1 is fixed such that $(\partial^2 u_0/\partial\varphi^2)|_{\varphi_0^{\min}} = (\partial i_0/\partial\varphi)|_{\varphi_0^{\min}} = 1$, see Fig. 4.2 (a). This type of current-phase relation arises, e.g., in Ref. [152]. For the dissipative current we use the current-voltage characteristic

$$i_d(v) = \frac{v}{Q}\left[1 + c_3\frac{v}{\delta v}\exp\left\{-\frac{1}{2}\left(\frac{v^2}{\delta v^2} - 1\right)\right\}\right], \tag{B.13}$$

see in Fig. 4.2 (b). The exponential factor in the asymmetric term serves to give Ohmic behavior at large voltages. As parameters we use $Q = 10$ and $\theta = 0.1$ throughout. If an asymmetric current-phase relation is needed we use $\tilde{\phi} = 0.6$ and $c_2/c_1 = 0.2$. Otherwise we use a sinusoidal current-phase relation. For the asymmetric current-voltage characteristic we use $c_3 = 0.3$, $\delta v = 5$. Otherwise we use an Ohmic current-phase relation.

All our Langevin simulations employ the Euler-Maruyama algorithm with time step $d\tau = 0.01$. In order to obtain hysteretic behaviour, we sweep the bias current from $i_b = -0.7$ to $i_b = 0.7$ [$i_b = -1.5$ to $i_b = 1.5$ in Fig. 4.1 and $i_b = -0.9$ to $i_b = 0.9$ in Fig. 4.3 (b)] and back at a rate $r = |\mathrm{d}i/\mathrm{d}\tau| = 10^{-5}$. The time-averaged voltage is calculated for 500 points in each direction. Switching and retrapping currents are extracted as maxima of the discrete derivative of the time-averaged voltage data. For the histograms we run 1000 sweeps.

B.3 RUNNING STATE TRAJECTORY

We want an expression for $(\varphi_{\text{run}}, v_{\text{run}})(t)$ in the underdamped limit $i_d(v)/v \ll 1$. As φ_{run} is monotonous in each period we can invert $t = t(\varphi)$ and consider $v_{\text{run}}(\varphi)$ instead. This is the periodic solution to

$$\frac{\mathrm{d}v_{\text{run}}}{\mathrm{d}\varphi} = -\frac{1}{v_{\text{run}}}[u'(\varphi) + i_d(v_{\text{run}})]. \tag{B.14}$$

From now on we drop the "run"-label. It is clear that a solution is of the order of v_0, where $i_b = i_d(v_0)$, with $v_0 = i_b[v_0/i_d(v_0)] \gg 1$. Defining

$$v = v_0(1+y),\ y \ll 1, \tag{B.15}$$

we expand to leading order in y. This gives

$$\frac{\mathrm{d}y}{\mathrm{d}\varphi} \simeq -\frac{1}{v_0^2}\{i_0(\varphi) + [i_d'(v_0)v_0 - i_0(x)]y\}. \tag{B.16}$$

Here we assumed that $i_d'(v_0)v_0 \sim 1$. From this, we expect $y = y_2 + y_4 + \ldots$, where $y_n \sim v_0^n$. Thus, altogether we have

$$v_{\mathrm{R}}(\varphi) \simeq v_0 - \frac{u_0(\varphi)}{v_0} + \frac{1}{v_0^3}\int^{\varphi} \mathrm{d}\tilde{\varphi}\, [i_d'(v_0)v_0 - i_0(\tilde{\varphi})]u_0(\tilde{\varphi}). \tag{B.17}$$

Note that the integration constants are chosen s.t. $\int_0^{2\pi} \mathrm{d}\varphi\, v_R = v_0$.

B.4 KELDYSH CONTOUR AND GENERATING FUNCTIONAL

Consider a system evolving under a time-dependent Hamiltonian $H(t)$. The density matrix satisfies the von-Neumann equation

$$\dot{\rho}(t) = -i[H(t), \rho(t)]. \tag{B.18}$$

This is formally solved by

$$\rho(t) = \mathcal{U}(t,-\infty)\rho(-\infty)[\mathcal{U}(t,-\infty)]^\dagger = \mathcal{U}(t,-\infty)\rho(-\infty)\mathcal{U}(-\infty,t), \tag{B.19}$$

in terms of the time evolution operator

$$\begin{aligned}\mathcal{U}(t,t') &= \lim_{N\to\infty} \exp\{-iH(t-\delta t)\delta t\}\ldots\exp\{-iH(t-N\delta t)\delta t\} && \text{(B.20a)}\\ &\equiv \mathrm{T}\exp\left\{-i\int_{t'}^{t}\mathrm{d}t'' H(t'')\right\}, && \text{(B.20b)}\end{aligned}$$

where $(t-t')/N = \delta t$ and T is the time-ordering symbol. The expectation value of a Schrödinger picture operator $\mathcal{O}(t)$ is obtained via

$$\begin{aligned}\langle\mathcal{O}(t)\rangle &= \mathrm{tr}[\mathcal{O}(t)\rho(t)] && \text{(B.21a)}\\ &= \mathrm{tr}[\mathcal{U}(-\infty,\infty)\mathcal{U}(\infty,t)\mathcal{O}(t)\mathcal{U}(t,-\infty)\rho(-\infty)] && \text{(B.21b)}\\ &= \mathrm{tr}[\mathcal{U}(-\infty,t)\mathcal{O}(t)\mathcal{U}(t,\infty)\mathcal{U}(\infty,-\infty)\rho(-\infty)]. && \text{(B.21c)}\end{aligned}$$

In the second and third line we extended the time evolution to $+\infty$ for later convenience. Time evolution from $-\infty$ to $+\infty$ and back is the Keldysh contour. Whether the operator $\mathcal{O}(t)$ is introduced during the forward or backward propagation does not matter. One may express $\langle\mathcal{O}(t)\rangle$ as functional derivative of an appropriate generating functional. To this end, we define the Keldysh evolution operator

$$\begin{aligned}\mathcal{U}_{\mathcal{C}}[\eta_+,\eta_-] &= \mathcal{U}_{\eta_-}(-\infty,\infty)\mathcal{U}_{\eta_+}(\infty,-\infty), && \text{(B.22a)}\\ \mathcal{U}_{\eta}(t,t') &= \mathrm{T}\exp\left\{-i\int_{t'}^{t}\mathrm{d}t''\,[H(t'')+\eta(t'')\mathcal{O}(t'')]\right\}, && \text{(B.22b)}\end{aligned}$$

including the source terms $\eta_\pm(t)$ on the forward and backward branch, respectively. The generating functional is

$$\mathcal{Z}[\eta_+,\eta_-] = \mathrm{tr}\,\{\mathcal{U}_{\mathcal{C}}[\eta_+,\eta_-]\rho(-\infty)\}. \tag{B.23}$$

The expectation value $\langle\mathcal{O}(t)\rangle$ can be obtained by differentiating with respect to $\eta_+(t)$ or $\eta_-(t)$,

$$\langle\mathcal{O}(t)\rangle = \pm i\frac{\delta}{\delta\eta_\pm(t)}\mathcal{Z}[\eta_+,\eta_-]\bigg|_{\eta=0}. \tag{B.24}$$

Differentiating twice gives the time-ordered, anti-time ordered, lesser and greater correlation functions,

$$\langle \mathrm{T}\mathcal{O}(t_1)\mathcal{O}(t_2)\rangle = i^2 \frac{\delta^2}{\delta\eta_+(t_1)\delta\eta_+(t_2)} \mathcal{Z}[\eta_+,\eta_-]\bigg|_{\eta=0}, \tag{B.25a}$$

$$\left\langle \tilde{\mathrm{T}}\mathcal{O}(t_1)\mathcal{O}(t_2)\right\rangle = i^2 \frac{\delta^2}{\delta\eta_-(t_1)\delta\eta_-(t_2)} \mathcal{Z}[\eta_+,\eta_-]\bigg|_{\eta=0}, \tag{B.25b}$$

$$-\langle \mathcal{O}(t_1)\mathcal{O}(t_2)\rangle = i^2 \frac{\delta^2}{\delta\eta_-(t_1)\delta\eta_+(t_2)} \mathcal{Z}[\eta_+,\eta_-]\bigg|_{\eta=0}, \tag{B.25c}$$

$$-\langle \mathcal{O}(t_2)\mathcal{O}(t_1)\rangle = i^2 \frac{\delta^2}{\delta\eta_+(t_1)\delta\eta_-(t_2)} \mathcal{Z}[\eta_+,\eta_-]\bigg|_{\eta=0}. \tag{B.25d}$$

It will prove useful to introduced the symmetrized and anti-symmetrized combinations $\eta_{\mathrm{cl}} = (\eta_+ + \eta_-)/2$ and $\eta_{\mathrm{q}} = \eta_+ - \eta_-$. Differentiation with respect to η_{q} twice gives the symmetrized correlation function $\langle \mathcal{O}(t_1)\mathcal{O}(t_2) + \mathcal{O}(t_2)\mathcal{O}(t_1)\rangle/2$. This is the Keldysh correlation function. Differentiation with respect to η_{cl} twice gives 0. The crossed combinations give the retarded and advanced correlation functions. $\mathcal{Z}$ is the moment generating functional. The associated cumulants may be obtained by instead taking derivatives with respect to $\ln \mathcal{Z}$.

B.5 GRASSMANN INTEGRALS FOR SPIN-ORBIT COUPLED SUPERCONDUCTORS

Complex fermionic field theories require the evaluation of Grassmann integrals such as

$$\int \prod_{\alpha=1}^{N} \mathrm{d}\overline{\psi}_\alpha \mathrm{d}\psi_\alpha \, \exp\{\overline{\psi}A\psi\} = \det A. \tag{B.26}$$

Note that the Grassmann vector ψ and $\overline{\psi}$ are independently integrated over. Consider now a fermionic theory in the four-dimensional Nambu representation,

$$\mathcal{Z} = \int \prod_{\alpha=1}^{N} \mathrm{d}\rho_\alpha \mathrm{d}\psi_\alpha \, \exp\left\{\frac{1}{2}\left[\rho A\psi - \psi A^T\rho + \rho D\rho + \psi D^\dagger\psi\right]\right\}. \tag{B.27}$$

Here, we renamed $\overline{\psi} \to \rho$ for clarity. Due to fermionic statistics, D is antisymmetric. Expressed in terms of "real" or Majorana Grassmann vector $\phi = (\rho, \psi)$, this gives the standard result

$$\mathcal{Z} = \int \prod_{a=1}^{2N} \mathrm{d}\phi_a \, \exp\left\{\frac{1}{2}\phi M\phi\right\} = \mathrm{Pf}\, M, \quad M = \begin{pmatrix} D & A \\ -A^T & D^\dagger \end{pmatrix} = -M^T. \tag{B.28}$$

The Pfaffian of the matrix M is related to its determinant through $[\mathrm{Pf}\,M]^2 = \det M$. We may thus reexponentiate

$$\mathrm{Pf}\,M = \exp\left\{\frac{1}{2} 2 \ln \mathrm{Pf}\,M,\right\} = \exp\left\{\frac{1}{2} \ln \det M \pm i\pi\right\} = \pm \exp\left\{\frac{1}{2} \ln \det M\right\}. \quad \text{(B.29)}$$

The BCS Green function is related to M via $M = iu^\dagger \mathcal{G}^{-1} u \tau_x$, where $u = \mathrm{diag}(1, i\sigma_y)$ in particle-hole space. Thus, with $\det AB = \det A \det B$ it is

$$\mathcal{Z} \propto \exp\left\{\frac{1}{2} \operatorname{Tr} \ln[i\mathcal{G}^{-1}]\right\}. \quad \text{(B.30)}$$

Contour-ordered correlation functions follow from

$$\langle \phi_a \phi_b \rangle = \frac{1}{\mathcal{Z}} \int \prod_{c=1}^{2N} \mathrm{d}\phi_c \, \phi_a \phi_b \exp\left\{\frac{1}{2} \phi M \phi\right\} = -[M^{-1}]_{ab}. \quad \text{(B.31)}$$

This produces the expected result

$$\mathcal{G} = -iu\tau_x \langle \phi \otimes \phi \rangle u^\dagger = -i\big\langle \mathrm{T}_{\mathcal{C}} \Psi \otimes \Psi^\dagger \big\rangle. \quad \text{(B.32)}$$

B.6 SOLVING THE DYSON EQUATION

Here, we show how the Dyson equation for the diagonal Green function, Eq. (4.167), can be solved at all orders within the adiabatic approximation. To this end, we expand in Fourier components with respect to the phase difference,

$$\mathcal{G}^{\mathrm{d}}(\varphi, V; \omega) = \sum_m \mathcal{G}^{\mathrm{d}}_m(V; \omega) e^{im\varphi}, \; \mathcal{G}^{\mathrm{d}}_m(V; \omega) = \int \frac{\mathrm{d}\varphi}{2\pi} \mathcal{G}^{\mathrm{d}}(\varphi, V; \omega) e^{-im\varphi}. \quad \text{(B.33)}$$

With this, the Dyson equation becomes (suppressing the voltage arguments, and using the Moyal product to expand the convolutions)

$$\mathcal{G}^{\mathrm{d}}_m(\omega) = \mathcal{G}_0(\omega)\delta_{m,0} + \mathcal{G}_0(\omega - meV)\lambda_z \sum_n \Sigma_{m-n}(\omega - neV)\lambda_z \mathcal{G}^{\mathrm{d}}_n(\omega + (m-n)eV). \quad \text{(B.34)}$$

Do not confuse $\mathcal{G}_0$ (bare Green function) with $\mathcal{G}^{\mathrm{d}}_{m=0}$ (zeroth Fourier component of full Green function). Similar expressions hold for the off-diagonal Green function and hence for the full

Green function. It is useful to shift $\omega \to \omega - meV$. Defining $\mathcal{G}^{\mathrm{d}}_{m}(\omega - meV) \equiv v_m(\omega)$, the Dyson equation may be written as a matrix equation

$$v_m(\omega) = \mathcal{G}_0(\omega)\delta_{m,0} + \sum_n M_{mn}(\omega)v_n(\omega), \tag{B.35a}$$

$$M_{mn}(\omega) = \mathcal{G}_0(\omega - 2meV)\lambda_z\Sigma_{m-n}(\omega - (n+m)eV)\lambda_z. \tag{B.35b}$$

This is solved by $v = (1-M)^{-1}(..., 0, \mathcal{G}_0, 0, ...)^T$, which can be evaluated numerically for given ω and V.

B.7 BCS SPECTRAL FUNCTION

The retarded BCS Green function is defined as

$$\mathcal{G}^r_{\alpha\beta}(t,t') = -i\Big\langle\Big\{\Psi_\alpha(t), \Psi^\dagger_\beta(t')\Big\}\Big\rangle\Theta(t-t'). \tag{B.36}$$

Its Lehmann representation defines the BCS spectral matrix,

$$\begin{aligned}\mathcal{A}_{\alpha\beta}(\omega) &= \frac{i}{2\pi}\{\mathcal{G}^r_{\alpha\beta}(\omega) - [\mathcal{G}^r_{\alpha\beta}(\omega)]^\dagger\} && \text{(B.37a)}\\ &= \frac{1}{Z}\sum_{nn'} M_{nn'}\langle n'|\Psi_\alpha|n\rangle\langle n|\Psi^\dagger_\beta|n'\rangle\delta(\omega - E_{nn'}). && \text{(B.37b)}\end{aligned}$$

Here, $M_{nn'} = e^{-E_n/T} + e^{-E_{n'}/T}$, $|n\rangle$ is a many-body eigenstate of the BCS Hamiltonian associated with energy E_n, and $E_{nn'} = E_n - E_{n'}$. Consider its particle-hole diagonal blocks. In the two-dimensional Nambu representation $\Psi = [\psi_\uparrow, \psi^\dagger_\downarrow]$, the diagonal entries of the BCS spectral matrix satisfies

$$\mathcal{A}^e_{ab}(\omega) = \frac{1}{Z}\sum_{nn'} M_{nn'}\langle n'|\psi_{a,\uparrow}|n\rangle\langle n|\psi^\dagger_{b,\uparrow}|n'\rangle\delta(\omega - E_{nn'}) \equiv A^\uparrow_{ab}(\omega), \tag{B.38a}$$

$$\mathcal{A}^h_{ba}(-\omega) = \frac{1}{Z}\sum_{nn'} M_{nn'}\langle n'|\psi_{a,\downarrow}|n\rangle\langle n|\psi^\dagger_{b,\downarrow}|n'\rangle\delta(\omega - E_{nn'}) \equiv A^\uparrow_{ab}(\omega), \tag{B.38b}$$

where $A^\sigma_{ab}(\omega)$ is the normal spin resolved spectral matrix. Relevant for tunneling from an unstructured lead are the diagonal elements of the spectral matrix in the position basis, $A^\sigma(x;\omega)$, where x is the position of the tunneling contact. $A^\sigma(x;\omega)$ is referred to as the (spin-resolved) spectral function. In the spin indiscriminate case, tunneling instead probes

$$A(x;\omega) = \sum_\sigma A^\sigma(x;\omega) = \mathcal{A}^e(x;\omega) + \mathcal{A}^h(x;-\omega) = \mathrm{tr}_{\text{p-h}}\,\mathcal{A}(x;\omega\tau_z). \tag{B.39}$$

	V_{offset} [mV]	I_{offset} [nA]	δV [mV]	A [nA]	B [nA]	C [nA/mV]	D [nA/mV^2]	E [nA/mV^3]
Pb	0.0187	0.0292	0.135	16.4	-20.6	7.00	0.121	-21.8
Cr	0.0210	0.00169	0.140	5.96	-7.71	4.01	2.47	-1.01
Mn	0.0129	-0.123	0.138	8.47	-10.7	3.66	-2.52	15.1

Table B.1: Quasiparticle current fitting parameters. Fitting parameters for extracting the quasiparticle current $I_{\text{qp}}(V)$ from the measured current $I_{\text{meas}}(V)$ by subtracting the Josephson peak due to incoherent Cooper-pair tunneling, see Eq. (B.43) and corresponding text.

See Eq. (2.20) for the zero temperature expression. Note that the two-dimensional Nambu representation does not capture spin flip correlations such as $A^{\uparrow\downarrow}$. If such processes play a role (i.e. if S^z_{tot} is not conserved), one has to resort to the four-dimensional Nambu representation $\Psi = [\psi_\uparrow, \psi_\downarrow, \psi_\downarrow^\dagger, -\psi_\uparrow^\dagger]$, with entries denoted by $i \in \{1,2,3,4\}$. The particle-hole diagonal part of the BCS spectral matrix satisfies now

$$\mathcal{A}^{11}_{ab}(\omega) = \mathcal{A}^{44}_{ba}(-\omega) = A^{\uparrow}_{ab}(\omega), \tag{B.40a}$$

$$\mathcal{A}^{22}_{ab}(\omega) = \mathcal{A}^{33}_{ba}(-\omega) = A^{\downarrow}_{ab}(\omega), \tag{B.40b}$$

as well as

$$\mathcal{A}^{12}_{ab}(\omega) = -\,\mathcal{A}^{34}_{ba}(-\omega) = A^{\uparrow\downarrow}_{ab}(\omega), \tag{B.40c}$$

$$\mathcal{A}^{21}_{ab}(\omega) = -\,\mathcal{A}^{43}_{ba}(-\omega) = A^{\downarrow\uparrow}_{ab}(\omega). \tag{B.40d}$$

The spin-indiscriminate spectral function therefore may be expressed as

$$A(x;\omega) = \frac{1}{2}\,\mathrm{tr}_i\,\mathcal{A}(x;\omega\tau_z) = \frac{1}{2}\,\mathrm{tr}_{\text{p-h,spin}}\,\mathcal{A}(x;\omega\tau_z). \tag{B.41}$$

Similarly, traces over the spin indices of the BCS spectral function may be expressed in terms of the physical spectral function via

$$\frac{1}{2}\,\mathrm{tr}_{\text{spin}}\left[\mathcal{A}^e_L(x;\omega_1)\mathcal{A}^e_R(x;\omega_2) + \mathcal{A}^h_L(x;-\omega_1)\mathcal{A}^h_R(x;-\omega_2)\right] = \sum_{\sigma\sigma'}\left[A^{\sigma\sigma'}_L(x;\omega_1)A^{\sigma'\sigma}_R(x;\omega_2)\right]. \tag{B.42}$$

B.8 Extraction of quasiparticle current

We extract the quasiparticle contribution to the dissipative current $I_{\text{qp}}(V)$ from voltage-biased measurements of Pb, Cr, and Mn junctions at the normal-state conductance of $G_{\text{N}} = 50\ \mu$S. In addition to the quasiparticle current, these traces include a Josephson peak originating from incoherent Cooper-pair tunneling. We remove the Josephson contribution $I_{\mathrm{J}}(V)$ by fitting to the phenomenological expressions [299]

$$I_{\text{meas}}(V) = I_{\mathrm{J}}(V + V_{\text{offset}}) + I_{\text{qp},0}(V + V_{\text{offset}}) + I_{\text{offset}}, \tag{B.43a}$$

$$I_{\mathrm{J}}(V) = A\frac{V\delta V}{V^2 + \delta V^2} + B\frac{V^3\delta V}{(V^2 + \delta V^2)^2}, \tag{B.43b}$$

$$I_{\text{qp},0}(V) = CV + DV^2 + EV^3, \tag{B.43c}$$

over a voltage range $e|V| \ll \Delta$, which contains the Josephson peak. (We choose $e|V| < 0.32$ meV.) We account also for offsets in the measured voltage and current through the parameters V_{offset} and I_{offset}. The fit parameters are collected in Table B.1. We then subtract the Josephson contribution as well as the offsets from the measured data to isolate the quasiparticle contribution. To reduce the fluctuations at small V associated with the Josephson contribution, a Gaussian filter (width $\sigma = 5$ datapoints $\simeq 0.55$ mV) is applied to the isolated quasiparticle current data. Finally, $I_{\text{qp}}(V)$ is obtained by interpolation using a linear splining procedure, enforcing $I_{\text{qp}}(0) = 0$. The fitting and quasiparticle current extraction procedure is summarized in Fig. B.1.

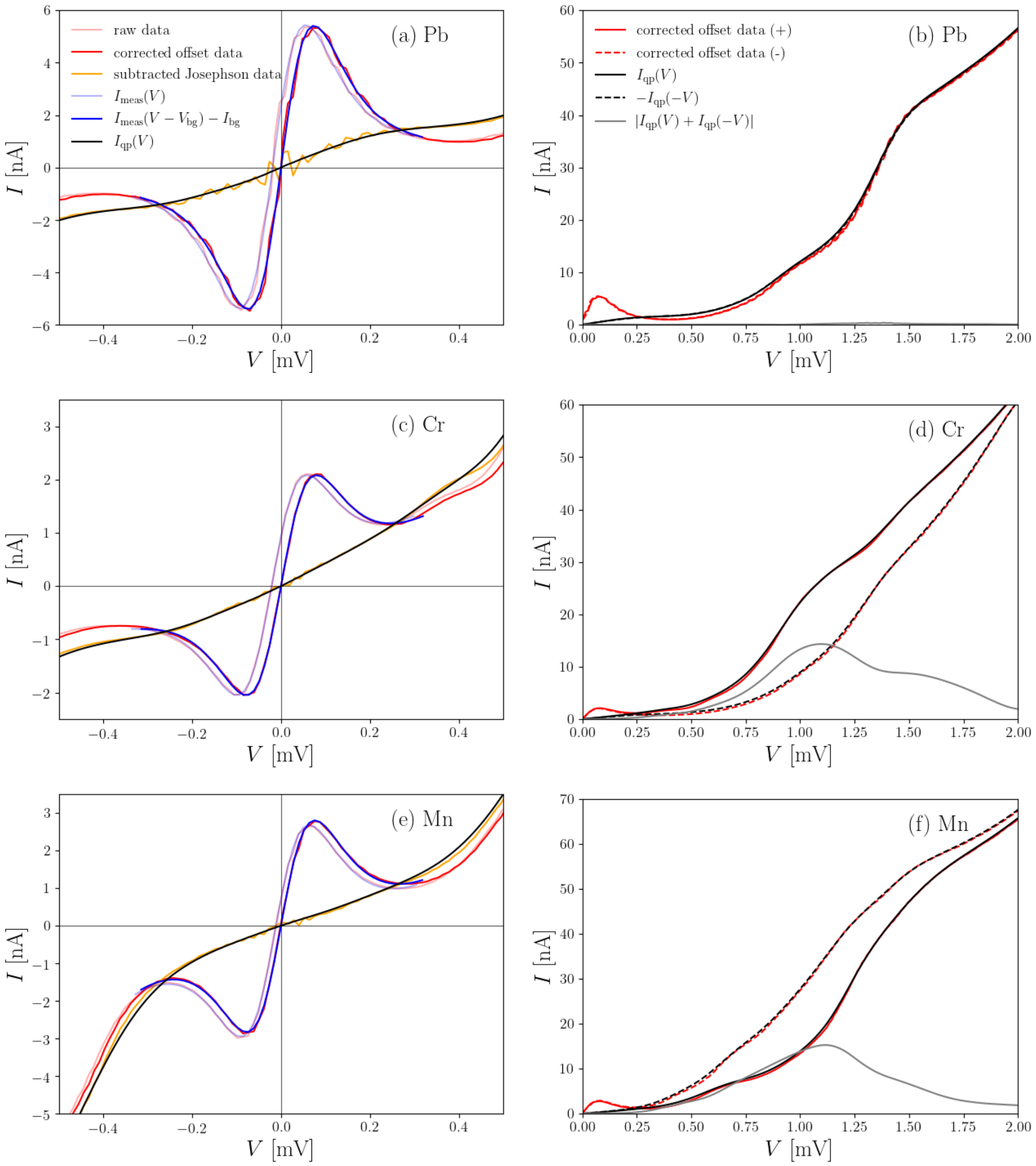

Figure B.1: Extraction of quasiparticle current. (a),(c),(e) Measured I-V traces before (light red curve) and after (red curve) accounting for voltage and current offsets, as well as $I - V$ trace obtained by correcting offsets and subtracting the Josephson contribution (orange curve) for (a) Pb, (c) Cr and (e) Mn, respectively. Also shown are the fit curves $I_{\mathrm{meas}}(V)$ before (light blue curve) and after accounting (blue curve) for voltage and current offsets, as well as the final extracted quasiparticle current entering the theoretical simulations (black curve). (b),(d),(f) Measured $|I| - |V|$ after accounting for voltage and current offsets (red curves) as well as extracted quasiparticle current (black curves) corresponding to positive (solid curves) and negative (dashed curves) bias voltages in an extended voltage range for (b) Pb, (d) Cr and (f) Mn, respectively. The asymmetric part of the quasi-particle current $\left|I_{\mathrm{qp}}(V) + I_{\mathrm{qp}}(-V)\right|$ (grey curve) is roughly zero for Pb. For Cr and Mn the asymmetric part is clearly nonvanishing.

APPENDIX C

C.1 MAJORANA QUBITS AND QUANTUM DOT – NOTATION AND DEFINITIONS

In this appendix, we summarize details of our definitions and conventions for the quantum states of the coupled system of Majorana qubit and quantum dot.

C.1.1 CHOICE OF BASIS STATES

A set of $2m$ Majorana bound states labeled by $i = 1, \dots, 2m$ is described by hermitian fermionic operators $\hat{\gamma}_i = \hat{\gamma}_i^\dagger$ which satisfy $\{\hat{\gamma}_i, \hat{\gamma}_j\} = 2\delta_{ij}$. The associated 2^m-dimensional Hilbert space is spanned by the Fock occupations $\hat{n}_{ij} = \hat{f}_{ij}^\dagger \hat{f}_{ij}$ of complex fermions $\hat{f}_{ij} = (\hat{\gamma}_i + i\hat{\gamma}_j)/2$.

The total fermion parity of these basis states is given by the operator

$$\hat{P} = (-i)^m \prod_{j=1}^{m} \hat{\gamma}_{2j-1}\hat{\gamma}_{2j} \tag{C.1}$$

As quantum superpositions exist only for states of the same fermion parity, a qubit requires at least four Majorana bound states. States with even and odd fermion parity can be split energetically by a charging energy, Eq. (5.1), as they have different charge $N = 2N_C + N_M$, where N_C is the number of Cooper pairs and N_M the charge in the Majorana sector. For definiteness, we choose the ground (excited) states of the Majorana qubit to have $N = 0$ ($N = -1$). The Hilbert space is spanned by $\{|N, n_{12}, n_{34}\rangle\}$. Due to the parity constraint

$$P = (-1)^N = (-1)^{n_{12}+n_{34}}, \tag{C.2}$$

it is sufficient to specify the state as $|N, n_{12}\rangle$.

In the main text, we choose a slightly different labeling of the basis states. First, instead of using the label n_{12}, we specify n_{12} via the eigenvalue $z \in \{1, -1\} \equiv \{\uparrow, \downarrow\}$ of the Pauli-Z operator

$$\hat{Z} = -i\hat{\gamma}_1\hat{\gamma}_2 = 1 - 2\hat{n}_{12} = (-1)^{\hat{n}_{12}}.$$

Second, the Majorana qubit only exchanges charge with the quantum dot. We always initialize the system to have even total parity with Majorana-qubit charge $N = 0$ and quantum dot charge $n = 0$, so that these charges are related as $n = -N$ in general. We then label the basis states by the quantum dot charge n and the eigenvalue z of the Pauli-Z operator of the Majorana qubit,

$$|z, n\rangle \equiv \left| N = -n, n_{12} = \frac{1-z}{2}, n_{34} = \frac{1-z(-1)^n}{2} \right\rangle. \tag{C.3}$$

With this definition, the constraint (C.2) is automatically satisfied. Furthermore, with our choices, all participating states have even total fermion parity $P_{\text{tot}} = P(-1)^n$.

The four basis states $|z, n\rangle$ differ in the local parity $\hat{\pi} = \hat{Z}(-1)^{\hat{n}}$. We choose a basis $\{|\uparrow, 0\rangle$, $|\downarrow, 1\rangle$, $|\downarrow, 0\rangle$, $|\uparrow, 1\rangle\}$, where the first (last) two states have local parity $\pi = +1$ ($\pi = -1$). We can then define Pauli matrices acting in a subspace of fixed local parity,

$$\sigma_z^\pi = |\pi, 0\rangle\langle\pi, 0| - |-\pi, 1\rangle\langle-\pi, 1|, \tag{C.4a}$$

$$\sigma_x^\pi = |\pi, 0\rangle\langle-\pi, 1| + |-\pi, 1\rangle\langle\pi, 0|, \tag{C.4b}$$

$$\sigma_y^\pi = i\sigma_x^\pi\sigma_z^\pi. \tag{C.4c}$$

In the main text, we drop the π label whenever this does not lead to confusion. In terms of these Pauli matrices, the quantum dot charge is

$$n = \frac{1}{2}(\sigma_0 - \sigma_z). \tag{C.5}$$

C.1.2 COUPLED MAJORANA QUBIT-QUANTUM DOT SYSTEM

In addition, we define a set of Pauli matrices using the eigenbasis of the Hamiltonian in Eq. (5.7) which also act within the subspaces with fixed π,

$$\tau_z^\pi = |g_\pi\rangle\langle g_\pi| - |e_\pi\rangle\langle e_\pi|, \tag{C.6a}$$

$$\tau_x^\pi = |e_\pi\rangle\langle g_\pi| + |g_\pi\rangle\langle e_\pi| = \tau_+^\pi + \tau_-^\pi, \tag{C.6b}$$

$$\tau_y^\pi = i\tau_x^\pi\tau_z^\pi. \tag{C.6c}$$

Here, the ground states are given by Eq. (5.11), while the excited states are

$$|e_+\rangle = \cos\frac{\theta_+}{2}|\uparrow, 0\rangle + \sin\frac{\theta_+}{2}e^{i\phi_+}|\downarrow, 1\rangle, \tag{C.7a}$$

$$|e_-\rangle = \cos\frac{\theta_-}{2}|\downarrow, 0\rangle + \sin\frac{\theta_-}{2}e^{i\phi_-}|\uparrow, 1\rangle. \tag{C.7b}$$

In terms of these Pauli matrices, $h_\pi = \Omega_\pi \tau_z^\pi$ and

$$\begin{aligned}\hat{n} &= \sum_{z=\pm 1} |z,1\rangle\langle z,1| &\text{(C.8a)}\\ &= \sum_{\pi=\pm 1} \Big[\cos^2\frac{\theta_\pi}{2}|g_\pi\rangle\langle g_\pi| + \sin^2\frac{\theta_\pi}{2}|e_\pi\rangle\langle e_\pi| \\ &\qquad - 2\cos\frac{\theta_\pi}{2}\sin\frac{\theta_\pi}{2}(|e_\pi\rangle\langle g_\pi| + |g_\pi\rangle\langle e_\pi|)\Big] &\text{(C.8b)}\\ &= \frac{1}{2}\sum_{\pi=\pm 1} [\tau_0^\pi + \cos\theta_\pi \tau_z^\pi - \sin\theta_\pi \tau_x^\pi]. &\text{(C.8c)}\end{aligned}$$

In the Heisenberg picture, the quantum dot charge $\hat{n}(t) = \exp(i\hat{H}t)\,\hat{n}\,\exp(-i\hat{H}t)$ becomes

$$\hat{n}(t) = \sum_{\pi=\pm 1}\Big[\frac{\tau_0^\pi + \cos\theta_\pi \tau_z^\pi}{2} - \frac{\sin\theta_\pi}{2}\big(e^{2i\Omega_\pi t}\tau_+^\pi + e^{-2i\Omega_\pi t}\tau_-^\pi\big)\Big]. \tag{C.9}$$

We find it convenient to define the time-independent part

$$\hat{c} = \sum_{\pi=\pm 1}\frac{\tau_0^\pi + \cos\theta_\pi \tau_z^\pi}{2}. \tag{C.10}$$

Finally, since we are performing our simulations in the charge basis, we need $\tau_\pm^\pi$ in the charge basis. Within a given π-block, it takes the form

$$\tau_-^\pi = \frac{1}{2}\begin{pmatrix} \sin\theta_\pi & (1-\cos\theta_\pi)e^{-i\phi_\pi} \\ (-1-\cos\theta_\pi)e^{i\phi_\pi} & -\sin\theta_\pi, \end{pmatrix} \tag{C.11}$$

with τ_+^π given by hermitian conjugation.

C.2 STROBOSCOPIC PROTOCOL FOR $\hat{Z}$ READOUT

C.2.1 MEASUREMENT PROTOCOL

Section 5.1 discusses projective measurements of $\hat{Z}$ based on a single projective measurement of $\hat{n}$. In addition to assuming instantaneous charge readout, this requires fine-tuned parameters. In subsequent sections of the main text, we relax both of these conditions. Here, we briefly discuss schemes which assume instantaneous charge readout, but allow for general system parameters t_i and ε. For general parameters, the measurement outcome for the charge of the quantum dot is no longer perfectly correlated with eigenstates of $\hat{Z}$. However, unless $\mathrm{Im}\{t_1 t_2^*\} = 0$, the charge measurement still provides partial information on the qubit state.

Once coupled, quantum dot and Majorana qubit evolve unitarily from initial state $|\psi\rangle = (\alpha|\uparrow\rangle + \beta|\downarrow\rangle)|0\rangle$ into

$$\hat{\mathcal{U}}|\psi\rangle = \alpha(c_{\uparrow,0}|\uparrow,0\rangle + c_{\downarrow,1}|\downarrow,1\rangle) + \beta(c_{\downarrow,0}|\downarrow,0\rangle + c_{\uparrow,1}|\uparrow,1\rangle). \tag{C.12}$$

The unitary time evolution $\hat{\mathcal{U}}$, entangling Majorana qubit and quantum dot, satisfies $[\hat{\mathcal{U}},\hat{\pi}] = 0$, but otherwise depends on details of the protocol. If the charge readout can be effected instantaneously (on the time scale of the hybridization between dot and qubit), or more realistically, qubit and quantum dot are rapidly decoupled following the unitary evolution, the quantum dot charge becomes a good quantum number during charge readout. Then, the measurement leaves the system in the state

$$|\psi_0'\rangle = \frac{1}{\sqrt{p_0}}(\alpha c_{\uparrow,0}|\uparrow\rangle + \beta c_{\downarrow,0}|\downarrow\rangle)|0\rangle, \tag{C.13a}$$

or

$$|\psi_1'\rangle = \frac{1}{\sqrt{p_1}}(\alpha c_{\downarrow,1}|\downarrow\rangle + \beta c_{\uparrow,1}|\uparrow\rangle)|1\rangle, \tag{C.13b}$$

with probabilities $p_0 = |\alpha c_{\uparrow,0}|^2 + |\beta c_{\downarrow,0}|^2$ and $p_1 = 1 - p_0$, respectively. The partial information on $\hat{Z}$ obtained from the measurement transfers weight between qubit states. This can be interpreted in terms of Bayesian inference [250],

$$p(\uparrow|n) = \frac{p(n|\uparrow)}{p_n}p(\uparrow),\ p(\downarrow|n) = \frac{p(n|\downarrow)}{p_n}p(\downarrow), \tag{C.14}$$

where we identify the prior probabilities of the qubit states with $p(\uparrow) = |\alpha|^2$ and $p(\downarrow) = |\beta|^2$ and $p(n|Z) = |c_{Z,n}|^2$ with the conditional probabilities to observe measurement outcome n.

Repeating this protocol results in a random walk in the space of qubit and quantum dot states. We find that the random walk has two distinct steady states corresponding to the $\hat{\pi}$ eigensectors. This becomes equivalent to the eigenstates of $\hat{Z}$, if for simplicity, we reset the qubit-quantum dot system in between steps, $|\downarrow,1\rangle \to |\uparrow,0\rangle$ and $|\uparrow,1\rangle \to |\downarrow,0\rangle$ after every charge readout that gave $n = 1$ (for a scheme implementing this reset, see App. C.2.2 below). With this reset, we effectively obtain a random walk in the space of qubit states, which can be described by the Kraus operators

$$\hat{M}_0 = \begin{pmatrix} c_{\uparrow,0} & 0 \\ 0 & c_{\downarrow,0} \end{pmatrix},\ \hat{M}_1 = \hat{X}\begin{pmatrix} 0 & c_{\uparrow,1} \\ c_{\downarrow,1} & 0 \end{pmatrix} \tag{C.15}$$

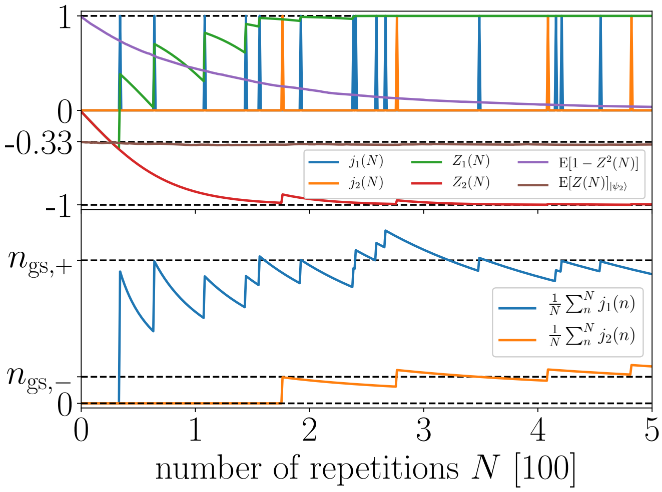

Figure C.1: Evolution under the stroboscopic measurement protocol for adiabatic coupling with initial state $|\psi\rangle = (|\uparrow\rangle + |\downarrow\rangle)|0\rangle/\sqrt{2}$, as function of time (number of iterations). Sample trajectories of $Z = \langle\hat{Z}\rangle$ (green and red traces) demonstrate the evolution towards the fixed points. The evolution tends slowly towards the $\downarrow$ state (corresponding to likely outcomes), interrupted by jumps (unlikely outcomes) that provide much more information, favoring the $\uparrow$ state and causing greater backaction. The measurement signal for two trajectories is shown by the blue and orange traces. Jumps in the trajectory are correlated with $n = 1$ outcomes. The correct statistics of the measurement is illustrated by the constant ensemble average of $Z(N)$ (brown trace), which we computed for the initial state $|\psi_2\rangle = (|\uparrow\rangle + \sqrt{2}|\downarrow\rangle)|0\rangle/\sqrt{3}$. Projection onto the fixed points is indicated by the decay of $\mathbb{E}[1 - Z^2(N)]$ (purple trace) to zero. Ensemble averages are over 10^4 trajectories. Parameters: $t_2 = t_1 e^{i\pi/4}$, $\varepsilon = 10t_1$. Figure from [VII].

acting on a qubit state $|\phi\rangle$, so that the qubit state $|\phi'_n\rangle$ conditioned on the measurement outcome n is given by

$$|\phi'_n\rangle = \frac{\hat{M}_n|\phi\rangle}{\sqrt{p_n}}, \tag{C.16}$$

with $p_n = \langle\phi|\hat{M}_n^\dagger\hat{M}_n|\phi\rangle$. The Pauli $\hat{X}$ in the definition of $\hat{M}_1$ makes the reset of the qubit-quantum dot system explicit.

Figure C.1 shows numerical simulations of this protocol for the adiabatic coupling scheme discussed in Sec. 5.1.2, so that $\hat{\mathcal{U}}$ involves the coefficients $c_{Z,n}$ of the state given in Eq. (5.10). The trajectories reach the fixed points $Z = \pm 1$ with the correct probabilities. Moreover, the measurement outcome can be extracted from the sequence of n outcomes of a single trajectory by noting that n averages to the ground-state charge corresponding to the respective fixed point. Thus, this protocol implements a projective measurement of $\hat{Z}$.

We conclude this section with a number of comments. First, resetting the quantum dot charge is not essential. Without intermediate resetting, the protocol projects $\hat{\pi} = \hat{Z}(-1)^{\hat{n}}$ (see discussion in the main text) and one may reset once the outcome of the measurement is determined. However, in this case, the average charge no longer equals the ground state charge and a more involved signal analysis (for instance using the Bayes theorem) is required. Second, qubit

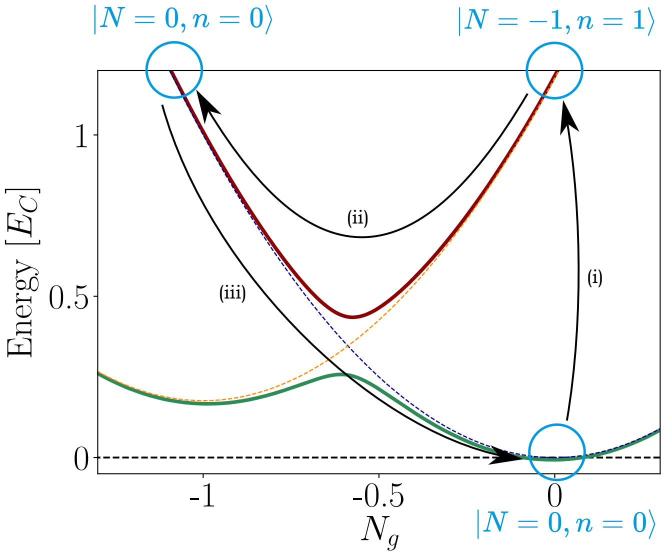

Figure C.2: Spectrum of the quantum dot-Majorana qubit system as a function of the qubit gate charge N_g. The dashed lines for $N = -1$ (orange) and $N = 0$ (blue) correspond to the energies of the system without coupling to the quantum dot. (The vertical shift of the orange curve reflects the energy of the quantum dot.) The full lines (red, green) refer to the coupled system and exhibit an avoided crossing. Initially, the Majorana qubit gate is tuned to $N_g = 0$ and the system is in the charge ground state $|\psi\rangle \propto |N = 0, n = 0\rangle$. (i) A measurement outcome of $n = 1$ transfers the system into the excited charge state $|\psi'\rangle \propto |N = -1, n = 1\rangle$. (ii) The charge state is reset by adiabatically changing $N_g \to -1$. The system state is now $\propto |N = 0, n = 0\rangle$ again. (iii) Suddenly set $N_g \to 0$, so that the system state does not change and the initial situation is restored. Alternatively, one may also decouple the quantum dot and slide down the dashed green curve adiabatically. Figure from [VII].

and quantum dot can also be entangled through evolution with the Hamiltonian (5.7). In this case, decoupling qubit and quantum dot in between steps is necessary only if charge readout is slower than tunneling. The resulting evolution is closely related to the continuous evolution discussed in the main text, which arises naturally from sequences of repeated measurements when relaxing more and more assumptions on the strengths of various couplings.

C.2.2 Resetting the qubit-quantum dot system

When the charge measurement yields $n = 1$, the Majorana qubit is in the excited charge state $N = -1$. To avoid uncontrolled charging events, the electron should be swiftly returned from quantum dot to Majorana qubit.

This can be achieved by adiabatic variations of ε and t_i, transforming

$$|\psi\rangle = (\alpha|{\downarrow}\rangle + \beta|{\uparrow}\rangle)|1\rangle \tag{C.17a}$$

into

$$|\psi_{\text{reset}}\rangle = (\alpha|{\uparrow}\rangle + \beta|{\downarrow}\rangle)|0\rangle \tag{C.17b}$$

for general α and β. We focus on the subspace $\pi = +1$ for definiteness.

Without fine tuning of the dynamical phase, $|{\downarrow}, 1\rangle$ can only be transformed into $|{\uparrow}, 0\rangle$ if it is an eigenstate of the initial Hamiltonian. Consider an initial Hamiltonian h_+ given by $\theta_+ = \theta_0$ and $\phi_+ = \phi_0$, and expand the initial state in eigenstates of h_+,

$$|{\downarrow}, 1\rangle = e^{-i\phi_0}\left(\sin\frac{\theta_0}{2}|e_+\rangle_0 - \cos\frac{\theta_0}{2}|g_+\rangle_0\right). \tag{C.18}$$

Adiabatically changing $\theta_0, \phi_0 \to \theta_1, \phi_1$, the eigenstates evolve as $|e_+\rangle_0 \to e^{i\chi_e}|e_+\rangle_1$ and $|g_+\rangle_0 \to e^{i\chi_g}|g_+\rangle_1$, where the subscripts distinguish eigenstates of the initial (θ_0, ϕ_0) and final (θ_1, ϕ_1) Hamiltonians. Then

$$|{\downarrow}, 1\rangle \to e^{-i\phi_0}\left(e^{i\chi_e}\sin\frac{\theta_0}{2}|e_+\rangle_1 - e^{i\chi_g}\cos\frac{\theta_0}{2}|g_+\rangle_1\right). \tag{C.19}$$

Writing $|e_+\rangle_1$ and $|g_+\rangle_1$ in the basis $|{\uparrow}\ 0\rangle$, $|{\downarrow}\ 1\rangle$ and setting the coefficient of $|{\downarrow}\ 1\rangle$ to zero yields the condition

$$e^{i\chi_g}\sin\frac{\theta_0}{2}\sin\frac{\theta_1}{2} + e^{i\chi_e}\cos\frac{\theta_0}{2}\cos\frac{\theta_1}{2} = 0. \tag{C.20}$$

Without fine tuning, χ_g and χ_e are arbitrary phases and the two terms need to vanish separately. This implies $\theta_0 = 0$ and $\theta_1 = \pi$, or vice versa, so that the state $|{\downarrow}, 1\rangle$ was an eigenstate of $h_+(\theta_0, \phi_0)$ to begin with.

The charge state of the quantum dot-Majorana qubit system may then be reset from the initial state $|\psi\rangle$ as follows:

1. Suddenly decouple quantum dot and Majorana qubit ($t_i = 0$ and $\varepsilon > 0$ or $(\theta_\pm)_0 = \pi$). Then, $|{\downarrow}, 1\rangle = |e_+\rangle_0$ and $|{\uparrow}, 1\rangle = |e_-\rangle_0$ are energy eigenstates. The system state $|\psi\rangle$ is now a superposition
$$|\psi\rangle = \alpha|e_+\rangle_0 + \beta|e_-\rangle_0. \tag{C.21}$$

2. Adiabatically swap $|e_\pm\rangle$ and $|g_\pm\rangle$, rotating the Hamiltonian $h_\pm$ from the south $(\theta_\pm)_0 = \pi$ to the north pole $(\theta_\pm)_1 = 0$ of the Bloch sphere,
$$\begin{aligned} |\psi\rangle &\to \alpha|e_+\rangle_1 + \beta e^{i\chi}|e_-\rangle_1 && \text{(C.22a)}\\ &= \alpha|g_+\rangle_0 + \beta e^{i\chi}|g_-\rangle_0, && \text{(C.22b)}\\ &= \big(\alpha|{\uparrow}\rangle + \beta e^{i\chi}|{\downarrow}\rangle\big)|0\rangle, && \text{(C.22c)} \end{aligned}$$
where χ is the relative dynamical phase between the $\hat{\pi}$ eigensectors introduced in the adiabatic evolution. Although uncontrolled, the relative phase does not affect the readout evolution as it preserves the weights in the $\hat{Z}$ eigenbasis. The step requires $t_i \neq 0$ at some point during the evolution to avoid gap closing, but eventually quantum dot and Majorana qubit are again decoupled.

3. Finally, suddenly reset the gates to their initial values, so that the quantum dot-Majorana qubit system again resides in a superposition of charge ground states.

This protocol requires a sign flip of $\varepsilon = E_C + \epsilon$, which can be realized by varying the quantum dot energy ϵ to compensate for the charging energy E_C of the Majorana qubit, or by also varying the spectrum of Majorana-qubit charge states by the gate offset N_g, see Fig. C.2.

The same procedure can be applied at the end of the continuous readout discussed in the main text which may also require a charge reset once the measurement outcome is certain.

C.3 DERIVATION OF THE STOCHASTIC MASTER EQUATION (5.20)

For completeness, we include a derivation of the stochastic master equation (5.20) which describes the evolution of the Majorana qubit-quantum dot system under continuous monitoring of the quantum dot charge by a quantum point contact, see, e.g., Ref. [300].

The Hamiltonian

$$\hat{H}_{\text{readout}} = \hat{H}_{\text{leads}} + \hat{H}_{\text{jct}} + \hat{n}\,\delta\hat{H}_{\text{jct}}. \tag{C.23}$$

of the quantum point contact describes two (left and right) free-fermion leads,

$$\hat{H}_{\text{leads}} = \sum_{\alpha}\left(\xi_{L\alpha}\hat{c}^{\dagger}_{L\alpha}\hat{c}_{L\alpha} + \xi_{R\alpha}\hat{c}^{\dagger}_{R\alpha}\hat{c}_{R\alpha}\right),$$

and a tunneling Hamiltonian

$$\hat{\mathcal{V}} = \hat{H}_{\text{jct}} + \hat{n}\,\delta\hat{H}_{\text{jct}} = (\tau + \chi\hat{n})\hat{\psi}^{\dagger}_{L}\hat{\psi}_{R}e^{ieVt} + \text{h.c.}, \tag{C.24}$$

which includes the coupling to the quantum dot charge $\hat{n}$. The chemical potentials of the two leads differ by the bias voltage V applied across the quantum point contact,

$$eV = \mu_L - \mu_R \tag{C.25}$$

The factor e^{ieVt} in the tunneling Hamiltonian (C.24) already accounts for a time-dependent unitary transformation such that the single-particle energies of the left and right leads are measured from the respective chemical potentials, $\xi_{L\alpha} = \epsilon_{L\alpha} - \mu - eV$ and $\xi_{R\alpha} = \epsilon_{R\alpha} - \mu$, with α labeling the single-particle eigenstates with corresponding electron operators $\hat{c}_{L\alpha}$ and $\hat{c}_{R\alpha}$. The electron operators evaluated at the junction position are denoted by $\hat{\psi}_L$ and $\hat{\psi}_R$. Importantly, there is only capacitive coupling, but no charge transfer between quantum dot and quantum point contact.

At zero temperature, the quantum point contact carries an average current

$$I_0 = 2\pi\nu_L\nu_R|\tau|^2 eV, \tag{C.26a}$$

when the quantum dot is unoccupied, and

$$I_1 = 2\pi\nu_L\nu_R|\tau + \chi|^2 eV, \tag{C.26b}$$

when the quantum dot is occupied. Here, $\nu_{L/R}$ denotes the lead density of states. The sensitivity of the detector depends on $\delta I = I_1 - I_0$. We assume that the quantum dot affects the current weakly, $\delta I \ll I_0$.

C.3.1 UNCONDITIONAL LINDBLAD MASTER EQUATION

We first derive the unconditional master equation for the quantum dot state following the standard procedure of tracing over the leads, assuming factorization of the system-lead density matrix at all times (Born approximation), and finally assuming fast decay of the lead correlation functions to obtain a Markovian equation of motion. We will subsequently use the Lindblad equation to identify the Kraus operators, which allows one to derive the conditional master equation which accounts for the monitoring of the quantum-point-contact current.

We start in the interaction picture, with operators and states evolving according to $\hat{H}_0 = \hat{H} + \hat{H}_{\text{leads}}$ and $\hat{\mathcal{V}} = \hat{H}_{\text{jct}} + \hat{n}\,\delta\hat{H}_{\text{jct}}$, respectively. The corresponding density matrix for system and leads, $\hat{\chi}$, satisfies the equation of motion

$$\frac{\mathrm{d}}{\mathrm{d}t}\hat{\chi}(t) = -i\left[\hat{\mathcal{V}}(t), \hat{\chi}(t_0)\right] - \int_{t_0}^{t} \mathrm{d}t' \left[\hat{\mathcal{V}}(t), \left[\hat{\mathcal{V}}(t'), \hat{\chi}(t')\right]\right]. \tag{C.27}$$

Weak coupling between system and quantum point contact allows for the Born approximation $\hat{\chi}(t) = \hat{\rho}(t) \otimes e^{-\beta H_{\text{leads}}}/Z$ since the effect on the density matrices of the leads remains small at all times. We can then trace out the leads, which enter the resulting equation for the (interaction-picture) density matrix $\hat{\rho}(t)$ of the system only through correlation functions. The first term in (C.27) vanishes since cross-lead correlation functions are assumed zero. The second term evaluates to

$$\begin{aligned}
-\int_{t_0}^{t} \mathrm{d}t' \Big\{ & G_L^<(t'-t)G_R^>(t-t')e^{ieV(t-t')}\left[\hat{m}(t)\hat{m}^\dagger(t')\hat{\rho}(t') - \hat{m}^\dagger(t')\hat{\rho}(t')\hat{m}(t)\right] \\
& -G_L^>(t'-t)G_R^<(t-t')e^{ieV(t-t')}\left[\hat{m}(t)\hat{\rho}(t')\hat{m}^\dagger(t') - \hat{\rho}(t')\hat{m}^\dagger(t')\hat{m}(t)\right] \\
& +G_L^>(t-t')G_R^<(t'-t)e^{ieV(t'-t)}\left[\hat{m}^\dagger(t)\hat{m}(t')\hat{\rho}(t') - \hat{m}(t')\hat{\rho}(t')\hat{m}^\dagger(t)\right] \\
& -G_L^<(t-t')G_R^>(t'-t)e^{ieV(t'-t)}\left[\hat{m}^\dagger(t)\hat{\rho}(t')\hat{m}(t') - \hat{\rho}(t')\hat{m}(t')\hat{m}^\dagger(t)\right] \Big\},
\end{aligned} \tag{C.28}$$

where we defined the shorthand $\hat{m}(t) = \tau + \chi\hat{n}(t)$ as well as the greater and lesser lead Green functions

$$G_j^>(t-t') = -i\left\langle \hat{\psi}_j(t)\hat{\psi}_j^\dagger(t')\right\rangle = -\nu_j \frac{\pi/\beta}{\sinh\frac{\pi(t-t'-i\eta)}{\beta}}, \tag{C.29a}$$

$$G_j^<(t-t') = i\left\langle \hat{\psi}_j^\dagger(t')\hat{\psi}_j(t)\right\rangle = -\nu_j \frac{\pi/\beta}{\sinh\frac{\pi(t-t'+i\eta)}{\beta}}. \tag{C.29b}$$

Here, β denotes the inverse temperature and η is a positive infinitesimal.

In the limit of a large bias voltage, the prefactors of the square brackets in the integrand on the right-hand side of Eq. (C.28) effectively become sharply peaked functions in $t - t'$. Using the Fourier transform of the function

$$g(E) = Eb(E) = -\int \frac{\mathrm{d}t}{2\pi} e^{iEt}\left(\frac{\pi/\beta}{\sinh\frac{\pi(t+i\eta)}{\beta}}\right)^2 \tag{C.30}$$

with the Bose distribution $b(E)$, we can thus approximate

$$G_L^<(t'-t)G_R^>(t-t')e^{ieV(t-t')} \simeq 2\pi\nu_L\nu_R g(-eV)\delta(t-t') + \text{imaginary}, \tag{C.31a}$$

$$G_L^>(t'-t)G_R^<(t-t')e^{ieV(t-t')} \simeq 2\pi\nu_L\nu_R g(eV)\delta(t-t') + \text{imaginary}, \tag{C.31b}$$

$$G_L^>(t-t')G_R^<(t'-t)e^{ieV(t'-t)} \simeq 2\pi\nu_L\nu_R g(eV)\delta(t-t') + \text{imaginary}, \tag{C.31c}$$

$$G_L^<(t-t')G_R^>(t'-t)e^{ieV(t'-t)} \simeq 2\pi\nu_L\nu_R g(-eV)\delta(t-t') + \text{imaginary}. \tag{C.31d}$$

Here, we do not specify the imaginary terms as they correspond to perturbative renormalizations of the system Hamiltonian. The approximate δ-functions in time have a width of order $1/eV$. We assume that both the density matrix $\rho(t)$ and the quantum dot occupation $\hat{n}(t)$ vary slowly within times of order $1/eV$. In particular, this requires that the applied bias is large compared to characteristic system frequencies, $eV \gg \Omega_\pm$. In this limit, the equation of motion for $\hat{\rho}(t)$ becomes Markovian, and we obtain

$$\frac{\mathrm{d}}{\mathrm{d}t}\hat{\rho}(t) = -i\left[\hat{H},\hat{\rho}\right] + \frac{k}{eV|\chi|^2}\Big\{g(-eV)\mathcal{D}[\tau^* + \chi^*\hat{n}] + g(eV)\mathcal{D}[\tau + \chi\hat{n}]\Big\}\hat{\rho}(t). \tag{C.32}$$

Here, we reverted from the interaction to the Schrödinger picture and defined the measurement strength $k = 2\pi\nu_L\nu_R|\chi|^2 eV$. The $(\tau^* + \chi^*\hat{n})$-term describes a process in which electrons tunnel from the left to the right lead. For positive eV, this happens even at $T = 0$. The $(\tau + \chi\hat{n})$-term describes a process in which electrons tunnel from the right to the left lead which cannot occur at $T = 0$. Absorbing a shift $2\pi\nu_L\nu_R eV\,\mathrm{Im}\,[\chi\tau^*]$ into the quantum dot energy ϵ in the Hamiltonian and taking the limit of zero temperature with $g(-eV) = eV$ and $g(eV) = 0$, we obtain the unconditional part of Eq. (5.20)

C.3.2 STOCHASTIC MASTER EQUATION

Since the tunneling amplitude depends only weakly on the quantum dot occupation, the current measurement constitutes a weak measurement of the quantum-dot-qubit system. The change of the system state

$$|\psi\rangle \to \frac{1}{\sqrt{p_i}} M_i |\psi\rangle, \tag{C.33}$$

due to these weak measurements is described by Kraus operators M_1 and M_0 which can be respectively associated with transmission or absence of transmission of electrons by the quantum point contact (still assuming $T = 0$ so that tunneling is unidirectional). The change in the density matrix $\hat{\rho}_c$ takes the form

$$\hat{\rho}_c \to \frac{1}{p_i} M_i \hat{\rho}_c M_i^\dagger. \tag{C.34}$$

In these expressions,

$$p_i = \langle\psi|M_i^\dagger M_i|\psi\rangle = \mathrm{tr}\left[M_i^\dagger M_i \hat{\rho}_c\right] \tag{C.35}$$

denotes the probability for outcome i.

The tunneling current through the quantum point contact can be described as a point process

$$I_c(t) = e\frac{\mathrm{d}N_c(t)}{\mathrm{d}t}, \tag{C.36}$$

where $\mathrm{d}N_c(t) \in \{0, 1\}$ is a Poisson element which is not infinitesimal but has an infinitesimal ensemble average

$$\mathbb{E}[\mathrm{d}N_c(t)] = \mathrm{tr}\left[M_1^\dagger M_1 \hat{\rho}_c(t)\right] \tag{C.37}$$

equal to the probability that an electron is transmitted in time $\mathrm{d}t$. To find the Kraus operator M_1, we note that the ensemble average of the current

$$\mathbb{E}[I_c(t)] = \frac{\mathrm{tr}\left[M_1^\dagger M_1 \hat{\rho}_c(t)\right]}{\mathrm{d}t} \tag{C.38}$$

has to equal I_0 for $n = 0$ and I_1 for $n = 1$. This is satisfied for

$$M_1 = (\tau^* + \chi^* \hat{n})\sqrt{\mathrm{d}t}, \tag{C.39}$$

where we rescaled $\sqrt{2\pi\nu_L\nu_R eV}\tau \to \tau$ and $\sqrt{2\pi\nu_L\nu_R eV}\chi \to \chi$ for notational simplicity (so that $I_0 = |\tau|^2$, $I_1 = |\tau + \chi|^2$, and $k = |\chi|^2$, setting $e = 1$).

To find the Kraus operator $M_0 = \mathbb{1} + \hat{A}\mathrm{d}t$, we equate $\mathbb{E}[\hat{\rho}_c(t+\mathrm{d}t)] = M_0\hat{\rho}(t)M_0^\dagger + M_1\hat{\rho}(t)M_1^\dagger$ and $\mathbb{E}[\hat{\rho}_c(t+\mathrm{d}t)] = \hat{\rho}(t+\mathrm{d}t) = (1+\mathcal{L}\mathrm{d}t)\hat{\rho}(t)$. Reading off the Liouvillian from Eq. (C.32), this yields

$$M_0 = \mathbb{1} - i\mathrm{d}t\hat{H} - \frac{1}{2}M_1^\dagger M_1$$

and thus $\hat{A} = -i\hat{H} - (I_0 + \delta I\hat{n})/2$. As mentioned below Eq. (C.32) above, we absorb a shift of the quantum dot energy into the Hamiltonian,

$$\hat{A} = -i\Big(\hat{H} + \mathrm{Im}\,[\tau^*\chi]\hat{n}\Big) - \frac{1}{2}[I_0 + (2\tau\chi^* + k)\hat{n}]. \tag{C.40}$$

Below, we will no longer display this shift of $\hat{H}$ explicitly.

The conditional evolution of $\hat{\rho}_c(t)$ takes the form

$$\hat{\rho}_c(t+\mathrm{d}t) = (1-\mathrm{d}N_c(t))\frac{M_0\hat{\rho}_c(t)M_0^\dagger}{\mathrm{tr}\Big[M_0\hat{\rho}_c(t)M_0^\dagger\Big]} + \mathrm{d}N_c(t)\frac{M_1\hat{\rho}_c(t)M_1^\dagger}{\mathrm{tr}\Big[M_1\hat{\rho}_c(t)M_1^\dagger\Big]}, \tag{C.41}$$

where the denominators ensure normalization. Expanding to linear order in $\mathrm{d}t$ and neglecting higher-order terms of the form $\mathrm{d}t\,\mathrm{d}N_c(t)$, we obtain

$$\begin{aligned} \mathrm{d}\hat{\rho}_c = \mathrm{d}t\Big\{ &- i\Big[\hat{H}, \hat{\rho}_c\Big] - \frac{1}{2}\{I_0 + k\hat{n}, \hat{\rho}_c\} \\ &- (\chi^*\tau\hat{n}\hat{\rho}_c + \tau^*\chi\hat{\rho}_c\hat{n}) + (I_0 + \delta I\langle\hat{n}\rangle)\hat{\rho}_c\Big\} \\ &+ \mathrm{d}N_c\left\{\frac{(\tau^* + \chi^*\hat{n})\hat{\rho}_c(\tau + \chi\hat{n})}{I_0 + \delta I\langle\hat{n}\rangle} - \hat{\rho}_c\right\}. \end{aligned} \tag{C.42}$$

This describes the stochastic evolution of $\hat{\rho}_c$ as the quantum dot is monitored by the quantum point contact. The evolution of $\hat{\rho}_c$ is conditioned on the stochastic measurement current $I_c(t)$ of the quantum point contact.

We can alternatively describe the evolution in terms of a stochastic Schrödinger equation which takes the form

$$\begin{aligned} \mathrm{d}|\psi_c\rangle = \mathrm{d}t\left\{-i\hat{H} - \frac{1}{2}[I_0 + (2\chi^*\tau + k)\hat{n}] + \frac{1}{2}[I_0 + \delta I\langle\hat{n}\rangle]\right\}|\psi_c\rangle \\ + \mathrm{d}N_c\left\{\frac{\tau^* + \chi^*\hat{n}}{\sqrt{I_0 + \delta I\,\langle\hat{n}\rangle}} - 1\right\}|\psi_c\rangle. \end{aligned} \tag{C.43}$$

C.3.3 DIFFUSIVE APPROXIMATION

The assumption that the average current I_0 is much larger than the shift δI induced by changes in the quantum-dot occupation allows one to approximate the point process by a Wiener process.

We consider a time interval δt which is short enough that the changes in the density matrix $\hat{\rho}_c$ remain small and the quantum expectation value of $\hat{n}$ remains approximately constant. Then, the probability distribution of the number N of tunneling events within the time interval δt is given by the Poisson distribution

$$P(N) = \frac{[(I_0 + \delta I\langle\hat{n}\rangle)\delta t]^N}{N!} e^{-(I_0+\delta I\langle\hat{n}\rangle)\delta t} \tag{C.44}$$

with ensemble average

$$\mathbb{E}[N] = [I_0 + \delta I\langle\hat{n}\rangle]\delta t, \tag{C.45}$$

and variance

$$\mathbb{V}[N] \simeq I_0\delta t. \tag{C.46}$$

The expression for the variance uses that $\delta I \ll I_0$. Assuming that $I_0\delta t$ is large, one can approximate the Poisson by a Gauss distribution with the same average and variance.

Assuming that δI is sufficiently small and the Hamiltonian dynamics sufficiently slow, we can approximate both the unitary dynamics and the changes of the density matrix $\hat{\rho}_c$ induced by the weak measurements of the quantum dot charge to linear order in the time interval δt,

$$\begin{aligned}\delta\hat{\rho}_c = \delta t\Big\{ -i\Big[\hat{H},\hat{\rho}_c\Big] - \frac{1}{2}\{I_0 + k\hat{n}, \hat{\rho}_c\} \\ - (\chi^*\tau\hat{n}\hat{\rho} + \tau^*\chi\hat{\rho}\hat{n}) + (I_0 + \delta I\langle\hat{n}\rangle)\hat{\rho}_c\Big\} \\ + \delta N_c\Big\{\frac{(\tau^* + \chi^*\hat{n})\hat{\rho}_c(\tau + \chi\hat{n})}{I_0 + \delta I\langle\hat{n}\rangle} - \hat{\rho}_c\Big\}.\end{aligned} \tag{C.47}$$

Here, δN_c describes the Wiener process

$$\delta N_c(t) = [I_0 + \delta I\langle\hat{n}\rangle]\delta t + \sqrt{I_0}\xi(t)\delta t \tag{C.48}$$

with a Gaussian random process $\xi(t)$ with variance $1/\delta t$. Writing this in the continuum limit, we find

$$\frac{\mathrm{d}}{\mathrm{d}t}\hat{\rho}_c = -i\Big[\hat{H}_{\text{eff}}, \hat{\rho}_c\Big] + k\mathcal{D}[\hat{n}]\hat{\rho}_c + \sqrt{k}\xi(t)\mathcal{H}\big[\hat{n}e^{i\phi}\big]\hat{\rho}_c \tag{C.49}$$

with $\tau^*\chi = |\tau\chi|e^{i\phi}$ and the δ-function correlator $\mathbb{E}[\xi(t)\xi(t')] = \delta(t-t')$. This simplifies to the evolution equation (5.20) in the main text if one fixes $\phi = \pi$ (corresponding to a decrease in current through the quantum point contact due to the presence of an electron on the quantum dot).

The measurement current is obtained by subtracting the background current I_0 and normalizing. For $\phi = \pi$, this yields

$$j(t) = \frac{1}{\delta I}\left(\frac{\delta N_c(t)}{\delta t} - I_0\right) = \langle \hat{n}(t)\rangle + \frac{1}{\sqrt{4k}}\xi(t) \tag{C.50}$$

in agreement with Eq. (5.19) of the main text.

C.3.4 Relaxation by the electromagnetic environment

Coupling to the electromagnetic environment leads to relaxation in the eigenbasis of the Majorana qubit-quantum dot system, as described by Eq. (5.31) in the main text. Here, we sketch its derivation.

The electrostatic potential of the electromagnetic environment is described as a free bosonic field

$$\hat{v}(\mathbf{r}) = \sum_{\mathbf{q}}\left[\tilde{m}^*_{\mathbf{q}}\hat{a}^\dagger_{\mathbf{q}}e^{i\mathbf{q}\mathbf{r}} + \tilde{m}_{-\mathbf{q}}\hat{a}_{-\mathbf{q}}e^{-i\mathbf{q}\mathbf{r}}\right], \tag{C.51}$$

with Hamiltonian

$$\hat{H}_v = \sum_{\mathbf{q}} \omega_{\mathbf{q}}\hat{a}^\dagger_{\mathbf{q}}\hat{a}_{\mathbf{q}}, \tag{C.52}$$

and is assumed to be in a thermal state $\hat{\rho}_v \propto \exp(-\hat{H}_v/T)$. The potential $\hat{v}$ is an additional contribution to the gate voltages of Majorana qubit and quantum dot and varies slowly in space compared to the spatial extent of the system. Majorana qubit and quantum dot are then subject to the same potential $\hat{v}$, and we obtain the interaction

$$\hat{V} = -\frac{2E_C C_g}{e}\hat{N}\hat{v} - \frac{2\epsilon_C c_g}{e}\hat{n}\hat{v} = \lambda\hat{n}\hat{v} = \hat{n}\sum_{\mathbf{q}}\left[m^*_{\mathbf{q}}\hat{a}^\dagger_{\mathbf{q}} + m_{-\mathbf{q}}\hat{a}_{-\mathbf{q}}\right], \tag{C.53}$$

where we used $\hat{N} = -\hat{n}$ due to charge conservation and absorbed

$$\lambda = \frac{2E_C C_g}{e} - \frac{2\epsilon_C c_g}{e} \tag{C.54}$$

into the coefficients $m_{\mathbf{q}}$. (Here, ϵ_C and c_g are charging energy and gate capacitance of the quantum dot, and C_g is the gate capacitance of the Majorana qubit.)

We write the charge operator in the interaction picture with respect to the system Hamiltonian as given in Eq. (C.9). Then, the coupling Hamiltonian in rotating wave approximation becomes

$$\hat{V}(t) \simeq \hat{c}[\hat{B}(t) + \hat{B}^\dagger(t)] - \frac{\sin\theta}{2}\Big(e^{2i\Omega t}\hat{\tau}_+\hat{B}(t) + e^{-2i\Omega t}\hat{\tau}_-\hat{B}^\dagger(t)\Big), \tag{C.55}$$

where we defined the shorthand

$$\hat{B}(t) = \sum_{\mathbf{q}} m_{\mathbf{q}} e^{-i\omega_{\mathbf{q}} t}\hat{a}_{\mathbf{q}}. \tag{C.56}$$

Notice that we suppressed π indices as $\hat{V}(t)$ conserves $\hat{\pi}$ and does not mix the two subspaces.

Following the same steps as above, the master equation for a general system-bath interaction

$$\hat{H}_{SB} = \sum_i \hat{S}_i \otimes \hat{B}_i \tag{C.57}$$

with system operators $\hat{S}_i$, here associated with the Majorana qubit-quantum dot system, and bath operators $\hat{B}_i$, here associated with the electromagnetic environment, can be written as

$$\frac{\mathrm{d}}{\mathrm{d}t}\hat{\rho}(t) = -i\Big[\hat{H},\hat{\rho}\Big] - \sum_i \Big\{\hat{S}_i\hat{\mathcal{S}}_i^+\hat{\rho}(t) - \hat{\mathcal{S}}_i^+\hat{\rho}(t)\hat{S}_i + \hat{\rho}(t)\hat{\mathcal{S}}_i^-\hat{S}_i - \hat{S}_i\hat{\rho}(t)\hat{\mathcal{S}}_i^-\Big\}. \tag{C.58}$$

Here, we defined the (calligraphic) operators

$$\hat{\mathcal{S}}_i^+ = \sum_j \hat{\mathcal{S}}_{ij}^+ = \sum_j \int_0^\infty \mathrm{d}\tau\, C_{ij}(\tau)\hat{S}_j(-\tau), \tag{C.59a}$$

$$\hat{\mathcal{S}}_i^- = \sum_j \hat{\mathcal{S}}_{ij}^- = \sum_j \int_0^\infty \mathrm{d}\tau\, C_{ji}(-\tau)\hat{S}_j(-\tau), \tag{C.59b}$$

including the bath correlation functions

$$C_{ij}(t-t') = \Big\langle \hat{B}_i(t)\hat{B}_j(t')\Big\rangle. \tag{C.60}$$

We note that the $\hat{S}_i$ and $\hat{B}_i$ are not necessarily hermitian. If they are, $C^*_{ij}(\tau) = C_{ji}(-\tau)$ and thus $(\hat{\mathcal{S}}_i^-)^\dagger = \hat{\mathcal{S}}_i^+ \equiv \hat{\mathcal{S}}_i$.

Applying this to the problem at hand, we identify

$$\hat{S}_1 = \hat{c},\ \hat{S}_2 = -\sin\theta\exp(2i\Omega t)\hat{\tau}_+/2,\ \hat{S}_3 = -\sin\theta\exp(-2i\Omega t)\hat{\tau}_-/2, \tag{C.61}$$

and

$$\hat{B}_1 = \hat{B} + \hat{B}^\dagger,\ \hat{B}_2 = \hat{B},\ \hat{B}_3 = \hat{B}^\dagger. \tag{C.62}$$

One readily evaluates the basic bath correlation functions (with $\tau = t - t'$)

$$C_{BB^\dagger}(\tau) = \langle \hat{B}(t)\hat{B}^\dagger(t')\rangle = \int_0^\infty \mathrm{d}\omega\ J(\omega)e^{-i\omega\tau}(1 + b(\omega)), \tag{C.63a}$$

$$C_{B^\dagger B}(\tau) = \langle \hat{B}^\dagger(t)\hat{B}(t')\rangle = \int_0^\infty \mathrm{d}\omega\ J(\omega)e^{i\omega\tau}b(\omega). \tag{C.63b}$$

Within the rotating wave approximation, we retain only terms which are slowly varying on the scale of the system dynamics. Moreover, we retain only dissipative terms and drop renormalizations of the system Hamiltonian. This yields the result

$$\frac{\mathrm{d}\hat{\rho}}{\mathrm{d}t} = \underbrace{\left\{\frac{\cos^2\theta}{4}\Gamma_0\mathcal{D}[\hat{\tau}_z] + \frac{\sin^2\theta}{4}(\Gamma_+\mathcal{D}[\hat{\tau}_+] + \Gamma_-\mathcal{D}[\hat{\tau}_-])\right\}}_{\equiv\mathcal{L}'}\hat{\rho}, \tag{C.64}$$

where we defined

$$\Gamma_+ = 2\pi J(2\Omega)b(2\Omega), \tag{C.65a}$$

$$\Gamma_- = 2\pi J(2\Omega)(1 + b(2\Omega)), \tag{C.65b}$$

$$\Gamma_0 = \pi \lim_{\omega\to 0} J(\omega)(1 + 2b(\omega)). \tag{C.65c}$$

The Γ_0 term causes decoherence in the energy basis, whereas the $\Gamma_\pm$ terms cause transitions between ground and excited states. At low temperatures, $\Gamma_- \gg \Gamma_+$ with Γ_+ vanishing at $T = 0$ and Γ_- remaining finite. For this reason, we neglect Γ_+ relative to Γ_- in the main text.

C.4 SPECTRA AND EIGENMODES OF LIOUVILLIANS

C.4.1 EIGENVALUES AND EIGENMATRICES OF DIAGONAL BLOCK LIOUVILLIAN $\mathcal{L}_{\pi,\pi} + \mathcal{L}'_{\pi,\pi}$

This appendix gives the eigenvalues and eigenvectors of the diagonal blocks of the full Liouvillian including both measurement and relaxation dynamics, $\mathcal{L}_{\pi,\pi} + \mathcal{L}'_{\pi,\pi}$. To this end, we vectorize by columns, $\rho \to |\rho\rangle = (\rho_{11}, \rho_{21}, \rho_{12}, \rho_{22})^T$. In this notation, $\mathrm{tr}[AB] = \langle A^\dagger | B \rangle$ for square matrices A and B. The Liouvillian matrix is then given by

$$\mathcal{L}_{\pi,\pi} + \mathcal{L}'_{\pi,\pi} = -i\big(\mathbb{1} \otimes h_\pi - h_\pi^T \otimes \mathbb{1}\big) + k\mathrm{D}[n] \tag{C.66a}$$

$$+ \frac{\cos^2\theta_\pi}{4}\Gamma_0 \mathrm{D}[\tau_z] + \frac{\sin^2\theta_\pi}{4}\Gamma_- \mathrm{D}[\tau_-] \tag{C.66b}$$

$$= \sum_n \lambda_{\pi,n} |\psi_{\pi,n}\rangle\langle\phi_{\pi,n}|, \tag{C.66c}$$

where we defined the vectorized decoherence superoperator

$$\mathrm{D}[L] = L^* \otimes L - \frac{1}{2}\Big[\mathbb{1} \otimes L^\dagger L + \big(L^\dagger L\big)^T \otimes \mathbb{1}\Big], \tag{C.67}$$

and expanded in terms of left and right eigenvectors $|\psi_{\pi,n}\rangle$ and $|\phi_{\pi,n}\rangle$ to eigenvalue $\lambda_{\pi,n}$. In the following, we work to leading order in $t_i, k, \Gamma_-, \Gamma_0 \ll \Omega_\pi$ and will suppress π subscripts of θ and Ω. The eigenvalues are

$$\lambda_0 = 0, \ \lambda_{\text{slow}} = -\frac{\sin^2\theta}{4}(\Gamma_- + 2k), \tag{C.68a}$$

$$\lambda_{\text{fast},\pm} = \pm 2i\Omega - \frac{1+\cos^2\theta}{4}k - \frac{\sin^2\theta}{8}\Gamma_- - \frac{\cos^2\theta}{2}\Gamma_0. \tag{C.68b}$$

The corresponding right eigenvectors, written in the energy basis, are

$$|\psi_0\rangle \simeq \frac{1}{2}(1+R, 0, 0, 1-R)^T, \ |\psi_{\text{slow}}\rangle \simeq (1, 0, 0, -1)^T, \tag{C.69a}$$

$$|\psi_{\text{fast},+}\rangle \simeq (0, 0, -1, 0)^T, \ |\psi_{\text{fast},-}\rangle \simeq (0, 1, 0, 0)^T, \tag{C.69b}$$

where R was defined in Eq. (5.34), and the left eigenvectors are

$$\langle\phi_0| = (1, 0, 0, 1), \ \langle\phi_{\text{slow}}| \simeq \left(\frac{k}{\Gamma_- + 2k}, 0, 0, -\frac{\Gamma_- + k}{\Gamma_- + 2k}\right), \tag{C.70a}$$

$$\langle\phi_{\text{fast},+}| \simeq (0, 0, -1, 0), \ \langle\phi_{\text{fast},-}| \simeq (0, 1, 0, 0). \tag{C.70b}$$

Note that $|\psi_0\rangle = |\rho^\infty\rangle$ and $\langle\phi_0| = \langle\mathbb{1}_2|$. We normalized $\langle\phi_m|\psi_n\rangle = \delta_{mn}$ to leading order.

C.4.2 OFF-DIAGONAL BLOCK LIOUVILLIAN $\mathcal{L}_{+-}$ IN EQ. (5.24B)

In this appendix, we analyze the off-diagonal Liouvillian $\mathcal{L}_{+-}$ in Eq. (5.24b) with $h_\pm$ in Eq. (5.7) and one decoherence channel given by the quantum-point-contact coupling (i.e., without relaxation).

Appendix C

STEADY STATE OF ρ_{+-}

To understand the long-time behavior of the density matrix, we find the eigenvalues of $\mathcal{L}_{+-}$ and show that generically, the real parts of all eigenvalues are strictly negative. Thus, the only steady state is $\rho_{+-} = 0$.

We again write the superoperator $\mathcal{L}_{+-}$ in vectorized form with $\rho_{+-} \to (\rho^{11}_{+-}, \rho^{21}_{+-}, \rho^{12}_{+-}, \rho^{22}_{+-})^T$, such that (in the charge basis)

$$\mathcal{L}_{+-} = -i\big(\mathbb{1} \otimes h_+ - h_-^T \otimes \mathbb{1}\big) + k\left[n \otimes n - \frac{1}{2}(\mathbb{1} \otimes n + n \otimes \mathbb{1})\right] \tag{C.71}$$

$$= \begin{pmatrix} 0 & -it_1 - t_2 & it_1^* + t_2^* & 0 \\ -it_1^* + t_2^* & -i\varepsilon - k/2 & 0 & it_1^* + t_2^* \\ it_1 - t_2 & 0 & i\varepsilon - k/2 & -it_1 - t_2 \\ 0 & it_1 - t_2 & -it_1^* + t_2^* & 0 \end{pmatrix}. \tag{C.72}$$

The characteristic polynomial becomes

$$\chi(\tilde{\lambda}) = \tilde{\lambda}^4 + k\tilde{\lambda}^3 + (\varepsilon^2 + 4|t_1|^2 + 4|t_2|^2 + k^2/4)\tilde{\lambda}^2 + 2k(|t_1|^2 + |t_2|^2)\tilde{\lambda} + 16|t_1|^2|t_2|^2 \sin^2\varphi, \tag{C.73}$$

where φ denotes the phase difference between the tunneling amplitudes t_1 and t_2.

Evidently, $\mathcal{L}_{+-}$ has a zero eigenvalue when $\sin\varphi = 0$ or, equivalently, $\mathrm{Im}\{t_1 t_2^*\} = 0$. In this case, ρ_{+-} does not decay to zero and neither $\hat{\pi}$ not $\hat{Z}$ are projectively measured. Physically, the Rabi frequencies of the $\pi = +1$ and the $\pi = -1$ sectors are identical and the steady-state measurement currents of the two sectors are indistinguishable. Thus, the measurement reveals no information on the qubit state and does not decohere the system in the measurement basis.

Conversely, if $\sin\varphi \neq 0$, there is no zero eigenvalue. We now show that in this case, the eigenvalues have strictly negative real parts. They are non-positive since $\mathcal{L}_{+-} + \mathcal{L}_{+-}^\dagger$ is negative semi-definite. To show that the real parts of the eigenvalues are strictly negative, consider the characteristic polynomial. Taking $\sin\varphi \neq 0$, we assume that there is an imaginary eigenvalue $\tilde{\lambda} = iy$ with $y \in \mathbb{R}$. This eigenvalue satisfies

$$y^4 - iky^3 - (\varepsilon^2 + 4|t_1|^2 + 4|t_2|^2 + k^2/4)y^2 + i2k(|t_1|^2 + |t_2|^2)y + 16|t_1|^2|t_2|^2 \sin^2\varphi = 0. \tag{C.74}$$

The imaginary part of this equation, $y^3 = 2(|t_1|^2 + |t_2|^2)y$ has solutions $y = 0$ and $y = \pm[2(|t_1|^2 + |t_2|^2)]^{1/2}$. For $y = 0$, the real part of Eq. (C.74) implies $\sin^2\varphi = 0$, contradicting our assumptions. Similarly, for $y = \pm[2k(|t_1|^2 + |t_2|^2)]^{1/2}$, the real part implies

$$\frac{4|t_1|^2|t_2|^2}{(|t_1|^2 + |t_2|^2)^2}\sin^2\varphi - 1 = \frac{\epsilon^2 + k^2/4}{2(|t_1|^2 + |t_2|^2)}. \tag{C.75}$$

While the left hand side is non-positive, the right-hand side is strictly positive, so that there are no solutions. We conclude that $\mathcal{L}_{+-}$ has only eigenvalues with a strictly negative real part.

DECOHERENCE RATE

The decoherence rate is governed by the eigenvalue $\tilde{\lambda}_{\text{slow}}$ of $\mathcal{L}_{+-}$ with the largest real part (corresponding to the slowest decay). We perform perturbative analyses for small k as well for small $\sin^2\varphi$. Beyond the perturbative regime, we investigate the behavior of the eigenvalues numerically, see Fig. 5.6 in the main text. For simplicity, we specify to $t_1 = t_2 e^{-i\varphi}$ with t_1 real. We also define the shorthand $\tilde{\varepsilon}^2 = \varepsilon^2 + 8t_1^2$. Then, the characteristic polynomial takes the form

$$\chi(\tilde{\lambda}) = \tilde{\lambda}^4 + k\tilde{\lambda}^3 + (\tilde{\varepsilon}^2 + \frac{k^2}{4})\tilde{\lambda}^2 + 4kt_1^2\tilde{\lambda} + 16t_1^4\sin^2\varphi. \tag{C.76}$$

SMALL k: For weak coupling between quantum dot and quantum point contact, we determine the roots of the characteristic polynomial (C.73) to first order in k. Expanding $\tilde{\lambda} = \tilde{\lambda}_0 + k\tilde{\lambda}_1 + \ldots$, we obtain

$$0 = \tilde{\lambda}_0^4 + \tilde{\varepsilon}^2\tilde{\lambda}_0^2 + 16t_1^4\sin^2\varphi, \tag{C.77a}$$

$$0 = 4\tilde{\lambda}_0^3\tilde{\lambda}_1 + \tilde{\lambda}_0^3 + 2\tilde{\varepsilon}^2\tilde{\lambda}_0\tilde{\lambda}_1 + 4t_1^2\tilde{\lambda}_0 \tag{C.77b}$$

with the solutions

$$(\tilde{\lambda}_0^{\pm})^2 = -\frac{\tilde{\varepsilon}^2}{2} \pm \sqrt{\left(\frac{\tilde{\varepsilon}^2}{2}\right)^2 - 16t_1^4\sin^2\varphi} \tag{C.78a}$$

$$\tilde{\lambda}_1^{\pm} = -\frac{1}{4}\left[1 - \frac{\varepsilon^2}{2(\tilde{\lambda}_0^{\pm})^2 + \tilde{\varepsilon}^2}\right] = -\frac{1}{4}\left[1 \pm \frac{\varepsilon^2}{\sqrt{\varepsilon^4 + 16\varepsilon^2 t_1^2 + 64t_1^4\cos^2\varphi}}\right]. \tag{C.78b}$$

While $(\tilde{\lambda}_0^{\pm})^2 \leq 0$, so that the $\tilde{\lambda}_0$ are purely imaginary, the first-order correction $k\tilde{\lambda}_1$ is manifestly real and negative. For the slowly decaying eigenvalues, we choose the minus sign in the above expressions. In the limit $t_1 \ll \varepsilon$, the decay of ρ_{+-} is then controlled by

$$\text{Re}\left\{\tilde{\lambda}_{\text{slow}}\right\} \simeq \text{Re}\left\{\tilde{\lambda}_0^- + k\tilde{\lambda}_1^-\right\} = -2k\frac{t_1^2}{\varepsilon^2}. \tag{C.79}$$

For $\sin^2\varphi = 0$, $\tilde{\lambda}_0^-$ vanishes while $\tilde{\lambda}_1^-$ remains finite. Hence, perturbation theory breaks down close to $\sin^2\varphi = 0$. Requiring $|\tilde{\lambda}_1^-| \ll k|\tilde{\lambda}_2^-|$ yields the condition

$$\frac{k}{\varepsilon} \ll \left| |\sin\varphi| - \frac{1}{4|\sin\varphi|} \right|^{-1}. \tag{C.80}$$

The right side of this inequality vanishes for $\varphi = 0$, i.e. the expansion indeed breaks down.

Small $\sin^2\varphi$: The slowest decaying eigenvalue $\tilde{\lambda}_{\text{slow}}$ evolves from the zero eigenvalue for $\sin^2\varphi = 0$. For small $\sin^2\varphi$, we readily find

$$\tilde{\lambda}_{\text{slow}} = -\frac{4t_1^2\sin^2\varphi}{k} + \ldots \tag{C.81}$$

Notice that the expansion breaks down for vanishing k.

The fact that a perturbative expansion is impossible for small k and φ is in accordance with the numerical observation that exceptional lines emanate from this region, see Fig. 5.6.

C.5 Stochastic evolution of $\pi(t)$

It is instructive to analyze the stochastic evolution of the expectation value of the combined fermion parity $\hat{\pi}$. For $\hat{H}_T = 0$, Eq. (5.21) showed that the evolution of $n(t)$ ceases once $n = 0$ or $n = 1$. In the presence of tunneling, $\hat{H}_T \neq 0$, this is no longer the case due to the additional term $\langle i[\hat{H}_T, \hat{n}]\rangle$ in Eq. (5.22).

To analyze π, we consider the set of coupled stochastic differential equations obtained from Eq. (5.20). As a result of the transfer of weight between the π subspaces due to measurements, the stochastic term couples ρ_{++} and ρ_{--}. At the same time, these diagonal blocks of $\hat{\rho}$ remain uncoupled to ρ_{+-}. (However, the time evolution of ρ_{+-} depends on $\mathrm{tr}\rho_{\pi,\pi}$.) We write the coupled equations for the diagonal blocks using the Bloch-vector notation

$$\rho_{\pi,\pi} = \frac{p_\pi}{2} + \frac{1}{2}(\sigma_x x_\pi + \sigma_y y_\pi + \sigma_z z_\pi), \tag{C.82}$$

where $p_\pi = \mathrm{tr}\rho_{\pi,\pi} = \langle\hat{P}_\pi\rangle$ (with the projector $\hat{P}_\pi$ onto the π subspace). With this parametrization, Eq. (5.20) yields the stochastic differential equations

$$\begin{aligned}
\dot{p}_\pi &= -\sqrt{k}\xi(z_\pi - \mathcal{Z}p_\pi) && \text{(C.83a)}\\
\dot{z}_\pi &= 2\Omega_\pi(h_\pi^x y_\pi - h_\pi^y x_\pi) - \sqrt{k}\xi(p_\pi - \mathcal{Z}z_\pi), && \text{(C.83b)}\\
\dot{x}_\pi &= 2\Omega_\pi(h_\pi^y z_\pi - h_\pi^z y_\pi) - \frac{k}{2}x_\pi + \sqrt{k}\xi\mathcal{Z}x_\pi, && \text{(C.83c)}\\
\dot{y}_\pi &= 2\Omega_\pi(h_\pi^z x_\pi - h_\pi^x z_\pi) - \frac{k}{2}y_\pi + \sqrt{k}\xi\mathcal{Z}y_\pi, && \text{(C.83d)}
\end{aligned}$$

where $\mathcal{Z} = z_+ + z_-$ introduces the coupling between the diagonal blocks.

Fixed points of $\pi(t) = p_+ - p_- = 2p_+ - 1$ require that the right hand side of Eq. (C.83a) vanish, $M_\pi = z_\pi - \mathcal{Z}p_\pi = 0$. $p_\pi = 0$ implies $x_\pi = y_\pi = z_\pi = 0$. We then find by direct evaluation that $p_+ = 0$ (or similarly $p_- = 0$) implies $M_+ = M_- = 0$. We conclude that $p_+ = 0$ and $p_+ = 1$ are fixed points of the evolution of $p_+(t)$. These correspond to fixed points $\pi = -1$ and $\pi = +1$ of $\pi(t)$, respectively. We checked numerically that these are the only fixed points provided $\mathrm{Im}\{t_1 t_2^*\} \neq 0$. (This is indicated, e.g., by the fact that $\mathbb{E}[1-\pi^2] \to 0$ as shown in Fig. 5.3).

Now consider the case $\mathrm{Im}\{t_1 t_2^*\} = 0$. For simplicity we make the stronger assumption $h_+ = h_-$. To understand this case, it is easiest to consider the evolution in terms of

$$l_\pi^\perp = (h_\pi^x y_\pi - h_\pi^y x_\pi), \tag{C.84a}$$

$$l_\pi^\parallel = (h_\pi^x x_\pi + h_\pi^y y_\pi). \tag{C.84b}$$

Then, the evolution equations are

$$\dot{p}_\pi = -\sqrt{k}\xi(z_\pi - \mathcal{Z}p_\pi) \tag{C.85a}$$

$$\dot{z}_\pi = 2\Omega_\pi l_\pi^\perp - \sqrt{k}\xi(p_\pi - \mathcal{Z}z_\pi), \tag{C.85b}$$

$$\dot{l}_\pi^\perp = 2\Omega_\pi\left(h_\pi^z l_\pi^\parallel - \sin^2\theta_\pi z_\pi\right) - \frac{k}{2}l_\pi^\perp + \sqrt{k}\xi\mathcal{Z}l_\pi^\perp, \tag{C.85c}$$

$$\dot{l}_\pi^\parallel = -2\Omega_\pi h_\pi^z l_\pi^\perp - \frac{k}{2}l_\pi^\parallel + \sqrt{k}\xi\mathcal{Z}l_\pi^\parallel. \tag{C.85d}$$

We also define $L^\perp = l_+^\perp + l_-^\perp$ and $L^\parallel = l_+^\parallel + l_-^\parallel$. For $h_+ = h_- = h = \Omega\mathbf{h}\cdot\boldsymbol{\sigma}$, they satisfy a decoupled set of equations

$$\dot{\mathcal{Z}} = 2\Omega L^\perp - \sqrt{k}\xi\left(1 - \mathcal{Z}^2\right), \tag{C.86a}$$

$$\dot{L}^\perp = 2\Omega\left(h^z L^\parallel - \sin^2\theta\mathcal{Z}\right) - \frac{k}{2}L^\perp + \sqrt{k}\xi\mathcal{Z}L^\perp, \tag{C.86b}$$

$$\dot{L}^\parallel = -2\Omega h^z L^\perp - \frac{k}{2}L^\parallel + \sqrt{k}\xi\mathcal{Z}L^\parallel. \tag{C.86c}$$

Importantly, the equations for the l and L have identical form. We now show that the evolution of p_+ becomes frozen if the dynamics of the lower-case variables is locked to that of the upper-case variables, i.e., if

$$0 = z_+ - p_+\mathcal{Z}, \tag{C.87a}$$

$$0 = l_+^\perp - p_+L^\perp, \tag{C.87b}$$

$$0 = l_+^\parallel - p_+L^\parallel, \tag{C.87c}$$

independently of the value of p_+. If $h_+ = uh_- u^\dagger$ similar statements hold for linear combinations of these variables. For the above relations to indeed be fixed points, we need to show that also their Ito differentials vanish. Consider first the two lower lines,

$$\begin{aligned} \mathrm{d}(l_+ - p_+ L) &= \mathrm{d}l_+ - p_+ \mathrm{d}L - \mathrm{d}p_+(\ldots) \\ &= \ (\ldots)[z_+ - p_+ \mathcal{Z}] + (\ldots)\big[l_+^\perp - p_+ L^\perp\big] + (\ldots)\Big[l_+^\parallel - p_+ L^\parallel\Big], \end{aligned} \tag{C.88}$$

where we used that the evolution equations for l and L have identical form. The terms in square brackets vanish at the fixed point specified by Eq. (C.87), so that the detailed form of the terms in the parentheses does not matter. Similarly,

$$\mathrm{d}(z_+ - p_+ \mathcal{Z}) = \sqrt{k}\xi \mathcal{Z}(z_+ - p_+ \mathcal{Z}) + 2\Omega\big(l_+^\perp - p_+ L^\perp\big). \tag{C.89}$$

Thus, Eqs. (C.87) indeed describe fixed points with arbitrary p_+. If the system is initialized, the dynamics of the two sectors will then tend to lock. Once this has happened, p_+ remains constant. The ensemble averaged evolution of course has $p_+(t) = p_+(0)$.

C.6 NOISE SPECTRUM OF THE MEASUREMENT CURRENT

C.6.1 AUTOCORRELATION FUNCTION OF THE STEADY-STATE MEASUREMENT SIGNAL

The measurement outcomes $\pi = +1$ and $\pi = -1$ are distinguished by the noise spectrum of the steady-state measurement current $j_\pi(t)$ for a given π,

$$S(\tau) = \mathbb{E}[j(t)j(t+\tau)] - \mathbb{E}[j(t)]\mathbb{E}[j(t+\tau)] \tag{C.90a}$$

$$\begin{aligned} &= \frac{\delta(\tau)}{4k} + \frac{1}{\sqrt{4k}}\{\mathbb{E}[n(t)\xi(t+\tau)] + \mathbb{E}[n(t+\tau)\xi(t)]\} \\ &\quad + \mathbb{E}[n(t)n(t+\tau)] - \mathbb{E}[n(t)]\mathbb{E}[n(t+\tau)], \end{aligned} \tag{C.90b}$$

where we suppress all labels indicating the measurement outcome and used Eq. (5.19). Our evaluation of $S(\omega)$ follows Ref. [301] (see App. B).

First consider $\mathbb{E}[n(t+\tau)\xi(t)]$, which requires one to compute $\mathbb{E}[\hat{\rho}_c(t+\tau)\xi(t)]$. From Eqs. (C.47) and (C.50), it is evident that $\xi(t)$ is only correlated with the stochastic contribution to $\delta\rho_c$ for the next time step, from t to $t + \delta t$. We then find

$$\mathbb{E}[\hat{\rho}_c(t+\delta t)\xi(t)] = \sqrt{k}\mathbb{E}[\mathcal{H}[\hat{n}]\hat{\rho}_c(t)]\sqrt{4k}\left(\frac{\{\hat{n}, \hat{\rho}^\infty\}}{2} - \mathbb{E}[n(t)\hat{\rho}_c(t)]\right), \tag{C.91}$$

where we write $\mathbb{E}[\hat{\rho}_c] = \hat{\rho}^\infty$. Using the formal solution $\hat{\rho}_c(t) = \mathcal{U}(t,0)\hat{\rho}_c(0)$ of the stochastic master equation (5.20) with

$$\mathcal{U}(t,t') = \mathcal{T}\exp\left\{\mathcal{L}(t-t') + \sqrt{k}\int_{t'}^{t} \mathrm{d}t_1 \xi(t_1)\mathcal{H}[\hat{n}]\right\} \tag{C.92}$$

($\mathcal{T}$ is the time ordering operator) and exploiting that $\xi(t)$ is uncorrelated with any of the later $\xi(t_1)$, we conclude that

$$\mathbb{E}[\hat{\rho}_c(t+\tau)\xi(t)] = \sqrt{4k}\,\theta(\tau)\left(e^{\mathcal{L}\tau}\frac{\{\hat{n},\hat{\rho}^\infty\}}{2} - \mathbb{E}\big[n(t)e^{\mathcal{L}\tau}\hat{\rho}_c(t)\big]\right), \tag{C.93}$$

and thus

$$\begin{aligned}\frac{1}{\sqrt{4k}}\mathbb{E}[n(t+\tau)\xi(t)] &= \theta(\tau)\left(\mathrm{tr}\left[\hat{n}e^{\mathcal{L}\tau}\frac{\{\hat{n},\hat{\rho}^\infty\}}{2}\right] - \mathbb{E}\big[n(t)\mathrm{tr}\big[\hat{n}e^{\mathcal{L}\tau}\hat{\rho}_c(t)\big]\big]\right) &\text{(C.94a)}\\ &= \theta(\tau)\left(\mathrm{tr}\left[\hat{n}e^{\mathcal{L}\tau}\frac{\{\hat{n},\hat{\rho}^\infty\}}{2}\right] - \mathbb{E}[n(t)n(t+\tau)]\right). &\text{(C.94b)}\end{aligned}$$

In the last step, we used that

$$\mathbb{E}\big[n(t)\mathrm{tr}\big[\hat{n}e^{\mathcal{L}\tau}\hat{\rho}_c(t)\big]\big] = \mathbb{E}[n(t)\mathrm{tr}[\hat{n}\mathcal{U}(t+\tau,t)\hat{\rho}_c(t)]], \tag{C.95}$$

since all the additional stochastic terms introduced on the right-hand side average to zero.

Similarly, $\mathbb{E}[n(t)\xi(t+\tau)]$ is nonzero for $\tau < 0$ only. Then, time translation invariance of the stationary state implies

$$\mathbb{E}[n(t)\xi(t+\tau)] = \theta(-\tau)\mathbb{E}[n(t)\xi(t-|\tau|)] = \theta(-\tau)\mathbb{E}[n(t+|\tau|)\xi(t)] \tag{C.96}$$

and we conclude

$$\begin{aligned}&\frac{1}{\sqrt{4k}}\Big(\mathbb{E}[n(t+\tau)\xi(t)] + \mathbb{E}[n(t)\xi(t+\tau)]\Big)\\ &\qquad = \mathrm{tr}\left[\hat{n}e^{\mathcal{L}|\tau|}\frac{\{\hat{n},\hat{\rho}^\infty\}}{2}\right] - \mathbb{E}[n(t)n(t+\tau)].\end{aligned} \tag{C.97}$$

Inserting this into Eq. (C.90) gives

$$S(\tau) = \frac{\delta(\tau)}{4k} + \mathrm{tr}\left[\hat{n}e^{\mathcal{L}|\tau|}\frac{\{\hat{n},\hat{\rho}^\infty\}}{2}\right] - (n^\infty)^2 \tag{C.98}$$

with $n^\infty = \mathrm{tr}[\hat{n}\hat{\rho}^\infty]$.

C.6.2 Explicit evaluation

We now evaluate Eq. (C.98) explicitly for the steady states $\hat{\rho}_{+}^{\infty} = \mathrm{diag}(1 + R, 1 - R, 0, 0)/2$ and $\hat{\rho}_{-}^{\infty} = \mathrm{diag}(0, 0, 1 + R, 1 - R)/2$ of $\mathcal{L} + \mathcal{L}'$ [as given in Eq. (5.20) and Eq. (C.64)] corresponding to the two measurement outcomes $\pi = +1$ and $\pi = -1$, respectively. Note that we wrote the $\hat{\rho}_{\pi}^{\infty}$ in the energy basis here. Since $\mathcal{L} + \mathcal{L}'$ conserves $\hat{\pi}$, the trace in Eq. (C.98) reduces to a trace in one of the π subspaces. We thus have to evaluate

$$\mathrm{tr}\left[n e^{(\mathcal{L}_{\pi,\pi} + \mathcal{L}'_{\pi,\pi})|\tau|} \frac{\{n, \rho^{\infty}\}}{2} \right] \tag{C.99}$$

with $\rho^{\infty} = (\tau_0 + R\tau_z)/2$. Clearly, the remaining calculation is identical for the two subspaces. Suppressing π labels, we evaluate

$$\frac{\{n, \rho^{\infty}\}}{2} = \frac{n^{\infty}}{2} \left(\tau_0 + \frac{R + \cos\theta}{2n^{\infty}} \tau_z - \frac{\sin\theta}{2n^{\infty}} \tau_x \right) \tag{C.100a}$$

$$= n^{\infty} \left[\rho^{\infty} + \frac{R + \cos\theta - 2Rn^{\infty}}{4n^{\infty}} \tau_z - \frac{\sin\theta}{4n^{\infty}} \tau_x \right]. \tag{C.100b}$$

The first term cancels against the $-(n_{\infty})^2$ term in $S(\tau)$. We expand the exponential of the Liouvillian in eigenmodes,

$$e^{(\mathcal{L}_{\pi,\pi} + \mathcal{L}'_{\pi,\pi})|\tau|} = \sum_n e^{\lambda_n |\tau|} |\psi_n\rangle\!\langle \phi_n|, \tag{C.101}$$

where $|\psi_n\rangle$ and $|\phi_n\rangle$ are the right and left eigenmodes of $\mathcal{L}_{\pi,\pi} + \mathcal{L}'_{\pi,\pi}$ to eigenvalue λ_n, respectively (see App. C.4.1). Note that we can write $|\tau_z\rangle \simeq |\psi_{\text{slow}}\rangle$ and $|\tau_x\rangle \simeq -|\psi_{\text{fast},+}\rangle + |\psi_{\text{fast},-}\rangle$. With this, we can evaluate expression (C.99) to leading order,

$$\langle n | e^{(\mathcal{L}_{\pi,\pi} + \mathcal{L}'_{\pi,\pi})|\tau|} | \tau_z \rangle \simeq \cos\theta e^{\lambda_{\text{slow}} |\tau|}, \tag{C.102a}$$

$$\langle n | e^{(\mathcal{L}_{\pi,\pi} + \mathcal{L}'_{\pi,\pi})|\tau|} | \tau_x \rangle \simeq -\sin\theta \cos(2\Omega\tau) e^{\mathrm{Re}\{\lambda_{\text{fast}}\} |\tau|}. \tag{C.102b}$$

Here, we expanded $\langle n| = (\langle \phi_0| + \cos\theta \langle \tau_z| - \sin\theta \langle \tau_x|)/2$ and used the overlaps $\langle \tau_z | \psi_{\text{slow}} \rangle = 2$, $\langle \tau_x | \psi_{\text{slow}} \rangle = 0$, $\langle \tau_z | \psi_{\text{fast}} \rangle \simeq 0$ and $\langle \tau_x | \psi_{\text{fast},\pm} \rangle \simeq \mp 1$. This yields the autocorrelation function

$$S(\tau) \simeq \frac{\delta(\tau)}{4k} + \frac{1}{4} \left[\frac{2k}{\Gamma_- + 2k} \cos^2\theta e^{\lambda_{\text{slow}} |\tau|} + \sin^2\theta \cos(2\Omega\tau) e^{\mathrm{Re}\{\lambda_{\text{fast}}\} |\tau|} \right]. \tag{C.103}$$

Finally, we compute the noise spectrum

$$S(\omega) = \int_{-\infty}^{\infty} \mathrm{d}\tau e^{i\omega\tau} S(\tau), \tag{C.104}$$

which becomes

$$S(\omega) \simeq \frac{1}{4k} + \frac{\cos^2\theta k}{\Gamma_- + 2k}\frac{|\lambda_{\text{slow}}|}{\omega^2 + |\lambda_{\text{slow}}|^2} + \frac{\sin^2\theta}{4}\sum_{\pm}\frac{|\mathrm{Re}\{\lambda_{\text{fast}}\}|}{(\omega \pm 2\Omega)^2 + \left|\mathrm{Re}\{\lambda_{\text{fast}}\}^2\right|}. \tag{C.105}$$

Thus, the noise spectrum consists of Lorentzians centered at $\omega = 0$ due to λ_{slow} and at $\pm 2\Omega$ due to $\lambda_{\text{fast},\pm}$. For $|t_i| \ll \varepsilon$, we have $\theta \simeq \pi$ and the zero-frequency peak is higher than the finite-frequency peaks by a factor of order $(\varepsilon/|t_i|)^4$. Without relaxation, i.e., for $\Gamma_- = \Gamma_0 = 0$ this reduces to the expression (5.29) in the main text.

C.6.3 FLUCTUATIONS OF TIME-AVERAGED MEASUREMENT SIGNAL

In the presence of relaxation, readout can be based on the time-averaged measurement signal. To estimate readout times it is necessary to obtain the variance of the time-averaged measurement signal, see Sec. 5.2.4. The time-averaged measurement signal is

$$\jmath_{\text{int},\pi}(T) = \frac{1}{T}\int_0^T \mathrm{d}t\, \jmath_\pi(t) = \frac{1}{T}\int_0^T \mathrm{d}t \left\{ n_\pi(t) + \frac{X_0}{\sqrt{4kT}} \right\}, \tag{C.106}$$

where X_0 is a Gaussian random variable with zero mean and unit variance. Readout relies on

$$\mathbb{E}[\jmath_{\text{int},\pi}(T)] = n_\pi^\infty. \tag{C.107}$$

Here, we evaluate the variance of this quantity (suppressing π labels),

$$\mathbb{V}[\jmath_{\text{int},\pi}(T)] = \frac{1}{T^2}\int_0^T \mathrm{d}t \int_0^T \mathrm{d}t'\, \mathbb{E}[\jmath(t)\jmath(t')] - (n^\infty)^2 = \frac{2}{T^2}\int_0^T \mathrm{d}t \int_0^t \mathrm{d}\tau\, S(\tau). \tag{C.108}$$

As $|t_i| \ll \varepsilon$, we can neglect the $\sin^2\theta$ term in Eq. (C.103). Using

$$\frac{2}{T^2}\int_0^T \mathrm{d}t \int_0^t \mathrm{d}\tau\, e^{\lambda\tau} = 2\left(\frac{e^{\lambda T} - 1}{\lambda^2 T^2} - \frac{1}{\lambda T}\right) \simeq -\frac{2}{\lambda T} \tag{C.109}$$

for $\lambda T \ll -1$ (checking a posteriori that the measurement times indeed allow for this simplification), we obtain the final result

$$\mathbb{V}[\jmath_{\text{int}}(T)] = \frac{1}{T}\left[\frac{1}{4k} + \frac{k\cos^2\theta}{\Gamma_- + 2k}\frac{1}{|\lambda_{\text{slow}}|}\right] = \frac{1}{T}\left[\frac{1}{4k} + \frac{1}{\tan^2\theta}\frac{4k}{(\Gamma_- + 2k)^2}\right], \tag{C.110}$$

from which we find Eq. (5.38).

C.7 STEADY STATE IN THE PRESENCE OF MAJORANA HYBRIDIZATIONS

Here, we justify the statement in Sec. 5.2.5 that $\hat{\rho}^\infty = \mathrm{diag}(1,1,1,1)/4$ is the only zero mode of $\mathcal{L} + \mathcal{L}_{23}$ (in the absence of relaxation). For small ε_{23}, this result may be obtained as follows. We decompose $\hat{\rho}$ into the steady states $\hat{\rho}^\infty_\pm$ of $\mathcal{L}$ plus deviations $\delta\hat{\rho}$,

$$\hat{\rho} = |\alpha|^2 \hat{\rho}^\infty_+ + |\beta|^2 \hat{\rho}^\infty_- + \delta\hat{\rho}. \tag{C.111}$$

Importantly, $\delta\hat{\rho}$ is traceless. Note that

$$\mathcal{L}_{23}\hat{\rho}^\infty_\pm = \mp\frac{\varepsilon_{23}}{2}\begin{pmatrix} 0 & -i\mathbb{1}_2 \\ i\mathbb{1}_2 & 0 \end{pmatrix} \equiv \mp\frac{\varepsilon_{23}}{2}|Y\rangle, \tag{C.112a}$$

$$\mathcal{L}_{23}|Y\rangle = 4\varepsilon_{23}(\hat{\rho}^\infty_+ - \hat{\rho}^\infty_-). \tag{C.112b}$$

We also define the projector $\hat{P}$ onto the non-decaying subspace $\mathrm{span}(\hat{\rho}^\infty_+, \hat{\rho}^\infty_-)$, as well as its complement $\hat{P}_\perp = 1 - \hat{P}$ which projects onto the fast decaying subspace. We then project the eigenvalue equation

$$(\mathcal{L} + \mathcal{L}_{23})\hat{\rho} = \lambda\hat{\rho} \tag{C.113}$$

onto the two subspaces,

$$\lambda\big(|\alpha|^2 \hat{\rho}^\infty_+ + |\beta|^2 \hat{\rho}^\infty_-\big) = \hat{P}\mathcal{L}_{23}\delta\hat{\rho}, \tag{C.114a}$$

$$\lambda\delta\hat{\rho} = \mathcal{L}\delta\hat{\rho} + \mathcal{L}_{23}\big(|\alpha|^2 \hat{\rho}^\infty_+ + |\beta|^2 \hat{\rho}^\infty_-\big) + \hat{P}_\perp\mathcal{L}_{23}\delta\hat{\rho}. \tag{C.114b}$$

We formally solve the second equation for $\delta\hat{\rho}$ and insert it into the first equation. Using Eqs. (C.112) and the fact that only $|Y\rangle$ is mapped onto $\mathrm{span}(\hat{\rho}^\infty_+, \hat{\rho}^\infty_-)$, i.e., $\hat{P}\mathcal{L}_{23}\ldots = \mathcal{L}_{23}|Y\rangle\langle Y|\ldots/4$ (the factor of $1/4$ stems from the normalization $\langle Y|Y\rangle = 4$), we find, after tracing $\mathrm{tr}\big(\hat{\rho}^\infty_+\ldots\big)$ and using $|\beta|^2 = 1 - |\alpha|^2$,

$$\lambda|\alpha|^2 = \frac{1}{2}\varepsilon_{23}^2 \mathcal{G}_Y(\lambda)\big(2|\alpha|^2 - 1\big). \tag{C.115}$$

Here we defined the “propagator”

$$\mathcal{G}_Y(\lambda) = \langle Y|\frac{1}{\lambda - \mathcal{L} - \hat{P}_\perp\mathcal{L}_{23}}|Y\rangle. \tag{C.116}$$

We are interested in $\lambda = 0$. If $\mathcal{G}_Y(0) \neq 0$, it follows that a zero mode has $|\alpha|^2 = 1/2$. Inserting $\lambda = 0$ into the eigenvalue equations, we obtain the relations $\hat{P}\mathcal{L}_{23}\delta\hat{\rho} = 0$ and

$(\mathcal{L} + \hat{P}_\perp \mathcal{L}_{23})\delta\hat{\rho} = 0$. The first equation gives $\langle Y|\delta\hat{\rho}\rangle = 0$, i.e., the steady state has no weight in the span of $|Y\rangle$. With this, the second equation becomes

$$(\mathcal{L} + \mathcal{L}_{23})\delta\hat{\rho} = 0. \tag{C.117}$$

By assumption, $\mathcal{L}$ has no zero mode that is traceless and therefore $\mathcal{L}$ acting on $\delta\hat{\rho}$ does not vanish. Hence, for weak perturbations $\varepsilon_{23} \ll |\operatorname{Re}\{\tilde{\lambda}_{\text{slow}}\}|, |\lambda_{\text{slow},\pi}|$, it follows that $\delta\hat{\rho} = 0$. Finally, it is straightforward to check numerically that $\mathcal{G}_Y(0)$ is indeed non-vanishing within the relevant parameter range by expanding in left and right eigenvectors of $\mathcal{L} + \hat{P}_\perp \mathcal{L}_{23}$. Thus, the completely mixed state is indeed the only steady state.

APPENDIX D

D.1 CONFINED WEYL FERMION WAVE FUNCTIONS

In this appendix we derive the explicit form of the eigenfunctions of Eq. (6.4) in the slab geometry $0 < z < W$. Writing the momentum operator p_z in the spatial basis, $p_z = -i\partial_z$ the Weyl equation $H\psi(z) = E\psi(z)$ can be written as

$$-i\partial_z\psi(z) = \mathcal{P}_z\psi(z), \tag{D.1}$$

where the generalized momentum $\mathcal{P}_z$ was defined in Eq. (6.6). The Weyl equation is formally solved by Eq. (6.5). Defining an orthonormal basis for our model of zero out-of-plane current states,

$$|\alpha_\pm\rangle = \frac{1}{\sqrt{2}}\begin{pmatrix} 1 \\ \pm e^{i\alpha} \end{pmatrix},\ |\beta_\pm\rangle = \frac{1}{\sqrt{2}}\begin{pmatrix} 1 \\ \pm e^{i\beta} \end{pmatrix}, \tag{D.2}$$

the generic boundary conditions at the two surfaces can be written as

$$\psi(0) \propto |\alpha_+\rangle, \qquad \psi(W) \propto |\beta_+\rangle. \tag{D.3}$$

From the boundary conditions, the quantized eigenvalues p_z are the solutions of

$$0 = \sin\frac{\alpha-\beta}{2} + \frac{\tan(p_z W)}{p_z}\left[p_x \mp \chi p \cos\frac{\alpha-\beta}{2}\right], \tag{D.4}$$

where p_x is in the basis of Fig. 6.2(c). Solutions with real p_z correspond to bulk states, imaginary solutions correspond to surface "arc" states, which we will now discuss in more detail.

D.1.1 ARC STATES

For an imaginary p_z, normalizable wavefunctions are found that are localized at the bottom (b) and top (t) surfaces,

$$\psi^{\mathrm{b}}_{\mathrm{arc}}(z) = \sqrt{2\mathbf{p}\cdot\boldsymbol{\alpha}_2}\, e^{-\mathbf{p}\cdot\boldsymbol{\alpha}_2 z}|\alpha_+\rangle = \left\langle z\middle|\mathrm{arc,b},\mathbf{p}_\parallel\right\rangle, \tag{D.5a}$$

$$\psi^{\mathrm{t}}_{\mathrm{arc}}(z) = \sqrt{-2\mathbf{p}\cdot\boldsymbol{\beta}_2}\, e^{\mathbf{p}\cdot\boldsymbol{\beta}_2(W-z)}|\beta_+\rangle = \left\langle z\middle|\mathrm{arc,t},\mathbf{p}_\parallel\right\rangle. \tag{D.5b}$$

(These expressions assume $W|\mathbf{x}_2 \cdot \mathbf{p}| \gg 1$ for $x \in \{\alpha, \beta\}$). From the criterion of normalizability, the momenta of Fermi arcs are bound to

$$\mathbf{p} \cdot \boldsymbol{\alpha}_2 > 0, \quad \mathbf{p} \cdot \boldsymbol{\beta}_2 < 0. \tag{D.6}$$

The dispersion relations read

$$E^{\mathrm{b}}_{\mathrm{arc}} = \chi v \mathbf{p} \cdot \boldsymbol{\alpha}_1, \; E^{\mathrm{t}}_{\mathrm{arc}} = \chi v \mathbf{p} \cdot \boldsymbol{\beta}_1, \tag{D.7}$$

and hence the velocity expectation values are

$$\mathbf{v}^{\mathrm{b}}_{\mathrm{arc}} = \chi v \boldsymbol{\alpha}_1, \; \mathbf{v}^{\mathrm{t}}_{\mathrm{arc}} = \chi v \boldsymbol{\beta}_1. \tag{D.8}$$

The directions $\boldsymbol{\alpha}_i$ and $\boldsymbol{\beta}_i$ are thus the directions in which the Fermi arcs emanate from the Weyl node ($i = 1$) and the directions of their motion ($i = 2$), both up to the sign, as indicated in Fig. 6.2.

D.1.2 BULK STATES

For real p_z, from (6.5) the normalized wavefunctions of the conduction $(+)$ and valence band $(-)$ read

$$\psi_{\mathbf{p}\pm}(z) = \frac{[p_z \cos p_z z - \boldsymbol{\alpha}_2 \cdot \mathbf{p} \sin p_z z]|\alpha_+\rangle + i[\pm\chi p - \boldsymbol{\alpha}_1 \cdot \mathbf{p}] \sin p_z z|\alpha_-\rangle}{\sqrt{W N_{\mathbf{p}\pm}}} \tag{D.9a}$$

$$= \langle z|\text{bulk}, \pm, \mathbf{p}\rangle, \tag{D.9b}$$

where the normalization factor, isolating the finite-size correction $\sim 1/W$, is given by

$$N_{\mathbf{p}\pm} = p(p \mp \chi \boldsymbol{\alpha}_1 \cdot \mathbf{p}) + \delta N_{\mathbf{p}\pm}, \tag{D.10a}$$

$$\delta N_{\mathbf{p}\pm} = -\frac{\sin(W p_z)}{W p_z}\Big[\big(p_\parallel^2 \mp \chi p \, \boldsymbol{\alpha}_1 \cdot \mathbf{p}\big) \cos(W p_z) + p_z \boldsymbol{\alpha}_2 \cdot \mathbf{p} \sin(W p_z)\Big]. \tag{D.10b}$$

The velocity expectation values read

$$\mathbf{v}_{\mathbf{p}\pm} = \pm v \frac{\mathbf{p}_\parallel}{p} + \delta \mathbf{v}_{\mathbf{p}\pm}, \; \delta \mathbf{v}_{\mathbf{p}\pm} = \frac{\partial E_{\mathbf{p}\pm}}{\partial p_z} \frac{\mathrm{d} p_z}{\mathrm{d}\mathbf{p}} = \pm v \frac{p_z}{p} \frac{\mathrm{d} p_z}{\mathrm{d}\mathbf{p}}, \tag{D.11}$$

where we again isolated the finite-size correction $\delta \mathbf{v}_{\mathbf{p}\pm} \sim 1/W$, which stems from the weak $\mathbf{p}_\parallel$ dependence of the quantized p_z, as implicitly given in (6.8). Note that $v_z = 0$ due to the boundary conditions for all states.

D.2 ANISOTROPIC WEYL NODE

Here we generalize our calculations to Weyl fermions with anisotropic velocity. We consider the Hamiltonian

$$h'(\mathbf{p}) = v_{ij}\sigma_i p_j \equiv \chi v \mathbf{p}' \cdot \boldsymbol{\sigma} = h(\mathbf{p}'), \tag{D.12}$$

where $v_{ij} = v_{ji}$ and we defined $p'_i = \tilde{v}_{ij}p_j$ in terms of

$$\tilde{v}_{ij} = \chi \frac{v_{ij}}{v}, \; v > 0. \tag{D.13}$$

The chirality of the anisotropic Weyl node is $\chi = \mathrm{sign}(\det v)$. Undashed symbols refer to the isotropic case discussed in the main text. The current operator is

$$j'_i = -ev_{ij}\sigma_j = \tilde{v}_{ij}j_j. \tag{D.14}$$

To avoid complications in the boundary condition we specify to

$$v = \mathrm{diag}(v_{\parallel}, v_z), \tag{D.15}$$

where $v_{\parallel}$ is a 2x2 matrix acting only on components parallel to the boundary. Furthermore, we set $v = |v_z|$. With this we may again employ the boundary conditions of Eq. (6.7). Then, the arc and bulk wave-functions may be obtained by simply replacing $\mathbf{p} \to \mathbf{p}'$ in Eqs. (D.5a), (D.5b) and Eq. (D.9). Similarly, the velocities can be expressed in terms of the isotropic expressions via

$$\left(\mathbf{v}'_{\mathbf{p},n}\right)_i = \frac{\mathrm{d}E'_{\mathbf{p},n}}{\mathrm{d}p_i} = \frac{\partial p'_i}{\partial p_i}\frac{\mathrm{d}E_{\mathbf{p}',n}}{\mathrm{d}p'_i} = \tilde{v}_{ij}\left(\mathbf{v}_{\mathbf{p}',n}\right)_j. \tag{D.16}$$

Altogether, the response tensor of the anisotropic Weyl node is related to the isotropic node via (c.f. Eq. (6.22))

$$\Gamma'_{ijk} = \frac{8\pi\eta\tau}{W}\int d^2p_{\parallel}\sum_{q_zp_z}\left(\frac{\mathbf{v}'_{\mathbf{p}+}}{v} - \frac{\mathbf{v}'_{\mathbf{q}-}}{v}\right)_i \delta\left(1 - \frac{E'_{\mathbf{p}}}{\omega} - \frac{E'_{\mathbf{q}}}{\omega}\right)\left[\mathbf{M}'_{\mathbf{pq}} \otimes (\mathbf{M}'_{\mathbf{pq}})^*\right]_{jk} \tag{D.17a}$$

$$= \frac{\tilde{v}_{il}\tilde{v}_{jm}\tilde{v}_{kn}}{|\det\tilde{v}|}\frac{8\pi\eta\tau}{W}\int d^2p'_{\parallel}\sum_{q'_zp'_z}\left(\frac{\mathbf{v}_{\mathbf{p}'+}}{v} - \frac{\mathbf{v}_{\mathbf{q}'-}}{v}\right)_l$$

$$\times\,\delta\left(1 - \frac{E_{\mathbf{p}'}}{\omega} - \frac{E_{\mathbf{q}'}}{\omega}\right)\left[\mathbf{M}_{\mathbf{p}'\mathbf{q}'} \otimes \mathbf{M}^*_{\mathbf{p}'\mathbf{q}'}\right]_{mn} \tag{D.17b}$$

$$= \frac{\tilde{v}_{il}\tilde{v}_{jm}\tilde{v}_{kn}}{|\det\tilde{v}|}\Gamma_{lmn}, \tag{D.17c}$$

where the determinant stems from the change of variables $\mathbf{p}_{\parallel}$ to $\mathbf{p}'_{\parallel}$ (using $\left|\det\tilde{v}_{\parallel}\right| = |\det\tilde{v}|$ due to our choice of v).

D.3 SYMMETRY CONSIDERATIONS

D.3.1 THICK SLAB

We work in the basis of the thick slab $\boldsymbol{\alpha}_1 = \hat{\mathbf{x}},\ \boldsymbol{\alpha}_2 = \hat{\mathbf{y}}$. The heterostructure Hamiltonian Eq. (6.12) of the semi-infinite system under consideration can be written as

$$H_{\chi m} = \chi v \mathbf{p} \cdot \boldsymbol{\sigma} + \begin{cases} -\chi m \sigma_y & z < 0 \\ 0 & z > 0 \end{cases}. \tag{D.18}$$

where the vacuum at $z < 0$ is modeled by a large mass term with $m \to \infty$, which acts like a magnetization in breaking the intra-node TR symmetry, as discussed in the main text. We consider spatial mirror-plane reflections $R_i, i = x, y, z$, with $i = x$ corresponding to reflection w.r.t. the yz plane, etc. A single reflection reverses the component of the momentum and the current that is normal to the mirror plane and the components of the spin that are parallel to the mirror plane. The action of the reflections on the Hamiltonian thus read

$$R_x H_{\chi m} R_x = H_{-\chi m}, \qquad R_y H_{\chi m} R_y = H_{-\chi -m}. \tag{D.19}$$

In words, reflection R_x reverses the chirality and reflection R_y reverses the chirality and the magnetization.

From this we can infer on the transformation behavior of the response tensor. First, note that the (anti)symmetric part of the response tensor, Γ^{s} (Γ^{a}), is generally odd (even) under TR [160] – the (anti)symmetric part is thus odd (even) under $m \to -m$. Second, in Sec. 6.3 we have shown that the (anti)symmetric part of the response tensor is even (odd) under $\chi \to -\chi$. Taking also into account the transformation of the current under reflections, we obtain for the symmetric part,

$$R_x \Gamma^{\mathrm{s}}_x R_x = -\Gamma^{\mathrm{s}}_x,\ R_x \Gamma^{\mathrm{s}}_y R_x = \Gamma^{\mathrm{s}}_y, \tag{D.20a}$$

$$R_y \Gamma^{\mathrm{s}}_x R_y = -\Gamma^{\mathrm{s}}_x,\ R_y \Gamma^{\mathrm{s}}_y R_y = \Gamma^{\mathrm{s}}_y, \tag{D.20b}$$

while the antisymmetric part satisfies

$$R_x \Gamma^{\mathrm{as}}_x R_x = \Gamma^{\mathrm{as}}_x,\ R_x \Gamma^{\mathrm{as}}_y R_x = -\Gamma^{\mathrm{as}}_y, \tag{D.21a}$$

$$R_y \Gamma^{\mathrm{as}}_x R_y = -\Gamma^{\mathrm{as}}_x,\ R_y \Gamma^{\mathrm{as}}_y R_y = \Gamma^{\mathrm{as}}_y. \tag{D.21b}$$

From this follows

$$\Gamma_x^{\text{thick}} = \begin{pmatrix} 0 & \Gamma_{xxy} & 0 \\ \Gamma_{xxy} & 0 & \Gamma_{xyz} \\ 0 & -\Gamma_{xyz} & 0 \end{pmatrix}, \; \Gamma_y^{\text{thick}} = \begin{pmatrix} \Gamma_{yxx} & 0 & -\Gamma_{yzx} \\ 0 & \Gamma_{yyy} & 0 \\ \Gamma_{yzx} & 0 & \Gamma_{yzz} \end{pmatrix}. \tag{D.22}$$

D.3.2 Thin slab

We now work in the basis of the thin slab, depiceted in Fig. 6.2(c). We now consider the full heterostructure Hamiltonian (6.12),

$$H_{\chi m} = \chi v \mathbf{p} \cdot \boldsymbol{\sigma} + \begin{cases} -\chi m \, \boldsymbol{\sigma} \cdot \boldsymbol{\alpha}_2 & z < 0 \\ 0 & 0 < z < W, \\ \chi m \, \boldsymbol{\sigma} \cdot \boldsymbol{\beta}_2 & z > W \end{cases} \tag{D.23}$$

with $m \to \infty$. The behavior under reflections and TR is as in the previous section but now with two TR-breaking magnetizations.

We consider two symmetry transformations. First we note that the combined reflection R_z, which swaps the top and bottom surfaces, and R_y, which interchanges $\boldsymbol{\sigma} \cdot \boldsymbol{\alpha}_2$ and $\boldsymbol{\sigma} \cdot \boldsymbol{\beta}_2$, leave the Hamiltonian invariant. Second, the combination of R_x and R_y inverts both $\boldsymbol{\sigma} \cdot \boldsymbol{\alpha}_2$ and $\boldsymbol{\sigma} \cdot \boldsymbol{\beta}_2$, which can be compensated by $m \to -m$. Altogether,

$$R_y R_z H_{\chi m} R_z R_y = H_{\chi m}, \; R_x R_y H_{\chi m} R_y R_x = H_{\chi -m}. \tag{D.24}$$

Both the symmetric and the antisymmetric parts of the response tensor thus satisfy

$$R_y R_z \Gamma_x R_z R_y = \Gamma_x, \; R_y R_z \Gamma_y R_z R_y = -\Gamma_y, \tag{D.25a}$$

and, since the symmetric part is odd under $m \to -m$, it satisfies

$$R_x R_y \Gamma^{\text{s}}_x R_y R_x = \Gamma^{\text{s}}_x, \; R_x R_y \Gamma^{\text{s}}_y R_y R_x = \Gamma^{\text{s}}_y, \tag{D.26a}$$

while the antisymmetric part satisfies

$$R_x R_y \Gamma^{\text{as}}_x R_x R_y = -\Gamma^{\text{as}}_x, \; R_x R_y \Gamma^{\text{as}}_y R_x R_y = -\Gamma^{\text{as}}_y. \tag{D.27a}$$

From this follows,

$$\Gamma_x^{\text{thin}} = \begin{pmatrix} \Gamma_{xxx} & 0 & 0 \\ 0 & \Gamma_{xyy} & \Gamma_{xyz} \\ 0 & -\Gamma_{xyz} & \Gamma_{xzz} \end{pmatrix}, \quad \Gamma_y^{\text{thin}} = \begin{pmatrix} 0 & \Gamma_{yxy} & -\Gamma_{yzx} \\ \Gamma_{yxy} & 0 & 0 \\ \Gamma_{yzx} & 0 & 0 \end{pmatrix}. \tag{D.28}$$

Finally, we may also constrain the dependency of the components with respect to the angle $\Delta = (\beta - \alpha)/2 \in [-\pi, \pi]$. In terms of Δ, the magnetization directions are given by $\boldsymbol{\alpha}_2 = (-\sin\Delta, \cos\Delta)$ and $\boldsymbol{\beta}_2 = (\sin\Delta, \cos\Delta)$. First, note that the transformation $\Delta \to -\Delta$ may be compensated by R_x. From this follows that components of the symmetric part of Γ are odd under $\Delta \to -\Delta$ while components of the anti-symmetric part are even. Next note, that $\Delta \to \Delta + \pi$ inverts both magnetizations and may be compensated by TR. From this follows that components of the symmetric part of Γ are odd under $\Delta \to \Delta + \pi$ while components of the anti-symmetric part are even.

D.4 PHOTOGALVANIC CURRENT DUE TO ARC-BULK EXCITATIONS

As explained in the main text, the leading-order current contribution due to arc-bulk excitations is of the same order of magnitude as the subleading contributions from bulk-bulk excitations. Other types of finite-size corrections that we had to account for when considering bulk-bulk excitations can now be disregarded, as they would give corrections of higher order. In particular, we can replace the momentum sum over p_z by integrals in both the thick and thin slab regimes. Furthermore, we can assume $W \to \infty$ and $\delta \to \infty$ in both regimes and neglect the finite light momentum $\mathbf{k}$. In the thick slab limit only the bottom arc is relevant, in the thin slab limit both arcs contribute.

The response tensor due to the bottom arc is

$$\begin{aligned} \boldsymbol{\Gamma}_{ij}^{\text{ab,b}} = \frac{8\eta\tau}{W} \int \frac{d^3p}{p}\, \Theta(p_z)\Theta(p_y) \\ \times \Bigg\{ \Theta(-\chi p_x)\delta(1 - p + \chi p_x) \left[\frac{\mathbf{p}_\parallel}{p} - \chi \boldsymbol{\alpha}_1\right] M_i^{\text{ab,b},+} \left(\mathbf{M}_j^{\text{ab,b},+}\right)^* \\ + \Theta(\chi p_x)\delta(1 - \chi p_x - p) \left[\chi \boldsymbol{\alpha}_1 + \frac{\mathbf{p}_\parallel}{p}\right] M_i^{\text{ab,b},-} \left(\mathbf{M}_j^{\text{ab,b},-}\right)^* \Bigg\}, \end{aligned} \tag{D.29}$$

where all momenta are dimensionless (in the appendix we suppress the tilde, which denotes dimensionless units in the main text). The first line captures transitions between conduction band and arc sheet, while the second captures transitions between the arc sheet and the valence band (the first Heaviside-Θ function enforces normalizability of the arc states, the second allows transitions between empty and occupied states only). We also defined the arc-bulk matrix elements $[\mathbf{p} = p(\sin\theta\cos\phi, \sin\theta\sin\phi, \cos\theta)]$

$$\mathbf{M}^{\mathrm{ab,b,+}} = \sqrt{Wp}\langle \mathrm{bulk}, +, \mathbf{p}|\boldsymbol{\sigma}\big|\mathrm{arc,b}, \mathbf{p}_{\|}\big\rangle = \sqrt{\frac{2\cos^2\theta\sin\theta\sin\phi}{1-\chi\sin\theta\cos\phi}}\frac{(-\boldsymbol{\alpha}_2 - i\hat{\mathbf{z}})}{\chi + \sin\theta\cos\phi}, \tag{D.30a}$$

$$\mathbf{M}^{\mathrm{ab,b,-}} = \sqrt{Wp}\big\langle \mathrm{arc,b}, \mathbf{p}_{\|}\big|\boldsymbol{\sigma}|\mathrm{bulk}, -, \mathbf{p}\rangle = \sqrt{\frac{2\cos^2\theta\sin\theta\sin\phi}{1+\chi\sin\theta\cos\phi}}\frac{(\boldsymbol{\alpha}_2 - i\hat{\mathbf{z}})}{\chi - \sin\theta\cos\phi}. \tag{D.30b}$$

Letting $p_x \to -p_x$ in the second term of Eq. (D.29) the current may be written as

$$\begin{aligned}\boldsymbol{\Gamma}^{\mathrm{ab,b}}_{ij} = \frac{16\eta\tau}{\tilde{W}}\int\frac{\mathrm{d}^3p}{p}&\Theta(\cos\theta)\Theta(\sin\phi)\Theta(-\chi\cos\phi)\\ &\times\frac{\delta(1-p(1-\chi\sin\theta\cos\phi))\cos^2\theta\sin\theta\sin\phi}{(1-\chi\sin\theta\cos\phi)(1+\chi\sin\theta\cos\phi)^2}\\ &\times\left\{\begin{pmatrix}\sin\theta\cos\phi-\chi\\ \sin\theta\sin\phi\end{pmatrix}(\boldsymbol{\alpha}_2+i\hat{\mathbf{z}})_i(\boldsymbol{\alpha}_2-i\hat{\mathbf{z}})_j\right.\\ &\left.+\begin{pmatrix}-\sin\theta\cos\phi+\chi\\ \sin\theta\sin\phi\end{pmatrix}(\boldsymbol{\alpha}_2-i\hat{\mathbf{z}})_i(\boldsymbol{\alpha}_2+i\hat{\mathbf{z}})_j\right\}.\end{aligned} \tag{D.31}$$

This may be evaluated straightforwardly. The resulting response tensor in the thick slab basis is

$$\Gamma^{\mathrm{ab,thick}}_x = \frac{\eta\tau}{W}\begin{pmatrix}0 & 0 & 0\\ 0 & 0 & i\frac{16\pi}{3}\chi\\ 0 & -i\frac{16\pi}{3}\chi & 0\end{pmatrix}, \ \Gamma^{\mathrm{ab,thick}}_y = \frac{\eta\tau}{W}\begin{pmatrix}0 & 0 & 0\\ 0 & 2\pi\ln 2 & 0\\ 0 & 0 & 2\pi\ln 2\end{pmatrix}. \tag{D.32}$$

Note that in the thin slab, the bottom arc contribution is simply $\boldsymbol{\Gamma}^{\mathrm{ab,thick}} = \boldsymbol{\Gamma}^{\mathrm{ab,b}}$. The current due to the top arc (present only in the thin slab regime) may be obtained analogously. The result for the top arc in the basis $\hat{\mathbf{x}} = \boldsymbol{\beta}_1, \hat{\mathbf{y}} = \boldsymbol{\beta}_2$ is

$$\Gamma^{\mathrm{ab,t}}_x = \frac{\eta\tau}{W}\begin{pmatrix}0 & 0 & 0\\ 0 & 0 & i\frac{16\pi}{3}\chi\\ 0 & -i\frac{16\pi}{3}\chi & 0\end{pmatrix}, \ \Gamma^{\mathrm{ab,t}}_y = -\frac{\eta\tau}{W}\begin{pmatrix}0 & 0 & 0\\ 0 & 2\pi\ln 2 & 0\\ 0 & 0 & 2\pi\ln 2\end{pmatrix}. \tag{D.33}$$

In the thin-slab case both contributions combine into the total arc-bulk contribution. Introducing the rotation operator

$$R(\varphi)=\begin{pmatrix}\cos\varphi & -\sin\varphi & 0\\ \sin\varphi & \cos\varphi & 0\\ 0 & 0 & 1\end{pmatrix}, \tag{D.34}$$

the total arc-bulk contribution, in the thin-slab basis [Fig. 6.2(c)], is given by

$$\Gamma^{\mathrm{ab,thin}}_{abc}=R(\Delta)_{ai}R(\Delta)_{bj}R(\Delta)_{ck}\Gamma^{\mathrm{ab,t}}_{ijk}+R(-\Delta)_{ai}R(-\Delta)_{bj}R(-\Delta)_{ck}\Gamma^{\mathrm{ab,b}}_{ijk}. \tag{D.35}$$

The resulting expression is given in Eq. (6.39) of the main text.

D.5 PHOTOGALVANIC CURRENT DUE TO BULK-BULK EXCITATIONS

This appendix section is structured as follows. First we perform some general manipulations. Next we discuss the thick and thin slab limits separately. In the thick slab limit, we may let $W\to\infty$ and ignore the quantization condition Eq. (6.8). Corrections to the infinite system response arise from the spatial variation of the electromagnetic field corresponding to finite $\mathbf{k}$, $1/\delta$. These are of the same order of magnitude as the current due to arc-bulk excitations. Conversely, in the thin slab limit, the spatial dependence of the electromagnetic field may be ignored ($\mathbf{k}=0, 1/\delta=0$), but the quantization condition due to finite W leads to corrections of the same order as the arc-bulk current.

We start from Eq. (6.22) and specify to bulk states $m=(\mathbf{p},+)$ and $n=(\mathbf{q},-)$,

$$\boldsymbol{\Gamma}^{\mathrm{bb}}_{ij}=\frac{8\pi\eta\tau}{\tilde{W}^3}\int \mathrm{d}^2\tilde{p}_\parallel\sum_{\tilde{p}_z\tilde{q}_z}(\hat{\mathbf{v}}_{\mathbf{p}+}+\hat{\mathbf{v}}_{\mathbf{q}-})\delta(1-\tilde{p}-\tilde{q})\left[\tilde{\mathbf{M}}^{\mathrm{bb}}\otimes\left(\tilde{\mathbf{M}}^{\mathrm{bb}}\right)^*\right]_{ij}\Bigg|_{\mathbf{q}_\parallel=\mathbf{p}_\parallel-\mathbf{k}_\parallel} \tag{D.36}$$

where we defined the dimensionless bulk-bulk matrix elements

$$\tilde{\mathbf{M}}^{\mathrm{bb}}=\tilde{W}\langle\mathrm{bulk},+,\tilde{\mathbf{p}}|\boldsymbol{\sigma}e^{i\tilde{z}\tilde{k}_z-\tilde{z}/\tilde{\delta}}|\mathrm{bulk},-,\tilde{\mathbf{q}}\rangle. \tag{D.37}$$

Note that as opposed to the main text here we explicitly include the light momentum $\mathbf{k}$. Since $k=\omega/c$, the light momentum is a factor v/c smaller than the typical momenta of excited states $\sim 1/\ell=\omega/v$. We will show below that it does not contribute at the relevant order of magnitude, in agreement with the argumentation in the main text. We set $\mathbf{k}=(k_\parallel\cos\gamma, k_\parallel\sin\gamma, k_z)$ and keep terms to first order in $\tilde{k}_z$, $\tilde{k}_\parallel\sim v/c$.

We proceed by performing the integral over $p_\|$ using the conservation of energy. The delta function gives the condition

$$g(p_\|) = 1 - \sqrt{p_\|^2 + p_z^2} - \sqrt{p_\|^2 + q_z^2 - 2p_\| k_\| \cos(\phi - \gamma) + k_\|^2} = 0.$$

This has a real solution if, to leading order in $k_\|$,

$$p_z + q_z < 1 \text{ or } P < 1/2, \tag{D.38}$$

where we defined new variables

$$P = \frac{1}{2}(p_z + q_z),\ Q = \frac{1}{2}(p_z - q_z) \tag{D.39}$$

with $P > 0,\ P > Q > -P$. The solution to $g(p_\|) = 0$ is given by

$$p_\| = \frac{1}{2}\sqrt{(1 - 4P^2)(1 - 4Q^2)} + \frac{k_\|}{2}\cos(\phi - \gamma)(1 + 4PQ). \tag{D.40}$$

Performing the integration over $p_\|$ also gives rise to the Jacobian factor

$$\frac{1}{|g'(p_\|)|} = \left[\frac{p_\| + p_z(\mathrm{d}p_z/\mathrm{d}p_\|)}{p} + \frac{p_\| + q_z(\mathrm{d}q_z/\mathrm{d}p_\|) - k_\| \cos(\phi - \gamma)}{q}\right]^{-1}. \tag{D.41}$$

The derivatives $\mathrm{d}p_z/\mathrm{d}p_\|$ may be obtained from the boundary condition Eq. D.4. They contribute at order $1/W$. Altogether, the bulk-bulk response tensor is now

$$\Gamma_{ijk}^{\mathrm{bb}} = \frac{8\pi\eta\tau}{W^3} \int \mathrm{d}\phi \sum_{p_z q_z} \frac{p_\|}{|g'(p_\|)|} (\hat{\mathbf{v}}_{\mathbf{p}+} + \hat{\mathbf{v}}_{\mathbf{q}-})_i \times M_j^{\mathrm{bb}} \left(M_k^{\mathrm{bb}}\right)^* \Theta[1 - p_z - q_z] \Bigg|_{p_\| = p_\|(p_z, q_z, \phi),\ \mathbf{q}_\| = \mathbf{p}_\| - \mathbf{k}_\|}. \tag{D.42}$$

Next, consider the matrix elements, M_i^{bb}. We can split them into a normalization factor that is common to all M_i and a factor that depends on i,

$$M_i^{\mathrm{bb}} = W \langle \text{bulk}, +, \mathbf{p} | \sigma_i e^{ik_z z - z/\delta} | \text{bulk}, -, \mathbf{q} \rangle = \frac{1}{\sqrt{N_{\mathbf{p}+} N_{\mathbf{q}-}}} \mathcal{M}_i, \tag{D.43}$$

where the $N_{\mathbf{p}\pm}$ are defined in Eq. (D.10). Using

$$\langle \alpha_+ | \boldsymbol{\sigma} | \alpha_+ \rangle = -\langle \alpha_- | \boldsymbol{\sigma} | \alpha_- \rangle = \boldsymbol{\alpha}_1,\ \langle \alpha_+ | \boldsymbol{\sigma} | \alpha_- \rangle = \langle \alpha_- | \boldsymbol{\sigma} | \alpha_+ \rangle^* = i\boldsymbol{\alpha}_2 + \hat{\mathbf{z}}, \tag{D.44}$$

the $\mathcal{M}_i$ read

$$\begin{aligned}\mathcal{M}_1 &= p_z q_z I_1 + [p_2 q_2 + (p - \chi p_1)(q + \chi q_1)] I_2 - (p_z q_2 I_3 + p_2 q_z I_4), && \text{(D.45a)}\\ \mathcal{M}_2 &= [\chi(p q_2 - p_2 q) - (p_1 q_2 + p_2 q_1)] I_2 \\ &\quad + (p_z q_1 I_3 + p_1 q_z I_4) + \chi(p_z q I_3 - p q_z I_4), && \text{(D.45b)}\\ \mathcal{M}_z &= i\Big\{[\chi(p q_2 + p_2 q) - (p_1 q_2 - p_2 q_1)] I_2 \\ &\quad - (p_z q_1 I_3 - p_1 q_z I_4) - \chi(p_z q I_3 + p q_z I_4)\Big\}, && \text{(D.45c)}\end{aligned}$$

where we defined $x_i = \boldsymbol{\alpha}_i \cdot \mathbf{x}$ as well as the integrals

$$I_1 = \int_0^W \mathrm{d}z\, e^{(ik_z - 1/\delta)z} \cos p_z z \cos q_z z, \quad I_2 = \int_0^W \mathrm{d}z\, e^{(ik_z - 1/\delta)z} \sin p_z z \sin q_z z, \tag{D.46a}$$

$$I_3 = \int_0^W \mathrm{d}z\, e^{(ik_z - 1/\delta)z} \cos p_z z \sin q_z z, \quad I_4 = \int_0^W \mathrm{d}z\, e^{(ik_z - 1/\delta)z} \sin p_z z \cos q_z z. \tag{D.46b}$$

These lead to conservation of "momentum" perpendicular to the boundary if W or δ become large. It will prove convenient to also define the combinations

$$I_\pm = p_z I_3 \pm q_z I_4 = P(I_3 \pm I_4) + Q(I_3 \mp I_4), \tag{D.47}$$

To leading order in $k_\parallel$, this gives

$$p_z q I_3 \pm p q_z I_4 = \frac{1}{2}\big[I_\pm - \big(4PQ + 2\mathbf{k}_\parallel \cdot \mathbf{p}_\parallel\big) I_\mp\big]. \tag{D.48}$$

D.5.1 THICK SLAB $W \gg \delta$

In this regime, the dominant term is of order δ/W, and corrections are of order $1/W$. We are hence expanding in $1/\delta \ll 1$. (Note that we still use dimensionless units, not writing the tilde to avoid clutter.) The corrections stem from the decay of the light field $1/\delta$ and the finite light momentum $\mathbf{k}$ with $k \sim 1/\delta$. Ignoring the quantization of p_z, q_z, which give corrections of order $1/W \ll 1/\delta$ we replace

$$\sum_{p_z q_z} \to \int_0^\infty \mathrm{d}p_z \int_0^\infty \mathrm{d}q_z \to \frac{2W^2}{\pi^2} \int_0^\infty \mathrm{d}P \int_{-P}^P \mathrm{d}Q. \tag{D.49}$$

We expand the bulk-bulk current in orders of $1/\delta$ and k_i.

LEADING ORDER BULK-BULK CONTRIBUTION $\Gamma^{\mathrm{BB,THICK}}$

For the leading-order contributions we set $\mathbf{k}_{\|} = 0$ (i.e., $\mathbf{p}_{\|} = \mathbf{q}_{\|}$) and analyze integrals of the type

$$\int_0^{1/2} \mathrm{d}P \int_{-P}^{P} \mathrm{d}Q \, I_i I_j^* f(P,Q), \tag{D.50}$$

which enter the current formula with a smooth kernel $f(P,Q) \sim \partial_{P,Q} f(P,Q) \sim 1$ (f does not depend on the small parameter). Considering $i = j = 1$, we find

$$|I_1|^2 \simeq \frac{4\left(\frac{1}{\delta^2} + k_z^2\right)\left(P^2+Q^2\right)^2}{\left(\frac{1}{\delta^2} + (k_z-2P)^2\right)\left(\frac{1}{\delta^2} + (k_z+2P)^2\right)\left(\frac{1}{\delta^2} + (k_z-2Q)^2\right)\left(\frac{1}{\delta^2} + (k_z+2Q)^2\right)}. \tag{D.51}$$

The leading contribution after integration is the term proportional to P^4. Next, we use that

$$\int_{-\infty}^{\infty} \mathrm{d}Q \frac{4(k_z^2 + \frac{1}{\delta^2})}{\left(\frac{1}{\delta^2} + (k_z-2Q)^2\right)\left(\frac{1}{\delta^2} + (k_z+2Q)^2\right)} = \pi\delta, \tag{D.52}$$

so that to leading order in k_z and $1/\delta$ we can simplify

$$\frac{4(k_z^2 + \frac{1}{\delta^2})}{\left(\frac{1}{\delta^2} + (k_z-2Q)^2\right)\left(\frac{1}{\delta^2} + (k_z+2Q)^2\right)} \to (\pi\delta)\delta(Q). \tag{D.53}$$

$|I_2|^2$ and $I_1 I_2^*$ are similar to $|I_1|^2$ with $\left(P^2+Q^2\right)^2$ replaced by $\left(P^2-Q^2\right)^2$ or $(P^4 - Q^4)$, respectively. They clearly give the same leading order behaviour. For $P \gg v/c$ we have to leading order

$$|I_1|^2 \simeq |I_2|^2 \simeq I_1 I_2^* \simeq \frac{\pi\delta}{16}\delta(Q). \tag{D.54}$$

This gives an overall factor of δ and hence contributes at leading order. Since $f(P,Q)$ is smooth, corrections from small $P \sim v/c$ are of higher order in v/c. Consider next $|I_\pm|^2$ and the corresponding cross-term. It is

$$|I_+|^2 \simeq \frac{4\left(\frac{1}{\delta^2} + k_z^2\right)^2\left(P^2+Q^2\right)^2}{\left(\frac{1}{\delta^2} + (k_z-2P)^2\right)\left(\frac{1}{\delta^2} + (k_z+2P)^2\right)\left(\frac{1}{\delta^2} + (k_z-2Q)^2\right)\left(\frac{1}{\delta^2} + (k_z+2Q)^2\right)} \tag{D.55}$$

The latter may be approximated as

$$|I_+|^2 \simeq \frac{\pi\left(\frac{1}{\delta^2} + k_z^2\right)\delta}{16}\delta(Q). \tag{D.56}$$

Due to the extra factor of $\frac{1}{\delta^2} + k_z^2$ this does not contribute at leading order. However,

$$|I_-|^2 \simeq \frac{64P^2Q^2(P^2 - Q^2)^2}{\left(\frac{1}{\delta^2} + (k_z - 2P)^2\right)\left(\frac{1}{\delta^2} + (k_z + 2P)^2\right)\left(\frac{1}{\delta^2} + (k_z - 2Q)^2\right)\left(\frac{1}{\delta^2} + (k_z + 2Q)^2\right)} \tag{D.57}$$

does not come with a small factor in the numerator at all. Naively one might expect a contribution of order δ^3. The factor of Q^2 reduces this to a contribution of order δ. The leading order contribution stems from the lowest power in Q, i.e. the term proportional to P^6Q^2. Then,

$$\int_{-P}^{P} \mathrm{d}Q\, \frac{64Q^2 f(P,Q)}{\left(\frac{1}{\delta^2} + (k_z - 2Q)^2\right)\left(\frac{1}{\delta^2} + (k_z + 2Q)^2\right)} \tag{D.58a}$$

$$= -\frac{4\delta}{k_z}\int_{-P}^{P} \mathrm{d}Q\, Q f(P,Q)\partial_Q\left[\frac{\pi}{2} - \arctan\left(\frac{\frac{1}{\delta^2} - k_z^2 + 4Q^2}{2k_z/\delta}\right)\right] \tag{D.58b}$$

$$\simeq 4\pi\delta f(P,0) \tag{D.58c}$$

Here, we integrated by parts and used

$$\frac{1}{k_z}\int_{-\infty}^{\infty} \mathrm{d}Q\left[\frac{\pi}{2} - \arctan\left(\frac{\frac{1}{\delta^2} - k_z^2 + 4Q^2}{2k_z/\delta}\right)\right] = \pi, \tag{D.59}$$

s.t. the integrand is again a delta function for $k_z, 1/\delta \to 0$. Hence, for $P \gg v/c$

$$|I_-|^2 \simeq \frac{\pi\delta}{4}P^2\delta(Q). \tag{D.60}$$

Thus, $|I_-|^2$ contributes at leading order. For the cross-term we find by a similar argument

$$I_+I_-^* \simeq -\frac{\pi(k_z + i/\delta)^2}{16}\delta P\partial_Q\delta(Q), \tag{D.61}$$

which is subleading. Finally, consider cross-terms of the type $I_1I_+^*$, $I_2I_+^*$, $I_1I_-^*$, $I_2I_-^*$. The former two read to leading order

$$I_iI_+^* \simeq \frac{4(k_z^2 + \frac{1}{\delta^2})(\delta^{-1} + ik_z)P^4}{\left(\frac{1}{\delta^2} + (k_z - 2P)^2\right)\left(\frac{1}{\delta^2} + (k_z + 2P)^2\right)\left(\frac{1}{\delta^2} + (k_z - 2Q)^2\right)\left(\frac{1}{\delta^2} + (k_z + 2Q)^2\right)}, \tag{D.62}$$

which yields

$$I_i I_+^* \simeq \frac{\pi(\delta^{-1} + ik_z)}{16}\delta\,\delta(Q), \tag{D.63}$$

and is thus overall subleading. Similarly, the latter two read

$$I_i I_-^* \simeq \frac{-16(1/\delta - ik_z)P^5 Q}{\left(\frac{1}{\delta^2} + (k_z - 2P)^2\right)\left(\frac{1}{\delta^2} + (k_z + 2P)^2\right)\left(\frac{1}{\delta^2} + (k_z - 2Q)^2\right)\left(\frac{1}{\delta^2} + (k_z + 2Q)^2\right)}, \tag{D.64}$$

evaluating to

$$I_i I_-^* \simeq \frac{\pi(k_z\delta - i)}{16} P\partial_Q \delta(Q). \tag{D.65}$$

This is also subleading. Having identified the leading combinations $I_i I_j^*$, we can now easily calculate the bulk-bulk current in the thick slab limit at leading order: We simply drop all combinations $I_i I_j^*$ with $i, j \in \{1, 2, +, -\}$ which do not give a order-δ contribution. The remaining combinations all give a delta function $\delta(Q)$, corresponding to conservation of perpendicular momentum, $p_z = q_z$, and hence $p = q = 1/2$ and $p_\| = \sqrt{1 - 4P^2}/2 = \sqrt{1 - p_z^2}/2$. Identifying the combinations $I_i I_j^*$ giving rise to order-δ terms motivates the following definition:

$$\boldsymbol{\mathcal{M}} \simeq \mathbf{\Sigma}_0 \mathcal{I}_0 + \mathbf{\Sigma}_1 \mathcal{I}_1, \tag{D.66}$$

where $\mathcal{I}_0 \simeq 2p^2 I_1 \simeq 2p^2 I_2$ and $\mathcal{I}_1 = p^2 I_-/P$. Here $\mathbf{\Sigma}_0$ is (up to normalization) the matrix element at fixed momentum,

$$\begin{aligned} \mathbf{\Sigma}_0 &\equiv \left(1 - \sin^2\theta \cos^2\phi\right)\boldsymbol{\alpha}_1 - \sin^2\theta\cos\phi\sin\phi\,\boldsymbol{\alpha}_2 + i\chi\sin\theta\sin\phi\,\hat{\mathbf{z}} && \text{(D.67a)} \\ &\propto \langle +, \mathbf{p}|\boldsymbol{\sigma}|-, \mathbf{p}\rangle, && \text{(D.67b)} \end{aligned}$$

in terms of the spherical coordinates $p_z = p\cos\theta$, $p_\| = p\sin\theta$, while

$$\mathbf{\Sigma}_1 \equiv \chi\cos\theta\,\boldsymbol{\alpha}_2 - i\cos\theta\sin\theta\cos\phi\,\hat{\mathbf{z}}.$$

This term in the matrix element only arises if one allows for $p_z \neq q_z$. It arises because $I_{3,4}$ may become large if $p_z - q_z \sim 1/\delta$ even though they vanish for $p_z = q_z$ (or $p_z - q_z \sim 1/W$ if the integral is cut off by the thickness of the slab, see below). The normalization factor evaluates to

$$\frac{1}{N_{\mathbf{p}+}N_{\mathbf{p}-}} = \frac{1}{p^4(1 - \sin^2\theta\cos^2\phi)}. \tag{D.68}$$

Altogether, after transforming $P = (\cos\theta)/2$, we have

$$\boldsymbol{\Gamma}^{\text{bb,thick}}_{0,ij} = \frac{\eta\tau\delta}{W} \int \mathrm{d}\Omega \, \frac{\Theta(\cos\theta)\begin{pmatrix}\cos\phi \\ \sin\phi\end{pmatrix}\sin\theta}{1 - \sin^2\theta\cos^2\phi} \big\{\Sigma_{0,i}\Sigma^*_{0,j} + \Sigma_{1,i}\Sigma^*_{1,j}\big\}. \tag{D.69}$$

The angular integrals may be evaluated straightforwardly. This gives Eq. (6.41). Note that the result is symmetric under rotations in the x, y-plane and thus independent of the direction of the boundary conditions.

Subleading order bulk-bulk contributions $\delta\Gamma^{\text{bb,thick}}$

We now consider the leading corrections δJ^{bb} to J^{bb}. From the above calculations, one can expect a correction of order

$$\frac{\delta\Gamma^{\text{bb}}}{\Gamma^{\text{bb}}} \sim \frac{v}{c} \ll 1. \tag{D.70}$$

stemming from two different sources: first, from an in-plane momentum shift due to the finite light momentum $\mathbf{k}_\parallel$, and second, from the corrections to the integrals $I_i I_j^*$ of order $(1/\delta)^0$, k_z^0. Consider first corrections due to finite light momentum. Since these are already of the same magnitude as the corrections due to finite-size as well as the arc-bulk current, one may ignore the slab geometry here. It is straightforward to verify that for a bulk Weyl cone these corrections vanish. We thus expect that the relevant corrections due to a finite $\mathbf{k}$ vanish also in the slab. We first consider finite $k_\parallel$. The products $I_i I_j^*$ do not involve $k_\parallel$ and are thus approximated as in the leading-order calculation above. In $\boldsymbol{\mathcal{M}}$ we can thus again separate out $\mathcal{I}_0 \simeq 2p^2 I_1 \simeq 2p^2 I_2$ and $\mathcal{I}_1 = p^2 I_- / P$ and expand the prefactors up to leading order in $k_\parallel$,

$$\boldsymbol{\mathcal{M}} \simeq \boldsymbol{\Sigma}'_0 \mathcal{I}_0 + \boldsymbol{\Sigma}'_1 \mathcal{I}_1, \text{ where } \boldsymbol{\Sigma}'_i = \boldsymbol{\Sigma}_i + k_\parallel \delta\boldsymbol{\Sigma}_i + \mathcal{O}\big(k_\parallel^2\big), \tag{D.71}$$

where, introducing the shorthand notation $c_x = \cos x$, $s_x = \sin x$,

$$\begin{aligned} \delta\boldsymbol{\Sigma}_0 = {} & \frac{1}{2}\big[\big(\chi s_\theta^2 c_\phi^2 + 2 s_\theta c_\phi s_\phi^2 - \chi\big)c_\gamma + c_\phi s_\phi\big(\chi s_\theta^2 - 2 s_\theta c_\phi\big)s_\gamma\big]\boldsymbol{\alpha}_1 \\ & + \frac{1}{2}\big[c_\phi s_\phi\big(\chi s_\theta^2 - 2 s_\theta c_\phi\big)c_\gamma + \big(\chi s_\theta^2 s_\phi^2 - 2 s_\theta c_\phi s_\phi^2 - \chi\big)s_\gamma + s_\theta s_{\phi+\gamma}\big]\boldsymbol{\alpha}_2 \\ & - \frac{i}{2} s_{\gamma-\phi}[s_\theta - \chi c_\phi]\hat{\mathbf{z}}, \end{aligned} \tag{D.72a}$$

$$\delta\boldsymbol{\Sigma}_1 = \frac{1}{2}\big\{s_\gamma \boldsymbol{\alpha}_1 - c_\gamma \boldsymbol{\alpha}_2 + i\big[-\big(s_\phi^2 + \chi s_\theta c_\phi\big)c_\gamma + (s_\phi c_\phi - \chi s_\theta s_\phi)s_\gamma\big]\hat{\mathbf{z}}\big\}. \tag{D.72b}$$

Other terms entering the current formula may be expanded as (up to linear order in $k_\parallel$)

$$\frac{p_\parallel(\hat{\mathbf{v}}_{\mathbf{p}+} + \hat{\mathbf{v}}_{\mathbf{q}-})}{\left|g'(p_\parallel)\right|} \simeq \frac{s_\theta}{2}\begin{pmatrix} c_\phi \\ s_\phi \end{pmatrix} + \frac{k_\parallel}{2}\begin{pmatrix} c_{\gamma-2\phi} \\ -s_{\gamma-2\phi} \end{pmatrix}, \tag{D.73a}$$

$$N_{\mathbf{p}+}N_{\mathbf{p}-} \simeq \frac{\left(1 - s_\theta^2 c_\phi^2\right)}{16} + \frac{k_\parallel}{8}[(s_\theta c_\phi - \chi)c_\gamma + (\chi s_\theta - c_\phi)s_\theta c_\phi c_{\gamma-\phi}]. \tag{D.73b}$$

We now specify to the basis of the thick slab, $\hat{\mathbf{x}} = \boldsymbol{\alpha}_1, \hat{\mathbf{y}} = \boldsymbol{\alpha}_2$. For $\gamma = 0$ (i.e., $\mathbf{k}_\parallel = k_\parallel\hat{\mathbf{x}}$) this combines to the total correction of the response tensor

$$\begin{aligned} \delta\Gamma_x^{\mathrm{bb},\mathbf{k}_\parallel} \propto & \int_0^{\frac{\pi}{2}} \mathrm{d}\theta \int_0^{2\pi} \mathrm{d}\phi \\ & \begin{pmatrix} c_\theta^2 - 4s_\theta^2 s_\phi^4 + (5s_\theta^2 - 2)s_\phi^2 & 2s_\theta^2 c_\phi s_\phi\left(2s_\phi^2 - 1\right) & is_\theta s_\phi\left(3s_\phi^2 - 2\right) \\ 2s_\theta^2 c_\phi s_\phi\left(2s_\phi^2 - 1\right) & 1 + 4s_\theta^2 s_\phi^4 + (3c_\theta^2 - 5)s_\phi^2 & ic_\phi s_\theta\left(1 - 3s_\phi^2\right) \\ -is_\phi s_\theta\left(3s_\phi^2 - 2\right) & -ic_\phi s_\theta\left(1 - 3s_\phi^2\right) & -s_\theta^2\left(2s_\phi^2 - 1\right) \end{pmatrix}, \end{aligned} \tag{D.74a}$$

$$\begin{aligned} \delta\Gamma_y^{\mathrm{bb},\mathbf{k}_\parallel} \propto & \int_0^{\frac{\pi}{2}} \mathrm{d}\theta \int_0^{2\pi} \mathrm{d}\phi \\ & \begin{pmatrix} c_\phi s_\phi\left(2c_\theta^2 + 4s_\theta^2 s_\phi^2\right) & s_\theta^2 s_\phi^2\left(4s_\phi^2 - 3\right) & -3ic_\phi s_\theta s_\phi^2 \\ s_\theta^2 s_\phi^2\left(4s_\phi^2 - 3\right) & c_\phi s_\phi\left(2 - 4s_\theta^2 s_\phi^2\right) & is_\theta s_\phi\left(2 - 3s_\phi^2\right) \\ 3ic_\phi s_\theta s_\phi^2 & is_\theta s_\phi\left(3s_\phi^2 - 2\right) & 2s_\theta^2 c_\phi s_\phi \end{pmatrix}. \end{aligned} \tag{D.74b}$$

It is straightforward to confirm that these expressions vanish upon integration over ϕ. Similar expressions for $\gamma = \pi/2$ (i.e., $\mathbf{k}_\parallel = k_\parallel\hat{\mathbf{y}}$) also vanish.

The remaining corrections are corrections to the products $I_i I_j$, which have been discussed above, of order $(k_z \pm i/\delta)^0$. We verified numerically, that the correction due to a finite k_z vanishes as expected. Fitting the numerically evaluated response tensor (for $\delta \in \{10^2, 2 \times$

	$\delta\Gamma^{\rm bb}_{xxy}$	$\delta\Gamma^{\rm bb}_{xyz}$	$\delta\Gamma^{\rm bb}_{yxx}$	$\delta\Gamma^{\rm bb}_{yyy}$	$\delta\Gamma^{\rm bb}_{yzz}$	$\delta\Gamma^{\rm bb}_{yzx}$
Error	5×10^{-4}	3×10^{-3}	5×10^{-5}	5×10^{-3}	1×10^{-3}	1×10^{-5}

Table D.1: Estimated inaccuracy of numerical results for the subleading bulk-bulk response tensor $\delta\Gamma^{\rm bb}$. The error corresponds to the statistical relative standard error of a fit with first order polynomial in $1/\delta$ and $\delta \in \{10^{2.8}, 10^{3.0}, ..., 10^{3.4}\}$ (for larger values of δ the integration is no longer stable due to the sharply peaked nature of the integrals I_i). Use of higher order polynomials or inclusion of smaller δ-points gives comparable results and deviations.

$10^2, ..., 10^3\}$) to an expansion up to second order in $1/\delta$ we find (rounding to the second decimal)

$$\frac{\delta\Gamma^{\rm bb,thick}_x}{\eta\tau/\tilde{W}} = \begin{pmatrix} 0 & 4.19 & 0 \\ 4.19 & 0 & -16.75i\chi \\ 0 & 16.75i\chi & 0 \end{pmatrix}, \tag{D.75a}$$

$$\frac{\delta\Gamma^{\rm bb,thick}_y}{\eta\tau/\tilde{W}} = \begin{pmatrix} -4.19 & 0 & 9.87i\chi \\ 0 & -4.20 & 0 \\ -9.87i\chi & 0 & -8.40 \end{pmatrix}. \tag{D.75b}$$

To estimate the accuracy of these results we compare the numerical values given here to those obtained by fitting expansions to higher order in $1/\delta$ as well as by adding/removing data points corresponding to the smallest values of δ. These changes in the fitting procedure lead to changes in the numerical coefficients of $\leq 0.5\%$. The error analysis is summarized in Table D.1.

D.5.2 THIN SLAB $\delta \gg W \gg \ell$

In this limit, the leading finite-size corrections are $\sim 1/W$, as discussed in the main text. Corrections due to the spatial variation of the external field, which we found to give corrections of order $\sim 1/\delta$, are thus negligible and we can set $\mathbf{k} = 0,\ \delta \to \infty$. We now work in the basis of the thin slab.

LEADING ORDER $\Gamma^{\rm BB,THIN}$

To calculate the leading order response we disregard the quantization of p_z, q_z. Considering leading-order terms of the integral products I_iI_j, the dominant contributions read

$$I_1^2 \simeq I_2^2 \simeq I_1I_2 \simeq \frac{\pi\tilde{W}}{8}\delta(Q),\ I_-^2 \simeq \frac{\pi\tilde{W}P^2}{2}\delta(Q), \tag{D.76}$$

all other combinations contribute only at higher order. Since the difference to the leading contribution of the thick-slab case is in the constant prefactor, the leading-order bulk-bulk contribution in the thin slab limit is given by the thick-slab result replacing $\delta/2 \to W$. The final response tensor reads

$$\Gamma^{\mathrm{bb}}_{ijk} = i\chi\frac{4\pi\eta\tau}{3}\varepsilon_{ijk}(1-\delta_{i,z}). \tag{D.77}$$

SUBLEADING ORDER $\delta\Gamma^{\mathrm{BB,THIN}}$

The leading corrections to the bulk-bulk contribution in the thin slab limit are of order $1/W$. They can stem from the quantization of p_z, q_z, the associated corrections to the velocity in Eq. (D.11), and the corrections $\delta N_{\mathbf{p}\pm}$ to the wavefunction normalization. The current is given by Eq. (D.42) with p_z, q_z solutions of

$$\sin\Delta = \frac{\tan(p_z W)}{p_z}\left[p_\| \cos\phi - \chi p\cos\Delta\right], \tag{D.78a}$$

$$\sin\Delta = \frac{\tan(q_z W)}{q_z}\left[p_\| \cos\phi + \chi q\cos\Delta\right], \tag{D.78b}$$

where we defined the characteristic angle

$$\Delta = \frac{\beta-\alpha}{2} \in [-\pi,\pi]. \tag{D.79}$$

These expressions as well as the tensors below are in the basis of the thin slab. Note that energy conservation makes $p_\|$ and thus also p and q depend on (p_z, q_z). To evaluate the expression for the current for a given value of Δ we resort to numerics. We then attempt to extract the functional dependence of the nonzero tensor components by fitting appropriate polynomials in $\sin\Delta$ and $\cos\Delta$.

We briefly outline the numerical strategy employed to extract the response tensor. For ϕ-integration at fixed W we employ standard numerical techniques relying on evaluation of the integrand for a discrete set of ϕ-points. For each ϕ-point we numerically determine all solutions to Eqs. (D.78) in the region $p_z + q_z < 1$. To determine $\delta\Gamma^{\mathrm{bb}}$ we evaluate Eq. (D.42) at $W \in \{100, 150, 200, 250\}$ and subtract the leading order term, Eq. (D.77). We then fit to an expansion up to second order in $1/W$ and extract the coefficient of the $1/W$ term. In this way we determine all symmmetry-allowed elements of $\delta\Gamma^{\mathrm{bb}}$ for 30 values of $\Delta \in [0, \pi/2]$ (the intervals $[-\pi, 0]$ and $[\pi/2, \pi]$ may be obtained from symmetry considerations, see Sec. D.3).

Finally, we fit the components of the symmetric part of the response tensor to each element to an appropriate expansion in Fourier modes,

$$\sum_{n\ \text{odd}}^{n_{\text{max}}} a_n^{\text{s}} \sin(n\Delta),$$

where we exploit that they are odd under $\Delta \to -\Delta$ and $\Delta \to \Delta + \pi$. Similarly, we fit the components of the anti-symmetric part to

$$a_0^{\text{as}} + \sum_{n\ \text{even}}^{n_{\text{max}}} a_n^{\text{as}} \cos(n\Delta),$$

where we use that they are even under the above transformations. We found that $n_{\text{max}} = 3$ gives sufficiently good results with higher order coefficients satisfying $a_{n>3}/(\max a_{n\leq 3}) \lesssim 10^{-3}$. Rounding to 10^{-2}, the nonzero entries of the subleading order response tensor due to bulk-bulk excitations in the thin slab limit are

$$\frac{\delta\Gamma_{xxx}^{\text{bb,thin}}}{\eta\tau/W} = -14.14 \sin\Delta + 4.71 \sin 3\Delta, \tag{D.80a}$$

$$\frac{\delta\Gamma_{xyy}^{\text{bb,thin}}}{\eta\tau/W} = -21.47 \sin\Delta - 4.71 \sin 3\Delta, \tag{D.80b}$$

$$\frac{\delta\Gamma_{xzz}^{\text{bb,thin}}}{\eta\tau/W} = -23.04 \sin\Delta, \tag{D.80c}$$

$$\frac{\delta\Gamma_{xyz}^{\text{bb,thin}}}{\eta\tau/W} = -i\chi(26.71 + 6.88 \cos 2\Delta), \tag{D.80d}$$

$$\frac{\delta\Gamma_{yxy}^{\text{bb,thin}}}{\eta\tau/W} = 3.67 \sin\Delta - 4.71 \sin 3\Delta, \tag{D.80e}$$

$$\frac{\delta\Gamma_{yzx}^{\text{bb,thin}}}{\eta\tau/W} = -i\chi(26.50 - 6.89 \cos 2\Delta). \tag{D.80f}$$

These results are accurate to the first decimal: the error estimates of the numerical integration scheme are on the order of 10^{-1} to 10^{-2}. Similarly, altering the fitting procedure (e.g. by fitting to a first order expansion in $1/W$ or by removing data-points in W) leads to changes in the numerical coefficients on the order of roughly 10^{-2} with the largest changes, at about 1%, observed for the Δ-independent terms in the circular components. Note that averaging over $\Delta \in [-\pi, \pi]$ restores rotational symmetry around the z-axis, which implies that the Δ-independent terms of Γ_{xyz} and Γ_{yzx} should actually be equal. Here, they differ by roughly 0.5%, consistent with our error estimate.

BIBLIOGRAPHY

I. J. F. Steiner, C. Mora, K. J. Franke, and F. von Oppen, “Quantum magnetism and topological superconductivity in Yu-Shiba-Rusinov chains”, Phys. Rev. Lett. **128**, 036801 (2022).

II. E. Liebhaber, L. M. Rütten, G. Reecht, J. F. Steiner, S. Rohlf, K. Rossnagel, F. von Oppen, and K. J. Franke, “Quantum spins and hybridization in artificially-constructed chains of magnetic adatoms on a superconductor”, Nat. Commun. **13**, 2160 (2022).

III. H. Schmid, J. F. Steiner, K. J. Franke, and F. von Oppen, “Quantum Yu-Shiba-Rusinov dimers”, Phys. Rev. B **105**, 235406 (2022).

IV. J. F. Steiner, L. Melischek, M. Trahms, K. J. Franke, and F. von Oppen, “Diode effects in current-biased Josephson junctions”, Phys. Rev. Lett. **130**, 177002 (2023).

V. M. Trahms, L. Melischek, J. F. Steiner, B. Mahendru, I. Tamir, N. Bogdanoff, O. Peters, G. Reecht, C. B. Winkelmann, F. von Oppen, and K. Franke, “Diode effect in Josephson junctions with a single magnetic atom”, Nature **615**, 628 (2023).

VI. J. F. Steiner, L. Melischek, F. von Oppen, and K. J. Franke, “Keldysh effective action and Langevin dynamics of nonreciprocal Josephson junctions”, unpublished (2023).

VII. J. F. Steiner and F. von Oppen, “Readout of Majorana qubits”, Phys. Rev. Res. **2**, 033255 (2020).

VIII. J. F. Steiner, A. V. Andreev, and M. Breitkreiz, “Surface photogalvanic effect in Weyl semimetals”, Phys. Rev. Res. **4**, 023021 (2022).

IX. J. F. Steiner, A. V. Andreev, and D. A. Pesin, “Anomalous Hall effect in type-I Weyl metals”, Phys. Rev. Lett. **119**, 036601 (2017).

1. A. G. J. MacFarlane, J. P. Dowling, and G. J. Milburn, “Quantum technology: the second quantum revolution”, Philos. Trans. R. Soc. **361**, 1655 (2003).
2. X. G. Wen and Q. Niu, “Ground-state degeneracy of the fractional quantum Hall states in the presence of a random potential and on high-genus Riemann surfaces”, Phys. Rev. B **41**, 9377 (1990).
3. M. Z. Hasan and C. L. Kane, “Colloquium: Topological insulators”, Rev. Mod. Phys. **82**, 3045 (2010).
4. D. Xiao, M.-C. Chang, and Q. Niu, “Berry phase effects on electronic properties”, Rev. Mod. Phys. **82**, 1959 (2010).
5. L. Yu, “Bound state in superconductors with paramagnetic impurities”, Acta Phys. Sin. **21**, 75 (1965).

6. H. Shiba, “Classical spins in superconductors”, Prog. Theor. Phys. **40**, 435 (1968).
7. A. I. Rusinov, “Superconcductivity near a paramagnetic impurity”, JETP Lett. **9**, 85 (1969).
8. M. Ruby, B. W. Heinrich, Y. Peng, F. von Oppen, and K. J. Franke, “Wave-function hybridization in Yu-Shiba-Rusinov dimers”, Phys. Rev. Lett. **120**, 156803 (2018).
9. D.-J. Choi, C. G. Fernández, E. Herrera, C. Rubio-Verdú, M. M. Ugeda, I. Guillamón, H. Suderow, J. I. Pascual, and N. Lorente, “Influence of magnetic ordering between cr adatoms on the Yu-Shiba-Rusinov states of the $\beta-\mathrm{Bi_2Pd}$ superconductor”, Phys. Rev. Lett. **120**, 167001 (2018).
10. A. Kamlapure, L. Cornils, J. Wiebe, and R. Wiesendanger, “Engineering the spin couplings in atomically crafted spin chains on an elemental superconductor”, Nat. Commun. **9**, 3253 (2018).
11. K. J. Franke, G. Schulze, and J. I. Pascual, “Competition of superconducting phenomena and Kondo screening at the nanoscale”, Science **332**, 940 (2011).
12. L. Farinacci, G. Ahmadi, G. Reecht, M. Ruby, N. Bogdanoff, O. Peters, B. W. Heinrich, F. von Oppen, and K. J. Franke, “Tuning the coupling of an individual magnetic impurity to a superconductor: quantum phase transition and transport”, Phys. Rev. Lett. **121**, 196803 (2018).
13. E. Liebhaber, S. Acero González, R. Baba, G. Reecht, B. W. Heinrich, S. Rohlf, K. Rossnagel, F. von Oppen, and K. J. Franke, “Yu–Shiba–Rusinov states in the charge-density modulated superconductor $\mathrm{NbSe_2}$”, Nano Lett. **20**, 339 (2020).
14. A. Odobesko, D. Di Sante, A. Kowalski, S. Wilfert, F. Friedrich, R. Thomale, G. Sangiovanni, and M. Bode, “Observation of tunable single-atom Yu-Shiba-Rusinov states”, Phys. Rev. B **102**, 174504 (2020).
15. D. M. Eigler and E. K. Schweizer, “Positioning single atoms with a scanning tunnelling microscope”, Nature **344**, 524 (1990).
16. W. Ko, C. Ma, G. D. Nguyen, M. Kolmer, and A.-P. Li, “Atomic-scale manipulation and in situ characterization with scanning tunneling microscopy”, Adv. Funct. Mater. **29**, 1903770 (2019).
17. A. Yazdani, B. A. Jones, C. P. Lutz, M. F. Crommie, and D. M. Eigler, “Probing the local effects of magnetic impurities on superconductivity”, Science **275**, 1767 (1997).
18. A. V. Balatsky, I. Vekhter, and J.-X. Zhu, “Impurity-induced states in conventional and unconventional superconductors”, Rev. Mod. Phys. **78**, 373 (2006).
19. S.-H. Ji, T. Zhang, Y.-S. Fu, X. Chen, X.-C. Ma, J. Li, W.-H. Duan, J.-F. Jia, and Q.-K. Xue, “High-resolution scanning tunneling spectroscopy of magnetic impurity induced bound states in the superconducting gap of Pb thin films”, Phys. Rev. Lett. **100**, 226801 (2008).
20. B. W. Heinrich, J. I. Pascual, and K. J. Franke, “Single magnetic adsorbates on s-wave superconductors”, Prog. Surf. Sci. **93**, 1 (2018).
21. S. Kezilebieke, M. Dvorak, T. Ojanen, and P. Liljeroth, “Coupled Yu-Shiba-Rusinov states in molecular dimers on $\mathrm{NbSe_2}$”, Nano Lett. **18**, 2311 (2018).

22. P. Beck, L. Schneider, L. Rózsa, K. Palotás, A. Lászlóffy, L. Szunyogh, J. Wiebe, and R. Wiesendanger, "Spin-orbit coupling induced splitting of Yu-Shiba-Rusinov states in antiferromagnetic dimers", Nat. Commun. **12**, 2040 (2020).
23. H. Huang, R. Drost, J. Senkpiel, C. Padurariu, B. Kubala, A. L. Yeyati, J. C. Cuevas, J. Ankerhold, K. Kern, and C. R. Ast, "Quantum phase transitions and the role of impurity-substrate hybridization in Yu-Shiba-Rusinov states", Commun. Physics **3**, 1227 (2020).
24. H. Ding, Y. Hu, M. T. Randeria, S. Hoffman, O. Deb, J. Klinovaja, D. Loss, and A. Yazdani, "Tuning interactions between spins in a superconductor", Proc. Natl. Acad. Sci. **118**, e2024837118 (2021).
25. F. Küster, S. Brinker, S. Lounis, S. S. P. Parkin, and P. Sessi, "Long range and highly tunable coupling between local spins coupled to a superconducting condensate", Nat. Commun. **12**, 6722 (2021).
26. F. Friedrich, R. Boshuis, M. Bode, and A. Odobesko, "Coupling of Yu-Shiba-Rusinov states in one-dimensional chains of Fe atoms on Nb (110)", Phys. Rev. B **103**, 235437 (2021).
27. L. Schneider, P. Beck, T. Posske, D. Crawford, E. Mascot, S. Rachel, R. Wiesendanger, and J. Wiebe, "Topological Shiba bands in artificial spin chains on superconductors", Nat. Phys. **17**, 943 (2021).
28. L. Schneider, P. Beck, J. Neuhaus-Steinmetz, L. Rózsa, T. Posske, J. Wiebe, and R. Wiesendanger, "Precursors of Majorana modes and their length-dependent energy oscillations probed at both ends of atomic Shiba chains", Nat. Nanutechnol. **17**, 384 (2022).
29. F. Küster, S. Brinker, R. Hess, D. Loss, S. S. Parkin, J. Klinovaja, S. Lounis, and P. Sessi, "Non-Majorana modes in diluted spin chains proximitized to a superconductor", Proc. Natl. Acad. Sci. **119**, e2210589119 (2022).
30. S. Nadj-Perge, I. K. Drozdov, J. Li, H. Chen, S. Jeon, J. Seo, A. H. MacDonald, B. A. Bernevig, and A. Yazdani, "Observation of Majorana fermions in ferromagnetic atomic chains on a superconductor", Science **346**, 602 (2014).
31. M. Ruby, F. Pientka, Y. Peng, F. von Oppen, B. W. Heinrich, and K. J. Franke, "End states and subgap structure in proximity-coupled chains of magnetic adatoms", Phys. Rev. Lett. **115**, 197204 (2015).
32. A. Mishra, P. Simon, T. Hyart, and M. Trif, "Yu-Shiba-Rusinov qubit", PRX Quantum **2**, 040347 (2021).
33. G. Sharma and S. Tewari, "Yu-Shiba-Rusinov states and topological superconductivity in Ising paired superconductors", Phys. Rev. B **94**, 094515 (2016).
34. J. Senkpiel, C. Rubio-Verdú, M. Etzkorn, R. Drost, L. M. Schoop, S. Dambach, C. Padurariu, B. Kubala, J. Ankerhold, C. R. Ast, and K. Kern, "Robustness of Yu-Shiba-Rusinov resonances in the presence of a complex superconducting order parameter", Phys. Rev. B **100**, 014502 (2019).
35. C.-K. Chiu and Z. Wang, "Yu-Shiba-Rusinov states in a superconductor with topological $\mathbb{Z}_2$ bands", Phys. Rev. Lett. **128**, 237001 (2022).

36. J. Ortuzar, S. Trivini, M. Alvarado, M. Rouco, J. Zaldivar, A. L. Yeyati, J. I. Pascual, and F. S. Bergeret, “Yu-Shiba-Rusinov states in two-dimensional superconductors with arbitrary Fermi contours”, Phys. Rev. B **105**, 245403 (2022).
37. U. Kamber, Y. Hu, Y.-C. Tsui, K. Gu, D. Shulman, H. Ding, P. Rosa, B. Lian, and A. Yazdani, “Yu-Shiba-Rusinov states as a probe of the order parameter symmetry in UTe_2”, Bulletin of the American Physical Society (2023).
38. S. Nadj-Perge, I. K. Drozdov, B. A. Bernevig, and A. Yazdani, “Proposal for realizing Majorana fermions in chains of magnetic atoms on a superconductor”, Phys. Rev. B **88**, 020407 (2013).
39. F. Pientka, L. I. Glazman, and F. von Oppen, “Topological superconducting phase in helical Shiba chains”, Phys. Rev. B **88**, 155420 (2013).
40. A. Y. Kitaev, “Unpaired Majorana fermions in quantum wires”, Phys.-Usp. **44**, 131 (2001).
41. A. Y. Kitaev, “Fault-tolerant quantum computation by anyons”, Ann. Phys. **303**, 2 (2003).
42. N. Read and D. Green, “Paired states of fermions in two dimensions with breaking of parity and time-reversal symmetries and the fractional quantum Hall effect”, Phys. Rev. B **61**, 10267 (2000).
43. D. A. Ivanov, “Non-abelian statistics of half-quantum vortices in p-wave superconductors”, Phys. Rev. Lett. **86**, 268 (2001).
44. C. Nayak, S. H. Simon, A. Stern, M. Freedman, and S. Das Sarma, “Non-Abelian anyons and topological quantum computation”, Rev. Mod. Phys. **80**, 1083 (2008).
45. T. Karzig, C. Knapp, R. M. Lutchyn, P. Bonderson, M. B. Hastings, C. Nayak, J. Alicea, K. Flensberg, S. Plugge, Y. Oreg, C. M. Marcus, and M. H. Freedman, “Scalable designs for quasiparticle-poisoning-protected topological quantum computation with Majorana zero modes”, Phys. Rev. B **95**, 235305 (2017).
46. S. Plugge, L. A. Landau, E. Sela, A. Altland, K. Flensberg, and R. Egger, “Roadmap to Majorana surface codes”, Phys. Rev. B **94**, 174514 (2016).
47. C. Wille, R. Egger, J. Eisert, and A. Altland, “Simulating topological tensor networks with Majorana qubits”, Phys. Rev. B **99**, 115117 (2019).
48. Y. You and F. von Oppen, “Building fracton phases by Majorana manipulation”, Phys. Rev. Res. **1**, 013011 (2019).
49. K. Flensberg, F. von Oppen, and A. Stern, “Engineered platforms for topological superconductivity and Majorana zero modes”, Nat. Rev. Mater. **6**, 944 (2021).
50. R. M. Lutchyn, J. D. Sau, and S. Das Sarma, “Majorana fermions and a topological phase transition in semiconductor-superconductor heterostructures”, Phys. Rev. Lett. **105**, 077001 (2010).
51. Y. Oreg, G. Refael, and F. von Oppen, “Helical liquids and Majorana bound states in quantum wires”, Phys. Rev. Lett. **105**, 177002 (2010).
52. V. Mourik, K. Zuo, S. M. Frolov, S. Plissard, E. P. Bakkers, and L. P. Kouwenhoven, “Signatures of Majorana fermions in hybrid superconductor-semiconductor nanowire devices”, Science **336**, 1003 (2012).

53. E. Prada, P. San-Jose, M. W. de Moor, A. Geresdi, E. J. Lee, J. Klinovaja, D. Loss, J. Nygård, R. Aguado, and L. P. Kouwenhoven, "From Andreev to Majorana bound states in hybrid superconductor-semiconductor nanowires", Nat. Rev. Phys. **2**, 575 (2020).
54. A. Kitaev, "Periodic table for topological insulators and superconductors", AIP conf. proc. **1134**, 22 (2009).
55. S. Ryu, A. P. Schnyder, A. Furusaki, and A. W. Ludwig, "Topological insulators and superconductors: tenfold way and dimensional hierarchy", New J. Phys. **12**, 065010 (2010).
56. X. Wan, A. M. Turner, A. Vishwanath, and S. Y. Savrasov, "Topological semimetal and Fermi-arc surface states in the electronic structure of pyrochlore iridates", Phys. Rev. B **83**, 205101 (2011).
57. H. Weyl, "Gravitation and the electron", Proc. Natl. Acad. Sci. **15**, 323 (1929).
58. H. B. Nielsen and M. Ninomiya, "No-go theorem for regularizing chiral fermions", Phys. Lett. B **105**, 219 (1981).
59. H. B. Nielsen and M. Ninomiya, "The Adler-Bell-Jackiw anomaly and Weyl fermions in a crystal", Phys. Lett. B **130**, 389 (1983).
60. S. Murakami, "Phase transition between the quantum spin Hall and insulator phases in 3d: emergence of a topological gapless phase", New J. Phys. **9**, 356 (2007).
61. P. Hosur, S. A. Parameswaran, and A. Vishwanath, "Charge transport in Weyl semimetals", Phys. Rev. Lett. **108**, 046602 (2012).
62. M. M. Vazifeh and M. Franz, "Electromagnetic response of Weyl semimetals", Phys. Rev. Lett. **111**, 027201 (2013).
63. K.-Y. Yang, Y.-M. Lu, and Y. Ran, "Quantum Hall effects in a Weyl semimetal: possible application in pyrochlore iridates", Phys. Rev. B **84**, 075129 (2011).
64. K. Fukushima, D. E. Kharzeev, and H. J. Warringa, "Chiral magnetic effect", Phys. Rev. D **78**, 074033 (2008).
65. D. T. Son and B. Z. Spivak, "Chiral anomaly and classical negative magnetoresistance of Weyl metals", Phys. Rev. B **88**, 104412 (2013).
66. B. Z. Spivak and A. V. Andreev, "Magnetotransport phenomena related to the chiral anomaly in Weyl semimetals", Phys. Rev. B **93**, 085107 (2016).
67. P. E. C. Ashby and J. P. Carbotte, "Chiral anomaly and optical absorption in Weyl semimetals", Phys. Rev. B **89**, 245121 (2014).
68. C.-K. Chan, P. A. Lee, K. S. Burch, J. H. Han, and Y. Ran, "When chiral photons meet chiral fermions: photoinduced anomalous Hall effects in Weyl semimetals", Phys. Rev. Lett. **116**, 026805 (2016).
69. T. Morimoto, S. Zhong, J. Orenstein, and J. E. Moore, "Semiclassical theory of nonlinear magneto-optical responses with applications to topological Dirac/Weyl semimetals", Phys. Rev. B **94**, 245121 (2016).

70. K. Taguchi, T. Imaeda, M. Sato, and Y. Tanaka, "Photovoltaic chiral magnetic effect in Weyl semimetals", Phys. Rev. B **93**, 201202 (2016).
71. C.-K. Chan, N. H. Lindner, G. Refael, and P. A. Lee, "Photocurrents in Weyl semimetals", Phys. Rev. B **95**, 041104 (2017).
72. F. de Juan, A. G. Grushin, T. Morimoto, and J. E. Moore, "Quantized circular photogalvanic effect in Weyl semimetals", Nat. Commun. **8**, 15995 (2017).
73. L. E. Golub, E. L. Ivchenko, and B. Z. Spivak, "Photocurrent in gyrotropic Weyl semimetals", JETP Lett. **105**, 782 (2017).
74. E. J. König, H.-Y. Xie, D. A. Pesin, and A. Levchenko, "Photogalvanic effect in Weyl semimetals", Phys. Rev. B **96**, 075123 (2017).
75. D. E. Kharzeev, Y. Kikuchi, R. Meyer, and Y. Tanizaki, "Giant photocurrent in asymmetric Weyl semimetals from the helical magnetic effect", Phys. Rev. B **98**, 014305 (2018).
76. E. Witten, "Three lectures on topological phases of matter", Rivista del Nuovo Cimento **39**, 313 (2016).
77. A. C. Potter, I. Kimchi, and A. Vishwanath, "Quantum oscillations from surface Fermi arcs in Weyl and Dirac semimetals", Nat. Commun. **5**, 5161 (2014).
78. A. A. Burkov, "Anomalous Hall Effect in Weyl Metals", Phys. Rev. Lett. **113**, 187202 (2014).
79. P. J. W. Moll, N. L. Nair, T. Helm, A. C. Potter, I. Kimchi, A. Vishwanath, and J. G. Analytis, "Transport evidence for Fermi-arc-mediated chirality transfer in the Dirac semimetal Cd_3As_2", Nat. Lett. **535**, 266 (2016).
80. C. M. Wang, H. P. Sun, H. Z. Lu, and X. C. Xie, "3D quantum Hall effect of Fermi arc in topological semimetals", Phys. Rev. Lett. **119**, 136806 (2017).
81. G. Resta, S.-T. Pi, X. Wan, and S. Y. Savrasov, "High surface conductivity of Fermi-arc electrons in Weyl semimetals", Phys. Rev. B **97**, 085142 (2018).
82. J. Behrends, R. Ilan, and J. H. Bardarson, "Anomalous conductance scaling in strained Weyl semi-metals", Phys. Rev. Res. **1**, 032028 (2019).
83. C. Zhang, Z. Ni, J. Zhang, X. Yuan, Y. Liu, Y. Zou, Z. Liao, Y. Du, A. Narayan, H. Zhang, T. Gu, X. Zhu, L. Pi, S. Sanvito, X. Han, J. Zou, Y. Shi, X. Wan, S. Y. Savrasov, and F. Xiu, "Ultrahigh conductivity in Weyl semimetal NbAs nanobelts", Nat. Mater. **18**, 482 (2019).
84. P. O. Sukhachov, M. V. Rakov, O. M. Teslyk, and E. V. Gorbar, "Fermi arcs and DC transport in nanowires of Dirac and Weyl semimetals", Ann. Phys. **532**, 1900449 (2019).
85. M. Breitkreiz and P. W. Brouwer, "Large contribution of Fermi arcs to the conductivity of topological metals", Phys. Rev. Lett. **123**, 066804 (2019).
86. V. Kaladzhyan and J. H. Bardarson, "Quantized Fermi-arc-mediated transport in Weyl semimetal nanowires", Phys. Rev. B **100**, 085424 (2019).

87. C. Zhang, Y. Zhang, H.-Z. Lu, X. C. Xie, and F. Xiu, “Cycling Fermi arc electrons with Weyl orbits”, Nat. Rev. Phys. **3**, 660 (2021).

88. M. Breitkreiz, “Parabolic Hall effect due to co-propagating surface modes”, Phys. Rev. Res. **2**, 012071(R) (2020).

89. P. M. Perez-Piskunow, N. Bovenzi, A. R. Akhmerov, and M. Breitkreiz, “Chiral anomaly trapped in Weyl metals: nonequilibrium valley polarization at zero magnetic field”, SciPost Phys. **11**, 46 (2021).

90. B. Q. Lv, H. M. Weng, B. B. Fu, X. P. Wang, H. Miao, J. Ma, P. Richard, X. C. Huang, L. X. Zhao, G. F. Chen, Z. Fang, X. Dai, T. Qian, and H. Ding, “Experimental discovery of Weyl semimetal TaAs”, Phys. Rev. X **5**, 031013 (2015).

91. L. X. Yang, Z. K. Liu, Y. Sun, H. Peng, H. F. Yang, T. Zhang, B. Zhou, Y. Zhang, Y. F. Guo, M. Rahn, D. Prabhakaran, Z. Hussain, S.-K. Mo, C. Felser, B. Yan, and Y. L. Chen, “Weyl semimetal phase in the non-centrosymmetric compound TaAs”, Nat. Phys. **11**, 728 (2015).

92. S.-Y. Xu, N. Alidoust, I. Belopolski, Z. Yuan, G. Bian, T.-R. Chang, H. Zheng, V. N. Strocov, D. S. Sanchez, G. Chang, C. Zhang, D. Mou, Y. Wu, L. Huang, C.-C. Lee, S.-M. Huang, B. Wang, A. Bansil, H.-T. Jeng, T. Neupert, A. Kaminski, H. Lin, S. Jia, and M. Zahid Hasan, “Discovery of a Weyl fermion state with Fermi arcs in niobium arsenide”, Nat. Phys. **11**, 748 (2015).

93. E. Liu, Y. Sun, N. Kumar, L. Muechler, A. Sun, L. Jiao, S.-Y. Yang, D. Liu, A. Liang, Q. Xu, J. Kroder, V. Süß, H. Borrmann, C. Shekhar, Z. Wang, C. Xi, W. Wang, W. Schnelle, S. Wirth, Y. Chen, S. T. B. Goennenwein, and C. Felser, “Giant anomalous Hall effect in a ferromagnetic kagome-lattice semimetal”, Nat. Phys. **14**, 1125 (2018).

94. T. Suzuki, R. Chisnell, A. Devarakonda, Y.-T. Liu, W. Feng, D. Xiao, J. W. Lynn, and J. G. Checkelsky, “Large anomalous Hall effect in a half-Heusler antiferromagnet”, Nat. Phys. **12**, 1119 (2016).

95. D. Rees, K. Manna, B. Lu, T. Morimoto, H. Borrmann, C. Felser, J. Moore, D. H. Torchinsky, and J. Orenstein, “Helicity-dependent photocurrents in the chiral Weyl semimetal RhSi”, Sci. Adv. **6**, eaba0509 (2020).

96. V. Fatemi, A. R. Akhmerov, and L. Bretheau, “Weyl Josephson circuits”, Phys. Rev. Res. **3**, 013288 (2021).

97. J. Cano, B. Bradlyn, Z. Wang, M. Hirschberger, N. P. Ong, and B. A. Bernevig, “Chiral anomaly factory: creating Weyl fermions with a magnetic field”, Phys. Rev. B **95**, 161306 (2017).

98. R. Ilan, A. G. Grushin, and D. I. Pikulin, “Pseudo-electromagnetic fields in 3d topological semimetals”, Nat. Rev. Phys. **2**, 29 (2020).

99. E. J. Sie, C. M. Nyby, C. D. Pemmaraju, S. J. Park, X. Shen, J. Yang, M. C. Hoffmann, B. K. Ofori-Okai, R. Li, A. H. Reid, S. Weathersby, E. Mannebach, N. Finney, D. Rhodes, D. Chenet, A. Antony, L. Balicas, J. Hone, T. P. Devereaux, T. F. Heinz, X. Wang, and A. M. Lindenberg, “An ultrafast symmetry switch in a Weyl semimetal”, Nature **565**, 61 (2019).

100. C.-L. Zhang, S.-Y. Xu, C. M. Wang, Z. Lin, Z. Z. Du, C. Guo, C.-C. Lee, H. Lu, Y. Feng, S.-M. Huang, G. Chang, C.-H. Hsu, H. Liu, H. Lin, L. Li, C. Zhang, J. Zhang, X.-C. Xie, T. Neupert, M. Z. Hasan, H.-Z. Lu, J. Wang, and S. Jia, "Magnetic-tunnelling-induced Weyl node annihilation in TaP", Nat. Phys. **13**, 979 (2017).

101. M.-X. Guan, E. Wang, P.-W. You, J.-T. Sun, and S. Meng, "Manipulating Weyl quasiparticles by orbital-selective photoexcitation in WTe_2", Nat. Commun. **12**, 1885 (2021).

102. S. Chen, A. Bouhon, R.-J. Slager, and B. Monserrat, "Non-abelian braiding of Weyl nodes via symmetry-constrained phase transitions", Phys. Rev. B **105**, L081117 (2022).

103. K. Pöyhönen, A. Westström, J. Röntynen, and T. Ojanen, "Majorana states in helical Shiba chains and ladders", Phys. Rev. B **89**, 115109 (2014).

104. A. Heimes, P. Kotetes, and G. Schön, "Majorana fermions from Shiba states in an antiferromagnetic chain on top of a superconductor", Phys. Rev. B **90**, 060507 (2014).

105. Y. Kim, M. Cheng, B. Bauer, R. M. Lutchyn, and S. Das Sarma, "Helical order in one-dimensional magnetic atom chains and possible emergence of Majorana bound states", Phys. Rev. B **90**, 060401 (2014).

106. P. M. R. Brydon, S. Das Sarma, H.-Y. Hui, and J. D. Sau, "Topological Yu-Shiba-Rusinov chain from spin-orbit coupling", Phys. Rev. B **91**, 064505 (2015).

107. S. Hoffman, J. Klinovaja, T. Meng, and D. Loss, "Impurity-induced quantum phase transitions and magnetic order in conventional superconductors: competition between bound and quasiparticle states", Phys. Rev. B **92**, 125422 (2015).

108. M. Schecter, K. Flensberg, M. H. Christensen, B. M. Andersen, and J. Paaske, "Self-organized topological superconductivity in a Yu-Shiba-Rusinov chain", Phys. Rev. B **93**, 140503 (2016).

109. V. Kaladzhyan, C. Bena, and P. Simon, "Characterizing p-wave superconductivity using the spin structure of Shiba states", Phys. Rev. B **93**, 214514 (2016).

110. S. Körber, B. Trauzettel, and O. Kashuba, "Collective Yu-Shiba-Rusinov states in magnetic clusters at superconducting surfaces", Phys. Rev. B **97**, 184503 (2018).

111. C. F. Hirjibehedin, C.-Y. Lin, A. F. Otte, M. Ternes, C. P. Lutz, B. A. Jones, and A. J. Heinrich, "Large magnetic anisotropy of a single atomic spin embedded in a surface molecular network", Science **317**, 1199 (2007).

112. N. Tsukahara, K.-i. Noto, M. Ohara, S. Shiraki, N. Takagi, Y. Takata, J. Miyawaki, M. Taguchi, A. Chainani, S. Shin, and M. Kawai, "Adsorption-induced switching of magnetic anisotropy in a single iron(ii) phthalocyanine molecule on an oxidized Cu(110) surface", Phys. Rev. Lett. **102**, 167203 (2009).

113. B. W. Heinrich, L. Braun, J. I. Pascual, and K. J. Franke, "Protection of excited spin states by a superconducting energy gap", Nat. Phys. **9**, 765 (2013).

114. S. Kezilebieke, R. Zitko, M. Dvorak, T. Ojanen, and P. Liljeroth, "Observation of coexistence of Yu-Shiba-Rusinov states and spin-flip excitations", Nano Lett. **19**, 4614 (2019).

115. V. Madhavan, W. Chen, T. Jamneala, M. F. Crommie, and N. S. Wingreen, “Tunneling into a single magnetic atom: spectroscopic evidence of the Kondo resonance”, Science **280**, 567 (1998).

116. J. Li, W.-D. Schneider, R. Berndt, and B. Delley, “Kondo scattering observed at a single magnetic impurity”, Phys. Rev. Lett. **80**, 2893 (1998).

117. N. Hatter, B. W. Heinrich, D. Rolf, and K. J. Franke, “Scaling of Yu-Shiba-Rusinov energies in the weak-coupling Kondo regime”, Nat. Commun. **8**, 2016 (2017).

118. L. Farinacci, G. Ahmadi, M. Ruby, G. Reecht, B. W. Heinrich, C. Czekelius, F. von Oppen, and K. J. Franke, “Interfering tunneling paths through magnetic molecules on superconductors: asymmetries of Kondo and Yu-Shiba-Rusinov resonances”, Phys. Rev. Lett. **125**, 256805 (2020).

119. C. Rubio-Verdú, J. Zaldívar, R. Zitko, and J. I. Pascual, “Coupled Yu-Shiba-Rusinov states induced by a many-body molecular spin on a superconductor”, Phys. Rev. Lett. **126**, 017001 (2021).

120. A. Kamlapure, L. Cornils, R. Zitko, M. Valentyuk, R. Mozara, S. Pradhan, J. Fransson, A. I. Lichtenstein, J. Wiebe, and R. Wiesendanger, “Investigation of the Yu-Shiba-Rusinov states of a multi-impurity Kondo system”, arXiv:1911.03794 (2019).

121. F. von Oppen and K. J. Franke, “Yu-Shiba-Rusinov states in real metals”, Phys. Rev. B **103**, 205424 (2021).

122. N. Y. Yao, C. P. Moca, I. Weymann, J. D. Sau, M. D. Lukin, E. A. Demler, and G. Zaránd, “Phase diagram and excitations of a Shiba molecule”, Phys. Rev. B **90**, 241108 (2014).

123. T. Giamarchi, *Quantum physics in one dimension*, Oxford University Press, 2003.

124. D.-J. Choi, N. Lorente, J. Wiebe, K. von Bergmann, A. F. Otte, and A. J. Heinrich, “Colloquium: atomic spin chains on surfaces”, Rev. Mod. Phys. **91**, 041001 (2019).

125. Y. Makhlin, G. Schön, and A. Shnirman, “Quantum-state engineering with Josephson-junction devices”, Rev. Mod. Phys. **73**, 357 (2001).

126. J. Clarke and A. Braginski, *The squid handbook: applications of squids and squid systems, volume II*, Wiley, 2006.

127. S. M. Girvin, “Circuit QED: superconducting qubits coupled to microwave photons”, in *Quantum machines: measurement and control of engineered quantum systems*, Oxford University Press, 2014, pp. 113–256.

128. R. Wakatsuki, Y. Saito, S. Hoshino, Y. M. Itahashi, T. Ideue, M. Ezawa, Y. Iwasa, and N. Nagaosa, “Nonreciprocal charge transport in noncentrosymmetric superconductors”, Sci. Adv. **3**, e1602390 (2017).

129. F. Ando, Y. Miyasaka, T. Li, J. Ishizuka, T. Arakawa, Y. Shiota, T. Moriyama, Y. Yanase, and T. Ono, “Observation of superconducting diode effect”, Nature **584**, 373 (2020).

130. H. Narita, J. Ishizuka, R. Kawarazaki, D. Kan, Y. Shiota, T. Moriyama, Y. Shimakawa, A. V. Ognev, A. S. Samardak, Y. Yanase, and T. Ono, “Field-free superconducting diode effect in noncentrosymmetric superconductor/ferromagnet multilayers”, Nat. Nanotechnol. **17**, 823 (2022).

131. Y.-Y. Lyu, J. Jiang, Y.-L. Wang, Z.-L. Xiao, S. Dong, Q.-H. Chen, M. V. Milošević, H. Wang, R. Divan, J. E. Pearson, P. Wu, F. M. Peeters, and W.-K. Kwok, "Superconducting diode effect via conformal-mapped nanoholes", Nat. Commun. **12**, 2703 (2021).
132. J. Shin, S. Son, J. Yun, G. Park, K. Zhang, Y. J. Shin, J.-G. Park, and D. Kim, "Magnetic proximity-induced superconducting diode effect and infinite magnetoresistance in van der Waals heterostructure", arXiv:2111.05627 (2021).
133. J.-X. Lin, P. Siriviboon, H. D. Scammell, S. Liu, D. Rhodes, K. Watanabe, T. Taniguchi, J. Hone, M. S. Scheurer, and J. I. A. Li, "Zero-field superconducting diode effect in small-twist-angle trilayer graphene", Nat. Phys. **18**, 1221 (2022).
134. Y. Hou, F. Nichele, H. Chi, A. Lodesani, Y. Wu, M. Ritter, D. Haxell, M. Davydova, S. Ilić, S. Bergeret, A. Kamra, L. Fu, P. Lee, and J. Moodera, "Ubiquitous superconducting diode effect in superconductor thin films", arXiv:2205.09276 (2022).
135. A. Sundaresh, J. I. Vayrynen, Y. Lyanda-Geller, and L. P. Rokhinson, "Supercurrent non-reciprocity and vortex formation in superconductor heterostructures", arXiv:2207.03633 (2022).
136. H. Wu, Y. Wang, Y. Xu, P. K. Sivakumar, C. Pasco, U. Filippozzi, S. S. P. Parkin, Y.-J. Zeng, T. McQueen, and M. N. Ali, "The field-free Josephson diode in a van der Waals heterostructure", Nature **604**, 653 (2022).
137. C. Baumgartner, L. Fuchs, A. Costa, S. Reinhardt, S. Gronin, G. C. Gardner, T. Lindemann, M. J. Manfra, P. E. F. Junior, D. Kochan, J. Fabian, N. Paradiso, and C. Strunk, "Supercurrent rectification and magnetochiral effects in symmetric Josephson junctions", Nat. Nanotechnol. **17**, 39 (2021).
138. J. Diez-Merida, A. Diez-Carlon, S. Y. Yang, Y.-M. Xie, X.-J. Gao, K. Watanabe, T. Taniguchi, X. Lu, K. T. Law, and D. K. Efetov, "Magnetic Josephson junctions and superconducting diodes in magic angle twisted bilayer graphene", arXiv:2110.01067 (2021).
139. L. Bauriedl, C. Bäuml, L. Fuchs, C. Baumgartner, N. Paulik, J. M. Bauer, K.-Q. Lin, J. M. Lupton, T. Taniguchi, K. Watanabe, C. Strunk, and N. Paradiso, "Supercurrent diode effect and magnetochiral anisotropy in few-layer $NbSe_2$", Nat. Commun. **13**, 4266 (2022).
140. B. Pal, A. Chakraborty, P. K. Sivakumar, M. Davydova, A. K. Gopi, A. K. Pandeya, J. A. Krieger, Y. Zhang, M. Date, S. Ju, N. Yuan, N. B. M. Schröter, L. Fu, and S. S. P. Parkin, "Josephson diode effect from Cooper pair momentum in a topological semimetal", Nat. Phys. **18**, 1228 (2022).
141. K.-R. Jeon, J.-K. Kim, J. Yoon, J.-C. Jeon, H. Han, A. Cottet, T. Kontos, and S. S. P. Parkin, "Zero-field polarity-reversible Josephson supercurrent diodes enabled by a proximity-magnetized Pt barrier", Nat. Mat. **21**, 1008 (2022).
142. B. Turini, S. Salimian, M. Carrega, A. Iorio, E. Strambini, F. Giazotto, V. Zannier, L. Sorba, and S. Heun, "Josephson diode effect in high-mobility InSb nanoflags", Nano Lett. **22**, 8502 (2022).
143. M. Gupta, G. V. Graziano, M. Pendharkar, J. T. Dong, C. P. Dempsey, C. Palmstrøm, and V. S. Pribiag, "Superconducting diode effect in a three-terminal Josephson device", arXiv:2206.08471 (2022).

144. J. Chiles, E. G. Arnault, C.-C. Chen, T. F. Q. Larson, L. Zhao, K. Watanabe, T. Taniguchi, F. Amet, and G. Finkelstein, "Non-reciprocal supercurrents in a field-free graphene Josephson triode", arXiv:2210.02644 (2022).

145. J. Hu, C. Wu, and X. Dai, "Proposed design of a Josephson diode", Phys. Rev. Lett. **99**, 067004 (2007).

146. T. Yokoyama, M. Eto, and Y. V. Nazarov, "Josephson current through semiconductor nanowire with spin–orbit interaction in magnetic field", J. Phys. Soc. Jpn. **82**, 054703 (2013).

147. F. Dolcini, M. Houzet, and J. S. Meyer, "Topological Josephson ϕ_0 junctions", Phys. Rev. B **92**, 035428 (2015).

148. Y. Zhang, Y. Gu, J. Hu, and K. Jiang, "General theory of Josephson diodes", arXiv:2112.08901 (2021).

149. A. A. Kopasov, A. G. Kutlin, and A. S. Mel'nikov, "Geometry controlled superconducting diode and anomalous Josephson effect triggered by the topological phase transition in curved proximitized nanowires", Phys. Rev. B **103**, 144520 (2021).

150. M. Davydova, S. Prembabu, and L. Fu, "Universal Josephson diode effect", Sci. Adv. **8**, eabo0309 (2022).

151. R. S. Souto, M. Leijnse, and C. Schrade, "The Josephson diode effect in supercurrent interferometers", arXiv:2205.04469 (2022).

152. Y. Tanaka, B. Lu, and N. Nagaosa, "Theory of giant diode effect in d-wave superconductor junctions on the surface of a topological insulator", Phys. Rev. B **106**, 214524 (2022).

153. K. Misaki and N. Nagaosa, "Theory of the nonreciprocal Josephson effect", Phys. Rev. B **103**, 245302 (2021).

154. S. Plugge, A. Rasmussen, R. Egger, and K. Flensberg, "Majorana box qubits", New J. Phys. **19**, 012001 (2017).

155. D. Litinski, M. S. Kesselring, J. Eisert, and F. von Oppen, "Combining topological hardware and topological software: color-code quantum computing with topological superconductor networks", Phys. Rev. X **7**, 031048 (2017).

156. D. Litinski and F. von Oppen, "Quantum computing with Majorana fermion codes", Phys. Rev. B **97**, 205404 (2018).

157. A. R. Akhmerov, "Topological quantum computation away from the ground state using Majorana fermions", Phys. Rev. B **82**, 020509(R) (2010).

158. J. Liu, F. Xia, D. Xiao, F. J. García de Abajo, and D. Sun, "Semimetals for high-performance photodetection", Nat. Mater. **19**, 830 (2020).

159. D. A. Kleinman, "Theory of second harmonic generation of light", Phys. Rev. **128**, 1761 (1962).

160. V. I. Belinicher and B. I. Sturman, "The photogalvanic effect in media lacking a center of symmetry", Phys.-Usp. **23**, 199 (1980).

161. K. Sun, S.-S. Sun, L.-L. Wei, C. Guo, H.-F. Tian, G.-F. Chen, H.-X. Yang, and J.-Q. Li, “Circular photogalvanic effect in the Weyl semimetal TaAs”, Chin. Phys. Lett. **34**, 117203 (2017).
162. Q. Ma, S.-Y. Xu, C.-K. Chan, C.-L. Zhang, G. Chang, Y. Lin, W. Xie, T. Palacios, H. Lin, S. Jia, P. A. Lee, P. Jarillo-Herrero, and N. Gedik, “Direct optical detection of Weyl fermion chirality in a topological semimetal”, Nat. Phys. **13**, 842 (2017).
163. Y. Zhang, H. Ishizuka, J. van den Brink, C. Felser, B. Yan, and N. Nagaosa, “Photogalvanic effect in Weyl semimetals from first principles”, Phys. Rev. B **97**, 241118 (2018).
164. J. Ahn, G.-Y. Guo, and N. Nagaosa, “Low-frequency divergence and quantum geometry of the bulk photovoltaic effect in topological semimetals”, Phys. Rev. X **10**, 041041 (2020).
165. H. Watanabe and Y. Yanase, “Chiral photocurrent in parity-violating magnet and enhanced response in topological antiferromagnet”, Phys. Rev. X **11**, 11001 (2021).
166. Q. Wang, J. Zheng, Y. He, J. Cao, X. Liu, M. Wang, J. Ma, J. Lai, H. Lu, S. Jia, D. Yan, Y. Shi, J. Duan, J. Han, W. Xiao, J.-H. Chen, K. Sun, Y. Yao, and D. Sun, “Robust edge photocurrent response on layered type II Weyl semimetal WTe_2”, Nat. Commun. **10**, 5736 (2019).
167. G. Chang, J.-X. Yin, T. Neupert, D. S. Sanchez, I. Belopolski, S. S. Zhang, T. A. Cochran, Z. Chéng, M.-C. Hsu, S.-M. Huang, B. Lian, S.-Y. Xu, H. Lin, and M. Z. Hasan, “Unconventional photocurrents from surface Fermi arcs in topological chiral semimetals”, Phys. Rev. Lett. **124**, 166404 (2020).
168. S. Li and A. V. Andreev, “Spiraling Fermi arcs in Weyl materials”, Phys. Rev. B **92**, 201107 (2015).
169. N. Bovenzi, M. Breitkreiz, T. E. O’Brien, J. Tworzydło, and C. W. J. Beenakker, “Twisted Fermi surface of a thin-film Weyl semimetal”, New J. Phys. **20**, 023023 (2018).
170. A. Altland and B. D. Simons, *Condensed matter field theory*, Cambridge University Press, 2010.
171. V. Ambegaokar and A. Baratoff, “Tunneling between superconductors”, Phys. Rev. Lett. **10**, 486 (1963).
172. A. Zazunov, V. Shumeiko, E. Bratus, J. Lantz, and G. Wendin, “Andreev level qubit”, Phys. Rev. Lett. **90**, 087003 (2003).
173. C. Janvier, L. Tosi, L. Bretheau, Ç. Ö. Girit, M. Stern, P. Bertet, P. Joyez, D. Vion, D. Esteve, M. F. Goffman, H. Pothier, and C. Urbina, “Coherent manipulation of Andreev states in superconducting atomic contacts”, Science **349**, 1199 (2015).
174. M. Hays, V. Fatemi, D. Bouman, J. Cerrillo, S. Diamond, K. Serniak, T. Connolly, P. Krogstrup, J. Nygård, A. L. Yeyati, A. Geresdi, and M. H. Devoret, “Coherent manipulation of an Andreev spin qubit”, Science **373**, 430 (2021).
175. A. O. Caldeira and A. J. Leggett, “Influence of dissipation on quantum tunneling in macroscopic systems”, Phys. Rev. Lett. **46**, 211 (1981).
176. P. W. Anderson, “Theory of dirty superconductors”, J. Phys. Chem. Solids **11**, 26 (1959).
177. M. A. Ruderman and C. Kittel, “Indirect exchange coupling of nuclear magnetic moments by conduction electrons”, Phys. Rev. **96**, 99 (1954).

178. T. Kasuya, "A theory of metallic ferro- and antiferromagnetism on Zener's model", Prog. Theor. Phys. **16**, 45 (1956).
179. K. Yosida, "Magnetic properties of cu-mn alloys", Phys. Rev. **106**, 893 (1957).
180. J. Kondo, "Resistance minimum in dilute magnetic alloys", Prog. Theo. Phys. **32**, 37 (1964).
181. P. W. Anderson, "A poor man's derivation of scaling laws for the Kondo problem", J. Phys. C **3**, 2436 (1970).
182. K. G. Wilson, "The renormalization group: critical phenomena and the Kondo problem", Rev. Mod. Phys. **47**, 773 (1975).
183. P. Nozieres, "A "fermi-liquid" description of the Kondo problem at low temperatures", J. Low Temp. Phys. **17**, 31 (1974).
184. K. Satori, H. Shiba, O. Sakai, and Y. Shimizu, "Numerical renormalization group study of magnetic impurities in superconductors", J. Phys. Soc. Jpn. **61**, 3239 (1992).
185. O. Sakai, Y. Shimizu, H. Shiba, and K. Satori, "Numerical renormalization group study of magnetic impurities in superconductors. ii. dynamical excitation spectra and spatial variation of the order parameter", J. Phys. Soc. Jpn. **62**, 3181 (1993).
186. R. Zitko, O. Bodensiek, and T. Pruschke, "Effects of magnetic anisotropy on the subgap excitations induced by quantum impurities in a superconducting host", Phys. Rev. B **83**, 054512 (2011).
187. J. Alicea, Y. Oreg, G. Refael, F. von Oppen, and M. P. A. Fisher, "Non-abelian statistics and topological quantum information processing in 1D wire networks", Nat. Phys. **7**, 412 (2011).
188. G. Goldstein and C. Chamon, "Decay rates for topological memories encoded with Majorana fermions", Phys. Rev. B **84**, 205109 (2011).
189. D. Rainis and D. Loss, "Majorana qubit decoherence by quasiparticle poisoning", Phys. Rev. B **85**, 174533 (2012).
190. M. J. Schmidt, D. Rainis, and D. Loss, "Decoherence of Majorana qubits by noisy gates", Phys. Rev. B **86**, 085414 (2012).
191. Y. Hu, Z. Cai, M. A. Baranov, and P. Zoller, "Majorana fermions in noisy Kitaev wires", Phys. Rev. B **92**, 165118 (2015).
192. C. Knapp, T. Karzig, R. M. Lutchyn, and C. Nayak, "Dephasing of Majorana-based qubits", Phys. Rev. B **97**, 125404 (2018).
193. T. Li, W. A. Coish, M. Hell, K. Flensberg, and M. Leijnse, "Four-Majorana qubit with charge readout: dynamics and decoherence", Phys. Rev. B **98**, 205403 (2018).
194. R. V. Mishmash, B. Bauer, F. von Oppen, and J. Alicea, "Dephasing and leakage dynamics of noisy Majorana-based qubits: topological versus Andreev", Phys. Rev. B **101**, 075404 (2020).
195. A. A. Clerk, M. H. Devoret, S. M. Girvin, F. Marquardt, and R. J. Schoelkopf, "Introduction to quantum noise, measurement, and amplification", Rev. Mod. Phys. **82**, 1155 (2010).

196. C. Herring, “Accidental degeneracy in the energy bands of crystals”, Phys. Rev. **52**, 365 (1937).
197. R. Pawlak, S. Hoffman, J. Klinovaja, D. Loss, and E. Meyer, “Majorana fermions in magnetic chains”, Prog. Part. Nucl. Phys. **107**, 1 (2019).
198. B. Jäck, Y. Xie, and A. Yazdani, “Detecting and distinguishing Majorana zero modes with the scanning tunneling microscope”, Nat. Rev. Phys. **3**, 541 (2021).
199. R. Pawlak, M. Kisiel, J. Klinovaja, T. Meier, S. Kawai, T. Glatzel, D. Loss, and E. Meyer, “Probing atomic structure and Majorana wavefunctions in mono-atomic Fe chains on superconducting Pb surface”, npj Quantum Inf. **2**, 16035 (2016).
200. B. E. Feldman, M. T. Randeria, J. Li, S. Jeon, Y. Xie, Z. Wang, I. K. Drozdov, B. Andrei Bernevig, and A. Yazdani, “High-resolution studies of the Majorana atomic chain platform”, Nat. Phys. **13**, 286 (2017).
201. S. Jeon, Y. Xie, J. Li, Z. Wang, B. A. Bernevig, and A. Yazdani, “Distinguishing a Majorana zero mode using spin-resolved measurements.”, Science **358**, 772 (2017).
202. H. Kim, A. Palacio-Morales, T. Posske, L. Rózsa, K. Palotás, L. Szunyogh, M. Thorwart, and R. Wiesendanger, “Toward tailoring Majorana bound states in artificially constructed magnetic atom chains on elemental superconductors”, Sci. Adv. **4**, eaar5251 (2018).
203. J. Li, H. Chen, I. K. Drozdov, A. Yazdani, B. A. Bernevig, and A. H. Macdonald, “Topological superconductivity induced by ferromagnetic metal chains”, Phys. Rev. B **90**, 235433 (2014).
204. Y. Peng, F. Pientka, L. I. Glazman, and F. von Oppen, “Strong localization of Majorana end states in chains of magnetic adatoms”, Phys. Rev. Lett. **114**, 106801 (2015).
205. A. Sakurai, “Comments on superconductors with magnetic impurities”, Prog. Theor. Phys. **44**, 1472 (1970).
206. E. J. Lee, X. Jiang, M. Houzet, R. Aguado, C. M. Lieber, and S. De Franceschi, “Spin-resolved Andreev levels and parity crossings in hybrid superconductor-semiconductor nanostructures”, Nat. Nanotechnol. **9**, 79 (2014).
207. P. A. Lee, N. Nagaosa, and X.-G. Wen, “Doping a mott insulator: physics of high-temperature superconductivity”, Rev. Mod. Phys. **78**, 17 (2006).
208. R. Zitko, M. Lee, R. López, R. Aguado, and M.-S. Choi, “Josephson current in strongly correlated double quantum dots”, Phys. Rev. Lett. **105**, 116803 (2010).
209. E. Vecino, A. Martín-Rodero, and A. L. Yeyati, “Josephson current through a correlated quantum level: andreev states and π junction behavior”, Phys. Rev. B **68**, 035105 (2003).
210. K. A. Chao, J. Spałek, and A. M. Oleś, “Canonical perturbation expansion of the Hubbard model”, Phys. Rev. B **18**, 3453 (1978).
211. B. Doucot and X. G. Wen, “Instability of the nagaoka state with more than one hole”, Phys. Rev. B **40**, 2719 (1989).
212. E. M. Stoudenmire, J. Alicea, O. A. Starykh, and M. P. Fisher, “Interaction effects in topological superconducting wires supporting Majorana fermions”, Phys. Rev. B **84**, 014503 (2011).

213. T.-P. Choy, J. M. Edge, A. R. Akhmerov, and C. W. J. Beenakker, “Majorana fermions emerging from magnetic nanoparticles on a superconductor without spin-orbit coupling”, Phys. Rev. B **84**, 195442 (2011).

214. J. D. Sau and S. D. Sarma, “Realizing a robust practical Majorana chain in a quantum-dot-superconductor linear array”, Nat. Commun. **3**, 964 (2012).

215. I. C. Fulga, A. Haim, A. R. Akhmerov, and Y. Oreg, “Adaptive tuning of Majorana fermions in a quantum dot chain”, New J. Phys. **15**, 045020 (2013).

216. K. Grove-Rasmussen, G. Steffensen, A. Jellinggaard, M. H. Madsen, R. Zitko, J. Paaske, and J. Nygard, “Yu–Shiba–Rusinov screening of spins in double quantum dots”, Nat. Commun. **9**, 2376 (2018).

217. J. C. Estrada Saldaña, A. Vekris, R. Zitko, G. Steffensen, P. Krogstrup, J. Paaske, K. Grove-Rasmussen, and J. Nygård, “Two-impurity Yu-Shiba-Rusinov states in coupled quantum dots”, Phys. Rev. B **102**, 195143 (2020).

218. J. P. Dehollain, U. Mukhopadhyay, V. P. Michal, Y. Wang, B. Wunsch, C. Reichl, W. Wegscheider, M. S. Rudner, E. Demler, and L. M. K. Vandersypen, “Nagaoka ferromagnetism observed in a quantum dot plaquette”, Nature **579**, 528 (2020).

219. J. H. Scaff and R. S. Ohl, “Development of Silicon Crystal Rectifiers for Microwave Radar Receivers”, Bell Syst. Tech. J. **26**, 1 (1947).

220. W. Shockley, “The Theory of p-n Junctions in Semiconductors and p-n Junction Transistors”, Bell Syst. Tech. J. **28**, 435 (1949).

221. Y. Tokura and N. Nagaosa, “Nonreciprocal responses from non-centrosymmetric quantum materials”, Nat. Commun. **9**, 3740 (2018).

222. A. Daido, Y. Ikeda, and Y. Yanase, “Intrinsic superconducting diode effect”, Phys. Rev. Lett. **128**, 037001 (2022).

223. J. J. He, Y. Tanaka, and N. Nagaosa, “A phenomenological theory of superconductor diodes”, New J. Phys. **24**, 053014 (2022).

224. S. Ilić and F. S. Bergeret, “Theory of the supercurrent diode effect in Rashba superconductors with arbitrary disorder”, Phys. Rev. Lett. **128**, 177001 (2022).

225. N. F. Q. Yuan and L. Fu, “Supercurrent diode effect and finite momentum superconductivity”, Proc. Natl. Acad. Sci. **119**, e2119548119 (2022).

226. V. Ambegaokar, U. Eckern, and G. Schön, “Quantum dynamics of tunneling between superconductors”, Phys. Rev. Lett. **48**, 1745 (1982).

227. U. Eckern, G. Schön, and V. Ambegaokar, “Quantum dynamics of a superconducting tunnel junction”, Phys. Rev. B **30**, 6419 (1984).

228. R. L. Kautz and J. M. Martinis, “Noise-affected I-V curves in small hysteretic Josephson junctions”, Phys. Rev. B **42**, 9903 (1990).

229. W. C. Stewart, "Current-voltage characteristics of Josephson junctions", Appl. Phys. Lett. **12**, 277 (1968).

230. C. W. Gardiner, *Handbook of stochastic methods*, Springer Berlin Heidelberg, 1985.

231. A. Kamenev, *Field theory of non-equilibrium systems*, Cambridge University Press, 2011.

232. P. Hänggi, P. Talkner, and M. Borkovec, "Reaction-rate theory: fifty years after Kramers", Rev. Mod. Phys. **62**, 251 (1990).

233. H. A. Kramers, "Brownian motion in a field of force and the diffusion model of chemical reactions", Physica **7**, 284 (1940).

234. L. Farkas, "Keimbildungsgeschwindigkeit in übersättigten dämpfen", Z. Phys. Chem. **125**, 236 (1927).

235. E. Ben-Jacob, D. J. Bergman, B. J. Matkowsky, and Z. Schuss, "Lifetime of oscillatory steady states", Phys. Rev. A **26**, 2805 (1982).

236. R. Cristiano and P. Silvestrini, "Decay of the running state in underdamped Josephson junctions", J. Appl. Phys. **59**, 1401 (1986).

237. G. D. Mahan, *Many-particle physics*, Springer New York, 2000.

238. J. C. Cuevas, A. Martín-Rodero, and A. L. Yeyati, "Hamiltonian approach to the transport properties of superconducting quantum point contacts", Phys. Rev. B **54**, 7366 (1996).

239. J. C. Cuevas, A. Martín-Rodero, and A. L. Yeyati, "Shot noise and coherent multiple charge transfer in superconducting quantum point contacts", Phys. Rev. Lett. **82**, 4086 (1999).

240. D. Averin and A. Bardas, "Ac Josephson effect in a single quantum channel", Phys. Rev. Lett. **75**, 1831 (1995).

241. Y. V. Nazarov and Y. M. Blanter, *Quantum transport: introduction to nanoscience*, Cambridge University Press, 2009.

242. Y. Oreg and F. von Oppen, "Majorana zero modes in networks of cooper-pair boxes: topologically ordered states and topological quantum computation", Ann. Rev. Cond. Mat. Phys. **11**, 397 (2020).

243. R. M. Lutchyn, E. P. a. M. Bakkers, L. P. Kouwenhoven, P. Krogstrup, C. M. Marcus, and Y. Oreg, "Majorana zero modes in superconductor–semiconductor heterostructures", Nat. Rev. Mat. **3**, 52 (2018).

244. S. Vijay, T. H. Hsieh, and L. Fu, "Majorana fermion surface code for universal quantum computation", Phys. Rev. X **5**, 041038 (2015).

245. S. Hoffman, C. Schrade, J. Klinovaja, and D. Loss, "Universal quantum computation with hybrid spin-Majorana qubits", Phys. Rev. B **94**, 045316 (2016).

246. O. Zilberberg, B. Braunecker, and D. Loss, "Controlled-not gate for multiparticle qubits and topological quantum computation based on parity measurements", Phys. Rev. A **77**, 012327 (2008).

247. L. Fu, "Electron teleportation via Majorana bound states in a mesoscopic superconductor", Phys. Rev. Lett. **104**, 056402 (2010).

248. H. M. Wiseman and G. J. Milburn, *Quantum measurement and control*, Cambridge University Press, 2009.

249. S. Hoffman, D. Chevallier, D. Loss, and J. Klinovaja, "Spin-dependent coupling between quantum dots and topological quantum wires", Phys. Rev. B **96**, 045440 (2017).

250. A. N. Korotkov, "Continuous quantum measurement of a double dot", Phys. Rev. B **60**, 5737 (1999).

251. H.-S. Goan and G. J. Milburn, "Dynamics of a mesoscopic charge quantum bit under continuous quantum measurement", Phys. Rev. B **64**, 235307 (2001).

252. B. Baumgartner and H. Narnhofer, "Analysis of quantum semigroups with GKS–Lindblad generators: II. General", J. Phys. A: Math. Theor. **41**, 395303 (2008).

253. V. V. Albert and L. Jiang, "Symmetries and conserved quantities in Lindblad master equations", Phys. Rev. A **89**, 022118 (2014).

254. K. Mølmer, "Hypothesis testing with open quantum systems", Phys. Rev. Lett. **114**, 040401 (2015).

255. M. I. K. Munk, R. Egger, and K. Flensberg, "Fidelity and visibility loss in Majorana qubits by entanglement with environmental modes", Phys. Rev. B **99**, 155419 (2019).

256. A. L. Grimsmo and T. B. Smith, "Majorana qubit readout using longitudinal qubit-resonator interaction", Phys. Rev. B **99**, 235420 (2019).

257. L. Qin, X.-Q. Li, A. Shnirman, and G. Schön, "Transport signatures of a Majorana qubit and read-out-induced dephasing", New J. Phys. **21**, 043027 (2019).

258. K. Flensberg, "Non-abelian operations on Majorana fermions via single-charge control", Phys. Rev. Lett. **106**, 090503 (2011).

259. K. Yavilberg, E. Ginossar, and E. Grosfeld, "Fermion parity measurement and control in Majorana circuit quantum electrodynamics", Phys. Rev. B **92**, 075143 (2015).

260. C. Ohm and F. Hassler, "Microwave readout of Majorana qubits", Phys. Rev. B **91**, 085406 (2015).

261. D. Aasen, M. Hell, R. V. Mishmash, A. Higginbotham, J. Danon, M. Leijnse, T. S. Jespersen, J. A. Folk, C. M. Marcus, K. Flensberg, and J. Alicea, "Milestones toward Majorana-based quantum computing", Phys. Rev. X **6**, 031016 (2016).

262. K. Gharavi, D. Hoving, and J. Baugh, "Readout of Majorana parity states using a quantum dot", Phys. Rev. B **94**, 155417 (2016).

263. A. Romito and Y. Gefen, "Ubiquitous nonlocal entanglement with Majorana zero modes", Phys. Rev. Lett. **119**, 157702 (2017).

264. K. Zhou, C. Zhang, L. Qin, and X.-Q. Li, "Double-dot interferometer for quantum measurement of majorana qubits and stabilizers*", Chin. Phys. B **30**, 010301 (2021).
265. G. Széchenyi and A. Pályi, "Parity-to-charge conversion for readout of topological majorana qubits", Phys. Rev. B **101**, 235441 (2020).
266. A. Blais, R.-S. Huang, A. Wallraff, S. M. Girvin, and R. J. Schoelkopf, "Cavity quantum electrodynamics for superconducting electrical circuits: an architecture for quantum computation", Phys. Rev. A **69**, 062320 (2004).
267. J. R. Petta, A. C. Johnson, J. M. Taylor, E. A. Laird, A. Yacoby, M. D. Lukin, C. M. Marcus, M. P. Hanson, and A. C. Gossard, "Coherent manipulation of coupled electron spins in semiconductor quantum dots", Science **309**, 2180 (2005).
268. M. I. K. Munk, J. Schulenborg, R. Egger, and K. Flensberg, "Parity-to-charge conversion in majorana qubit readout", Phys. Rev. Res. **2**, 033254 (2020).
269. S.-Y. Xu, C. Liu, S. K. Kushwaha, R. Sankar, J. W. Krizan, I. Belopolski, M. Neupane, G. Bian, N. Alidoust, T.-R. Chang, H.-T. Jeng, C.-Y. Huang, W.-F. Tsai, H. Lin, P. P. Shibayev, F.-C. Chou, R. J. Cava, and M. Z. Hasan, "Observation of Fermi arc surface states in a topological metal", Science **347**, 294 (2015).
270. A. A. Burkov, "Weyl Metals", Annu. Rev. Condens. Matter Phys. **9**, 359 (2018).
271. S. L. Adler, "Axial-vector vertex in spinor electrodynamics", Phys. Rev. **177**, 2426 (1969).
272. J. S. Bell and R. Jackiw, "A PCAC puzzle: $\pi^0\rightarrow\gamma\gamma$ in the σ-model", Nuovo Cimento A Serie **60**, 47 (1969).
273. L. Balents, "Weyl electrons kiss", Physics (College. Park. Md). **4**, 36 (2011).
274. N. P. Armitage, E. J. Mele, and A. Vishwanath, "Weyl and Dirac semimetals in three dimensional solids", Rev. Mod. Phys. **90**, 015001 (2018).
275. E. Ivchenko and G. Pikus, *Superlattices and other heterostructures: symmetry and optical phenomena*, Springer Berlin Heidelberg, 1997.
276. J. E. Sipe and A. I. Shkrebtii, "Second-order optical response in semiconductors", Phys. Rev. B **61**, 5337 (2000).
277. G. B. Osterhoudt, L. K. Diebel, M. J. Gray, X. Yang, J. Stanco, X. Huang, B. Shen, N. Ni, P. J. W. Moll, Y. Ran, and K. S. Burch, "Colossal mid-infrared bulk photovoltaic effect in a type-I Weyl semimetal", Nat. Mater. **18**, 471 (2019).
278. Y. Zhang, T. Holder, H. Ishizuka, F. de Juan, N. Nagaosa, C. Felser, and B. Yan, "Switchable magnetic bulk photovoltaic effect in the two-dimensional magnet CrI_3", Nat. Commun. **10**, 3783 (2019).
279. T. Holder, D. Kaplan, and B. Yan, "Consequences of time-reversal-symmetry breaking in the light-matter interaction: Berry curvature, quantum metric, and diabatic motion", Phys. Rev. Res. **2**, 033100 (2020).

280. R. Fei, W. Song, and L. Yang, "Giant photogalvanic effect and second-harmonic generation in magnetic axion insulators", Phys. Rev. B **102**, 035440 (2020).

281. V. L. Alperovich, V. I. Belinicher, V. N. Novikov, and A. S. Terekhov, "Surface photogalvanic effect in solids - Theory and experiment for band-to-band transitions in gallium arsenide", Sov. Phys. JETP **53**, 1201 (1981).

282. L. I. Magarill and M. V. Ehntin, "Surface photogalvanic effect in metals", Sov. Phys. JETP **54**, 531 (1981).

283. J. E. Moore and J. Orenstein, "Confinement-induced berry phase and helicity-dependent photocurrents", Phys. Rev. Lett. **105**, 026805 (2010).

284. P. Hosur, "Circular photogalvanic effect on topological insulator surfaces: berry-curvature-dependent response", Phys. Rev. B **83**, 035309 (2011).

285. A. Junck, G. Refael, and F. von Oppen, "Photocurrent response of topological insulator surface states", Phys. Rev. B **88**, 075144 (2013).

286. N. H. Lindner, A. Farrell, E. Lustig, G. Refael, and F. von Oppen, "Lighting up topological insulators: large surface photocurrents from magnetic superlattices", arXiv:1403.0010 (2014).

287. K. W. Kim, T. Morimoto, and N. Nagaosa, "Shift charge and spin photocurrents in Dirac surface states of topological insulator", Phys. Rev. B **95**, 035134 (2017).

288. F. D. M. Haldane, "Attachment of surface "Fermi arcs" to the bulk Fermi surface: "Fermi-level plumbing" in topological metals", arXiv:1401.0529 (2014).

289. N. Morali, R. Batabyal, P. K. Nag, E. Liu, Q. Xu, Y. Sun, B. Yan, C. Felser, N. Avraham, and H. Beidenkopf, "Fermi-arc diversity on surface terminations of the magnetic Weyl semimetal $Co_3Sn_2S_2$", Science **365**, 1286 (2019).

290. J. Fujii, B. Ghosh, I. Vobornik, A. Sarkar, D. Mondal, C. Kuo, F. Bocquet, D. Boukhvalov, C. S. Lue, A. Agarwal, and A. Politano, "Mitrofanovite Pt_3Te_4: a topological metal with termination-dependent surface band structure and strong spin polarization", ACS Nano, 14786 (2021).

291. M. V. Berry and R. J. Mondragon, "Neutrino billiards: time-reversal symmetry-breaking without magnetic fields", Proc. R. Soc. Lond. A **412**, 53 (1987).

292. A. Avdoshkin, V. Kozii, and J. E. Moore, "Interactions remove the quantization of the chiral photocurrent at Weyl points", Phys. Rev. Lett. **124**, 196603 (2020).

293. P. J. Moll, "Focused ion beam microstructuring of quantum matter", Annu. Rev. Condens. Matter Phys. **9**, 147 (2018).

294. S. Nishihaya, M. Uchida, Y. Nakazawa, R. Kurihara, K. Akiba, M. Kriener, A. Miyake, Y. Taguchi, M. Tokunaga, and M. Kawasaki, "Quantized surface transport in topological Dirac semimetal films", Nat. Commun. **10**, 2564 (2019).

295. A. Bedoya-Pinto, A. K. Pandeya, D. Liu, H. Deniz, K. Chang, H. Tan, H. Han, J. Jena, I. Kostanovskiy, and S. S. Parkin, "Realization of epitaxial NbP and TaP Weyl semimetal thin films", ACS Nano **14**, 4405 (2020).

296. P. Qin, Z. Feng, X. Zhou, H. Guo, J. Wang, H. Yan, X. Wang, H. Chen, X. Zhang, H. Wu, Z. Zhu, and Z. Liu, “Anomalous Hall effect, robust negative magnetoresistance, and memory devices based on a noncollinear antiferromagnetic metal”, ACS Nano **14**, 6242 (2020).

297. S. Ghosh, V. Patil, A. Basu, Kuldeep, D. A. Jangade, R. Kulkarni, A. Thamizhavel, and M. M. Deshmukh, “High-temperature superconducting diode”, arXiv:2210.11256 (2022).

298. T. Golod and V. M. Krasnov, “Demonstration of a superconducting diode-with-memory, operational at zero magnetic field with switchable nonreciprocity”, Nat. Commun. **13**, 3658 (2022).

299. H. Grabert and G.-L. Ingold, “Mesoscopic Josephson effect”, Superlattices Microstruct. **25**, 915 (1999).

300. H.-S. Goan, G. J. Milburn, H. M. Wiseman, and H. Bi Sun, “Continuous quantum measurement of two coupled quantum dots using a point contact: a quantum trajectory approach”, Phys. Rev. B **63**, 125326 (2001).

301. H. M. Wiseman and G. J. Milburn, “Quantum theory of field-quadrature measurements”, Phys. Rev. A **47**, 642 (1993).